

# **Modelling, Analysis, and Simulation of Underwater Acoustic Channels**



**Meisam Naderi**

**Modelling, Analysis, and Simulation of  
Underwater Acoustic Channels**

Doctoral Dissertation for the Degree *Philosophiae Doctor (PhD)* at  
the Faculty of Engineering and Science, Specialization in  
Information and Communication Technology

University of Agder  
Faculty of Engineering and Science  
2017

Doctoral Dissertations at the University of Agder 169

ISBN: 978-82-7117-865-9

ISSN: 1504-9272

©Meisam Naderi, 2017

Printed by Wittusen & Jensen

Oslo

*To my wife, Vida*

*To my parents and my siblings*



# Preface and Acknowledgements

Praise be to God, the most merciful and the most gracious. Without his blessing my accomplishment would never been possible.

The research work in this dissertation was carried out at the Department of Information and Communication Technology (ICT), Mobile Communications Group (MCG) of the University of Agder (UiA) in Grimstad, Norway. To writ this dissertation and the papers produced during the author's PhD study,  $\LaTeX$  has been adopted. The mathematical calculations and simulation results are obtained by using MATLAB. The completion of this dissertation was a monumental task that I would have not been able to accomplish without the supports of many individuals to whom I would like to express my gratitude.

I am very grateful to my supervisor Prof. Matthias Pätzold. His excellent supervision, valuable comments, and constant supports helped me a lot in moulding my efforts into favorable outcomes. I am grateful to Prof. Alenka G. Zajić for hosting me at the Georgia Institute of Technology (GATECH) in Atlanta, USA. Moreover, I would like to express my gratitude to Dr. Alireza Borhani and Prof. Frank Y. Li from UiA for their useful comments and ideas.

I would like to thank the MCG secretary, Mrs. Katharina Pätzold, for her continual support. I also appreciate the timely advices of the coordinator of the PhD program at UiA, Mrs. Emma Elizabeth Horneman and advisor of ICT Department Mrs. Tonje Sti. My sincere gratitude goes to my Doctoral Fellows (present and former) in ICT department, especially to Parvaneh Sarshar, Mohamed Ali Saleh Abomhara, Nurilla Avazov, and Akmal Fayziyev. They made my stay in Grimstad very pleasant and I benefitted immensely from their knowledge and expertise.

Last but not least, my endless appreciation goes to my parents Abolfath and Marzyeh, my wife Vida, my sister Maryam, and my brothers Mohsen, Mohammad, and Farzad, My niece Parnis, and my nephew Arad for their encouragement, love, and support throughout my life, and especially during my doctoral studies.

Meisam Naderi  
May 2017  
Grimstad, Norway



# Abstract

One of the important applications of *acoustics* is related to underwater activities, where acoustic waves play the same role as radar and electromagnetic waves do in air. Underwater acoustic (UWA) communication systems have been widely used in oceanography due to their various applications for scientific and industrial purposes. UWA communication technologies call for the need to accurate UWA channel models (among other needs). UWA channel models provide system designers with important parameters that have a direct implication on the UWA communication system design. In other word, a UWA system designer needs to know the underlying UWA channel statistics to analyze the performance of proposed transmission schemes. Owing to the complexity imposed by physical aspects of the UWA channels, the number of UWA channel models proposed in the literature is very limited. The absence of a standard UWA channel model for capturing all physical features of ocean environments also adds to the depth of this gap.

In this dissertation, the geometry-based approach is employed for the development of three types of stationary UWA channel models; under the assumptions that the observation time is short enough, two geometry-based stochastic UWA channel models and one geometry-based deterministic UWA channel model are developed. Moreover, two measurement-based channel models are developed for the modelling of a stationary and a non-stationary UWA channels.

Under the assumption of rough ocean surface and bottom conditions as well as the isovelocity condition, a channel model is developed for stationary fixed-to-mobile (F2M) UWA communication systems. Starting from a rectangular geometrical model, a reference model is derived. Then, the corresponding simulation model is derived from the reference model assuming a limited number of scatterers. For the parametrization of the UWA simulation model, two methods, namely  $L_p$ -norm method (LPNM) and method of equally space scatterers (MESS) are employed. Moreover, owing to the fact that the isovelocity assumption does not hold in many real-world scenarios, a vehicle-to-vehicle (V2V) geometry-based stochastic UWA channel model is developed assuming a non-isovelocity condition. The effect of the non-isovelocity condition has been assessed regarding its influence on the statisti-

cal properties of the UWA channel model. The UWA channel model has also been validated by matching its main characteristic quantities against measurement data.

Due to the fact that the standard assumption of a flat ocean bottom does not hold in many realistic scenarios, a new geometry-based deterministic shallow UWA channel model is developed assuming that the ocean bottom can slope gently down/up. Thus, starting from a geometrical model, a deterministic channel model is developed for V2V UWA channels assuming a smooth ocean surface and bottom. The effect of the ocean-bottom slope angle on the statistical properties of the UWA channel model is investigated. The validation of the proposed UWA channel model has been performed by fitting its main characteristic quantities to measurement data. Theoretical and simulation results show that even a relatively small slope angle significantly influences the statistical properties of UWA channels.

As mentioned, two measurement-based UWA channel models are developed for shallow UWA communication systems. The first one utilizes the iterative nonlinear least square approximation (INLSA) algorithm for designing a stationary UWA channel model. The second one is developed for non-stationary UWA channels based on measured Doppler power spectrums (DPSs). The performance of the designed UWA channel simulators are assessed by comparing their statistical properties with the corresponding quantities of the measured UWA channels. The results of the assessment show an excellent match between the statistical properties of the UWA channel simulators and those of the real-world UWA channels.

Using the sum-of-sinusoids (SOS) principle, three methods are studied for the design of one-dimensional sea surface waves simulators with two main given wave spectra. A good match between the given sea surface models and the corresponding simulation model is achieved with respect to the main statistical properties of the sea surface waves. In addition, advantages and disadvantages of each parameter computation method are also discussed.

More traditionally, the performance of Alamouti-coded orthogonal frequency division multiplexing (OFDM) systems over a proposed UWA channel model is analyzed. A realistic UWA channel model has been considered, which can be correlated in either time or space or simultaneously in both domains. An exact analytical expression for the bit error probability (BEP) has been derived. The BEPs of two special cases are also studied, where the UWA channel is only correlated in either time or space. The performance of the Alamouti-coded OFDM system over the UWA channel has been assessed for different maximum Doppler frequencies and antenna spacings.

# List of Publications

All the papers listed below are an outcome of the research work carried out by the author of this dissertation, including one submitted and six published papers.

## Papers Included in the Dissertation

- Paper A:** M. Naderi, M. Pätzold, and A. G. Zajić, A geometry-based channel model for shallow underwater acoustic channels under rough surface and bottom scattering conditions, in *Proc. 5th Int. Conf. Commun. and Electron. (ICCE)*, DaNang, Vietnam, Jul./Aug. 2014, pp. 112-117.
- Paper B:** M. Naderi, M. Pätzold, and A. Zajić, A non-isovelocity geometrybased underwater acoustic channel model, Submitted to *IEEE Trans. Veh. Technol.*, 2017.
- Paper C:** M. Naderi, M. Pätzold, R. Hicheri, and N. Youssef, A geometry-based underwater acoustic channel model allowing for sloped ocean bottom conditions, *IEEE Trans. Wireless Commun.*, vol. 16, no. 4, pp. 2394–2408, Apr. 2017.
- Paper D:** M. Naderi, M. Pätzold, and A. G. Zajić, The design of measurement-based underwater acoustic channel simulators using the INLSA algorithm, in *Proc. IEEE OCEANS*, Genova, Italy, May 2015, pp. 1-6.
- Paper E:** M. Naderi, D. V. Ha, V. D. Nguyen, and M. Pätzold, Modelling the Doppler power spectrum of non-stationary underwater acoustic channels based on Doppler measurements, in *Proc. IEEE OCEANS*, Aberdeen, Scotland (accepted), Jun. 2017.
- Paper F:** M. Naderi and M. Pätzold, Design and analysis of a one-dimensional sea surface simulator using the sum-of-sinusoids principle, in *Proc. IEEE OCEANS*, Washington, USA, Oct. 2015, pp. 1-7.

**Paper G:** M. Naderi, G. Rafiq, and M. Pätzold, Performance analysis of Alamouti-coded OFDM systems over spatio-temporally correlated underwater acoustic channels, in *Proc. International Conference on Communications (ICC)*, Paris, France (accepted), May 2017.

# Contents

<b>Preface and Acknowledgements</b>	<b>vii</b>
<b>Abstract</b>	<b>ix</b>
<b>List of Publications</b>	<b>xi</b>
<b>List of Figures</b>	<b>xxi</b>
<b>List of Tables</b>	<b>xxiii</b>
<b>List of Abbreviations</b>	<b>xxv</b>
<b>PART I</b>	<b>3</b>
<b>1 Introduction</b>	<b>3</b>
1.1 The JANUS UWA Communications Standard . . . . .	5
1.2 Principles of UWA Channel Modelling . . . . .	5
1.3 Approaches and Features of UWA Channel Modelling . . . . .	6
1.4 Motivations . . . . .	8
1.5 Research Questions . . . . .	8
1.6 Organization of the Dissertation . . . . .	9
<b>2 Geometry-Based Stochastic UWA Channel Modelling</b>	<b>11</b>
2.1 Introduction . . . . .	11
2.2 Rough Surface and Bottom Scattering Conditions . . . . .	12
2.2.1 Reference Model . . . . .	13
2.2.2 Simulation Model and Parameter Computation Methods . . . . .	14
2.3 Non-Isovelocity Ocean Condition . . . . .	15
2.4 Chapter Summary and Conclusion . . . . .	18
<b>3 Geometry-Based Deterministic UWA Channel Modelling</b>	<b>19</b>
3.1 Introduction . . . . .	19
3.2 Slopped Ocean Bottom Condition . . . . .	19
3.3 Geometrical Model and Geometry-Based UWA Channel Model . . . . .	20

3.3.1	Geometrical Model . . . . .	20
3.3.2	Geometry-Based UWA Channel Model . . . . .	20
3.4	Chapter Summary and Conclusion . . . . .	22
<b>4</b>	<b>Measurement-Based Channel Modelling</b>	<b>23</b>
4.1	Introduction . . . . .	23
4.2	UWA Channel Modelling Using the INLSA Algorithm . . . . .	26
4.3	Non-Stationary UWA Channel Modelling . . . . .	26
4.4	Chapter Summary and Conclusion . . . . .	28
<b>5</b>	<b>The Sea Surface Simulator</b>	<b>29</b>
5.1	Introduction . . . . .	29
5.2	One-Dimensional Sea Surface Simulator . . . . .	31
5.2.1	Parametric Sea Surface Spectra . . . . .	31
5.2.2	SOS Principle . . . . .	32
5.2.3	Utilized Parameter Computation Methods . . . . .	32
5.3	Chapter Summary and Conclusion . . . . .	33
<b>6</b>	<b>Performance Analysis of Alamouti-Coded OFDM Systems</b>	<b>35</b>
6.1	Introduction . . . . .	35
6.2	Performance Analysis of Alamouti-Coded OFDM Systems . . . . .	36
6.2.1	The Utilized UWA Channel Model . . . . .	36
6.2.2	Performance Analysis . . . . .	36
6.3	Chapter Summary and Conclusion . . . . .	39
<b>7</b>	<b>Summary of Contributions and Future Work</b>	<b>41</b>
7.1	Major Contributions . . . . .	41
7.2	Future Work . . . . .	43
	<b>References</b>	<b>45</b>
	 <b>PART II</b>	 <b>61</b>
	Thumb Marks Index . . . . .	61
	 <b>Paper A</b>	 <b>63</b>
	 <b>Paper B</b>	 <b>81</b>
	 <b>Paper C</b>	 <b>121</b>
	 <b>Paper D</b>	 <b>161</b>

<b>Paper E</b>	<b>179</b>
<b>Paper F</b>	<b>197</b>
<b>Paper G</b>	<b>217</b>



# List of Figures

1.1	The role of channel models in the simulation of UWA communication systems. . . . .	6
1.2	V2V communications over a shallow UWA channel. . . . .	7
1.3	UWA channel modelling types used in this dissertation. . . . .	8
2.1	F2M communications over UWA channels assuming randomly distributed scatterers on the surface and bottom of a shallow-water ocean. . . . .	14
2.2	Impedance mismatch between the ocean water and air (surface reflection). . . . .	17
2.3	Impedance mismatch between the ocean water and ocean bed (bottom reflection). . . . .	17
3.1	A V2V communications over UWA channel assuming SOB shallow water ocean environment. . . . .	21
5.1	The PM spectrum $S_{\mu\mu}(\omega)$ for different value of wind speed $U$ . . . . .	30
5.2	The JONSWAP spectrum for different value of wind speed $U$ . . . . .	30
6.1	A 2-by-1 F2M UWA communication system. . . . .	37
A.1	A geometrical scattering model for a UWA channel with randomly distributed scatterers $S_{i,n}$ ( $\bullet$ ) on the surface ( $i = 1$ ) and the bottom ( $i = 2$ ) of a shallow-water ocean environment. . . . .	68
A.2	Initial position of the scatterers $S_{i,n}$ of the surface ( $i = 1$ ) and the bottom ( $i = 2$ ) of the ocean. . . . .	75
A.3	Evaluation of the error function $E(\delta_{x_i})$ in (A.30) to find the optimum value of $\delta_{x_i}$ ( $N_1 = N_2 = 13$ ). . . . .	76
A.4	Absolute value of the normalized T-FCF $ r_{HH}(\nu', \tau) $ of the reference model for a UWA channel. . . . .	77
A.5	Absolute value of the normalized T-FCF $ \hat{r}_{HH}(\nu', \tau) $ of the simulation model by using the MESS ( $N_1 = 80$ and $N_2 = 79$ ). . . . .	77

A.6	Absolute value of the normalized T-FCF $ \hat{r}_{HH}(\nu', \tau) $ of the simulation model by using the LPNM ( $N_1 = 80$ and $N_2 = 79$ ). . . . .	78
B.1	Refraction of a sound ray at the interface between two media with different speeds of sound $c_1$ and $c_2$ , where $c_1 < c_2$ . . . . .	87
B.2	An SSP example showing a piecewise linear sound speed variation in a shallow-water ocean environment with 5 different layers. . . . .	87
B.3	Illustration of the LOS macro-eigenray and several DA and UA macro-eigenrays which travel from $T_x$ to $R_x$ in a shallow UWA channel ( $N_s = 2, N_B = 1$ ). . . . .	89
B.4	Illustration of the LOS macro-eigenray which travels from $T_x$ to $R_x$ in a non-isovelocity ocean environment. . . . .	90
B.5	Illustration of a DA macro-eigenray ( $s = 1, \check{b} = 0$ ) and a UA macro-eigenray ( $b = 1, \check{s} = 0$ ) which travel from $T_x$ to $R_x$ in a non-isovelocity ocean environment ( $N_S = N_B = 1$ ). . . . .	90
B.6	LOS and DA macro-eigenrays in an <i>isovelocity</i> ocean environment ( $c_s = 1500$ m/s). . . . .	103
B.7	UA macro-eigenrays in an isovelocity ocean environment ( $c_s = 1500$ m/s). . . . .	103
B.8	Macro-eigenrays in a <i>non-isovelocity</i> ocean environment modeled by $K = 10$ layers and $g = 0.4$ s <sup>-1</sup> ( $c_s = 1500$ m/s). . . . .	104
B.9	Macro-eigenrays in a non-isovelocity ocean environment modeled by $K = 30$ layers and $g = 0.2$ s <sup>-1</sup> ( $c_s = 1500$ m/s). . . . .	104
B.10	Absolute value of the normalized temporal ACF $ r_{HH}(\tau) / r_{HH}(0) $ of the UWA channel model ( $\kappa = 160$ ). . . . .	106
B.11	Absolute value of the normalized temporal ACF $ r_{HH}(\tau) / r_{HH}(0) $ of the UWA channel model ( $g = 0.2$ s <sup>-1</sup> and $\kappa = 160$ ). . . . .	107
B.12	Evaluation of the error function $E(\kappa)$ in (B.47) for the various values of the number of layers $K$ . . . . .	107
B.13	Absolute value of the normalized FCF $ r_{HH}(\nu') / r_{HH}(0) $ of the UWA channel model. . . . .	108
B.14	Absolute value of the normalized FCF $ r_{HH}(\nu') / r_{HH}(0) $ of the UWA channel model ( $g = 0.2$ s <sup>-1</sup> and $\kappa = 160$ ). . . . .	109
B.15	The PDP $S_{\tau'}(\tau')$ of the UWA channel model for the isovelocity case ( $c_s = 1500$ m/s) by considering only macro-eigenrays. . . . .	109
B.16	The PDP $S_{\tau'}(\tau')$ of the UWA channel model for the non-isovelocity case by considering only macro-eigenrays. . . . .	110
B.17	The quantized form of the given SSP. . . . .	111
B.18	Absolute value of the measured TVCIR $ h(\tau', t) $ . . . . .	111

B.19	The absolute value of the normalized FCF of the measured UWA channel compared to that of the simulation model. . . . .	113
B.20	The PDP $\check{S}_{\tau'}(\tau')$ of the measured UWA channel. . . . .	114
B.21	The PDP $\check{S}_{\tau'}(\tau')$ of the simulation model. . . . .	114
C.1	Illustration of the LOS macro-eigenray and several DA and UA macro-eigenrays which travel from $T_x$ to $R_x$ in a shallow UWA channel ( $N_S = 2$ , $N_B = 1$ ) with the slope angle $\phi < 0$ . . . . .	128
C.2	The geometrical SOB model of a UWA channel in a shallow-water ocean environment with the slope angle $\phi < 0$ . . . . .	128
C.3	The effect of the slope angle $\phi < 0$ on the AOIs $\varphi_{sb}^{DA}$ of the DA macro-eigenray at the ocean surface/bottom for $s = 2$ and $\check{b} = 1$ . . . . .	133
C.4	The effect of the slope angle $\phi < 0$ on the AOIs $\varphi_{bs}^{UA}$ of the UA macro-eigenray at the ocean surface/bottom for $b = \check{s} = 1$ . . . . .	134
C.5	The PDF of the channel envelope. . . . .	142
C.6	The PDF of the instantaneous channel capacity. . . . .	144
C.7	Absolute value of the normalized temporal ACF $ r_{HH}(\tau) $ of the UWA channel model. . . . .	144
C.8	Absolute value of the normalized FCF $ r_{HH}(\nu') $ of the UWA channel model. . . . .	145
C.9	The Doppler PSD $S_{HH}(f)$ of the UWA channel model for the FOB case. . . . .	145
C.10	The Doppler PSD $S_{HH}(f)$ of the UWA channel model for the SOB case (slope angles $\phi = 3^\circ$ and $\phi = -3^\circ$ ). . . . .	146
C.11	The PDP $S_{\tau'}(\tau')$ of the UWA channel model for the FOB case. . . . .	146
C.12	The PDP $S_{\tau'}(\tau')$ of the UWA channel model or the SOB case (slope angles $\phi = 3^\circ$ and $\phi = -3^\circ$ ). . . . .	147
C.13	The effect of the slope angle $\phi$ on the average Doppler shift $B_{HH}^{(1)}$ , Doppler spread $B_{HH}^{(2)}$ , and the coherence time $T_C$ of the UWA channel model. . . . .	147
C.14	The effect of the slope angle $\phi$ on the average delay $B_{\tau'}^{(1)}$ , delay spread $B_{\tau'}^{(2)}$ , and the coherence bandwidth $B_C$ of the UWA channel model. . . . .	148
C.15	The measurement scenario of the experiment. . . . .	151
C.16	The PDP of measured UWA channel in comparison with that of the simulation model. . . . .	152
C.17	Evaluation of the error function $E(\phi)$ in (C.56) to find the optimum value of the slope angle $\phi$ . . . . .	152

C.18	Evaluation of the error function $E_{BC}(\phi)$ in (C.57) to find the optimum value of the slope angle $\phi$ . . . . .	153
C.19	The absolute value of the normalized FCF of the measured UWA channel against to those of the simulation model. . . . .	153
C.20	Double-bounce scattering scenario for a DA macro-eigenray ( $N_S = 1$ , $s = 1$ , and $\check{b} = 1$ ). . . . .	155
D.1	The measurement configuration of the experiment for SIMO fixed-to-fixed (F2F) communication. . . . .	172
D.2	Absolute value of the TVCIR $ \check{h}(\tau', t) $ of the measured UWA channel. . . . .	173
D.3	Absolute value of the TVCIR $ \tilde{h}(\tau', t) $ of the simulation model. . . . .	174
D.4	Absolute value of the normalized TFCF $ \check{r}_{HH}(\nu', \tau) $ of the measured UWA channel. . . . .	174
D.5	Absolute value of the normalized TFCF $ \tilde{r}_{HH}(\nu', \tau) $ of the simulation model. . . . .	175
D.6	The PDP $\check{S}_{\tau'}(\tau')$ of the UWA measured channel compared to the PDP $\tilde{S}_{\tau'}(\tau')$ of the simulation model. . . . .	175
D.7	The PDF of the UWA channel envelope . . . . .	176
E.1	Evaluation of the error function $E^{(1)}(N')$ in (E.11) as a function of the number of cisoids $N'$ . . . . .	188
E.2	Evaluation of the error function $E^{(2)}(N')$ in (E.12) as a function of the number of cisoids $N'$ . . . . .	188
E.3	Time-variant DPS $\check{S}_{\mu\mu}(f, t)$ of the measured UWA channel (first scenario). . . . .	189
E.4	The spectrogram $\tilde{S}_{\mu\mu}(f, t)$ of the simulation model (first scenario). . . . .	189
E.5	Time-variant DPS $\check{S}_{\mu\mu}(f, t)$ of the measured UWA channel (second scenario). . . . .	190
E.6	The spectrogram $\tilde{S}_{\mu\mu}(f, t)$ of the simulation model (second scenario). . . . .	190
E.7	Time-variant average Doppler shift (first scenario). . . . .	191
E.8	Time-variant average Doppler shift (second scenario). . . . .	192
E.9	Time-variant Doppler spread (first scenario). . . . .	192
E.10	Time-variant Doppler spread (second scenario). . . . .	193
F.1	The symmetrical PM spectrum $S_{\mu\mu}(\omega)$ for $\omega > 0$ . . . . .	202
F.2	The symmetrical JONSWAP spectrum $S_{\mu\mu}(\omega)$ for $\omega > 0$ . . . . .	203
F.3	The ACF $\hat{r}_{\mu\mu}(\tau)$ of sea surface waves simulator assuming the PM spectrum designed by the MEA ( $N = 40$ ) in comparison with the ACF $r_{\mu\mu}(\tau)$ of the reference model. . . . .	210

F.4	The ACF $\hat{r}_{\mu\mu}(\tau)$ of sea surface waves simulator assuming the JON-SWAP spectrum designed by the MEA ( $N = 40$ ) in comparison with the ACF $r_{\mu\mu}(\tau)$ of the reference model. . . . .	211
F.5	Sample function of the sea surface waves process $\hat{\mu}(t)$ designed by using the MEA ( $N = 40$ ) assuming the PM spectrum ( $U = 10$ m/s). . . . .	211
F.6	Sample function of the sea surface waves process $\hat{\mu}(t)$ designed by using the MEA ( $N = 40$ ) assuming the JONSWAP spectrum ( $U = 10$ m/s). . . . .	212
F.7	The distribution $\hat{p}_{\mu}(x)$ of the sea surface waves process $\hat{\mu}(t)$ designed by using the MEA ( $N = 40$ ) assuming the PM spectrum in comparison with the Gaussian distribution. . . . .	212
F.8	The distribution $\hat{p}_{\mu}(x)$ of the sea surface waves process $\hat{\mu}(t)$ designed by using the MEA ( $N = 40$ ) assuming the JONSWAP spectrum in comparison with the Gaussian distribution. . . . .	213
F.9	The distribution $p_H(x)$ of the maximum wave height $H$ designed by using the MEA ( $N = 40$ ) assuming the PM spectrum in comparison with the Rayleigh distribution. . . . .	213
G.1	A geometrical scattering model for a UWA channel with $N_i^S$ randomly distributed scatterers $S_{i,n}(\bullet)$ ( $n = 1, 2, \dots, N_i^S$ ) on the surface ( $i = 1$ ) and bottom ( $i = 2$ ) of the ocean. . . . .	221
G.2	The BEP performance of an Alamouti-coded OFDM system over an UWA channel correlated in space and time for different values of the maximum Doppler frequencies $f_{\max}^R = 5$ Hz and $f_{\max}^R = 50$ Hz and hydrophone spacing $\delta_T = 0.5\lambda$ and $\delta_T = 20\lambda$ . . . . .	230
G.3	The BEP performance of an Alamouti-coded OFDM system over UWA channels, which are only correlated in time for different values of the maximum Doppler frequencies $f_{\max}^R = 5$ Hz and $f_{\max}^R = 50$ Hz. . . . .	231
G.4	The BEP performance of an Alamouti-coded OFDM system over UWA channels, which are only correlated in space for different values of the hydrophone spacing $\delta_T = 0.5\lambda$ and $\delta_T = 20\lambda$ . . . . .	231



# List of Tables

1.1	The main parameters of the JANUS standard. . . . .	6
1.2	Identifying the research questions in different chapters and papers of the dissertation. The check mark (✓) indicates the presence of each question and where the solution is provided. . . . .	10
4.1	Summary of important UWA channel measurements. . . . .	25
6.1	Summary of the performance analysis of UWA communication systems. . . . .	38
7.1	Differences between UWA and mobile radio channels. . . . .	42
B.1	Definition and selected values of the channel model parameters. . . . .	98
B.2	Characteristic quantities of the measured UWA channel and the corresponding simulation model. . . . .	113
C.1	Definition and selected values of the channel parameters. . . . .	143
C.2	Characteristic quantities of the measured UWA channel and the corresponding simulation model. . . . .	151
D.1	Characteristic quantities of the UWA channel. . . . .	173
F.1	Comparison of the sea surface wave properties of the simulation model designed by the LPNM, MED, and MEA by using the PM spectrum ( $U = 15 \text{ m/s}$ ). . . . .	214
F.2	Comparison of the sea surface wave properties of the simulation model designed by the LPNM, MED, and MEA by using the JON-SWAP spectrum ( $U = 15 \text{ m/s}$ , $F = 10 \text{ km}$ , $\gamma = 3.3$ ). . . . .	214



# List of Abbreviations

2D	two-dimensional
ACDS	acoustic communications and data storage
ACF	autocorrelation function
AOA	angle-of-arrival
AOD	angle-of-departure
AOI	angle-of-incidence
AOM	angle-of-motion
AUV	autonomous underwater vehicle
BEP	bit error probability
BPSK	binary phase-shift keying
CCF	cross-correlation function
CIR	channel impulse response
CMRE	center for maritime research and experimentation
CSMA/CA	carrier-sense multiple access/collision avoidance
DA	downward arriving
DPS	Doppler power spectrum
ESPRIT	estimation of signal parameter via rotational invariance techniques
F2F	fixed-to-fixed
F2M	fixed-to-mobile
FCF	frequency correlation function
FOB	flat ocean bottom
INLSA	iterative nonlinear least square approximation
ISI	intersymbol-interference
JONSWAP	Joint North Sea Wave Project
LOS	line-of-sight
LPNM	$L_p$ -norm method
M2F	mobile-to-fixed
M2M	mobile-to-mobile
MAC	medium access control

MEA	method of equal areas
MED	method of equal distances
MESS	method of equally space scatterers
MIMO	multiple-input multiple-output
MISO	multiple-input single-output
MSE	mean squared error
NATO	north Atlantic treaty organization
OFDM	orthogonal frequency division multiplexing
PDF	probability density function
PDP	power delay profile
PM	Pierson-Moskowitz
PSD	power spectral density
SAGE	space alternating generalized expectation maximization
SER	symbol error rate
SFBC	space frequency block coding
SIMO	single-input multiple-output
SINR	signal-to-interference-plus-noise ratio
SISO	single-input single-output
SNR	signal-to-noise ratio
SOB	sloped ocean bottom
SOC	sum-of-cisoids
SOCUS	sum-of-cisoids uncorrelated scattering
SOS	sum-of-sinusoids
SSP	sound-speed profile
STBC	space-time block coding
STVCTF	space-time variant channel transfer function
TFCF	time frequency correlation function
TVCIR	time-variant channel impulse response
TVCTF	time-variant channel transfer function
UA	upward arriving
UWA	underwater acoustic
V2V	vehicle-to-vehicle
WSS	wide-sense stationary
WSSUS	wide-sense stationary uncorrelated scattering

# **PART I**



# Chapter 1

## Introduction

The implementation of communication links for transmitting information over large distances has been one of the main technological achievements in modern history. However, most of these systems use electromagnetic waves. Owing to the fact that electromagnetic waves can propagate in both atmosphere and outer space, their range of applications has been extended to terrestrial and satellite communications since humans entered space.

However, a considerable part of the Earth is inaccessible to electromagnetic signals. In other words, radio and radar signals cannot propagate in the underwater part of the Earth, which covers more than 70% of the Earth's surface. Indeed, electromagnetic waves are attenuated considerably and rapidly in water and especially in salt water, which has strong conductivity. Therefore, acoustic waves have been used as an alternative for long-range underwater acoustic (UWA) communications. Acoustic waves have better transmission properties in water compared to air. For instance, the speed of sound in the water (about 1500 m/s) is more than 4 times faster than the speed of sound in air (about 340 m/s). Moreover, acoustic propagation in water ranges up to thousands of kilometers; while in air, it rarely exceeds a few kilometers.

Although ocean/sea water is relatively favourable for acoustic wave propagation, it has several limitations:

- Propagation loss: including loss of signal energy as a result of geometrical spreading, attenuation, and reflection.
  - Geometrical spreading loss: due to spherical and cylindrical spreading, which happens if the acoustic intensity decreases exponentially with a certain range.
  - Attenuation loss: due to the absorption of acoustic signal energy in wa-

ter. In this case, the power attenuation of acoustic waves increases if the signal frequency increases.

- Reflection loss: due to the impedance mismatch between the ocean water and boundaries (ocean surface and ocean bottom/bed).
- Perturbation of propagation: caused by variations in the speed of sound and reflections on the ocean bottom and ocean surface.
- Ambient noise: caused by volcanic and seismic activity, shipping, living organisms, rain, etc.
- Low propagation velocity: although the speed of sound in water is much faster than speed of sound in air, it is not comparable with the speed of electromagnetic waves in air ( $3 \times 10^8$  m/s).
- Doppler effects: caused by ocean surface motion, moving transmitter and/or receiver, and moving objects in the ocean water.

Thus, there are many fundamental differences between UWA and terrestrial communication systems. Moreover, UWA communication systems work mostly with carrier frequencies between 1 and 20 kHz. In this case, the total communication bandwidth is very low. This means the bandwidth is not negligible with respect to the carrier frequency and thus the channel is a wideband channel.

In general, the water depth determines the propagation mechanism. In addition, the mechanisms of propagation in the ocean are different for *deep* and *shallow* water, and also depend on the frequency and the distance between the transmitter and receiver. The definition of shallow water is quite imprecise, but it usually means for depths less than 200 m [1]. The shallow water scenario includes reflections from the ocean surface, ocean bottom, and any objects in the ocean. It can also have a possible direct path. A ray bending phenomenon, which obeys Snell's law occurs mostly in deep water. In this case, the sound channel may be formed by bending of the rays toward the location where the sound speed reaches its minimum [1–4]. However, UWA channel modelling in deep water is not the focus of this dissertation.

UWA communication systems play a key role in the pollution monitoring [5, 6], scientific exploration of the ocean [7], UWA sensor networks [8–13], seismic monitoring [14, 15], offshore exploration [16], autonomous underwater vehicle (AUV) navigation [17, 18], and vehicle-to-vehicle (V2V) communications [19, 20], just to name a few examples. For the testing, development, design, and performance analysis of UWA communication systems, realistic channel models are required. This calls for statistical properties of UWA channels such as correlation functions,

Doppler power spectral density (PSD), power delay profile (PDP), distribution of the UWA channel envelope, etc. It should be mentioned that V2V communications represent a special case of mobile-to-mobile (M2M) communications where both the transmitter and receiver are in motion. Throughout this dissertation, the term V2V and M2M are used interchangeably. This issue happens also, in this dissertation, for Doppler PSD and Doppler power spectrum (DPS) which represent the same meaning.

## **1.1 The JANUS UWA Communications Standard**

For the time being, there is no digital UWA communication standard. However, a simple multiple access acoustic protocol namely JANUS has been developed and tested by the north Atlantic treaty organization (NATO) Center for Maritime Research and Experimentation (CMRE). This standard is in process to become a NATO standard but it is intended to be also for civil and international applications [21–23]. The JANUS standard supports both fixed-to-fixed (F2F) and fixed-to-mobile (F2M) communication scenarios. The digital signaling method used in JANUS is frequency-hopping-binary frequency shift keying (FH-BFSK), which has been chosen for its robustness and ease of implementation. For the medium access control (MAC) mechanism, JANUS exploits the carrier-sense multiple access with collision avoidance (CSMA/CA) method. Table 1.1 presents the main features of the JANUS standard.

## **1.2 Principles of UWA Channel Modelling**

Realistic UWA channel models allow us to analyse the performance of different modulation schemes, channel coding schemes, source coding schemes, and receiver techniques via computer simulations. In other words, accurate UWA channel models provide a powerful and cost efficient tool to assess the correctness of theoretical findings obtained analytically. Thus, there is no need for scenario-dependent hardware and employing inferior trial-and-error methods. Fig. 1.1 depicts the importance of channel modelling for UWA communications.

In a shallow underwater propagation scenario, a transmitted acoustic signal travels from a transducer at the transmitter side and arrives at the hydrophone at the receiver side via several paths. Fig. 1.2, depicts a typical V2V scenario in a shallow water environment. As can be seen in this figure, the transmitted signal arrives at the receiver after interacting with the ocean surface and/or ocean bottom or it

Table 1.1: The main parameters of the JANUS standard.

Parameter	Value/Feature
Data rate	Up to 40 kbps
Carrier frequency	900 Hz - 60 kHz
Communication range	up to 28 km
Digital signaling method	FH-BFSK
Channel bandwidth	$\frac{1}{3}$ of carrier frequency
Communication type	F2F/F2M
Channel coding	Convolutional coding
MAC mechanism	CSMA/CA

can travel directly between the transmitter and receiver under a line-of-sight (LOS) propagation condition.

Communication in UWA channels is challenging because of the reflection mechanisms, limited bandwidth, large delay spread as well as large Doppler shifts. Communication techniques, which have been developed for terrestrial wired and wireless channels need significant modifications for UWA channels.

### 1.3 Approaches and Features of UWA Channel Modelling

According to the literature [3, 19, 24–26], there are two main approaches in the area of channel modelling: geometry-based and measurement-based approaches. The principles, advantages and disadvantages of each approach are addressed in the following.

The geometry-based UWA channel modelling approach has two main subcategories namely geometry-based deterministic and geometry-based stochastic approaches. In the geometry-based deterministic approach, acoustic waves emitted from the transmitter are geometrically tracked over the scatterers located on the sur-

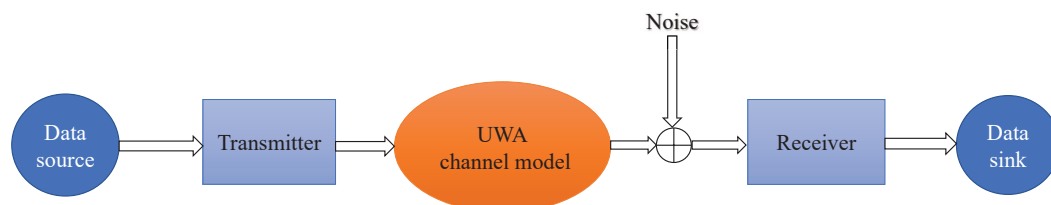


Figure 1.1: The role of channel models in the simulation of UWA communication systems.

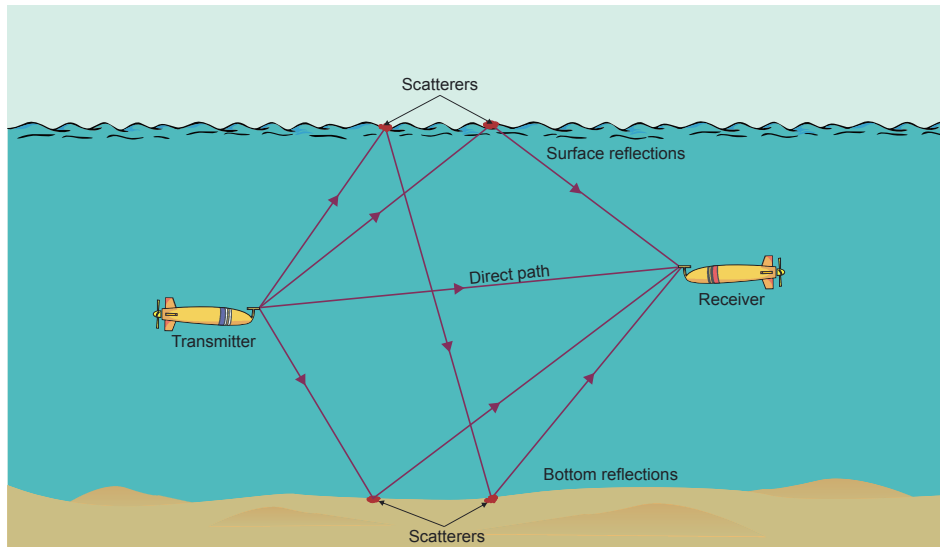


Figure 1.2: V2V communications over a shallow UWA channel.

face and bottom of the ocean up to the receiver. In this case, UWA channel models include only deterministic parameters except phase shifts of received waves, which are supposed to be uniform between  $0$  and  $2\pi$ .

The ray tracing approach is a deterministic approach. The ray tracing method is derived from the wave equation where some simplifying assumptions are introduced and the method is essentially a high-frequency approximation. However, ray tracing techniques have limitations and may not be valid for precise predictions of sound levels, especially in situations where refraction effects and focusing of sound are important [27].

The geometry-based stochastic approach presents synthetic channel responses that describe UWA channels with a high level of accuracy. Stochastic UWA channel models are often less complex than ray tracing models from a mathematical point of view. However, some assumptions such as the non-stationarity of the UWA channels may lead to very complex geometry-based stochastic UWA channel models.

Measurement-based UWA channel models are developed by collecting measured data from real-world UWA communication scenarios. The measurement-based channel models provide a very accurate tool for designing UWA communication systems, however, these channel models are very costly and scenario specific, and do not provide an idea about the channel behavior in average. The employed approaches for the modelling of UWA channels in this dissertation are summarized in Fig. 1.3.

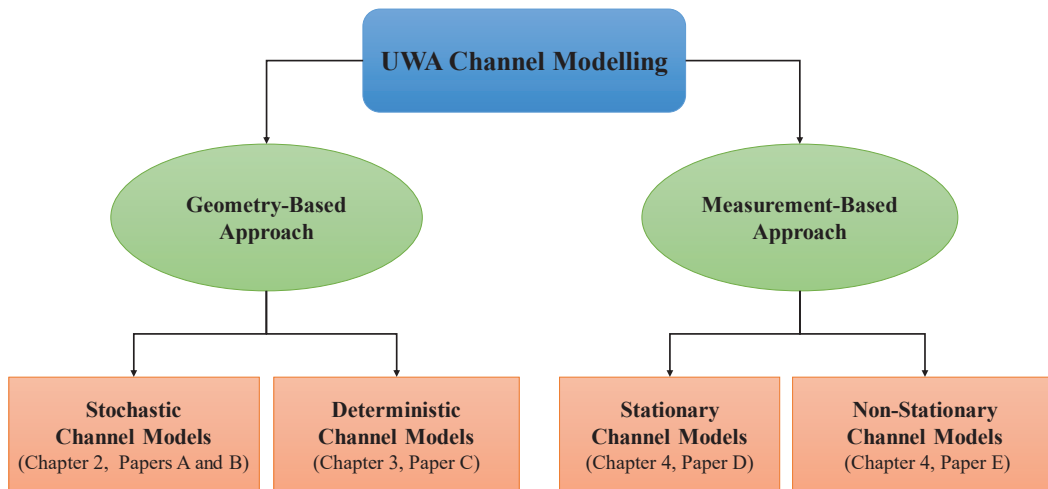


Figure 1.3: UWA channel modelling types used in this dissertation.

## 1.4 Motivations

For the time being, it is uncertain how underwater networks will develop as possible applications depend on network capabilities, which are still under research. Nevertheless, the number of geometry-based UWA channel models in the literature is very limited. To fill this gap, new UWA channel simulation models have to be developed which well describing the UWA multipath propagation in shallow water conditions. The consideration of the above-mentioned issues, motivated us to focus on developing and studying UWA channel models which provide a versatile tool for the design and performance analysis of UWA communication systems.

The statistical analysis of UWA channels in terms of correlation functions, Doppler PSD, and PDP is an open framework for future investigations. The main objective of this dissertation is to study the reference and simulation UWA channel models characterizing single-input single-output (SISO) UWA channels, which are of crucial importance for the development of future UWA communication systems.

## 1.5 Research Questions

In this section, we present several research questions raised based on the above discussion. This dissertation makes efforts to answer more specifically the following questions.

- **Question1** : How can the reference model and the corresponding simulation model for V2V shallow UWA channels be derived?

- **Question2** : What is the effect of considering non-isovelocity conditions on shallow UWA channel models?
- **Question3** : What is the effect of considering sloped-ocean bottom conditions on shallow UWA channel models?
- **Question4** : How can we derive measurement-based channel models from UWA communications measured data?
- **Question5** : How can we model one-dimensional ocean surface waves?
- **Question6** : How can we analyse the performance of shallow UWA communication systems?

Table 1.2 depicts the venues (chapters and papers) in this dissertation where our solutions for the research questions are proposed.

## **1.6 Organization of the Dissertation**

This dissertation is a collection of seven technical papers in which papers addressing similar topics are collected together to form chapters. In this case, the dissertation is structured in two parts where in **Part I**, the introduction, summary of research topics, contributions, and future work are provided. **Part II** is formed as an assortment of seven technical papers, which are scientific contributions of this dissertation. The rest of **Part I** is organized as follows.

- Chapter 2 covers **Papers A and B**. In this chapter, two geometry-based stochastic UWA channel models are proposed:
  - 1) The geometry-based stochastic UWA channel model under the assumption that scatterers are randomly distributed on the rough surface and bottom of the shallow-water ocean (**Paper A**).
  - 2) The geometry-based stochastic UWA channel model under non-isovelocity condition (**Paper B**).
- Chapter 3 covers **Paper C**, where a geometry-based deterministic UWA channel model is developed assuming a sloped-ocean-bottom (SOB) condition.
- Chapter 4 covers **Papers D and E**, which deal with measurement-based UWA channel modelling. **Papers D** develops a stationary UWA channel model and **E** proposes a non-stationary UWA channel model based on real-word measurement data.

Table 1.2: Identifying the research questions in different chapters and papers of the dissertation. The check mark (✓) indicates the presence of each question and where the solution is provided.

Questions	Chapters					Papers						
	ch. 2	ch. 3	ch. 4	ch. 5	ch. 6	A	B	C	D	E	F	G
Q1	✓	✓	...	...	...	✓	✓	✓	...	...	...	...
Q2	✓	...	...	...	...	...	✓	...	...	...	...	...
Q3	...	✓	...	...	...	...	...	✓	...	...	...	...
Q4	...	...	✓	...	...	...	...	...	✓	✓	...	...
Q5	...	...	...	✓	...	...	...	...	...	...	✓	...
Q6	...	...	...	...	✓	...	...	...	...	...	...	✓

- Chapter 5 covers **paper F**, where a one-dimensional ocean surface waves simulator is designed.
- Chapter 6 covers **Paper G** which analyzes the performance of an Alamouti-coded orthogonal frequency division multiplexing (OFDM) system over time-varying UWA channels.
- Chapter 7 summarizes major contributions of the dissertation and addresses some open problems and future work.

# Chapter 2

## Geometry-Based Stochastic UWA Channel Modelling

### 2.1 Introduction

A UWA channel is called *statistically stationary* if its statistical properties do not change in time. In V2V communication systems over UWA channels, the UWA channel is *physically non-stationary* if either the scatterers are moving, or the velocity (including the angle-of-motion (AOM) and/or speed) of the transmitter/receiver is changing [28]. However, in this dissertation, both F2M and V2V communication scenarios are assumed with constant transmitter velocity (in case of V2V scenario) and receiver velocity. Considering a short observation time, however, allows us to assume that the UWA channel is statistically stationary. Thus, the primary statistical quantities of the corresponding UWA channel model including its angle-of-arrival (AOA) and angle-of-departure (AOD) do not change in time. In this case, the statistical properties derived from those quantities, such as the Doppler frequencies, autocorrelation function (ACF) and consequently, Doppler PSD also become time independent.

UWA channel modelling is noted for its complexity as the ocean water properties and the geometry of the ocean impact significantly on the statistical properties of UWA channels. In the literature, several geometry-based channel models in the area of mobile radio channels exist such as the one-ring model [29] two-ring model [30], elliptical model [31], street scattering model [32], and T-junction model [33], etc., which all benefit from the wide-sense stationary uncorrelated scattering (WSSUS) assumption [34]. There are some papers in the literature that do not take WSSUS assumption into account [35–39], while this assumption is a fundamental assumption in this dissertation. A two-dimensional (2D) geometrical model which suits

shallow UWA channel modelling can be a rectangular shape ocean model, where scatterers are distributed on the surface and bottom of the ocean.

For telecommunication purposes, geometry-based stochastic UWA channel models, capturing fast statistical variations of the channel, are required to precisely explain the communication link properties such as the delay spread and Doppler spread. To this aim, several stochastic UWA channel models have been developed under isovelocity conditions [19, 26, 40–42]. For instance, in [40] and [19], the total distances that acoustic signals travel between the transmitter and the receiver have been computed by using the *method of image projections* [1]. Therein, the reference channel models have been developed by exploiting the deterministic ray-tracing concept along with statistical methods to account for the randomness of the propagation environment. However, the literature still lacks UWA channel models that take other scattering conditions into account.

In this chapter, two geometry-based stochastic UWA channel models based on two new propagation conditions are presented. The first UWA channel model is developed for F2M communication systems under isovelocity conditions where the distributions of the AOA and AOD are derived according to the distribution of scatterers on the rough surface and bottom of the ocean. To capture the non-isovelocity ocean condition, the second UWA channel is developed for V2V communication systems where *macro-* and *micro-scattering* effects are taken into account.

## 2.2 Rough Surface and Bottom Scattering Conditions

In this dissertation, it is assumed that the scatterers are located on the surface and bottom (boundaries) of the ocean. For ocean boundaries, two different types of reflection exist: specular and non-specular. The specular reflection happens if a ray from a single incoming direction reflects into a single outgoing direction. A prerequisite for the specular reflection is a smooth boundary and a larger dimension of the scatterer than that of the sound beam. In this case, the angle of incidence is equal to the angle of reflection, which is called macro scattering and can be modelled deterministically. Besides specular reflections, the ocean boundary condition will also result in non-specular scattering, which is called micro scattering and is associated with random ocean fluctuations, rough surfaces and/or irregular boundaries. Non-specular scattering occurs if the dimension of the scatterer is smaller than the diameter of the sound beam. In this situation, the incident beam reflects in many different directions, which could be modelled statistically [4].

Moreover, the distribution of the scatterers plays an important role in UWA

channel modelling, because it considerably influences the statistics of the AOD and AOA. In **Paper A**, it is assumed that scatterers are randomly distributed on the rough surface and rough bottom of the ocean. Then by using the distribution of the scatterers, the distributions of the AOA and AOD are derived. As the AOA and AOD are physically dependent, thus, the exact relationship between the AOA and AOD is also studied.

In geometry-based UWA channel modelling, the stochastic UWA channel model is developed under the assumption that scatterers are randomly distributed on the surface and bottom of the ocean. Considering the geometrical model, a reference model is derived assuming an infinite number of scatterers. In this case, a simulation model is developed assuming a limited number of scatterers such that the statistical properties of the simulation model match the reference model.

As mentioned in Chapter 1, there are three kinds of propagation losses in the UWA propagation mechanism: geometrical spreading, attenuation, and reflection loss. The loss as a result of geometrical spreading is divided into two categories: spherical spreading and cylindrical spreading. Spherical spreading normally occurs in long-range UWA transmission; while cylindrical spreading occurs in short-range UWA communications [43]. In this dissertation, long-range UWA transmissions are assumed, thus, spherical spreading is considered in analytical derivations. It should be mentioned that in **Paper A**, for simplicity, the reflection loss is not taken into account.

### **2.2.1 Reference Model**

**Paper A** develops a geometry-based stochastic channel model for wideband SISO shallow UWA channels under LOS propagation conditions assuming that the ocean surface and bottom are rough.

Fig. 2.1 depicts F2M communications over a shallow UWA channel. For simplicity, single-bounce scattering is considered, i.e., each transmitted plane wave arrives at the receiver after a single bounce on the surface or the bottom of the ocean. The transmitter is fixed and the receiver is moving (F2M case).

Starting from a geometrical model (Fig. A.1 presented in **Paper A**), a reference model is derived assuming that an infinite number of scatterers are randomly distributed on the surface and the bottom of the ocean water. In the absence of any given distribution of the scatterers accounting for scenarios in which the ocean surface and bottom are rough, it is assumed that the scatterers are uniformly distributed on the surface and the bottom of the ocean. Moreover, shallow water is considered as an isovelocity environment.

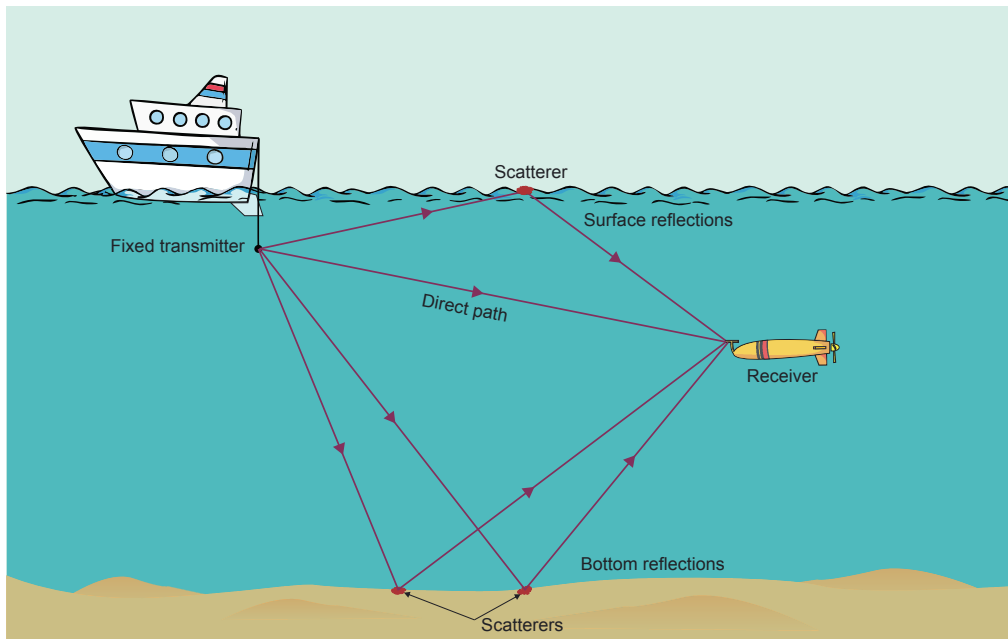


Figure 2.1: F2M communications over UWA channels assuming randomly distributed scatterers on the surface and bottom of a shallow-water ocean.

The time-variant channel impulse response (TVCIR) of the reference model is first derived under LOS propagation conditions. Then, the probability density functions (PDFs) of the AOD and the AOA are computed, which are required for the computation of the 2D time-frequency correlation function (TFCF).

## 2.2.2 Simulation Model and Parameter Computation Methods

The reference model presented in the previous section is based on the assumption that the number of scatterers is infinite implying a non-realizable reference model. From the reference model, the corresponding simulation model (sum-of-cisoids (SOC) channel simulator) is developed by applying the generalized concept of deterministic channel modelling [24, pp. 418]. The SOC channel simulator is a low-complexity channel simulator for the simulation of UWA channels under non-isotropic scattering conditions.

For the parametrization of the UWA channel simulator, a new method is proposed namely the method of equally-spaced scatterers (MESS). The performance of the MESS is compared with that of the  $L_p$ -norm method (LPNM) [24, pp. 189]. A good fitting between the reference model and the simulation model has been achieved with respect to the TFCF. **Paper A** shows that the MESS is not only faster, but also computationally simpler than the LPNM and also provides a closed-form solution, while the LPNM does not.

## 2.3 Non-Isovelocity Ocean Condition

UWA propagation scenarios can be fully described by solving the wave equation. However, solving the wave equation is well known to be a difficult problem [1, 40]. To circumvent this problem, approximations, such as deterministic ray-tracing methods [44–48], are often used to model the *high-frequencies* acoustic wave propagation phenomena in *deep* ocean environments [49, 50].

The fact that the speed of sound varies with depth [1, 51–53], motivated us to develop UWA channel models for the non-isovelocity UWA propagation condition (caused by ocean layers with different acoustic properties [54]).

In [55], a method has been proposed to model the signal transmission in UWA communications in a non-isovelocity condition. The proposed method is based on the approximation of the channel impulse response (CIR) for different samples of the transmitter/receiver trajectory. In this approach, for each transmitter/receiver position, the channel impulse response is calculated by using a field computation method, e.g., the ray-tracing method. This approach, however, results in a high complexity of implementation and calculations.

Although there are several papers in the literature that study the behavior of acoustic waves in non-isovelocity ocean environments [27, 54, 56–58], there is no design method that can directly be used to develop stochastic simulation models for non-isovelocity UWA channels, especially, for shallow UWA ones. To address this problem, a new geometry-based UWA channel model is proposed, which is suited for computer simulations and accounts for non-isovelocity propagation effects. The proposed channel model enables us to study analytically the statistical properties of UWA channels such as the temporal and frequency correlation functions, PDP, delay spread, and the coherence bandwidth under isovelocity/non-isovelocity ocean conditions. The proposed geometry-based stochastic UWA channel model characterizes acoustic signal propagation in shallow-water ocean environments by taking into account macro-scattering effects caused by specular reflection at the surface and bottom of the ocean. In addition, it addresses the randomness of the UWA channel by considering micro-scattering (diffuse scattering) effects. Moreover, the proposed UWA channel model is inspired by Snell’s law which describes the relationship between the angle-of-incidence (AOI) and angle-of-refraction (AOR). It refers to light, sound or other waves passing through a boundary between two different media. In the developed channel model, the sound speed profile (SSP) needs to be a piecewise linear type which can vary with depth.

Unlike **Paper A**, **Paper B** considers multiple-bounce scattering conditions. The exact positions of *macro-scatterers* are computable and depend on the waveguide

geometry and the number of macro-eigenrays. The roughness of the sea surface and sea bottom is characterized by *micro-scatterers*, which are randomly clustered around the positions of macro-scatterers. In other words, the propagation of deterministic macro-eigenrays and random micro-eigenrays is studied.

In the area of UWA channel modelling, the ocean bed is definitely the most complex boundary, exhibiting vastly different reflectivity characteristics in different geographical locations [59,60]. As mention in Section 2.2, two types of propagation loss, geometrical spreading and attenuation have been considered for developing the UWA channel model in **Paper A**. However, in **Paper B** the impedance mismatch between the ocean water and ocean bed is taken into account. The impedance mismatch (which causes reflection loss) between the ocean water and ocean bed causes the ocean bed to reflect some parts of an incident wave. For a smooth ocean bed, the value of the reflection coefficient  $A_b(\varphi)$  is considerably angle-dependent [1, Eq. (3.1.12)]. In this section, the reflection coefficient  $A_b(\varphi)$  is assessed for two ocean boundaries (ocean surface and ocean bed) in terms of the AOI  $\varphi$ , where the symbols  $c_s$ ,  $c_a$ , and  $c_b$  denote the speed of sound in the water, air, and the ocean bed, respectively. Moreover, the quantities  $\rho_s$ ,  $\rho_a$ , and  $\rho_b$  stand for the densities of the ocean water, air, and the ocean bed, respectively. As can be seen in Fig. 2.2, the reflection coefficient as a result of impedance mismatch between the ocean water and the air for different values of  $\varphi$  is very close to 1. In contrast, the reflection coefficient  $A_b(\varphi)$  due to the impedance mismatch between the ocean water and ocean bed, depicted in Fig. 2.3, is very AOI dependent. Thus, in the proposed UWA channel model, the reflection loss of the surface interactions is not taken into account.

Starting from a geometrical model (Figs. B.3 and B.4 presented in **Paper B**), a stochastic channel model for a SISO V2V UWA channel is developed assuming that the ocean surface and bottom are rough and the speed of sound varies with depth. In the first step, the TVCIR of the UWA channel model is derived under LOS propagation conditions assuming AOIs characterized by the von Mises distribution. Then, the effect of the non-isovelocity condition has been assessed regarding its influence on the temporal ACF, frequency correlation function (FCF), and the PDP of the UWA channel model.

The results of the assessment show significant differences of the channel characteristics if non-isovelocity propagation conditions are incorporated into the UWA channel model. For example, the results indicate that the coherence bandwidth and the coherence time of the non-isovelocity UWA channel model are significantly smaller than those of the isovelocity channel model. Finally, to verify the validity of the proposed UWA channel model, the main statistical properties, such as

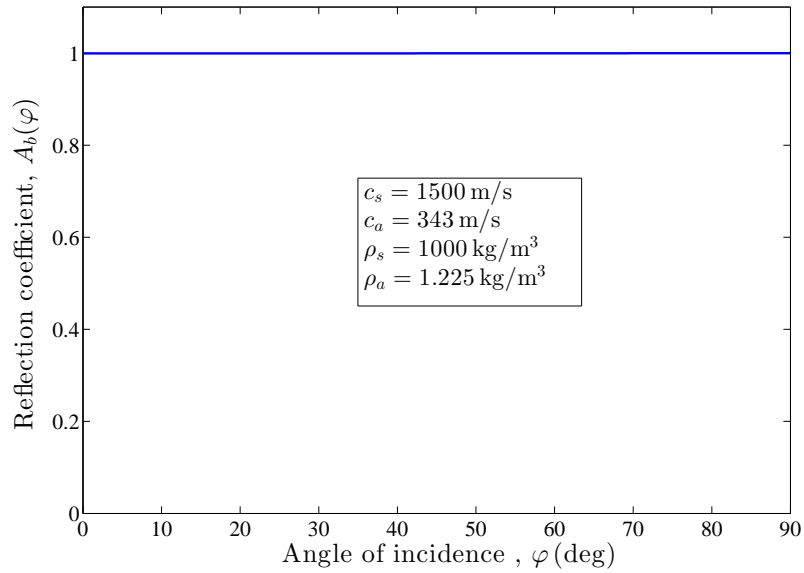


Figure 2.2: Impedance mismatch between the ocean water and air (surface reflection).

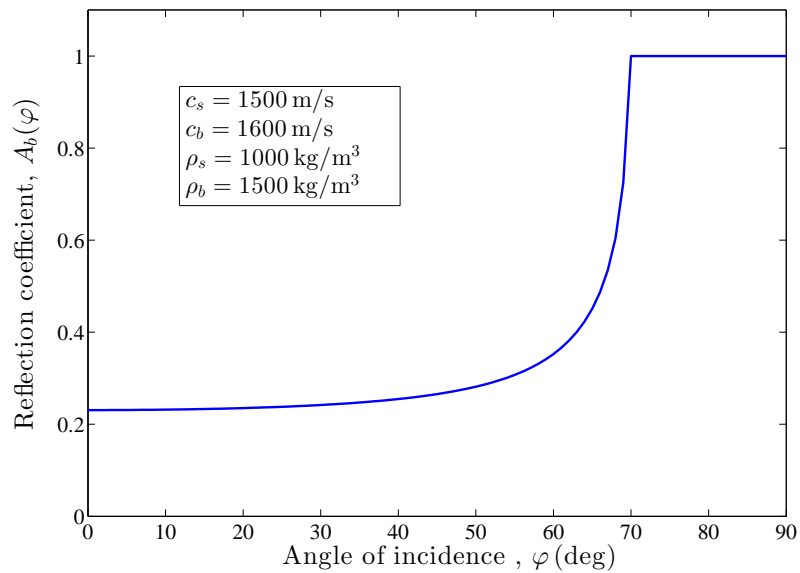


Figure 2.3: Impedance mismatch between the ocean water and ocean bed (bottom reflection).

the FCF, average delay, delay spread, and the coherence bandwidth are compared with those of a measured UWA channel, where good agreement between theory and measurement is observed.

## **2.4 Chapter Summary and Conclusion**

In this chapter, two new different geometry-based stochastic UWA channel models have been developed. First, a geometry-based shallow UWA channel model has been developed for isovelocity ocean conditions assuming single-bounce scattering on the rough surface and bottom of the ocean (see **Paper A**). The distributions of AOAs, AODs, and then the TFCF of the UWA channel model has been derived. In addition to this, the corresponding simulation model has been proposed. For the parametrization of the channel simulator, two methods, namely the MESS and the LPNM, have been used. The LPNM is a well-known method and has been widely adopted in the area of mobile radio channel modelling. However, the MESS has been especially developed for designing UWA channel simulators. The numerical results show a perfect match between the reference model and the corresponding simulation model with respect to the TFCF.

A geometry-based UWA channel model has also been developed which allows for the non-isovelocity ocean condition under the assumption that the shallow ocean surface and bottom are rough (see **Paper B**). Moreover, multiple-bounce scattering is considered on the surface and bottom of the ocean. The influence of the non-isovelocity propagation condition on the statistical properties of the UWA channel has been studied. The numerical results show that the non-isovelocity condition has a considerable impact on the properties of the UWA channel model. For instance, the coherence bandwidth and the coherence time of the non-isovelocity UWA channel model are considerably smaller than those of the isovelocity channel model. It has also been shown that by taking these conditions into account, the UWA channel model becomes more realistic.

## Chapter 3

# Geometry-Based Deterministic UWA Channel Modelling

### 3.1 Introduction

In shallow-water environments the energy of sound propagates along straight lines such as light rays, where the isovelocity assumption is taken into account [40, 61, 62]. As mentioned in Chapter 1, in the geometry-based deterministic approach, acoustic waves emitted from the transmitter are geometrically tracked over the scatterers located on the surface and bottom of the ocean up to the receiver.

### 3.2 Sloped Ocean Bottom Condition

Several stochastic channel models have been developed in the literature for UWA communication systems assuming the ocean bottom is flat [19, 26, 40–42]. However, the ocean bottom is not necessarily flat and most parts of the ocean bottom slope gradually from the shore into the ocean. This natural feature of oceans motivated us to develop a new geometrical model which we call the sloped-ocean-bottom (SOB) model.

In **Paper C**, a new geometry-based deterministic channel model is proposed for shallow-water ocean environments under the assumption that the ocean bottom slopes gently down/up. As mentioned above, the need for developing such a UWA channel model is driven by the fact that the standard assumption of a flat ocean bottom does not hold in many realistic scenarios [59].

### 3.3 Geometrical Model and Geometry-Based UWA Channel Model

In this chapter, a deterministic channel model is developed for wideband SISO V2V UWA channels assuming a *smooth* ocean surface and bottom. This chapter aims to develop a general deterministic UWA channel model that accounts for SOB conditions where the flat-ocean-bottom (FOB) model, which is widely used in the literature [19, 26, 40–42, 63–65], can be obtained as a special case of the proposed model if the slope angle is zero.

#### 3.3.1 Geometrical Model

Fig. 3.1 illustrates V2V communications over an SOB-UWA channel in a shallow-water ocean environment. Based on this schematic figure, a geometrical model is developed, which is presented in Fig. C.2, in **Paper C**. As shown in this figure, the two-dimensional geometrical SOB model is bounded by the ocean surface and bottom. These natural boundaries act as reflectors for acoustic waves such that several macro-eigenrays can travel from the transmitter to the receiver. In **Paper C**, the randomness of the UWA channel as a result of micro-scattering (or diffuse scattering) effects will not be discussed. In other words, a geometry-based UWA channel model is developed under the assumption that rays propagate in shallow-water ocean environments by taking macro-scattering effects into account. As already mentioned in Chapter 2, macro-scattering effects are caused by specular reflections at the surface and bottom of the ocean. In this case, the exact positions of the macro-scatterers are computable and depend on the waveguide geometry and the number of macro-eigenrays [19].

#### 3.3.2 Geometry-Based UWA Channel Model

From the geometrical SOB model, the TVCIR of the UWA channel model is derived. Expressions of the total distances that the macro-eigenrays travel from the transmitter to the receiver are also derived by assuming multiple-bounce scattering in shallow-water environments. The AOAs and AODs of the macro-eigenrays have also been studied. A few studies have been conducted to investigate the PDF of the UWA channel gains and the corresponding instantaneous capacity [66–70]. The study of these statistical characteristics is of great importance as it allows us to gain a deeper insight into the dynamical and temporal behavior of UWA channels. Thus, the influence of the ocean-bottom slope angle on the PDF of the UWA channel

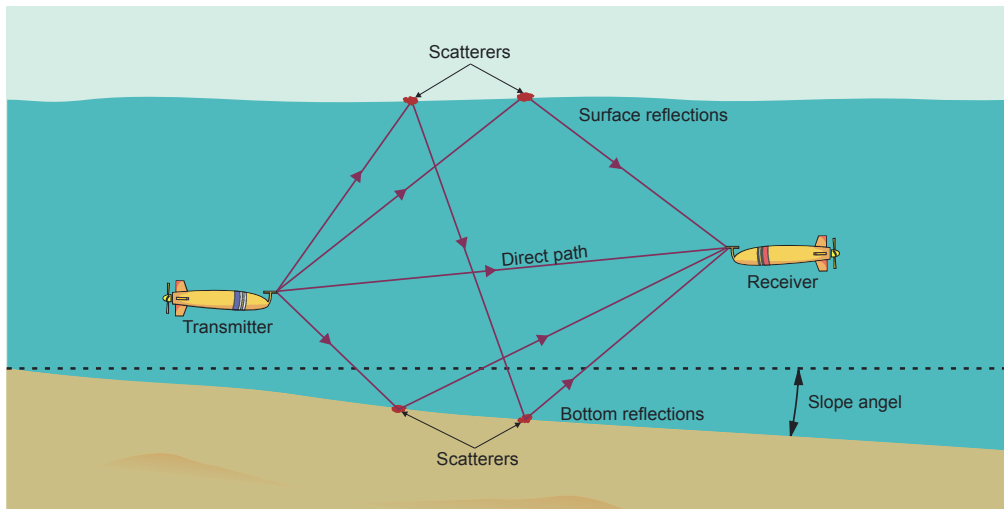


Figure 3.1: A V2V communications over UWA channel assuming SOB shallow water ocean environment.

envelope and the PDF of the instantaneous channel capacity is investigated.

In addition, the statistical quantities of the proposed SOB-UWA channel model, including the temporal ACF, FCF, Doppler PSD, and the PDP, are compared with those of the FOB-UWA channel model. The effect of the ocean-bottom slope angle on the important parameters of the UWA channel model such as the Doppler spread, average Doppler shift, coherence time, average delay, delay spread, and the coherence bandwidth is also studied. Moreover, the main statistical properties of the proposed UWA channel model, such as the FCF, average delay, delay spread, and the coherence bandwidth have been fitted against real-world measurement data of UWA channels and a great agreement has been observed.

In comparison with the conventional UWA channel model, which has been developed on the assumption of a flat ocean bottom, it is shown that the proposed UWA channel model enables the modelling of measured channels with higher precision. Moreover, the superiority of the SOB model over the FOB model is shown regarding the modelling of characteristic quantities (such as the delay spread and coherence bandwidth) of the measurement data, which are useful quantities for designing UWA communication systems. For instance, the knowledge of the Doppler spread is necessary for determining the minimum subcarrier spacing in OFDM systems.

### **3.4 Chapter Summary and Conclusion**

In this chapter, a new geometry-based deterministic UWA channel model has been developed under the assumption that the ocean surface and bottom are smooth and the ocean bottom slopes gently up/down (see **Paper C**). The waveguide model has been studied in a general form by considering the SOB case. The influence of the ocean-bottom slope angle on the statistical properties of the UWA channel model has been studied and the validity of the main analytical results is confirmed by measurement data. It has been shown by theoretical and simulation results that even a relatively small slope angle influences considerably the statistical properties of UWA channels, thus, it has to be considered in the area of UWA channel modelling.

# Chapter 4

## Measurement-Based Channel Modelling

### 4.1 Introduction

Geometry-based UWA channel models have been developed to capture the channel characteristics. Nevertheless, such models still need to be verified against measurement data. Measurement-based UWA channel modelling provides UWA channel simulators with a high level of accuracy; however, it is a scenario-specific approach. Measurement-based UWA channel modelling basically contains three steps: 1) collecting UWA channel data through measurement campaigns, 2) analyzing the measured UWA channel to understand its behavior, and 3) providing a stochastic/deterministic channel model which can reproduce the same statistical properties of the measured UWA channel.

Some few channel models for UWA channels have been developed in [19, 26, 40]; however, none of them can precisely capture all the physical properties of UWA channels. There are numerous studies focusing on the modelling of UWA channels, which are based on real-world measurement data collected in specific scenarios. For example, the distribution of the UWA channel envelope has been shown to be Rayleigh distributed in [71, 72], while the authors of [41, 66] have reported that the envelope follows the Rice distribution. Besides these distributions, the channel envelope may also follow the lognormal distribution or the  $K$ -distribution as claimed in [73] and [74], respectively. These controversial studies demonstrate that there is a need for a realistic UWA channel simulator. In the absence of a standardized model for UWA channels, measurement-based channel modelling is an alternative approach to model the behavior of real-world UWA channels. A summary of important UWA channel measurements is presented in Table 4.1. As can

be seen from the table, most of the measurement campaigns were conducted in shallow water environments for F2F communications. Thus, there is a need for measuring UWA channels for V2V communications in shallow/deep water. For the design of a measurement-based channel simulator, the model parameters need to be estimated, including the path gains, Doppler frequencies, propagation delays, and phase shifts. Hence, sophisticated and efficient parameter computation methods are required to precisely estimate these model parameters from real-world UWA measurement data. In the literature, many powerful parameter computation methods have been proposed. For example, an application of the estimation of signal parameters via the rotational invariance techniques (ESPRIT) algorithm is presented in [82] to design a measurement-based wideband channel model. The ESPRIT can be applied to a wide range of problems including accurate detection and estimation of sinusoids in noise. It exploits an underlying rotational invariance among signal subspaces induced by an array of sensors with a translational invariance structure. The space-alternating generalized expectation-maximization (SAGE) algorithm [83] is another parameter computation method, which is widely used in the area of channel parametrization because of its high performance. The SAGE algorithm updates the parameters sequentially by alternating between several small hidden-data spaces defined by algorithm designer. Furthermore, the iterative nonlinear least square approximation (INLSA) algorithm has been proposed in [84] to design measurement-based wideband channel simulators in which the authors showed that the INLSA algorithm has lower complexity and better performance compared with the SAGE algorithm. The INLSA algorithm has further been refined and developed in [85–87]. It has been shown in [88] that the INLSA outperforms the SAGE and ESPRIT algorithms with respect to their fitting accuracy to the ACF of a given reference model. In INLSA, the channel parameters are computed in  $L$  independent steps, each of which corresponds to the estimation of the parameters of the channel gain by minimizing an error norm. To solve each of the  $L$  minimization problems, an iterative parameter computation method has been considered. These aforementioned algorithms have been developed for the parametrization of stationary channels models, while modelling of non-stationary UWA channels is an open framework for future investigations. In this chapter, two measurement-based UWA channel models have been developed for a stationary UWA channel and a non-stationary one.

Table 4.1: Summary of important UWA channel measurements.

Paper	Carrier frequency (kHz)	Bandwidth (kHz)	Antenna configuration	Propagation environment	Communication type	Channel statistics
[40]	40/62	40/24	SISO	Shallow water	F2F	BER, delay spread, and average delay
[74]	11.5	3.9	multiple-input multiple-output (MIMO)	Shallow water	F2F	Channel envelope distribution, ACF, and Doppler spread
[75]	14/6	8/4	SISO	Shallow water	F2F	PDP
[55]	3	1	SISO	Deep water	F2M	CIR and BER
[26]	10/13.5/13	6/9/4	SISO	Shallow water	F2F/F2M	PDP, Channel envelope distribution, and ACF
[66]	12	12.5	MIMO	Shallow water	F2F	Channel envelope distribution
[51]	14/6	8/4	SISO	Shallow water	F2F	PDP, BER, CIR, and Doppler spread
[76]	38.5	23/3	MIMO	Shallow water	F2F	CIR and Channel envelope distribution
[71]	11.2	17.5	MIMO	Shallow water	F2F	Capacity and Channel envelope distribution
[77]	8/12	4	MIMO	Shallow water	F2F	CIR, Doppler PSD, and Doppler spread
[78]	5	4	SISO	Shallow water	F2F	PDP, BER, and ACF
[79]	-	20	SISO	Shallow water	F2F	Coherence time and BER
[80]	17	4	single-input multiple-output (SIMO)	Shallow water	F2F	CIR and BER
[81]	12	8	SISO	Shallow water	F2F	CIR, PDP, and Doppler spread

## 4.2 UWA Channel Modelling Using the INLSA Algorithm

In **Paper D**, a sum-of-cisoids uncorrelated scattering (SOCUS) channel simulator is proposed based on measured shallow UWA channels. To obtain the experiment data, a measurement campaign was launched near the New Jersey shore to measure a shallow UWA channel F2F communication system. Starting from the measured data, the TVCIR of the UWA channel is computed. The objective is to design a channel simulator that emulates the TVCIR of the measured channel. From the measurement-based UWA channel simulator, time-variant channel transfer function (TVCTF), TFCF, PDP, and the channel envelope's PDF are derived.

To determine the parameters of the simulation model, the INLSA method is adopted which had not been applied to UWA channel modelling. A procedure is presented in **Paper D** that allows us to easily use it for the area of measurement-based UWA channel modelling. The key point in using INLSA is that the delays for each path are known from the measured TVCIR. Thus, other model parameters, such as gains, Doppler frequencies, and phase shifts need to be obtained. The performance of the designed UWA channel simulator is assessed by comparing the TFCF, PDP, and the PDF of the channel envelope with the corresponding quantities of the measured UWA channel.

The results of the assessment in **Paper D** show an excellent agreement between the statistical properties of the UWA channel simulator, designed by the INLSA algorithm, and those of the real-world UWA channel. In other words, the INLSA algorithm estimates precisely the simulation model parameters and results in an excellent match with the statistical properties of real-world channels. It is also shown that the distribution of the channel envelope of our measurement data closely follows the Rayleigh distribution.

## 4.3 Non-Stationary UWA Channel Modelling

As mentioned in Chapter 2, a channel is called physically non-stationary if scatterers are moving or the velocity of the transmitter/receiver is changing. There is a need for developing such channel models which account for non-stationary properties of UWA channels. The motivation of developing such channel models is that changes in the speed and direction of the transmitter/receiver are undetachable parts of real-world UWA communication systems. Owing to the non-stationary nature of V2V UWA channels, considering the effect of varying transmitter's/receiver's ve-

locity (or even moving scatterers) is of particular importance in the corresponding UWA channel models.

**Paper E** proposes a non-stationary time-continuous channel simulator for UWA channels with given Doppler power spectrum (DPS) obtained from measurement data. While many researchers are concerned with the PDPs [75, 89, 90], the DPS have been less developed for UWA channels [78, 91]. The proposed channel simulator has been developed such that its statistical properties (average Doppler shift and Doppler spread) match as closely as possible to those of the measured real-world UWA channel. The performance of the designed UWA channel simulator is assessed by comparing the time varying average Doppler shift and time varying Doppler spread of the channel simulator with the corresponding quantities of the measured UWA channel. Under the standard assumption of WSSUS, the DPS of UWA channels can be computed by taking the Fourier transform of the temporal ACF of the received signal [77, 92]. However, the WSSUS assumption may not be valid due to the non-stationary behaviour of UWA channels [78].

In **Paper E**, a channel simulation model with complex channel gains is exploited based on a SOCUS model [93], which is an appropriate channel model for a large class of wideband measured channels under non-isotropic scattering conditions. However, unlike the conventional SOCUS model presented in **Paper D**, the channel gains are time-variant. For the design of measurement-based channel simulators, the model parameters, including the path gains, Doppler frequencies, and phase shifts need to be determined. The key point in parametrization of the non-stationary channel simulator is that the Doppler frequencies are known from measured DPSs and only the path gains need to be obtained. The phase shifts are modelled uniformly distributed between 0 and  $2\pi$ . In **Paper E**, an approach is used to compute time-continuous path gains for the simulation model. In this case, the time continuous gain corresponds to each snapshot interpolates the value between two consecutive and constant gains obtained from measurement data.

The statistical properties of the simulation model have been obtained by means of the concept of the spectrogram. The spectrogram has been widely used for analyzing time-variant signals and both stationary and non-stationary processes. Moreover, the spectrogram provides variations of the spectral density of a signal (or stochastic process) over time. The spectrogram of a time-varying signal is computed by dividing the signal into overlapping shorter signals and then computing the squared absolute value of the Fourier transform of the short-time signal [94].

To obtain the experimental data, a measurement campaign was launched in West Lake, Hanoi, Vietnam to measure a shallow UWA channel, which was used as a

starting point for computing the time-variant DPS. The measurement data was collected for two different scenarios. In the first measurement scenario, the receiver moved away from the fixed transmitter at an inconstant speed of around 0.5 m/s. In the second measurement scenario, the receiver moved towards the transmitter at a varying speed of around 0.5 m/s.

The numerical results show a good fit between the measured channel and the simulation model with respect to the DPS, average Doppler shifts and Doppler spread.

## **4.4 Chapter Summary and Conclusion**

In this chapter, two different measurement-based UWA channel simulators have been proposed, where the first one is developed for stationary UWA channels and the second one is developed for non-stationary ones. The latest version of the INLSA algorithm has been adopted for designing measurement-based UWA channel simulators for the stationary case (see **Paper D**). The algorithm has been applied to UWA measurement data to estimate the parameters of the channel simulator. The TVCIR, TFCF, PDP, and the channel envelope distribution of the channel simulator have been matched to corresponding quantities of the measured channel. It has been shown that the INLSA algorithm precisely estimates the channel model parameters and provides an excellent fit to measured UWA channels.

In addition, a non-stationary time-continuous channel simulator has been proposed for UWA channels by means of measured DPSs (see **Paper E**). Some main statistical properties of the UWA channel such as the time-variant DPS, time-variant average Doppler shift, and time-variant Doppler spread of the channel simulator have been matched to the corresponding quantities of the measured UWA channel. It has been shown that the new channel model provides an excellent fit to the measured UWA channels. As discussed in this chapter, measurement-based UWA channel modelling approach provide precise and accurate channel models, however, they are site-dependent.

# Chapter 5

## The Sea Surface Simulator

### 5.1 Introduction

Detailed knowledge of the statistics of the sea surface waves is important and useful for many practical applications, such as describing the behavior of the sea surface, the construction of coastal works like offshore structures [95] and for animating games and movies [96]. Moreover, the temporal elevation of the sea surface causes backscatterer signals influencing the Doppler frequency spectrum of UWA waves [97]. Moreover, in [90], a channel model has been developed for UWA communications by taking effects of wind-generated waves and bubbles into account. The wave spectrum provides insight into important statistical properties of the sea surface waves, such as the ACF of the sea surface waves, significant wave height, and the moments of the spectrum.

This chapter aims to exploit some techniques used in the area of mobile radio channel modelling for simulating sea surface waves. The sea surface simulator is designed by applying the concept of deterministic channel modelling to two main classical wave spectra, namely the Pierson-Moskowitz (PM) model [98] and JOint North Sea WAVE Project (JONSWAP) model [99]. By using the sum-of-sinusoids (SOS) principle, this chapter studies three methods for designing one-dimensional sea surface waves simulators with given wave spectra. The three well-known parameter computation methods adopted for the parametrization of the sea surface simulator are: the LPNM [100], method of equal distances (MED) [101], and the method of equal areas (MEA) [101]. Figs. 5.1 and 5.2 present the PM and JONSWAP spectra  $S_{\mu\mu}(\omega)$ , respectively, for different value of wind speed  $U$ .

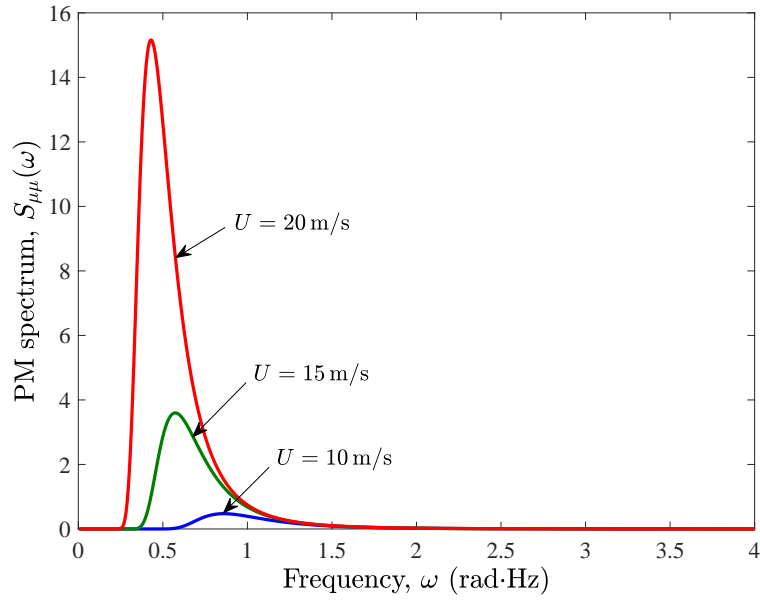


Figure 5.1: The PM spectrum  $S_{\mu\mu}(\omega)$  for different value of wind speed  $U$ .

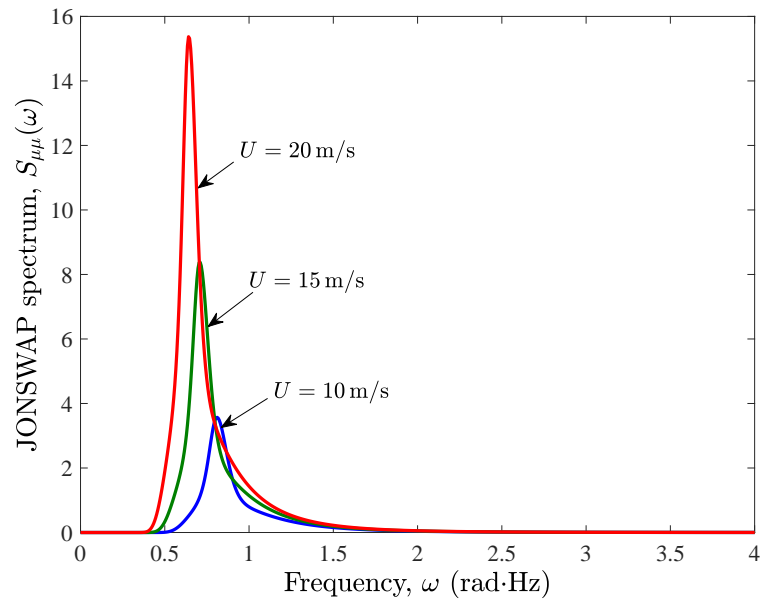


Figure 5.2: The JONSWAP spectrum for different value of wind speed  $U$ .

## **5.2 One-Dimensional Sea Surface Simulator**

Sea surface simulation is a popular research topic in ocean engineering [102] and computer graphics [103]. Sea surface waves greatly enhance the flux of energy and momentum between the atmosphere and the sea. However, to design more realistic channel models for UWA communications, accurate and realistic simulation models for the sea surface dynamics, which can capture the temporal elevation of the sea surface, are of great interest.

Two approaches, classified as physical and parametric/spectral methods, exist in the literature to simulate sea surface waves. The physical approaches (e.g., [104–106]), which aim to solve the wave equations are generally too complex to find analytical solutions. However, parametric/spectral approaches (e.g., [103, 107, 108]) are appropriate to model the periodic motion of the sea surface elevation in deep water environments. For instance, an adaptive spectrum sampling technique has been applied in [103] for obtaining the sea surface model parameters. Therein, a limited frequency range and selected waves are considered, which are the most typical representatives of the wave spectrum. A real-time additive sound synthesis method applied to the sea surface wave modelling has been described in [108] in which the authors considered the sea as partials of a sound by transposing the frequency and time domains to the wave number domain. However, the sea surface waves can be properly modelled by a random process with the help of a specified wave spectrum, such as the PM spectrum and JONSWAP spectrum.

### **5.2.1 Parametric Sea Surface Spectra**

The PM and JONSWAP models are two *non-symmetric* parametric models of the sea surface spectrum. However, a *symmetrical* PM (JONSWAP) spectrum is introduced in **Paper F** by mirroring the original spectrum model with respect to the y-axis. To have the same energy level as the one for the non-symmetric spectrum, the symmetrical spectrum is divided by two. In the PM model, the wave spectrum is a function of the wind speed and the wave frequency, while the JONSWAP spectrum is an extension of the PM spectrum for fetch-limited seas. Assuming the PM and JONSWAP spectra, the main statistical properties of the sea surface waves reference model are derived and compared with those of the sea surface waves simulator.

### 5.2.2 SOS Principle

The sea surface waves can be modeled as a superposition of sine waves using Rice's SOS [109, 110]. A simulation model for sea surface waves described by a stochastic SOS process  $\hat{\mu}(t)$  can be modelled as

$$\hat{\mu}(t) = \sum_{n=1}^N c_n \cos(\omega_n t + \theta_n) \quad (5.1)$$

where  $N$  is the number of sinusoids. The parameter  $c_n$  denotes the  $n$ th wave amplitude and the symbols  $\omega_n$  and  $\theta_n$  stand for the wave frequency and the phase shift of the  $n$ th sea surface wave, respectively.

### 5.2.3 Utilized Parameter Computation Methods

For the design of a sea surface simulator, the important task is obtaining the model parameters, which are the wave amplitudes, wave frequencies, and phase shifts. Three methods are described in **Paper F** for the computation of constant values for the wave amplitudes  $c_n$  and the wave frequencies  $\omega_n$ . The phase shifts  $\theta_n$  are supposed to be uniformly distributed random variables over the interval  $(0, 2\pi]$ . The aim is to compute the model parameters such that the ACF of the sea surface waves simulator matches the ACF of the reference model obtained by the PM and JONSWAP spectra.

A good fit between the reference model and the simulation model has been achieved with respect to the ACF, distribution of the sea surface elevation, and the moments of the PM and JONSWAP spectra. Although all methods have a relatively good performance, they have their own specific advantages and disadvantages. **Paper F** shows that the performance of the LPNM is slightly better than that of the other methods, but, the price to be paid for this achievement is a considerable increase in numerical complexity.

An excellent agreement between the given sea surface models and the corresponding simulation model is achieved with respect to the main statistical properties of the sea surface waves. The simulation results in **Paper F** show that the distribution of the simulated sea surface elevation follows closely the Gaussian distribution, which is in agreement with the results obtained from measurement data [111]. It is shown that for a given number of sinusoids, the LPNM and the MEA have almost the same performance, whereas the MED results in a sea surface waves simulator that suffers from a relatively small period.

### **5.3 Chapter Summary and Conclusion**

In this chapter, a sea surface waves simulator has been developed based on the SOS concept by using the PM and JONSWAP spectra (see **Paper F**). Three methods have been applied to compute the parameters of a sea surface waves simulator. Those three well-known parameter computation methods, namely the LPNM, MED, and the MEA, have widely been used in the area of mobile radio channel modelling. The results of the assessment show a good match between the main statistical properties of the sea surface waves simulator designed by the three parameter computation methods and those of the given reference model. It has been concluded that the LPNM and the MEA have almost the same performance, whereas the MED results in a sea surface waves simulator that has a relatively small period. The sea surface waves simulator can provide a deeper insight into the behavior of moving scatterers on the sea surface. Although it is important to study the influence of the moving scatterers on the delays and AOAs of the received rays at the receiver, this study is not a topic of this dissertation.



# Chapter 6

## Performance Analysis of Alamouti-Coded OFDM Systems

### 6.1 Introduction

UWA communication systems suffer from band-limited channels and low data rate transmissions. Multiple-input multiple-output (MIMO) OFDM systems, which are very advantageous for band-limited UWA channels, have been thoroughly investigated in recent years [112, 113]. Space-time block coding (STBC) techniques, such as the Alamouti scheme [114] coupled with OFDM provide more reliable communications with high data rate transmissions [115]. The application of the simple Alamouti scheme in UWA communication systems has been extensively studied in the literature [116–118]. For example, in [116], a detection algorithm has been proposed for UWA communication systems exploiting the Alamouti STBC scheme. Conversely, two different detection algorithms have been proposed in [117] and [118] for UWA communication systems exploiting Alamouti space-frequency block coding (SFBC) techniques.

In [119], it is shown that the Alamouti scheme performs well if the channel remains constant over the duration of an Alamouti codeword. Due to the fact that UWA channels cannot be assumed to be constant over the duration of two consecutive OFDM blocks [116], the effect of the temporal correlation of UWA channels on the performance of Alamouti-coded OFDM systems needs to be studied in the application of UWA communications. This degradation effect has been investigated in [120–122] for mobile radio communications over Rayleigh fading channels. It has been shown in [120] by simulation and in [121] and [122] by theory that the performance of Alamouti STBC OFDM systems depends on both the temporal and spatial correlations of a channel. A summary of analyses and investigations on the

performance of UWA communication systems for different scenarios is listed in Table 6.1. It should be mentioned that in all papers listed in Table 6.1, the performance of systems has been only analyzed by simulations (not analytical analysis).

For an accurate performance analysis of communication systems over spatio-temporally correlated UWA channels, an exact analytical expression for the bit error probability (BEP) is necessary. In this chapter, the UWA channel model developed in **Paper A** is first extended with respect to spatial selectivity. Then, the performance of Alamouti-coded OFDM systems is studied over the proposed UWA channel model, which is correlated in both time and space.

## **6.2 Performance Analysis of Alamouti-Coded OFDM Systems**

In **Paper G**, a realistic UWA channel model has been considered, which can be correlated in either time or space or simultaneously in both domains. Hence, by using this UWA channel model, an expression has been derived for the BEP of Alamouti-coded OFDM systems. In addition, the BEPs of two special cases are also studied, where the UWA channel is only correlated in either time or space.

### **6.2.1 The Utilized UWA Channel Model**

As mentioned above, the 1-by-1 UWA channel model (a SISO case) presented in **Paper A** is extended to a 2-by-1 UWA channel model to make it readily available for systems with two transmit antennas and one receiver antenna (a multiple-input single-output (MISO) case) as can be seen in Fig. 6.1.

**Paper G** studies the correlation properties of the UWA channel model required for the performance analysis of MISO-OFDM UWA communication systems. To this aim, the complex space-time variant channel transfer function (STVCTF) of the model is derived from which the space-time cross-correlation function (CCF) and the temporal ACF are computed.

### **6.2.2 Performance Analysis**

To analyze the performance of the system, the instantaneous output signal-to-interference-plus-noise ratio (SINR) is introduced, and then a general expression for the BEP of the Alamouti-coded OFDM system over UWA channels is derived. This expression can be used to study the performance for several specific cases, where

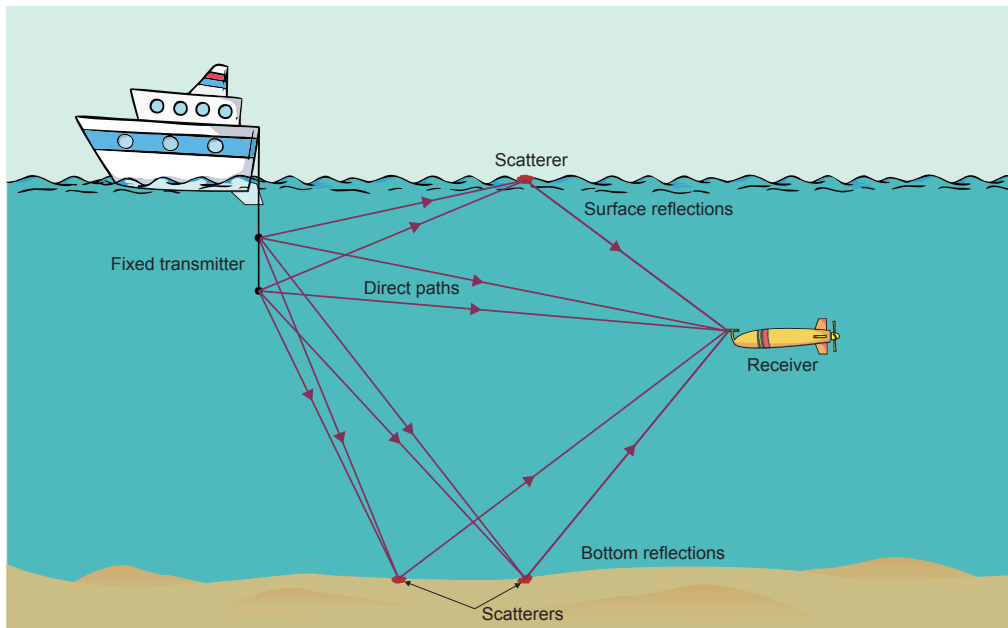


Figure 6.1: A 2-by-1 F2M UWA communication system.

the channel is correlated in time or space or even in both domains. The general expression is not limited to UWA channels. In fact, it can also be used for analyzing the performance of any time-varying multipath Rayleigh fading channel. Moreover, the obtained expressions for the BEP allow us to study the effect of the maximum Doppler frequency and antenna spacings on the performance of Alamouti-coded OFDM systems.

It is shown that the performance of Alamouti-coded OFDM systems depends greatly on the statistics of the UWA channel assessed at the antenna spacing and the symbol duration. From the results obtained in **Paper G**, it can also be concluded that an acceptable performance is attained if the antenna spacing, unlike that of mobile radio communications, is very large (e.g., more than 2 m).

Table 6.1: Summary of the performance analysis of UWA communication systems.

Paper	Carrier frequency (kHz)	Antenna configuration	Range (km)	Communication type	Computed statistics
[123]	12	MIMO	2 / 4	F2F	mean squared error (MSE) (to analyze carrier-phase tracking methods)
[124]	12	MIMO	3	F2F	BER
[125]	12	MIMO	1 / 1.3	F2F	BER
[126]	12	SISO	-	F2F	MSE performance of a channel estimator, BER
[118]	20	MIMO	3	F2F	symbol error rate (SER)
[127]	12	MIMO	1-11	mobile-to-fixed (M2F)/F2F	BER
[72]	50 / 55	SISO	-	F2F	BEP
[116]	13	MIMO	1	F2F	MSE
[113]	11.5 / 110	MIMO	0.5 / 1.5	F2F	BER, Doppler shift
[128]	1	SISO	5	F2F	Capacity
[112]	14	MIMO	1	F2F	MSE
[117]	13	MIMO	3.5 7	F2M	BER
[129]	12	SISO	-	M2M	SER and BER

### **6.3 Chapter Summary and Conclusion**

In this chapter, the performance of Alamouti-coded OFDM systems over a proposed UWA channel model correlated in time and/or space has been analyzed (see **Paper G**). Unlike the conventional assumption for Alamouti-coded systems, the channel envelope can change during two consecutive transmission time slots which account for realistic UWA propagation scenarios. An exact expression for the BEP of the system has been analytically derived for a spatio-temporally correlated UWA channel. The obtained expression for the BEP has been reduced to two special cases where the UWA channel is either correlated in time or correlated in space. The simulation results show that the performance of Alamouti-coded OFDM systems over the UWA channel depends strongly on the value of the STVCTF evaluated at the symbol duration and the antenna separation.



# Chapter 7

## Summary of Contributions and Future Work

This dissertation aims to make a bridge between the channel modelling for UWA communications and mobile radio communications, exploits possible approaches in mobile radio communications in UWA communications, and highlights differences between these two wireless communications. Table 7.1 summarises the differences between UWA channels and mobile radio channels.

### 7.1 Major Contributions

Although UWA channel modelling has been a hot topic for several decades, there is a considerable potential for further advancements in this area. The development of new upcoming technologies including V2V UWA communication systems, UWA sensor networks, water pollution monitoring systems requires robust and realistic UWA channel models. This dissertation studies various topics ranging from the modelling of F2M and V2V communication systems in different shallow UWA propagation scenarios to the performance analysis of UWA communication systems over UWA channels. The contribution of this dissertation is listed below.

- Developing a geometry-based stochastic UWA channel model under rough surface and bottom conditions. Derivation of the AOA and AOD distributions with respect to the distribution of scatterers on the surface and bottom of the ocean. Proposing a parameter computation method, namely the MESS for the parametrization of the corresponding simulation model.
- Developing a geometry-based stochastic channel model under the non-isovelocity condition for shallow UWA communication systems. Studying the be-

Table 7.1: Differences between UWA and mobile radio channels.

Parameters/Features	UWA channels	Mobile radio channels
Communication signals	acoustic	electromagnetic
Data rate	Low (in order of kbps)	High (in order of Mbps/Gbps)
Carrier frequency	Low (in order of kHz)	High (in order of MHz/GHz)
Communication range	Short and long	Short and long
Channel properties	Correlation functions, PDP, PSD, channel envelope distribution, delay and Doppler spread, etc.	Correlation functions, PDP, PSD, channel envelope distribution, delay and Doppler spread, etc.
Channel parametrization	LPNM/INLSA/MESS	LPNM/INLSA/MED/MEA, etc.
Number of paths	Low/Sparse	Very high
Simulation models	Stochastic/Deterministic /Ray tracing	Stochastic/Deterministic /Ray tracing
Performance analysis	BER	BER
Antenna configuration	SISO/MIMO/MISO/SIMO	SISO/MIMO/MISO/SIMO

havior of a shallow UWA channel model under the non-isovelocity ocean condition and validating the channel model by real-world UWA measurement data.

- Developing a new geometry-based deterministic UWA channel model by taking into account that the ocean bottom slopes gently up/down. This assumption is quite realistic and had not been considered in the area of UWA channel modelling. The effect of the slope ocean angle on the statistical properties of the UWA channel has been thoroughly investigated.
- Developing a measurement-based UWA channel model designed by means of the INLSA method. Studying the main statistical properties of the UWA channel.
- Developing a non-stationary time-continuous simulation model based on given DPSs obtained from measurements.
- Developing a one-dimensional sea surface simulator by using the principle of SOS. Moreover, studying three methods for the design of the sea surface waves simulator.
- Analyzing the an performance of Alamouti-coded OFDM system over time-varying UWA channels. Derivation of an exact analytical expression for the

BEP of Alamouti-coded OFDM systems. Studying two special cases where UWA channels are either correlated in time or correlated in space.

## **7.2 Future Work**

This dissertation is an effort to probe into the modelling, analysis, and simulation of UWA channels. However, several problems still remain which are not addressed in this dissertation. In this section, some problems are highlighted.

- A measurement campaign needs to be launched to measure UWA channels in a shallow ocean environment with a harsh ocean-bottom slope angle. In this case, the superiority of the developed geometry-based deterministic UWA channel model (presented in Chapter 3) developed under SOB condition will be more evident over the FOB model.
- The geometry-based deterministic UWA channel model developed under SOB condition (presented in Chapter 3) has been developed by taking only macro-scattering effects into account. However, to make the proposed UWA channel model more realistic, the channel model needs to be developed by taking also micro-scattering effects into account.
- Due to the fact that the statistical properties of UWA channels in most cases vary rapidly with time, robust geometry-based non-stationary UWA channel models need to be developed.
- In this dissertation, a one-dimensional sea surface simulator (presented in Chapter 5) has been developed. However, the effect of moving scatterers on the statistical properties of UWA channels has not been studied. Therefore, this big gap also needs to be addressed in future work.
- The performance of a 2-by-1 Alamouti-coded OFDM system has been analyzed over a proposed UWA channel; however, the system can be extended to a 2-by-2 UWA communication system.
- In the literature, the number of geometry-based stochastic UWA channel models developed for deep water is very limited. To fill this gap, new UWA channel simulation models describing acoustic wave propagation in deep water need to be developed.

## *Summary of Contributions and Future Work*

## REFERENCES

- [1] L. M. Brekhovskikh and Y. P. Lysanov, *Fundamentals of Ocean Acoustics*, 3rd ed. New York, NY, USA: Springer, 2002.
- [2] A. Quazi and W. Konrad, “Underwater acoustic communications,” *IEEE Commun. Mag.*, vol. 20, no. 2, pp. 24–30, Mar. 1982.
- [3] A. G. Zajić, *Mobile-to-Mobile Wireless Channels*, 1st ed. Artech House, Inc., Boston, London, 2013.
- [4] S. M. Flattè, *Sound Transmission through a Fluctuating Ocean*. Cambridge, UK: Cambridge University Press, 1979.
- [5] D. Shin, S. Y. Na, J. Kim, and S. J. Baek, “Fish robots for water pollution monitoring using ubiquitous sensor networks with sonar localization,” in *Proc. Int. Conf. Convergence Inf. Technol.*, Nov. 2007, pp. 1298–1303.
- [6] S. Zhang and L. Zhang, “Water pollution monitoring system based on Zig-Bee wireless sensor network,” in *Proc. Int. Conf. Electron., Commun., and Control (ICECC)*, Sep. 2011, pp. 1775–1779.
- [7] A. Baptista, B. Howe, J. Freire, D. Maier, and C. T. Silva, “Scientific exploration in the era of ocean observatories,” *Comput. Sci. Eng.*, vol. 10, no. 3, pp. 53–58, May 2008.
- [8] P. S. Rossi, D. Ciuonzo, T. Ekman, and H. Dong, “Energy detection for MIMO decision fusion in underwater sensor networks,” *IEEE Sensors Journal*, vol. 15, no. 3, pp. 1630–1640, Mar. 2015.
- [9] Y. Dong and H. Dong, “Simulation study on cross-layer design for energy conservation in underwater acoustic networks,” in *Proc. IEEE OCEANS*, San Diego, Sep. 2013, pp. 1–5.
- [10] B. Ali, N. Javaid, S. U. Islam, G. Ahmed, U. Qasim, and Z. A. Khan, “RSM and VSM: Two new routing protocols for underwater WSNs,” in *Proc. Int. Conf. on Intelligent Networking and Collaborative Systems (INCoS)*, Sep. 2016, pp. 173–179.
- [11] M. Ghaleb, E. Felemban, S. Subramaniam, A. A. Sheikh, and S. B. Qaisar, “A performance simulation tool for the analysis of data gathering in both terrestrial and underwater sensor networks,” *IEEE Access*, vol. 5, pp. 4190–4208, 2017.

- [12] P. Gjanci *et al.*, “Path finding for maximum value of information in multi-modal underwater wireless sensor networks,” *IEEE Transactions on Mobile Computing*, vol. pp, no. 99, pp. 1–1, 2017.
- [13] O. Pallares, J. del Rio, and P. J. Bouvet, “Time synchronization accuracy refinement for mobile shallow water acoustic sensor network,” in *Proc. IEEE OCEANS*, Shanghai, China, Apr. 2016, pp. 1–6.
- [14] A. K. Mohapatra, N. Gautam, and R. L. Gibson, “Combined routing and node replacement in energy-efficient underwater sensor networks for seismic monitoring,” *IEEE J. Ocean. Eng.*, vol. 38, no. 1, pp. 80–90, Jan 2013.
- [15] H. Matsumoto *et al.*, “A vertical hydrophone array coupled via inductive modem for detecting deep-ocean seismic and volcanic sources,” in *IEEE OCEANS*, Sep. 2010, pp. 1–7.
- [16] M. Dalbro *et al.*, “Wireless sensor networks for off-shore oil and gas installations,” in *Proc. 2nd Int. Conf. Sensor Technol. and Appl. (SENSORCOMM)*, Aug. 2008, pp. 258–263.
- [17] S. I. Siddiqui, M. Ludvigsen, and H. Dong, “Analysis, verification and optimization of AUV navigation using underwater acoustic models,” in *Proc. IEEE OCEANS*, Washington, Oct. 2015, pp. 1–6.
- [18] J. Gao, A. A. Proctor, Y. Shi, and C. Bradley, “Hierarchical model predictive image-based visual servoing of underwater vehicles with adaptive neural network dynamic control,” *IEEE Transactions on Cybernetics*, vol. 46, no. 10, pp. 2323–2334, Oct. 2016.
- [19] A. G. Zajić, “Statistical modeling of MIMO mobile-to-mobile underwater channels,” *IEEE Trans. Veh. Technol.*, vol. 60, no. 4, pp. 1337–1351, May 2011.
- [20] S. Liu, G. Qiao, L. Liu, L. Ma, and Y. Zhao, “A slide match and iteration approach for mobile underwater acoustic communication,” in *Proc. IEEE/OES China Ocean Acoustics (COA)*, Jan. 2016, pp. 1–5.
- [21] K. M. B. Tomasi and G. Zappa, “JANUS: The genesis, propagation and use of an underwater standard,” in *Proc. Eur. Conf. Underwater Acoust.*, Istanbul, Turkey, Jul. 2010, pp. 1–6.

- [22] J. Potter *et al.*, “The JANUS underwater communications standard,” in *Proc. IEEE Underwater Communications and Networking (UComms)*, Sep. 2014, pp. 1–4.
- [23] A. Smerdon, F. Bustamante, and M. Baker, “The SWIGacoustic standard: An acoustic communication standard for the offshore energy community,” in *Proc. IEEE 3rd. Underwater Communications and Networking Conf. (UComms)*, Aug. 2016, pp. 1–4.
- [24] M. Pätzold, *Mobile Fading Channels*, 2nd ed. Chichester, U.K.: John Wiley & Sons, 2011.
- [25] P. Almers *et al.*, “Survey of channel and radio propagation models for wireless MIMO systems,” *EURASIP J. Wireless Commun. Networking*, vol. 2007, 2007.
- [26] P. Qarabaqi and M. Stojanovic, “Statistical characterization and computationally efficient modeling of a class of underwater acoustic communication channels,” *IEEE J. Ocean. Eng.*, vol. 38, no. 4, pp. 701–717, Oct. 2013.
- [27] J. M. Hovem, “Ray trace modeling of underwater sound propagation: Modeling and measurement methods for acoustic waves and for acoustic microdevices,” in *Modeling and Measurement Methods for Acoustic Waves and for Acoustic Microdevices*. InTech, Aug. 2013, ch. 23, pp. 573–598.
- [28] A. Borhani, *Modelling and analysis of non-stationary mobile fading channels using Brownian random trajectory models*. Ph.D. dissertation, Faculty Eng. Sci., Univ. Agder, Grimstad, Norway, 2014.
- [29] M. Pätzold and B. O. Hogstad, “A space-time channel simulator for MIMO channels based on the geometrical one-ring scattering model,” in *Proc. 60th IEEE Semiannual Veh. Technol. Conf. (VTC), Fall*, vol. 1, Los Angeles, CA, USA, Sep. 2004, pp. 144–149.
- [30] B. O. Hogstad, M. Pätzold, N. Youssef, and D. Kim, “A MIMO mobile-to-mobile channel model: Part II – The simulation model,” in *Proc. 16th IEEE Int. Symp. on Personal, Indoor and Mobile Radio Communications, PIMRC 2005*, vol. 1. Berlin, Germany, Sep. 2005, pp. 562–567.
- [31] B. O. Hogstad and M. Pätzold, “On the stationarity of sum-of-cisoids-based mobile fading channel simulators,” in *Proc. IEEE 67th Vehicular Technology*

- Conference, IEEE VTC 2008-Spring*. Marina Bay, Singapore, May 2008, pp. 400–404.
- [32] A. Chelli and M. Pätzold, “A MIMO mobile-to-mobile channel model derived from a geometric street scattering model,” in *Proc. 4th IEEE International Symposium on Wireless Communication Systems, ISWCS 2007*. Trondheim, Norway, Oct. 2007, pp. 792–797.
- [33] ———, “A non-stationary MIMO vehicle-to-vehicle channel model based on the geometrical T-junction model,” in *Proc. International Conference on Wireless Communications and Signal Processing, WCSP 2009*. Nanjing, China, Nov. 2009.
- [34] P. A. Bello, “Characterization of randomly time-variant linear channels,” *IEEE Trans. Commun. syst.*, vol. 11, pp. 360–393, Dec. 1963.
- [35] F.-X. Socheleau, C. Laot, and J. M. Passerieux, “Stochastic replay of non-WSSUS underwater acoustic communication channels recorded at sea,” *IEEE Trans. Signal Process.*, vol. 59, no. 10, pp. 4838–4849, Oct. 2011.
- [36] P. A. van Walree and R. Otnes, “Ultrawideband underwater acoustic communication channels,” *IEEE J. Ocean. Eng.*, vol. 38, no. 4, pp. 678–688, Oct. 2013.
- [37] S. H. Huang, T. C. Yang, and C.-F. Huang, “Multipath correlations in underwater acoustic communication channels,” *J. Acoust. Soc. Amer.*, vol. 133, no. 4, pp. 2180–2190, 2013.
- [38] F.-X. Socheleau, C. Laot, and J. M. Passerieux, “Parametric replay-based simulation of underwater acoustic communication channels,” *IEEE J. Ocean. Eng.*, vol. 40, no. 4, pp. 796–806, Oct 2015.
- [39] I. Kočańska and I. Nissen, “Limitations of WSSUS modeling of stationary underwater acoustic communication channel,” *Hydroacoustics*, vol. 19, pp. 229–238, 2016.
- [40] M. Chitre, “A high-frequency warm shallow water acoustic communications channel model and measurements,” *J. Acoust. Soc. Amer.*, vol. 122, no. 5, pp. 2580–2586, Nov. 2007.
- [41] P. Qarabaqi and M. Stojanovic, “Statistical modeling of a shallow water acoustic communication channel,” in *Proc. Underwater Acoust. Meas. Conf.*, Nafplion, Greece, Jun. 2009, pp. 1341–1350.

- [42] A. Abdi and H. Guo, "Signal correlation modeling in acoustic vector sensor arrays," *IEEE Trans. Signal Process.*, vol. 57, no. 3, pp. 892–903, Mar. 2009.
- [43] R. J. Urick, *Principles of Underwater Sound*, 3rd ed. Los Altos, California: Peninsula Publishing, 1983.
- [44] M. B. Porter and H. P. Bucker, "Gaussian beam tracing for computing ocean acoustic fields," *J. Acoust. Soc. Amer.*, vol. 82, no. 4, pp. 1349–1359, Oct. 1987.
- [45] M. B. Porter, "The KRAKEN normal mode program (draft)," Washington, DC: Naval Res. Lab., <http://www.dtic.mil/dtic/tr/fulltext/u2/a252409.pdf>, Tech. Rep., May 1992.
- [46] M. Siderius and M. B. Porter, "Modeling broadband ocean acoustic transmissions with time-varying sea surfaces," *J. Acoust. Soc. Amer.*, vol. 124, no. 1, pp. 137–150, Jul. 2008.
- [47] J. C. Peterson and M. B. Porter, "Ray/beam tracing for modeling the effects of ocean and platform dynamics," *IEEE J. Ocean. Eng.*, vol. 38, no. 4, pp. 655–665, Oct. 2013.
- [48] M. B. Porter, "The BELLHOP manual and user's guide: Preliminary draft," Heat, Light, and Sound Research, Inc., <http://oalib.hlsresearch.com/Rays/HLS-2010-1.pdf>, Tech. Rep., Jan. 2011.
- [49] P. C. Etter, "Review of ocean-acoustic models," in *Proc. IEEE Oceans*, Biloxi, Mississippi, USA, Oct. 2009, pp. 1–6.
- [50] ———, "Advanced applications for underwater acoustic modeling," *Advances in Acoustics and Vibration*, vol. 2012, Article ID 214839, pp. 1–28, 2012.
- [51] R. Otnes, P. A. van Walree, and T. Jenserud, "Validation of replaybased underwater acoustic communication channel simulation," *IEEE J. Ocean. Eng.*, vol. 38, pp. 689–700, Oct. 2013.
- [52] W. Carey, J. Doust, and L. M. Dillman, "Shallow-water transmission measurements taken on the New Jersey continental shelf," Naval Undersea Warfare Center Detachment, <http://www.dtic.mil/dtic/tr/fulltext/u2/a251417.pdf>, Tech. Rep., Apr. 1992.

## REFERENCES

- [53] R. van Vossen *et al.*, “Improved active sonar tactical support by through-the-sensor estimation of acoustic seabed properties,” *IEEE J. Ocean. Eng.*, vol. 39, no. 4, pp. 755–768, Oct. 2014.
- [54] A. C. Arruda, M. W. Roeckel, and J. Wakeley, “A raytracing approach to underwater reverberation modeling,” Pennsylvania State University, Applied Research Laboratory, <http://www.dtic.mil/dtic/tr/fulltext/u2/a209410.pdf>, Tech. Rep., Jun. 1989.
- [55] C. Liu, Y. V. Zakharov, and T. Chen, “Doubly selective underwater acoustic channel model for a moving transmitter/receiver,” *IEEE Trans. Veh. Technol.*, vol. 61, no. 3, pp. 938–950, Mar. 2012.
- [56] X. Lurton, *An Introduction to Underwater Acoustics: Principles and Applications*, 2nd ed. Heidelberg, Germany: Springer, 2010.
- [57] H. Medwin and C. S. Clay, *Fundamentals of acoustical oceanography*. San Diego: Academic Press, 1997.
- [58] M. Stojanovic, *Acoustic (Underwater) Communications*. in Encyclopedia of Telecommunications, John G. Proakis (Ed.), New York: John Wiley & Sons, 2003.
- [59] F. B. Jensen, W. A. Kuperman, M. B. Porter, and H. Schmidt, *Computational Ocean Acoustics*, 2nd ed. New York, NY, USA: Springer, 2011.
- [60] P. C. Etter, *Underwater Acoustic Modeling and Simulation*, 4th ed. New York, NY, USA: CRC Press, 2013.
- [61] M. Stojanovic, “Underwater acoustic communications: Design considerations on the physical layer,” in *Proc. 5th Annu. Conf. Wireless Demand Netw. Syst. Services (WONS)*, Jan. 2008, pp. 1–10.
- [62] M. C. Domingo, “Overview of channel models for underwater wireless communication networks,” *Phys. Commun.*, vol. 1, no. 3, pp. 163 – 182, Sep. 2008.
- [63] E. Baktash, M. J. Dehghani, M. R. F. Nasab, and M. Karimi, “Shallow water acoustic channel modeling based on analytical second order statistics for moving transmitter/receiver,” *IEEE Trans. Signal Process.*, vol. 63, no. 10, pp. 2533–2545, May 2015.

- [64] A. G. Zaji'c "Statistical space-time-frequency characterization of MIMO shallow water acoustic channels," in *Proc. IEEE OCEANS*, Mississippi, MS, USA, Oct. 2009, pp. 1–6.
- [65] T. C. Yang, "A study of spatial processing gain in underwater acoustic communications," *IEEE J. Ocean. Eng.*, vol. 32, no. 3, pp. 689–709, Jul. 2007.
- [66] A. Radosevic, J. G. Proakis, and M. Stojanovic, "Statistical characterization and capacity of shallow water acoustic channels," in *Proc. IEEE EUROPE OCEANS*, Bremen, Germany, May 2009, pp. 1–8.
- [67] A. Radosevic, D. Fertonani, T. M. Duman, J. G. Proakis, and M. Stojanovic, "Capacity of MIMO systems in shallow water acoustic channels," in *Proc. IEEE Conf. Signals, Syst. and Computers (ASILOMAR), Conf. Record of the Forty Fourth Asilomar*, Nov. 2010, pp. 2164–2168.
- [68] P. J. Bouvet and A. LouSSERT, "Capacity analysis of underwater acoustic MIMO communications," in *Proc. IEEE OCEANS*, Sydney, NSW, Australia, May 2010, pp. 1–8.
- [69] R. Hicheri, M. Pätzold, B. Talha, and N. Youssef, "A study on the distribution of the envelope and the capacity of underwater acoustic channels," in *IEEE Int. Conf. Commun. Syst. (ICCS)*, Macau, China, Nov. 2014, pp. 394–399.
- [70] M. Stojanovic, "On the relationship between capacity and distance in an underwater acoustic communication channel," in *Proc. 1st ACM Int. Workshop Underwater Netw. (WUWNet)*, Los Angeles, CA, USA, Sep. 2006, pp. 41–47.
- [71] F.-X. Socheleau, J. M. Passerieux, and C. Laot, "Characterisation of time-varying underwater acoustic communication channel with application to channel capacity," in *Proc. Underwater Acoust. Meas. Conf.*, Nafplion, Greece, June 2009.
- [72] R. Galvin and R. F. W. Coats, "A stochastic underwater acoustic channel model," in *Proc. IEEE OCEANS Prospects for the 21st Century*, vol. 1, Sep. 1996, pp. 203–210.
- [73] B. Tomasi, P. Casari, L. Badia, and M. Zorzi, "A study of incremental redundancy hybrid ARQ over Markov channel models derived from experimental data," in *Proc. 5th ACM Int. Workshop on UnderWater Networks (WUWNet)*, Massachusetts, USA, Sep./Oct. 2010, pp. 1–8.

- [74] J. Zhang, J. Cross, and Y. R. Zheng, "Statistical channel modeling of wireless shallow water acoustic communications from experiment data," in *Proc. Conf. Military Commun. (MILCOM)*, Oct. 2010, pp. 2412–2416.
- [75] T. Jenserud and S. Ivansson, "Measurements and modeling of effects of out-of-plane reverberation on the power delay profile for underwater acoustic channels," *IEEE J. Ocean. Eng.*, vol. 40, no. 4, pp. 807–821, Oct. 2015.
- [76] S. Roy, T. M. Duman, V. McDonald, and J. G. Proakis, "High-rate communication for underwater acoustic channels using multiple transmitters and spacetime coding: Receiver structures and experimental results," *IEEE J. Ocean. Eng.*, vol. 32, no. 3, pp. 663–688, Jul. 2007.
- [77] C. C. Tsimenidis, B. S. Sharif, O. R. Hinton, and A. E. Adams, "Analysis and modelling of experimental doubly-spread shallow-water acoustic channels," in *Proc. Europe Oceans*, vol. 2, Jun. 2005, pp. 854–858.
- [78] P. A. van Walree, T. Jenserud, and M. Smedsrud, "A discrete-time channel simulator driven by measured scattering functions," *IEEE J. Sel. Areas Commun.*, vol. 26, no. 9, pp. 1628–1637, Dec. 2008.
- [79] T. C. Yang, "Toward continuous underwater acoustic communications," in *Proc. IEEE OCEANS*, Quebec City, QC, Canada, Sep. 2008, pp. 1–6.
- [80] A. G. Zajić and G. F. Edelmann, "Feasibility study of underwater acoustic communications between buried and bottom-mounted sensor network nodes," *IEEE J. Ocean. Eng.*, vol. 38, no. 1, pp. 109–116, Jan. 2013.
- [81] M. S. Caley and A. J. Duncan, "Wide-band shallow acoustic channel simulation with realistic Doppler and delay spreading for 3D evolving rough surfaces," in *Proc. IEEE 3rd. Underwater Communications and Networking Conf. (UComms)*, Aug. 2016, pp. 1–5.
- [82] J. Fuhl, J. P. Rossi, and E. Bonek, "High-resolution 3-D direction-of-arrival determination for urban mobile radio," *IEEE Antennas Propag. Mag.*, vol. 45, no. 4, pp. 672–682, Apr. 1997.
- [83] B. H. Fleury, M. Tschudin, R. Heddergott, D. Dahlhaus, and K. I. Pedersen, "Channel parameter estimation in mobile radio environments using the SAGE algorithm," *IEEE J. Sel. Areas Commun.*, vol. 17, no. 3, pp. 434–450, Mar. 1999.

- [84] D. Umansky and M. Pätzold, “Design of measurement-based wideband mobile radio channel simulators,” in *Proc. 4th IEEE Int. Symp. Wireless Commun. Syst. (ISWCS)*, Trondheim, Norway, Oct. 2007, pp. 229–235.
- [85] A. Fayziyev and M. Pätzold, “An improved iterative nonlinear least square approximation method for the design of measurement-based wideband mobile radio channel simulators,” in *Proc. Int. Conf. Adv. Technol. for Commun. (ATC)*, Danang, Vietnam, Aug. 2011, pp. 106–111.
- [86] ———, “An improved iterative nonlinear least square approximation method for the design of SISO wideband mobile radio channel simulators,” *REV J. Electron. Commun.*, vol. 2, no. 1–2, pp. 19–25, Jan./Jun. 2012.
- [87] A. Fayziyev, M. Pätzold, E. Masson, Y. Cocheril, and M. Berbineau, “A measurement-based channel model for vehicular communications in tunnels,” in *Proc. IEEE Conf. Wireless Commun. and Netw. (WCNC)*, Istanbul, Turkey, Apr. 2014, pp. 128–133.
- [88] A. Fayziyev and M. Pätzold, “The performance of the INLSA in comparison with the SAGE and ESPRIT algorithms,” in *Proc. Int. Conf. Adv. Technol. for Commun. (ATC)*, Hanoi, Vietnam, Oct. 2014.
- [89] T. Jenserud and S. Ivansson, “Modeling the power delay profile of underwater acoustic channels – The effects of out-of-plane scattering and reverberation,” in *Underwater Communications and Networking (UComms)*, Sep. 2014, pp. 1–5.
- [90] H. S. Dol, M. E. G. D. Colin, M. A. Ainslie, P. A. van Walree, and J. Janmaat, “Simulation of an underwater acoustic communication channel characterized by wind-generated surface waves and bubbles,” *IEEE J. Ocean. Eng.*, vol. 38, no. 4, pp. 642–654, Oct. 2013.
- [91] S. Watts, L. Rosenberg, S. Bocquet, and M. Ritchie, “Doppler spectra of medium grazing angle sea clutter; part 1: characterisation,” *IET Radar, Sonar Navigation*, vol. 10, no. 1, pp. 24–31, 2016.
- [92] H. Lasota and I. Kočańska, “Transmission parameters of underwater communication channels,” *Hydroacoustics*, vol. 14, pp. 119–126, 2011.
- [93] M. Pätzold and B. Talha, “On the statistical properties of sum-of-cisoids-based mobile radio channel models,” in *Proc. 10th Int. Symp. Wireless Pers. Multimedia Commun. (WPMC)*, Jaipur, India, Dec. 2007, pp. 394–400.

- [94] M. Pätzold and N. Youssef, "Spectrogram analysis of multipath fading channels," in *Proc. 26th IEEE Personal, Indoor and Mobile Radio Communications (PIMRC)*, Hong Kong, China, Aug./Sep. 2015, pp. 2214–2219.
- [95] R. Luppez, B. Düz, H. J. L. V. D. H. P. V. D. Plas, and A. E. p. Veldman, "Numerical simulation of extreme wave impact on offshore platforms and coastal constructions," in *Proc. 5th Int. Conf. Comput. Methods in Marine Eng. (MARINE)*, 2011, pp. 122–133.
- [96] Y. Kryachko, "Using vertex texture displacement for realistic water rendering," in *Proc. Int. Conf. GPU Gems*, 2005, pp. 283–294.
- [97] X. Cristol, "Narcissus-2005: a global model of fading channel for application to acoustic communication in marine environment," in *Proc. IEEE Europe OCEANS*, vol. 1, Jun. 2005, pp. 655–662.
- [98] W. J. Pierson and L. Moskowitz, "A proposed spectral form for fully developed wind seas," *J. of Geophysical Research*, vol. 69, pp. 5181–5203, Oct. 1963.
- [99] K. Hasselmann *et al.*, "Measurement of wind wave growth and swell decay during the joint North Sea Wave Project (JONSWAP)," *Deutsches Hydrographisches Institut*, vol. 12, pp. 1–95, Jan. 1973.
- [100] M. Pätzold, U. Killat, F. Laue, and Y. Li, "A new and optimal method for the derivation of deterministic simulation models for mobile radio channels," in *Proc. IEEE 46th Veh. Technol. Conf., (VTC)*, vol. 3, Atlanta, Georgia, USA, Apr./May 1996, pp. 1423–1427.
- [101] M. Pätzold, U. Killat, and F. Laue, "A deterministic model for a shadowed Rayleigh land mobile radio channel," in *Proc. 5th IEEE Int. Symp. Pers., Indoor and Mobile Radio Commun. (PIMRC)*, vol. 4, Hague, Netherlands, Sep. 1994, pp. 1202–1210.
- [102] X. Ma, Z. Chen, and G. Shi, "Real-time ocean wave motion simulation based on statistic model and GPU programming," in *Proc. 2nd Int. Conf. Inform. Science and Eng. (ICISE)*, Dec. 2010, pp. 3876–3880.
- [103] J. Fréchet, "Realistic simulation of ocean surface using wave spectra," in *Proc. 1st Int. Conf. Computer Graph. Theory and Appl. (GRAPP)*, Seyúbal, Portugal, Feb. 2006, pp. 76–83.

- [104] A. Arakawa and V. R. Lamb, “A potential enstrophy and energy conserving scheme for the shallow water equations,” *Monthly Weather Review*, vol. 109, no. 1, pp. 18–36, Jan. 1981.
- [105] D. Enright, S. Marschner, and R. Fedkiw, “Animation and rendering of complex water surfaces,” *ACM Trans. Graph.*, vol. 21, no. 3, pp. 736–744, Jul. 2002. [Online]. Available: <http://doi.acm.org/10.1145/566654.566645>
- [106] R. Sadourny, “The dynamics of finite-difference models of the shallow-water equations,” *J. Atmos. Sci.*, vol. 32, no. 1, pp. 680–689, Apr. 1975.
- [107] E. Darles, B. Crespin, D. Ghazanfarpour, and J. C. Gonzato, “A survey of ocean simulation and rendering techniques in computer graphics,” *Computer Graphics Forum*, vol. 30, no. 1, pp. 43–60, 2011. [Online]. Available: <http://dx.doi.org/10.1111/j.1467-8659.2010.01828.x>
- [108] M. Robine and J. Fréchet, “Fast additive sound synthesis for real-time simulation of ocean surface,” in *Proc. Int. Conf. Syst., Signals and Image Process. (IWSSIP)*, Budapest, Hungary, Sep. 2006, pp. 223–226.
- [109] S. O. Rice, “Mathematical analysis of random noise,” *Bell Syst. Tech. J.*, vol. 23, pp. 282–332, Jul. 1944.
- [110] ———, “Mathematical analysis of random noise,” *Bell Syst. Tech. J.*, vol. 24, pp. 46–156, Jan. 1945.
- [111] M. K. Ochi, *Ocean Waves: The Stochastic Approach*, 1st ed. New York: Cambridge University Press, 2005.
- [112] M. Stojanovic, “MIMO OFDM over underwater acoustic channels,” in *Proc. IEEE Conf. Signals, Syst. and Computers (ASILOMAR), Conf. Record of the Forty-Third Asilomar*, Nov. 2009, pp. 605–609.
- [113] B. Li *et al.*, “MIMO-OFDM for high-rate underwater acoustic communications,” *IEEE J. Ocean. Eng.*, vol. 34, no. 4, pp. 634–644, Oct. 2009.
- [114] S. M. Alamouti, “A simple transmit diversity technique for wireless communications,” *IEEE J. Sel. Areas Commun.*, vol. 16, no. 8, pp. 1451–1458, Oct. 1998.
- [115] T. M. Duman and A. Ghayeb, *Coding for MIMO Communication Systems*. Chichester: John Wiley & Sons, 2007.

- [116] B. Li and M. Stojanovic, "A simple design for joint channel estimation and data detection in an Alamouti OFDM system," in *IEEE OCEANS*, Sep. 2010, pp. 1–5.
- [117] E. V. Zorita and M. Stojanovic, "Space-frequency block coding for underwater acoustic communications," *IEEE J. Ocean. Eng.*, vol. 40, no. 2, pp. 303–314, Apr. 2015.
- [118] H. Eghbali, M. Stojanovic, and S. Muhaidat, "Differential decoding for SFBC OFDM systems in underwater MIMO channels," in *Proc. IEEE Int. Conf. Acoustics, Speech and Signal Processing (ICASSP)*, May 2014, pp. 8102–8105.
- [119] V. Tarokh, H. Jafarkhani, and A. R. Calderbank, "Space-time block coding for wireless communications: performance results," *IEEE J. Sel. Areas Commun.*, vol. 17, no. 3, pp. 451–460, Mar. 1999.
- [120] Y. Ma and M. Pätzold, "Performance comparison of space-time coded MIMO-OFDM systems using different wideband MIMO channel models," in *Proc. 4th IEEE Int. Symp. Wireless Commun. Syst. (ISWCS)*, Trondheim, Norway, Oct. 2007, pp. 762–766.
- [121] ———, "Performance analysis of STBC-OFDM systems in temporally and spatially correlated fading channels," in *Proc. Wireless Commun. and Netw. Conf. (WCNC)*, Sydney, Australia, Apr. 2010, pp. 1–5.
- [122] ———, "Performance analysis of Alamouti coded OFDM systems over Rayleigh fading channels correlated in space and time," in *Proc. IEEE 71st Vehicular Technol. Conf. (VTC)*, Spring, Taipei, Taiwan, May 2010, pp. 1–6.
- [123] G. Zhang and H. Dong, "Experimental research on adaptive multichannel equalization for underwater communications," in *Proc. IEEE Int. Instrumentation and Measurement Technol. Conf.*, May 2011, pp. 1–5.
- [124] G. Zhang, B. Peng, and H. Dong, "Experimental assessment of sparse channel estimations for passive-phase conjugation communications," in *Proc. IEEE Int. Conf. on Acoustics, Speech and Signal Processing (ICASSP)*, Mar. 2012, pp. 2701–2704.
- [125] B. Peng, P. S. Rossi, H. Dong, and K. Kansanen, "DSP based OFDM receiver for time-varying underwater acoustic channels," in *Proc. 24th European Signal Processing Conf. (EUSIPCO)*, Aug 2016, pp. 627–631.

- [126] —, “Time-domain oversampled OFDM communication in doubly-selective underwater acoustic channels,” *IEEE Commun. Lett.*, vol. 19, no. 6, pp. 1081–1084, Jun. 2015.
- [127] I. Karasalo, T. Öberg, B. Nilsson, and S. Ivansson, “A single-carrier turbo-coded system for underwater communications,” *IEEE J. Ocean. Eng.*, vol. 38, no. 4, pp. 666–677, Oct. 2013.
- [128] C. Polprasert, J. A. Ritcey, and M. Stojanovic, “Capacity of OFDM systems over fading underwater acoustic channels,” *IEEE J. Ocean. Eng.*, vol. 36, no. 4, pp. 514–524, Oct. 2011.
- [129] L. Liu *et al.*, “PN sequence based Doppler and channel estimation for underwater acoustic OFDM communication,” in *Proc. IEEE Int. Conf. on Signal Processing, Communications and Computing (ICSPCC)*, Aug. 2016, pp. 1–6.

## *REFERENCES*

## **PART II**



Paper A ..... 62      A

Paper B ..... 81      B

Paper C ..... 121      C

Paper D ..... 161      D

Paper E ..... 179      E

Paper F ..... 197      F

Paper G ..... 217      G

A

# Paper A

---

**Title:** A Geometry-Based Channel Model for Shallow Underwater Acoustic Channels Under Rough Surface and Bottom Scattering Conditions

**Authors:** Meisam Naderi<sup>1</sup>, Matthias Pätzold<sup>1</sup>, and Alenka G. Zajic<sup>2</sup>

**Affiliation:** <sup>1</sup> Faculty of Engineering and Science, University of Agder, P.O. Box 509, 4879 Grimstad, Norway

<sup>2</sup> School of Electrical and Computer Engineering, Georgia Institute of Technology, Atlanta, GA 30332-0280 USA

**Conference:** *Proc. 5th Int. Conf. Commun. and Electron. (ICCE)*, DaNang, Vietnam, Jul./Aug. 2014, pp. 112-117, DOI: 10.1109/CCE.2014.6916689

**Copyright ©:** IEEE

---



# A Geometry-Based Channel Model for Shallow Underwater Acoustic Channels Under Rough Surface and Bottom Scattering Conditions

Meisam Naderi, Matthias Pätzold, and Alenka G. Zajic

**Abstract** — This paper develops a stochastic geometry-based channel model for wideband single-input single-output (SISO) shallow underwater acoustic (UWA) channels under the assumption that the ocean surface and bottom are rough. Starting from a geometrical model, we derive a reference model assuming that the scatterers are randomly distributed on the surface and the bottom of the water. The probability density functions (PDFs) of the angle-of-departure (AOD) and the angle-of-arrival (AOA) of the reference model are analyzed. Furthermore, the two-dimensional (2D) time-frequency correlation function (TFCF) of the reference model is studied. From the reference model, we then derive the corresponding simulation model by applying the generalized concept of deterministic channel modelling. For the parametrization of the UWA channel simulator, we propose a new method which is further on called the method of equally spaced scatterers (MESS). The performance of the MESS is compared with that of the  $L_p$ -norm method (LPNM). It is shown that our design concept results in an excellent match between the T-FCF of the reference model and that of the simulation model. It is also shown that both the MESS and the LPNM have a similar performance, whereby the MESS provides a closed-form solution, while the LPNM does not.

**Keywords**—Channel modelling, shallow underwater acoustic channels, underwater acoustic communications, angle-of-arrival distribution, angle-of-departure distribution, wideband channels, time-frequency correlation function.

## I. INTRODUCTION

In the last century, underwater acoustic (UWA) communication systems were mainly in the focus of military research. In recent years, however, UWA communication networks have been studied in various areas because of their potential applications in scientific exploration of the ocean [1], pollution monitoring [13], offshore oil industry exploration [3], and support for underwater robots [12], just to name a few examples. For the design and performance analysis of UWA communication systems, realistic channel models are indispensable. This calls for the statistical

analysis of UWA channels in terms of correlation functions, Doppler power spectral densities (PSDs), and power delay profiles (PDPs).

Numerous studies have focused on the modelling of UWA channels. These studies are usually based on measured acoustic channel data collected in specific areas. For example, the envelope of UWA channels has been shown to be Rice distributed in [8], [11], while the authors of [14], [4] have reported that the envelope follows the Rayleigh distribution. Besides these distributions, the channel may also follow the lognormal distribution as claimed in [15]. The authors of [10] have analysed the limitation of the achievable data rate through MIMO communications over UWA channels by assuming perfect channel state information (CSI) at the receiver. The channel capacity of orthogonal frequency division multiplexing (OFDM) systems over UWA channels has been derived in [7] as a function of the distance between the transmitter and the receiver.

In channel modelling, the distribution of the scatterers plays a key role, because they affect greatly the statistics of the AOD and the AOA. Recently, some research studies have dealt with the design of MIMO channel models for UWA communication systems. For example, a stochastic reference channel model for wideband MIMO mobile-to-mobile (M2M) UWA channels has been proposed in [16]. Therein, it is assumed that the AOA and AOD are normally distributed. In [9], the authors considered isotropic scattering conditions, in which the AOA has a uniform distribution over the interval  $(0, 2\pi]$ .

In this paper, we develop a wideband SISO shallow UWA channel model from a geometrical scattering model under line-of-sight (LOS) propagation conditions. We suppose that the scatterers are randomly distributed on the surface and the bottom of the ocean. For the case of rough surface and bottom scattering conditions, we assume that the scatterers are uniformly distributed between the transmitter and the receiver. Moreover, shallow water is considered as an isovelocity environment. Starting from the geometry-based model, we study the PDFs of the AOA and the AOD and the exact relationship between them. Then, we derive an analytical expression for the T-FCF. We also present a sum-of-cisoids (SOC) channel simulator by applying the generalized principle of deterministic channel modelling [6, pp. 418]. To compute the parameters of the simulation model, we propose a new method, which is called the MESS. Its performance will be compared with that of the LPNM. A good fitting between the reference model and the simulation model has been achieved with respect to the TFCF. It should be mentioned that the MESS is not only faster, but also computationally simpler than the LPNM.

The rest of this paper is organized as follows. In Section II, the geometrical

model is presented. Section III deals with the modelling and analysis of the reference model, while the simulation model is presented in Section IV. The numerical results are illustrated in Section V. Finally, the conclusions are drawn in Section VI.

## II. THE GEOMETRICAL MODEL

Fig. A.1 presents the proposed geometrical scattering model for UWA communication channels under the assumption that the scatterers  $S_{i,n}$  ( $n = 1, 2, \dots, N_i$  and  $i = 1, 2$ ) are randomly distributed on the surface ( $i = 1$ ) and the bottom ( $i = 2$ ) of a shallow-water ocean environment. The randomness of the scatterers  $S_{i,n}$  is due to the assumption that the surface and bottom of the ocean are rough. For simplicity, we assume single-bounce scattering, i.e., each transmitted plane wave arrives at the receiver after a single bounce on the surface or the bottom of the ocean. It is also assumed that both the transmitter  $T_x$  and the receiver  $R_x$  are equipped with single omnidirectional antennas. Moreover, we assume that the transmitter  $T_x$  is fixed and located at the distances  $y_1^T$  and  $y_2^T$  from the surface and the bottom of the ocean, respectively. The receiver  $R_x$  is moving with velocity  $\vec{v}_R$  in the direction determined by the angle-of-motion  $\alpha_v^R$ . Its position is at  $y_1^R$  and  $y_2^R$  seen from the surface and the bottom of the ocean, respectively. The distance along the x-axis between the transmitter and the receiver is denoted by  $D$ . The symbol  $\beta_{i,n}$  ( $\alpha_{i,n}$ ) stands for the AOD (AOA) of the  $n$ th path associated with the surface ( $i = 1$ ) and the bottom ( $i = 2$ ). The symbol  $\alpha_0$  denotes the AOA of the LOS component.

## III. THE REFERENCE MODEL

In this section, we first present the time-variant channel impulse response (TVCIR) of the reference model for a fixed-to-mobile (F2M) UWA wideband fading channel under LOS propagation conditions. Then, we derive the PDFs of the AOD and the AOA, which are required for the computation of the TFCF. Furthermore, we derive an equation for the propagation delays of the UWA channel model.

### A. The TVCIR

According to the geometrical model shown in Fig. A.1, the TVCIR  $h(\tau', t)$  can be split into three parts. The first part  $h_0(\tau', t)$  is determined by the LOS component, whereas the second part  $h_1(\tau', t)$  and the third part  $h_2(\tau', t)$  comprise the scattered components from the surface and the bottom of the ocean, respectively. Hence, the TVCIR  $h(\tau', t)$  can be written as

$$h(\tau', t) = \sum_{k=0}^2 h_k(\tau', t). \quad (\text{A.1})$$

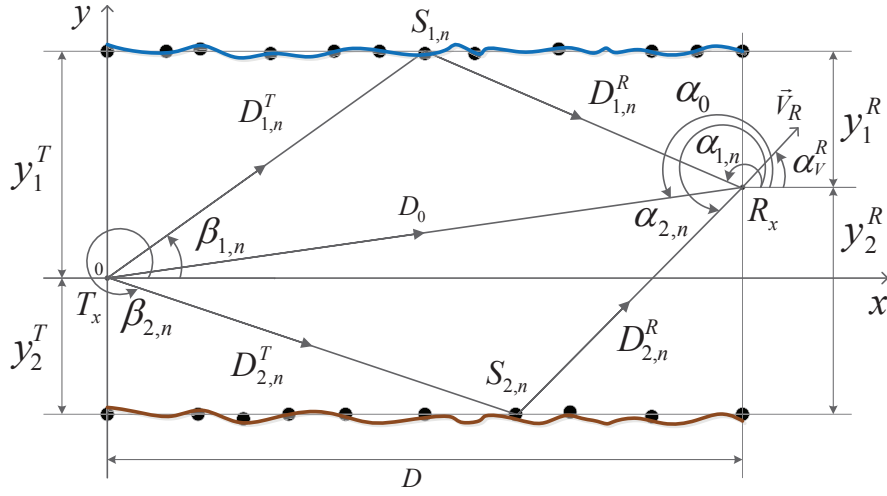


Figure A.1: A geometrical scattering model for a UWA channel with randomly distributed scatterers  $S_{i,n}$  ( $\bullet$ ) on the surface ( $i = 1$ ) and the bottom ( $i = 2$ ) of a shallow-water ocean environment.

The LOS part  $h_0(\tau', t)$  of the channel impulse response is described by the expression

$$h_0(\tau', t) = \sqrt{\frac{c_R}{1 + c_R}} A_s(D_0) A_a(D_0) e^{j(2\pi f_0 t + \theta_0)} \delta(\tau' - \tau'_0) \quad (\text{A.2})$$

in which  $c_R$  is the Rice factor, and  $\tau'_0$  denotes the propagation delay of the LOS component. The symbols  $f_0$  and  $\theta_0$  represent the Doppler frequency and phase shift of the LOS component, respectively. The Doppler frequency  $f_0$  is defined by

$$f_0 = f_{\max} \cos(\alpha_0 - \alpha_V^R) \quad (\text{A.3})$$

where  $f_{\max}$  denotes the maximum Doppler frequency, which is given by  $f_{\max} = v_R f_c / c_s$ . Therein,  $v_R = |\vec{v}_R|$  denotes the speed of the receiver,  $f_c$  indicates the carrier frequency, and  $c_s$  is the speed of sound, which is assumed to be 1500 m/s (isovelocity environment). With reference to Fig. A.1, the AOA  $\alpha_0$  and the propagation delay  $\tau'_0$  can be computed by using

$$\alpha_0 = \pi + \arctan\left(\frac{y_1^T - y_1^R}{D}\right) \quad (\text{A.4})$$

and

$$\tau'_0 = \frac{D_0}{c_s} \quad (\text{A.5})$$

where the total distance  $D_0$  between the transmitter  $T_x$  and the receiver  $R_x$  is given by

$$D_0 = \sqrt{D^2 + (y_1^T - y_1^R)^2}. \quad (\text{A.6})$$

The functions  $A_s(D_0)$  and  $A_a(D_0)$  in (A.2) denote the propagation loss coefficients due to spherical spreading and absorption, respectively. The propagation loss coefficient due to spherical spreading can be written as [9, Eq. (1)]

$$A_s(D) = \frac{1}{D} \quad (\text{A.7})$$

where  $D$  stands for the total propagation distance in meter. The absorption loss coefficient  $A_a(D)$  is given by [16, Eq. (4)]

$$A_a(D) = 10^{-\frac{D\beta}{20000}}. \quad (\text{A.8})$$

In the equation above, which is suitable for carrier frequencies between 3 and 500 kHz, the parameter  $\beta$  is computed as follows [2, Eq. (1.3.1)]

$$\beta = 8.68 \times 10^3 \left( \frac{S_a f_T f_c^2 A}{f_T^2 + f_c^2} + \frac{B f_c^2}{f_T} \right) \times (1 - 6.54 \times 10^{-4} P) \quad (\text{dB/km}) \quad (\text{A.9})$$

where  $A = 2.34 \times 10^{-6}$  and  $B = 3.38 \times 10^{-6}$ . The symbol  $S_a$  stands for the salinity (in parts per thousand),  $f_c$  is the carrier frequency (in kHz),  $f_T = 21.9 \times 10^6 - (1520/(T+273))$  is the relaxation frequency (in kHz), and  $T$  is the temperature (in °C). The symbol  $P$  denotes the hydrostatic pressure (in kg/cm<sup>2</sup>), which is determined by  $P = 1.01(1 + 0.1h)$ , where  $h$  denotes the water depth (in m). For brevity, we do not consider the loss due to the impedance mismatch between water and the bottom.

The second part  $h_1(\tau', t)$  and the third part  $h_2(\tau', t)$  of the TVCIR  $h(\tau', t)$  in (A.1) are given by

$$h_i(\tau', t) = \lim_{N_i \rightarrow \infty} \frac{1}{\sqrt{2N_i(1 + c_R)}} \sum_{n=1}^{N_i} A_s(D_{i,n}) A_a(D_{i,n}) e^{j(2\pi f_{i,n} t + \theta_{i,n})} \delta(\tau' - \tau'_{i,n}) \quad (\text{A.10})$$

for  $i = 1, 2$ , where  $f_{i,n}$  and  $\theta_{i,n}$  denote the Doppler shift and phase shift of the  $n$ th received component from the surface and bottom of the ocean. The phase shifts are modelled by independent and identically distributed (i.i.d.) random variables, which

are supposed to be uniformly distributed over the interval  $(-\pi, \pi]$ . The quantity  $\tau'_{i,n}$  represents the propagation delay of the  $n$ th path received from the surface and bottom of the ocean. The parameter  $N_1$  ( $N_2$ ) denotes the number of scatterers on the surface (bottom) of the ocean. The symbol  $D_{i,n}$  stands for the total distance that the transmitted acoustic wave travels from the transmitter  $T_x$  to the receiver  $R_x$  via the scatterer  $S_{i,n}$ . With reference to Fig. A.1, the total distances associated with the surface- and bottom-bounce rays can be described by

$$D_{i,n} = (-1)^{(i-1)} \left[ \frac{y_i^T}{\sin(\beta_{i,n})} + \frac{y_i^R}{\sin(\alpha_{i,n})} \right] \quad (\text{A.11})$$

for  $n = 1, 2, \dots, N_i$  and  $i = 1, 2$  ( $\alpha_{i,n} \neq \pi, \beta_{i,n} \neq 0$ ).

### B. The PDFs of the AOD and the AOA

In this section, we derive the PDFs of the AOD and the AOA. In the absence of any given distribution of the scatterers  $S_{i,n}$  accounting for scenarios in which the ocean surface and bottom are rough, we assume that the scatterers  $S_{i,n}$  are uniformly distributed on the surface ( $y = y_1^T$ ) and the bottom ( $y = -y_2^T$ ) of the ocean between  $x = 0$  and  $x = D$ . If the number of scatterers tends to infinity, then the discrete random variables  $x_{i,n}$  and  $y_i$  become continuous random variables denoted by  $x$  and  $y$ , respectively. Thus, the joint distribution  $p_{xy}(x, y)$  of the positions of the scatterers can be modelled as

$$p_{xy}(x, y) = \begin{cases} \frac{1}{2D} [\delta(y - y_1^T) + \delta(y + y_2^T)], & \text{if } 0 \leq x \leq D, \\ 0, & \text{otherwise.} \end{cases} \quad (\text{A.12})$$

With reference to Fig. A.1, the AOD  $\beta$  can be expressed by

$$\beta = \begin{cases} \arctan\left(\frac{y_1^T}{x}\right), & \text{if } 0 \leq x \leq D, \\ \frac{3\pi}{2} + \arctan\left(\frac{x}{y_2^T}\right), & \text{if } 0 \leq x \leq D. \end{cases} \quad (\text{A.13})$$

By applying the concept of transformation of random variables [5, pp. 130], the PDF  $p_\beta(\beta)$  of the AOD  $\beta$  can be computed as

$$p_\beta(\beta) = \begin{cases} \frac{y_1^T}{2D \sin^2(\beta)}, & \text{if } \arctan\left(\frac{y_1^T}{D}\right) \leq \beta \leq \frac{\pi}{2}, \\ \frac{y_2^T}{2D \sin^2(\beta)}, & \text{if } \frac{3\pi}{2} \leq \beta \leq \frac{3\pi}{2} + \arctan\left(\frac{D}{y_2^T}\right). \end{cases} \quad (\text{A.14})$$

Referring to Fig. A.1, the AOA  $\alpha$  can be expressed by

$$\alpha = \begin{cases} \frac{\pi}{2} + \arctan\left(\frac{D-x}{y_1^R}\right), & \text{if } 0 \leq x \leq D, \\ \pi + \arctan\left(\frac{y_2^R}{D-x}\right), & \text{if } 0 \leq x \leq D. \end{cases} \quad (\text{A.15})$$

Analogously, we can obtain the PDF  $p_\alpha(\alpha)$  of the AOA  $\alpha$  by applying again the concept of transformation of random variables, which results in

$$p_\alpha(\alpha) = \begin{cases} \frac{y_1^R}{2D \sin^2(\alpha)}, & \text{if } \frac{\pi}{2} \leq \alpha \leq \frac{\pi}{2} + \arctan\left(\frac{D}{y_1^R}\right), \\ \frac{y_2^R}{2D \sin^2(\alpha)}, & \text{if } \pi + \arctan\left(\frac{y_2^R}{D}\right) \leq \alpha \leq \frac{3\pi}{2}. \end{cases} \quad (\text{A.16})$$

The AOD  $\beta$  can be expressed as a function of the AOA  $\alpha$  by using the following relationship

$$\beta(\alpha) = \begin{cases} \arctan\left(\frac{y_1^T \tan(\alpha)}{D \tan(\alpha) + y_1^R}\right), & \text{if} \\ \frac{\pi}{2} \leq \alpha \leq \frac{\pi}{2} + \arctan\left(\frac{D}{y_1^R}\right), \\ \frac{3\pi}{2} + \arctan\left(\frac{D \tan(\alpha - \pi) - y_2^R}{y_2^T \tan(\alpha - \pi)}\right), & \text{if} \\ \pi + \arctan\left(\frac{y_2^R}{D}\right) \leq \alpha \leq \frac{3\pi}{2}, \end{cases} \quad (\text{A.17})$$

which is needed for the computation of the propagation delays and the T-FCF, as we will see in the following two subsections.

### C. The Propagation Delays

The propagation delay  $\tau'_{i,n}$  of the  $n$ th path is determined by

$$\tau'_{i,n} = \frac{D_{i,n}}{c_s} \quad (\text{A.18})$$

for  $n = 1, 2, \dots, N_i$  and  $i = 1, 2$ . After substituting (A.11) in (A.18), and using (A.15) and (A.17), we obtain the following expression for the propagation delays  $\tau'(\alpha)$  as a function of the AOA  $\alpha$

$$\tau'(\alpha) = \begin{cases} \frac{1}{c_s} \left( \frac{y_1^T}{\sin(\beta(\alpha))} + \frac{y_1^R}{\sin(\alpha)} \right), & \text{if} \\ \frac{\pi}{2} \leq \alpha \leq \frac{\pi}{2} + \arctan\left(\frac{D}{y_1^R}\right), \\ \frac{1}{c_s} \left( \frac{y_2^T}{\sin(\beta(\alpha))} + \frac{y_2^R}{\sin(\alpha)} \right), & \text{if} \\ \pi + \arctan\left(\frac{y_2^R}{D}\right) \leq \alpha \leq \frac{3\pi}{2}. \end{cases} \quad (\text{A.19})$$

#### D. Derivation of the TFCF

For the computation of the TFCF, we need first to derive the time-variant channel transfer function (TVCTF). According to [6, Eq. (2.139)], the TVCTF  $H(f', t)$  is obtained by taking the Fourier transform of TVCIR  $h(\tau', t)$  with respect to the propagation delays  $\tau'$ , which gives

$$H(f', t) = \sum_{k=0}^2 H_k(f', t) \quad (\text{A.20})$$

where

$$H_0(f', t) = \sqrt{\frac{c_R}{1 + c_R}} A_s(D_0) A_a(D_0) e^{j[2\pi(f_0 t - f' \tau'_0) + \theta_0]} \quad (\text{A.21})$$

$$H_i(f', t) = \lim_{N_i \rightarrow \infty} \frac{1}{\sqrt{2N_i(1 + c_R)}} \sum_{n=1}^{N_i} A_s(D_{i,n}) A_a(D_{i,n}) e^{j[2\pi(f_{i,n} t - f' \tau'_{i,n}) + \theta_{i,n}]} \quad (\text{A.22})$$

for  $i = 1, 2$ . According to the central limit theorem, the TVCTFs  $H_1(f', t)$  and  $H_2(f', t)$  are independent zero-mean complex-valued Gaussian processes. The channel transfer function enables us to compute the TFCF. Under the assumption that UWA channel is wide-sense stationary in frequency  $f'$  and time  $t$ , the normalized T-FCF  $r_{HH}(\nu', \tau)$  between two TVCTFs  $H(f', t)$  and  $H(f' + \nu', t + \tau)$  is defined by

$$r_{HH}(\nu', \tau) = \frac{E\{H^*(f', t) H(f' + \nu', t + \tau)\}}{E\{|H(f', t)|^2\}}, \quad (\text{A.23})$$

which gives

$$r_{HH}(\nu', \tau) = \sum_{k=0}^2 r_{H_k H_k}(\nu', \tau) \quad (\text{A.24})$$

where  $(\cdot)^*$  represents the complex conjugate operation, and  $E\{\cdot\}$  is the statistical expectation operator. The symbols  $\nu'$  and  $\tau$  denote the frequency and time separation variables, respectively. The LOS part of the normalized TFCF  $r_{HH}(\nu', \tau)$  is

determined by

$$r_{H_0 H_0}(\nu', \tau) = \frac{E\{H_0^*(f', t)H_0(f' + \nu', t + \tau)\}}{\eta_0} = \frac{c_R}{1 + c_R} e^{j2\pi[f_{\max} \cos(\alpha_0 - \alpha_v^R)\tau - \nu'\tau_0']} \quad (\text{A.25})$$

where  $\eta_0 = A_s^2(D_0)A_a^2(D_0)$ .

The second part  $r_{H_1 H_1}(\nu', \tau)$  and the third part  $r_{H_2 H_2}(\nu', \tau)$  of the normalized T-FCF  $r_{HH}(\nu', \tau)$  in (A.24) can be expressed as

$$r_{H_i H_i}(\nu', \tau) = \frac{1}{\eta_i(1 + c_R)} \int_{\alpha \in I_{\alpha, i}} [A_s(D_i(\alpha))A_a(D_i(\alpha))]^2 \times e^{j2\pi[f_{\max} \cos(\alpha - \alpha_v^R)\tau - \nu'\tau'(\alpha)]} p_\alpha(\alpha) d\alpha \quad (\text{A.26})$$

for  $i = 1, 2$ . In the equation above,  $\eta_i = E\{A_s^2(D_i(\alpha))A_a^2(D_i(\alpha))\}$ , and  $I_{\alpha, i}$  is the domain of the PDF  $p_\alpha(\alpha)$  in (A.16).

#### IV. THE SIMULATION MODEL

The reference model presented in the previous section is based on the assumption that the numbers of scatterers  $N_1$  and  $N_2$  are infinite, implying that the reference model is non-realizable. In this section, we present a low-complexity SOC channel simulator for the simulation of UWA channels under non-isotropic scattering conditions. For the parametrization of the channel simulator, we propose a new parameter computation method, which is called the MESS. Its performance will be compared to that of the LPNM [6, pp. 189].

According to the generalized principle of deterministic channel modelling [6, pp. 418], an ergodic stochastic simulation model can be derived from the reference model by using only a finite number of scatterers  $S_{i,n}$  and placing them at fixed positions  $(x_{i,n}, y_i)$  on the surface ( $i = 1$ ) and the bottom ( $i = 2$ ) of the ocean. Without proof, we mention that the resulting TFCF of the simulation model can be expressed by

$$\hat{r}_{HH}(\nu', \tau) = \frac{c_R}{1 + c_R} e^{j2\pi(f_0\tau - \tau_0'\nu')} + \frac{1}{1 + c_R} \left[ \sum_{i=1}^2 \sum_{n=1}^{N_i} c_{i,n}^2 e^{j2\pi(f_{i,n}\tau - \tau_{i,n}'\nu')} \right] \quad (\text{A.27})$$

where  $f_0$  is given by (A.3),  $f_{i,n} = f_{\max} \cos(\alpha_{i,n} - \alpha_v^R)$ , and  $c_{i,n}$  denotes the normalized channel gain of the  $n$ th path received from the surface or bottom of the

ocean, which is given by

$$c_{i,n} = \frac{A_s(D_{i,n})A_a(D_{i,n})}{\sqrt{2 \sum_{n=1}^{N_i} (A_s(D_{i,n})A_a(D_{i,n}))^2}} \quad (\text{A.28})$$

for  $n = 1, 2, \dots, N_i$  and  $i = 1, 2$ .

#### A. The MESS

The MESS is based on the idea that the coordinates  $(x_{i,n}, y_i)$  are computed such that the scatterers  $S_{i,n}$  are located equidistantly on the surface and the bottom of the ocean, respectively. Recall that the coordinates  $(x_{i,n}, y_i)$  of the scatterer  $S_{i,n}$  determine the AOA  $\alpha_{i,n}$ . By determining the coordinates  $(x_{i,n}, y_i)$ , and thus the AOAs  $\alpha_{i,n}$ , we can compute the channel parameters  $\{c_{i,n}\}_{n=1}^{N_i}$ ,  $\{f_{i,n}\}_{n=1}^{N_i}$ , and  $\{\tau'_{i,n}\}_{n=1}^{N_i}$  for  $i = 1, 2$ . Let us start by computing the coordinates  $(x_{i,n}, y_i)$  of the scatterers  $S_{i,n}$  as follows

$$x_{i,n} = \Delta x_i(n-1) + \delta_{x_i}, \text{ if } n = 1, 2, \dots, N_i, i = 1, 2 \quad (\text{A.29a})$$

$$y_i = \begin{cases} y_1^T, & \text{if } i = 1, \\ -y_2^T, & \text{if } i = 2, \end{cases} \quad (\text{A.29b})$$

where  $\Delta x_i = D/N_i$ . As can be seen in Fig. A.2,  $\delta_{x_i} \in [0, \Delta x_i]$  determines the position of the first scatterer on the surface (bottom) of the ocean. To find the optimum value of  $\delta_{x_i}$ , we consider the error function

$$E(\delta_{x_i}) = \frac{1}{\nu'_{\max} \tau_{\max}} \int_0^{\nu'_{\max}} \int_0^{\tau_{\max}} |r_{HH}(\nu', \tau) - \hat{r}_{HH}(\nu', \tau)|^2 d\tau d\nu' \quad (\text{A.30})$$

where  $\nu'_{\max}(\tau_{\max})$  defines an appropriate frequency-lag (time-lag) interval  $[0, \nu'_{\max}]$  ( $[0, \tau_{\max}]$ ) over which the approximation of  $r_{HH}(\nu', \tau)$  is of importance. From the results shown in Fig. A.3, we conclude that the minimum of  $E(\delta_{x_i})$  is reached at  $\delta_{x_i} = \delta_{x_i}^{\text{opt}} = \Delta x_i/2$ . Thus, we can rewrite (A.29a) and obtain the optimum values of  $x_{i,n}$  by

$$x_{i,n}^{\text{opt}} = \frac{D}{N_i} \left( n - \frac{1}{2} \right) \quad (\text{A.31})$$

for  $n = 1, 2, \dots, N_i$  and  $i = 1, 2$ . Hence, the MESS results in the closed-form expressions (A.29b) and (A.31) for the computation of the coordinates  $(x_{i,n}, y_i)$ . By means of (A.29b) and (A.31), we can compute the discrete AOA  $\alpha_{i,n}$  by us-

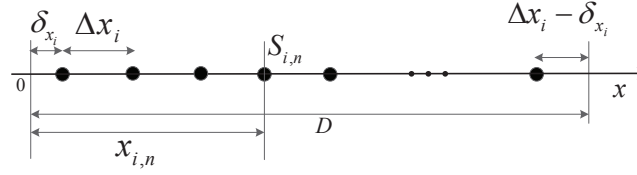


Figure A.2: Initial position of the scatterers  $S_{i,n}$  of the surface ( $i = 1$ ) and the bottom ( $i = 2$ ) of the ocean.

ing (A.15). With the knowledge of the AOAs  $\alpha_{i,n}$ , we then compute the AOD  $\beta_{i,n}$  by using (A.17). Substituting  $\alpha_{i,n}$  and  $\beta_{i,n}$  in (A.11), allows us to compute the normalized channel gains  $c_{i,n}$  by using (A.28). The corresponding Doppler frequencies  $\{f_{i,n}\}_{n=1}^{N_i}$  of the channel simulator are obtained after substituting (A.15) in  $f_{i,n} = f_{\max} \cos(\alpha_{i,n} - \alpha_v^R)$ . Finally, we can compute the propagation delays  $\{\tau'_{i,n}\}_{n=1}^{N_i}$  by substituting  $\alpha_{i,n}$  in (A.19).

### B. The LPNM

In this section, we apply the LPNM [6, pp. 189] to find the channel parameters. The application of the LPNM on the given parametrization problem requires the minimization of the following error function

$$E_p(\alpha_{i,n}) = \left[ \frac{1}{\nu'_{\max} \tau_{\max}} \int_0^{\nu'_{\max}} \int_0^{\tau_{\max}} |r_{HH}(\nu', \tau) - \hat{r}_{HH}(\nu', \tau)|^p d\tau d\nu' \right]^{\frac{1}{p}}. \quad (\text{A.32})$$

After the minimization of  $E_p(\alpha_{i,n})$  by using numerical optimization techniques, we obtain a set  $\{\alpha_{i,n}^{\text{opt}}\}$  of optimized values of the AOAs. The initial values required for the numerical optimization are obtained from the MESS.

## V. NUMERICAL RESULTS

In this section, we illustrate and verify the theoretical results presented in the previous sections. For simplicity, we assume that the LOS component is absent, i.e.,  $c_R = 0$ . The UWA channel simulator is designed by choosing  $N_1 = 80$  and  $N_2 = 79$ . We set the carrier frequency  $f_c$  to 10kHz and assume that the receiver is moving at a speed of 9m/s, which results in a maximum Doppler frequency of 60Hz. The remaining parameters have been set as follows:  $y_1^R = y_2^R = y_1^T = y_2^T = 90$  m,  $D = 1$  km, and  $\alpha_v^R = 0^\circ$ . The performance of the UWA channel simulator has been assessed by comparing its TFCF in (A.27) with that of the reference model (see (A.24)–(A.26)).

The absolute value of the normalized TFCF  $|r_{HH}(\nu', \tau)|$  of the reference model

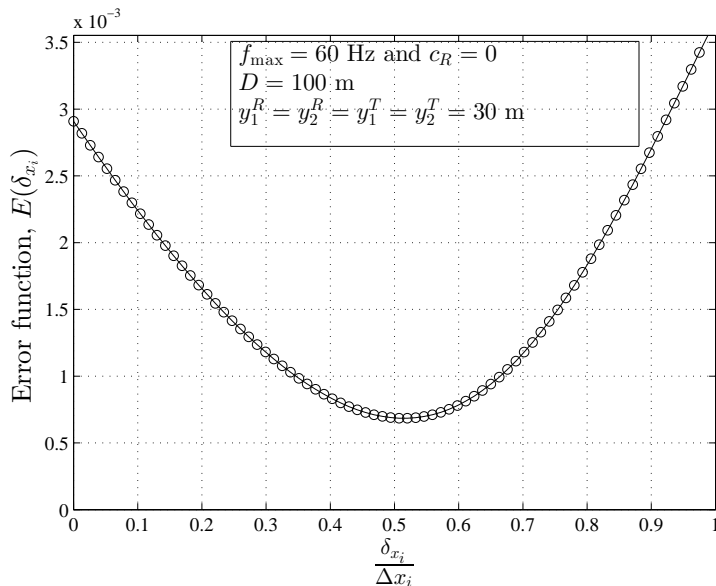


Figure A.3: Evaluation of the error function  $E(\delta_{x_i})$  in (A.30) to find the optimum value of  $\delta_{x_i}$  ( $N_1 = N_2 = 13$ ).

is presented in Fig. A.4, whereas Fig. A.5 illustrates that of the simulation model designed by using the MESS. As can be seen, a good match can be achieved between the reference model and the simulation model with respect to the T-FCF. The performance of the MESS has been analyzed by using (A.30) with  $\tau_{\max} = 0.14$  s and  $\nu'_{\max} = 160$  Hz. For the MESS, the integral square error  $E(\delta_{x_i})$  in (A.30) results in  $2.19 \times 10^{-4}$ .

By using the LPNM, we have found a better fitting in terms of the absolute value of the normalized T-FCF  $|\hat{r}_{HH}(\nu', \tau)|$  compared to the MESS. Fig. A.6 shows the absolute value  $|\hat{r}_{HH}(\nu', \tau)|$  of the simulation model's T-FCF designed by applying the LPNM. For the LPNM, the integral square error  $E(\delta_{x_i})$  is  $8.32 \times 10^{-5}$ , which is by a factor of 2.55 lower than that of the MESS. The price to be paid for this achievement is a considerable increase in numerical complexity.

## VI. CONCLUSION

In this paper, we have developed a new geometry-based shallow UWA channel model under the assumption that the surface and the bottom of the ocean are rough. We have derived the AOA PDF, AOD PDF, and the TFCF of the channel model. We have also presented the corresponding simulation model. The parameters of the simulation model have been computed by means of two methods, namely the MESS and the LPNM. The MESS has been developed especially for the design of UWA channel simulators, whereas the LPNM is well-known and widely used in the

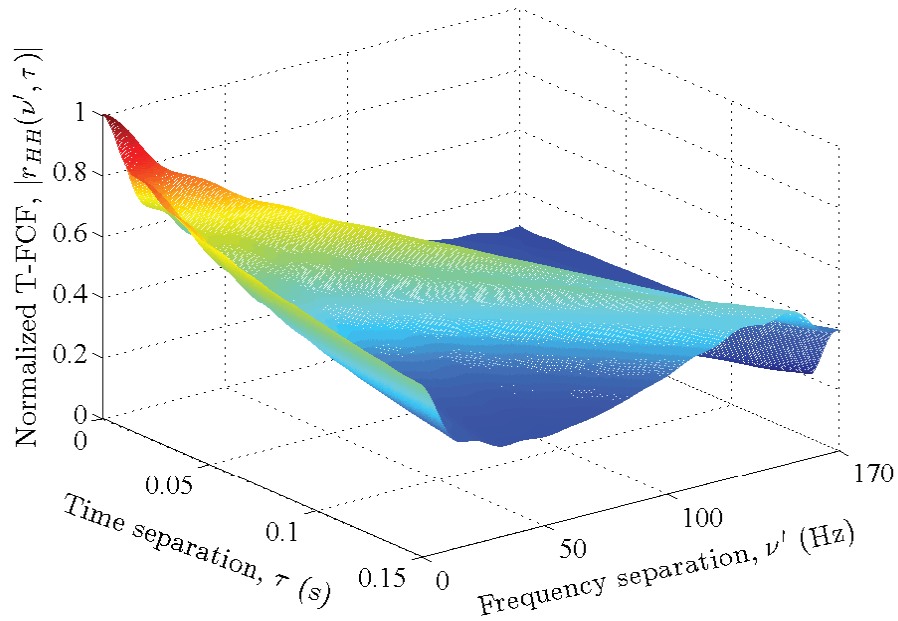


Figure A.4: Absolute value of the normalized T-FCF  $|r_{HH}(\nu', \tau)|$  of the reference model for a UWA channel.

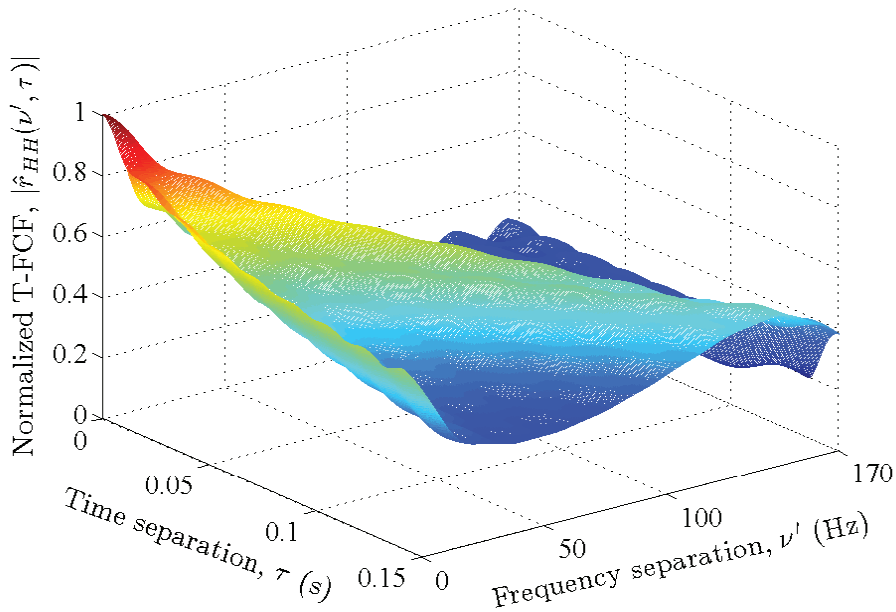


Figure A.5: Absolute value of the normalized T-FCF  $|\hat{r}_{HH}(\nu', \tau)|$  of the simulation model by using the MESS ( $N_1 = 80$  and  $N_2 = 79$ ).

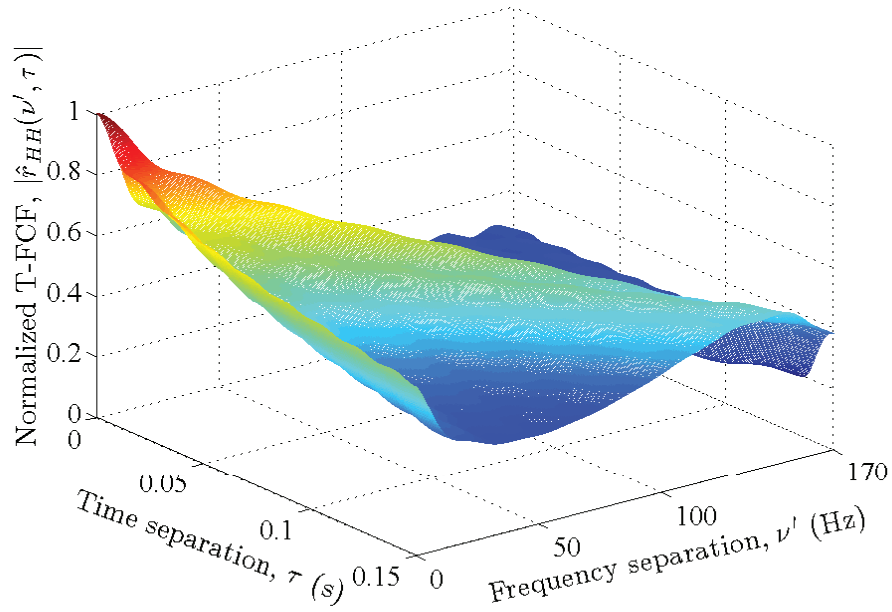


Figure A.6: Absolute value of the normalized T-FCF  $|\hat{r}_{HH}(\nu', \tau)|$  of the simulation model by using the LPNM ( $N_1 = 80$  and  $N_2 = 79$ ).

area of channel modelling. An excellent agreement could be observed between the simulation model and the underlying reference model.

## PAPER A: REFERENCES

### PAPER A: REFERENCES

- [1] A. Baptista, B. Howe, J. Freire, D. Maier, and C. T. Silva. Scientific exploration in the era of ocean observatories. *Comput. Sci. Eng.*, 10(3):53–58, May 2008.
- [2] L. M. Brekhovskikh and Y. P. Lysanov. *Fundamentals of Ocean Acoustics*. New York, NY, USA: Springer, 3rd edition, 2002.
- [3] M. Dalbro et al. Wireless sensor networks for off-shore oil and gas installations. In *Proc. 2nd Int. Conf. Sensor Technol. and Appl. (SENSORCOMM)*, pages 258–263, Aug. 2008.
- [4] R. Galvin and R. F. W. Coats. A stochastic underwater acoustic channel model. In *Proc. IEEE OCEANS Prospects for the 21st Century*, volume 1, pages 203–210, Sep. 1996.
- [5] A. Papoulis. *Probability, Random Variables, and Stochastic Processes*. New York, NY, USA: McGraw-Hill, 4rd edition, 2002.
- [6] M. Pätzold. *Mobile Fading Channels*. Chichester, U.K.: John Wiley & Sons, 2nd edition, 2011.
- [7] C. Polprasert, J. A. Ritcey, and M. Stojanovic. Capacity of OFDM systems over fading underwater acoustic channels. *IEEE J. Ocean. Eng.*, 36(4):514–524, Oct. 2011.
- [8] P. Qarabaqi and M. Stojanovic. Statistical modeling of a shallow water acoustic communication channel. In *Proc. Underwater Acoust. Meas. Conf.*, pages 1341–1350, Nafplion, Greece, Jun. 2009.
- [9] P. Qarabaqi and M. Stojanovic. Statistical characterization and computationally efficient modeling of a class of underwater acoustic communication channels. *IEEE J. Ocean. Eng.*, 38(4):701–717, Oct. 2013.
- [10] A. Radošević, D. Fertoni, T. M. Duman, J. G. Proakis, and M. Stojanovic. Capacity of MIMO systems in shallow water acoustic channels. In *Proc. IEEE Conf. Signals, Syst. and Computers (ASILOMAR), Conf. Record of the Forty Fourth Asilomar*, pages 2164–2168, Nov. 2010.
- [11] A. Radošević, J. G. Proakis, and M. Stojanovic. Statistical characterization and capacity of shallow water acoustic channels. In *Proc. IEEE EUROPE OCEANS*, pages 1–8, Bremen, Germany, May 2009.

## PAPER A: REFERENCES

- [12] M. T. Rashid, A. A. Ali, R. S. Ali, L. Fortuna, M. Frasca, and M. G. Xibilia. Wireless underwater mobile robot system based on ZigBee. In *Proc. Int. Conf. Future Commun. Netw. (ICFCN)*, pages 117–122, Apr. 2012.
- [13] D. Shin, S. Y. Na, J. Kim, and S. J. Baek. Fish robots for water pollution monitoring using ubiquitous sensor networks with sonar localization. In *Proc. Int. Conf. Convergence Inf. Technol.*, pages 1298–1303, Nov. 2007.
- [14] F.-X. Socheleau, J. M. Passerieux, and C. Laot. Characterisation of time-varying underwater acoustic communication channel with application to channel capacity. In *Proc. Underwater Acoust. Meas. Conf.*, Nafplion, Greece, June 2009.
- [15] B. Tomasi, P. Casari, L. Badia, and M. Zorzi. A study of incremental redundancy hybrid ARQ over Markov channel models derived from experimental data. In *Proc. 5th ACM Int. Workshop on UnderWater Networks (WUWNet)*, pages 1–8, Massachusetts, USA, Sep./Oct. 2010.
- [16] A. G. Zajić. Statistical modeling of MIMO mobile-to-mobile underwater channels. *IEEE Trans. Veh. Technol.*, 60(4):1337–1351, May 2011.

# Paper B

---

B

**Title:** A Non-Isovelocity Geometry-Based Underwater Acoustic Channel Model

**Authors:** Meisam Naderi<sup>1</sup>, Alenka G. Zajic<sup>2</sup>, and Matthias Pätzold<sup>1</sup>

**Affiliation:** <sup>1</sup> Faculty of Engineering and Science, University of Agder, P.O. Box 509, 4879 Grimstad, Norway

<sup>2</sup> School of Electrical and Computer Engineering, Georgia Institute of Technology, Atlanta, GA 30332-0280 USA

**Journal:** Submitted to *IEEE Trans. Veh. Technol.* .

---



## **A Non-Isovelocity Geometry-Based Underwater Acoustic Channel Model**

Indika Meisam Naderi, Alenka G. Zajic, and Matthias Pätzold

***Abstract*** — This paper proposes a new geometry-based shallow underwater acoustic (UWA) channel model allowing for non-isovelocity ocean conditions. The fact that the isovelocity assumption does not hold in many real-world scenarios motivates the need for developing channel models for non-isovelocity UWA propagation environments. Starting from a geometrical model, we develop a stochastic channel model for a wideband single-input single-output (SISO) vehicle-to-vehicle (V2V) UWA channel assuming that the ocean surface and bottom are rough and that the speed of sound varies with depth. The effect of the non-isovelocity condition has been assessed regarding its influence on the temporal autocorrelation function (ACF), the frequency correlation function (FCF), and the power delay profile (PDP) of the UWA channel model. The UWA channel model has also been validated by matching its FCF as well as the therefrom derived main characteristic quantities, such as the average delay, delay spread, and coherence bandwidth against measurement data. The proposed UWA channel model is very useful for the design and performance analysis of UWA communication systems under realistic propagation conditions.

***Keywords***—Shallow underwater acoustic channels, non-isovelocity condition, vehicle-to-vehicle communications, power delay profile, temporal autocorrelation function, frequency correlation function.

## I. INTRODUCTION

Underwater acoustic (UWA) communication systems are expected to play an important role in oceanography. As laser beams and electromagnetic waves suffer from high path loss in ocean water, acoustic signals are being used, especially, in medium- and long-range ( $> 1$  km [26, p. 38]) underwater communications. Realistic channel models are very important for the design and performance analysis of communication systems allowing for extensive simulations of communication scenarios without employing inferior trial-and-error methods.

UWA propagation scenarios can be fully described by solving the wave equation. However, solving the wave equation is well known to be a difficult problem [3, 5]. To circumvent this problem, approximations, such as deterministic ray-tracing methods [19–22, 24], are often used to model the high-frequencies acoustic wave propagation phenomena in deep ocean environments [7, 8]. To overcome this problem, several geometry-based stochastic UWA channel models have been developed under *isovelocity* conditions [5, 15, 16, 23, 32]. For example, in [5, 15, 32], the total distances that acoustic signals travel between the transmitter and the receiver have been computed by using the *method of image projections* [3].

In general, the geometry-based stochastic UWA channel modelling approach presents synthetic channel responses that describe UWA channels with a high level of accuracy. Stochastic UWA channel models are often less complex than ray tracing models from a mathematical point of view. The ray tracing method is derived from the wave equation where some simplifying assumptions are introduced and the method is essentially a high-frequency approximation. However, ray tracing techniques have limitations and may not be valid for precise predictions of sound levels, especially in situations where refraction effects and focusing of sound are important [11]. For telecommunication purposes, UWA channel models which can address the fast statistical variations of channels are required to accurately predict the communication link properties like the Doppler spread and delay spread.

Owing to the fact that the speed of sound varies with depth [3, 4, 12, 17], the non-isovelocity property (caused by ocean layers with different acoustic properties [1]) has to be taken into account for the geometry-based stochastic UWA channel modelling. There are several papers in the literature that study the behavior of acoustic waves in non-isovelocity ocean environments [1, 11, 13]. Moreover, in [6], a channel model has been developed for UWA communications under non-isovelocity condition by taking effects of wind-generated waves and bubbles into account. However, there is no design method that can directly be used to develop stochastic simulation models for non-isovelocity UWA channels. To address this

problem, we propose a new geometry-based UWA channel model that is suited for computer simulations and accounts for non-isovelocity propagation effects. The proposed channel model enables us to study analytically the statistical properties of UWA channels such as temporal and frequency correlation functions, power delay profile (PDP), delay spread, and the coherence bandwidth under isovelocity/non-isovelocity ocean conditions. Because of the non-stationary behaviour of UWA channels, there are some papers in the literature that do not take the wide-sense stationary uncorrelated scattering (WSSUS) assumption [2] into account [25, 28, 29], while this assumption is a fundamental assumption in this paper.

In the first step, we have extended the geometrical model in [32] with respect to non-isovelocity propagation conditions. Then, by starting from the geometrical model, we further derive the time-variant channel impulse response (TVCIR) of the UWA channel model under line-of-sight (LOS) propagation conditions. The proposed geometry-based channel model characterizes acoustic signal propagation in shallow-water ocean environments by taking into account *macro-scattering* effects caused by specular reflection at the surface and bottom of the ocean. In addition, it addresses the randomness of the UWA channel by considering *micro-scattering* (diffuse scattering) effects. Using the proposed geometry-based channel model, we derive expressions for the temporal autocorrelation function (ACF), frequency correlation function (FCF). To illustrate the impact of non-isovelocity on UWA channels, we study its effect on the characteristics of the acoustic wave propagation. Moreover, the statistical quantities of the proposed UWA channel model, such as the temporal ACF, FCF, and the PDP, are compared with those of isovelocity channel models. The results of this comparative study show significant differences of the channel characteristics if non-isovelocity propagation conditions are incorporated into the UWA channel model. For example, the results indicate that the coherence bandwidth and the coherence time of the non-isovelocity UWA channel model are significantly smaller than those of the isovelocity channel model. Finally, to verify the validity of the proposed UWA channel model, the main statistical properties, such as the FCF, average delay, delay spread, and the coherence bandwidth, are compared with those of a measured UWA channel, where a good agreement between theory and measurement is observed.

The rest of this paper is structured as follows. In Section II, the geometrical UWA model is described. The stochastic UWA channel model is derived from the geometrical UWA model in Section III. Section IV studies the statistical properties of the proposed UWA channel model. In Section V, the numerical results are illustrated. Section VI validates the main theoretical results by comparing them with

measurement data. The paper is concluded in Section VII.

## II. THE GEOMETRICAL NON-ISOVELOCITY MODEL

In this section, we briefly review Snell's law and describe a multi-layered sound-speed profile (SSP). Then, a new geometrical model is presented for a wideband single-input single-output (SISO) shallow-water ocean environment assuming non-isovelocity condition. In this paper, we consider medium and long-range shallow UWA communication links between moving transmitters and receivers under LOS propagation conditions. The UWA channel is assumed to fulfill the WSSUS condition. Time-dependent propagation delays caused by the non-stationary behaviour of the channel are not considered in this paper. However, in this case, physically non-stationary behavior of UWA channels coming from, for example, moving scatterers and changing the velocity of transmitters (or/and receivers) cannot be captured by the proposed channel model.

### A. Snell's Law

Snell's law (also known as the law of refraction) describes the relationship between the angle-of-incidence (AOI) and angle-of-refraction (AOR). It refers to light, sound or other waves passing through a boundary between two different media. As can be seen in Fig. B.1, the AOI  $\varphi_1$  is defined as the angle that an incident ray makes with a perpendicular to the surface at the point of incidence. Based on Snell's law, the relationship between the AOI  $\varphi_1$  and the corresponding AOR  $\varphi_2$  for a wave impinging on an interface between two media equals [14, Eq. (2.2.3)]

$$\frac{\sin(\varphi_1)}{c_1} = \frac{\sin(\varphi_2)}{c_2} = a \quad (\text{B.1})$$

where  $a$  denotes the constant ray parameter. The parameters  $c_1$  and  $c_2$  stand for speed of sound in media 1 and 2, respectively. According to (B.1), the AOI  $\varphi_1$  is smaller (larger) than the AOR  $\varphi_2$  if  $c_1 < c_2$  ( $c_1 > c_2$ ). Moreover, (B.1) only holds if  $\sin(\varphi_2) \leq 1$ , i.e., the maximum value of  $\sin(\varphi_1)$  is  $c_1/c_2$ . Thus, a critical angle  $\varphi_c$  can be defined and computed as

$$\varphi_c = \arcsin(c_1/c_2). \quad (\text{B.2})$$

In other words, if the AOI  $\varphi_1$  at the incidence point is larger than the critical angle, i.e.,  $\varphi_1 > \varphi_c$ , then the signal energy will be reflected, otherwise it will be refracted. In this paper, only refracted signals are considered.

### B. SSP

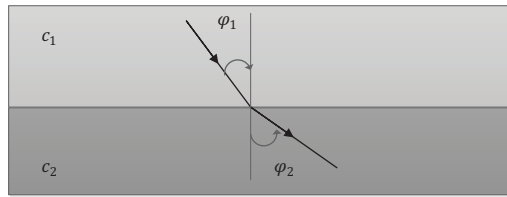


Figure B.1: Refraction of a sound ray at the interface between two media with different speeds of sound  $c_1$  and  $c_2$ , where  $c_1 < c_2$ .

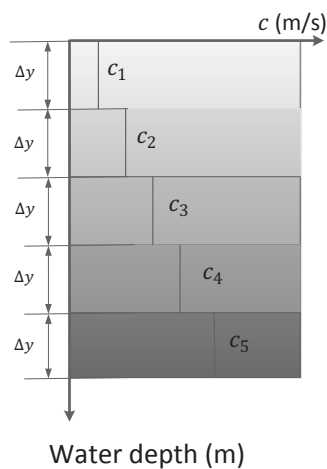


Figure B.2: An SSP example showing a piecewise linear sound speed variation in a shallow-water ocean environment with 5 different layers.

In this paper, we assume a piecewise linear variation of the sound speed with depth as shown in Fig. B.2. It should be mentioned that the following SSP is only an example for a piecewise linear variation of the sound speed with depth. Other piecewise linear SSPs can therefore also be used in the proposed UWA channel model. As can be seen in Fig. B.2, the one-dimensional geometrical sound speed model has been divided into  $K$  different equally wide layers, each with width  $\Delta y$  and speed of sound  $c_k$ ,  $k = 1, 2, \dots, K$ . The layer width is given by  $\Delta y = h/K$  in which the quantity  $h$  is the shallow water depth (in m). In our computer simulations, the SSP has been modeled as

$$c_k = c_s + g \cdot k \cdot \Delta y \quad \text{for } k = 1, 2, \dots, K \quad (\text{B.3})$$

where  $c_s$  is the initial speed of sound (in m/s) and  $g$  denotes the speed gradient (in  $\text{s}^{-1}$ ). From (B.3), we can obtain a vector for the speed of sound  $\mathbf{c}_k = [c_1, c_2, \dots, c_K]$ .

### C. Geometrical Model Description

Fig. B.3 presents the geometrical model of a UWA channel in a shallow-water non-isovelocity ocean environment. The geometrical model is bounded by the ocean surface and bottom, which are assumed to be rough. These natural boundaries act as reflectors for acoustic waves such that several *macro-eigenrays* can travel from the transmitter  $T_x$  to the receiver  $R_x$ . As can be seen in Fig. B.3, there are three kinds of macro-eigenrays. They are grouped into downward arriving (DA) macro-eigenrays, upward arriving (UA) macro-eigenrays, and a LOS macro-eigenray. Each of the DA macro-eigenrays, where the last reflection originates from the ocean surface, can have a different number of  $s$  surface reflections and  $\check{b}$  bottom reflections. Let  $N_S$  denote the maximum number of surface interactions that a DA macro-eigenray can have with the ocean surface, then  $s$  and  $\check{b}$  are limited by  $1 \leq s \leq N_S$  and  $s - 1 \leq \check{b} \leq s$ , respectively. For instance, if a DA macro-eigenray has only one interaction with the ocean surface, i.e.,  $N_S = 1$ , then there are two possible paths on which this macro-eigenray can travel from the transmitter  $T_x$  to the receiver  $R_x$ . The first path reaches at  $R_x$  after a single bounce on the surface of the ocean, i.e.,  $s = 1$ , and  $\check{b} = 0$ . The second path is a double-bounced path if a DA macro-eigenray starts downward. This means the macro-eigenray first interacts with the ocean bottom and then, after interacting with the ocean surface, arrives at  $R_x$ , i.e.,  $s = 1$  and  $\check{b} = 1$ . Thus, at any time instance  $t$ , the receiver  $R_x$  receives  $2N_S$  DA macro-eigenrays. The UA macro-eigenrays, where the last reflection originates from the ocean bottom, can have a different number of  $b$  bottom reflections and  $\check{s}$  surface reflections. Analogously, let  $N_B$  stand for the maximum number of bottom interactions that a UA macro-eigenray can have, then  $b$  and  $\check{s}$  are limited by  $1 \leq b \leq N_B$  and  $b - 1 \leq \check{s} \leq b$ , respectively. Similarly, at any time instance  $t$ , the receiver  $R_x$  receives  $2N_B$  UA macro-eigenrays. It needs to be mentioned that experimental results obtained from medium- and long-range shallow UWA communication scenarios have shown that the number of macro-eigenrays which arrive at  $R_x$  rarely exceeds 8, i.e.,  $2N_S + 2N_B = 8$  [5, 30–32].

The exact positions of *macro-scatterers* are computable and depend on the waveguide geometry and the number of macro-eigenrays. The roughness of the sea surface and sea bottom is characterized by *micro-scatterers*, which are randomly clustered around the positions of macro-scatterers. In other words, we study the propagation of deterministic macro-eigenrays and random micro-eigenrays. For each  $s$  and  $\check{b}$  the parameter  $S_{sb}^S$  in Fig. B.3 stands for the last macro-scatterer with which each DA macro-eigenray interacts with the ocean surface before arriving at  $R_x$ . The pa-

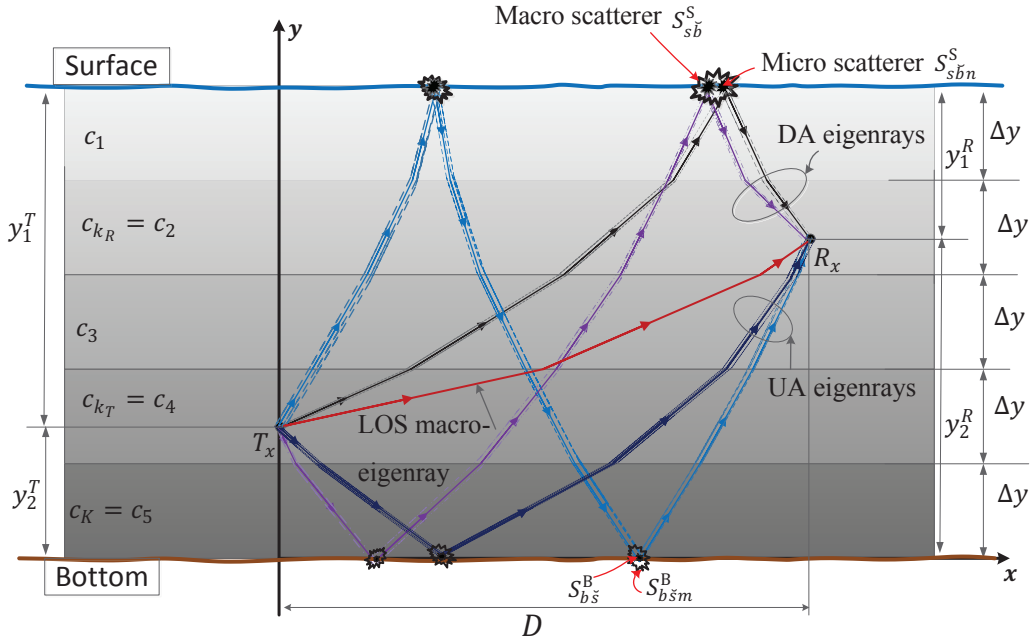


Figure B.3: Illustration of the LOS macro-eigenray and several DA and UA macro-eigenrays which travel from  $T_x$  to  $R_x$  in a shallow UWA channel ( $N_s = 2, N_B = 1$ ).

parameter  $S_{sb^n}^S$  denotes the  $n$ th micro-scatterer around the macro-scatterer  $S_{sb}^S$ , where  $1 < n < N_{sb}$ . In which the parameter  $N_{sb}$  denotes the maximum number of micro-scatterers  $S_{sb^n}^S$  around the macro-scatterer  $S_{sb}^S$ . Analogously, the macro-scatterer  $S_{bs}^B$  is the last macro-scatterer with which each UA macro-eigenray interacts before arriving at  $R_x$ . The parameter  $S_{bs^m}^B$  stands for the  $m$ th micro-scatterer around the macro-scatterer  $S_{bs}^B$ , where  $1 < m < M_{bs}$  and  $M_{bs}$  denotes the maximum number of micro-scatterers  $S_{bs^m}^B$  around the macro-scatterer  $S_{bs}^B$ . The total distances which eigenrays travel in non-isovelocity ocean environments after their interactions with macro- and micro-scatterers have been derived in this paper by using geometrical methods in combination with Snell's law.

Moreover, we assume that the transmitter  $T_x$  (receiver  $R_x$ ) is moving with velocity  $\vec{v}_T$  ( $\vec{v}_R$ ) in the direction determined by the angle-of-motion (AOM)  $\alpha_v^T$  ( $\alpha_v^R$ ). As shown in Figs. B.4 and B.5, the distance along the x-axis between the transmitter  $T_x$  and the receiver  $R_x$  is denoted by  $D$ . According to these figures,  $T_x$  ( $R_x$ ) is located at the distances  $y_1^T$  ( $y_1^R$ ) and  $y_2^T$  ( $y_2^R$ ) from the ocean surface and ocean bottom, respectively. As can be seen in Fig. B.4, the AOD (AOA) of the LOS component is denoted by  $\beta_0$  ( $\alpha_0$ ). With reference to Fig. B.5, the symbol  $\beta_{sb^n}^{\text{DA}}$  ( $\alpha_{sb^n}^{\text{DA}}$ ) stands for the AODs (AOAs) of the  $n$ th DA micro-eigenrays associated with the number of surface interactions  $s$  and bottom interactions  $\check{b}$ . Analogously, the symbol  $\beta_{bs^m}^{\text{UA}}$  ( $\alpha_{bs^m}^{\text{UA}}$ ) denotes the  $m$ th AODs (AOAs) of UA micro-eigenray associated with the number



position of  $T_x$  is at  $\Delta y_1^T$  and  $\Delta y_2^T$  seen from the surface and bottom of the layer  $k_T$ , which can be computed as

$$\Delta y_1^T = y_1^T - (k_T - 1)\Delta y \quad (\text{B.4a})$$

$$\Delta y_2^T = k_T\Delta y - y_1^T. \quad (\text{B.4b})$$

Analogously, the parameters  $\Delta y_1^R$  and  $\Delta y_2^R$ , which denote the position of the transmitter  $R_x$  in the layer  $k_R$ , can be computed as

$$\Delta y_1^R = y_1^R - (k_R - 1)\Delta y \quad (\text{B.5a})$$

$$\Delta y_2^R = k_R\Delta y - y_1^R. \quad (\text{B.5b})$$

#### D. Angle-of-Incidence

The parameters  $\varphi_{sbn(k_T)}^{\text{DA}}$  and  $\varphi_{b\check{s}m(k_T)}^{\text{UA}}$  denote the AOIs at the transmitter  $T_x$  for DA and UA micro-eigenrays, respectively, which are assumed to be random variables characterized by the von Mises distributions

$$p_{\varphi_{sbn(k_T)}^{\text{DA}}} \left( \varphi_{sbn(k_T)}^{\text{DA}} \right) = \frac{e^{\kappa \cos \left( \varphi_{sbn(k_T)}^{\text{DA}} - \mu_{sbn(k_T)}^{\text{DA}} \right)}}{2\pi I_0(\kappa)}, \quad \text{for } 0 \leq \varphi_{sbn(k_T)}^{\text{DA}} \leq \pi/2 \quad (\text{B.6})$$

and

$$p_{\varphi_{b\check{s}m(k_T)}^{\text{UA}}} \left( \varphi_{b\check{s}m(k_T)}^{\text{UA}} \right) = \frac{e^{\kappa \cos \left( \varphi_{b\check{s}m(k_T)}^{\text{UA}} - \mu_{b\check{s}m(k_T)}^{\text{UA}} \right)}}{2\pi I_0(\kappa)}, \quad \text{for } 0 \leq \varphi_{b\check{s}m(k_T)}^{\text{UA}} \leq \pi/2 \quad (\text{B.7})$$

respectively. Where  $\mu_{sbn(k_T)}^{\text{DA}}$  and  $\mu_{b\check{s}m(k_T)}^{\text{UA}}$  are the mean values of  $\varphi_{sbn(k_T)}^{\text{DA}}$  and  $\varphi_{b\check{s}m(k_T)}^{\text{UA}}$ , respectively. The function  $I_0(\cdot)$  denotes the zeroth-order modified Bessel function of the first kind. The parameter  $\kappa$  stands for the concentration parameter such that  $1/\kappa$  is the variance of the von Mises distribution. The other AOIs  $\varphi_{sbn(\cdot)}^{\text{DA}}$  and  $\varphi_{b\check{s}m(\cdot)}^{\text{UA}}$  at different layers can be computed by using Snell's law (B.1) as

$$\varphi_{sbn(k)}^{\text{DA}} = \arcsin \left( \frac{c_k}{c_{k_T}} \sin \varphi_{sbn(k_T)}^{\text{DA}} \right), \quad \text{for } k = 1, 2, \dots, K \text{ and } k \neq k_T \quad (\text{B.8})$$

and

$$\varphi_{b\check{s}m(k)}^{\text{UA}} = \arcsin \left( \frac{c_k}{c_{k_T}} \sin \varphi_{b\check{s}m(k_T)}^{\text{UA}} \right), \quad \text{for } k = 1, 2, \dots, K \text{ and } k \neq k_T \quad (\text{B.9})$$

respectively. The parameters  $\varphi_{0(k_T)}$  and  $\varphi_{0(k_R)}$  seen in Fig. B.4 stand for the AOIs

of the LOS macro-eigenray at  $T_x$  and  $R_x$ , respectively.

### III. THE GEOMETRY-BASED UWA CHANNEL MODEL

In this section, we develop a stochastic model for the acoustic wave propagation through non-isovelocity shallow-water environments. First, we present the TVCIR of the proposed geometry-based channel model for a vehicle-to-vehicle (V2V) UWA wideband channel under LOS propagation conditions. Then, we derive the expressions of the total distances which eigenrays travel from  $T_x$  to  $R_x$  after their interaction with the rough surface and bottom of the ocean. The AODs and the AOAs, which are required for computing the Doppler frequencies, are also studied. Finally, we derive the time-variant channel transfer function (TVCTF).

#### A. TVCIR

According to the geometrical model shown in Figs. B.4 and B.5, the TVCIR  $h(\tau', t)$  can be split into three parts. The first part  $h^{\text{LOS}}(\tau', t)$  describes the LOS component, whereas the second part  $h^{\text{DA}}(\tau', t)$  and the third part  $h^{\text{UA}}(\tau', t)$  comprise the DA eigenrays and the UA eigenrays, respectively. Thus, the TVCIR  $h(\tau', t)$  can be expressed by

$$h(\tau', t) = h^{\text{LOS}}(\tau', t) + h^{\text{DA}}(\tau', t) + h^{\text{UA}}(\tau', t). \quad (\text{B.10})$$

The LOS part  $h^{\text{LOS}}(\tau', t)$  of the TVCIR can be written as

$$h^{\text{LOS}}(\tau', t) = c_0 e^{j(2\pi f_0 t + \theta_0)} \delta(\tau' - \tau'_0) \quad (\text{B.11})$$

in which the gain  $c_0$  is defined by

$$c_0 = \sqrt{c_R / (1 + c_R)} A_s(D_0) A_a(D_0). \quad (\text{B.12})$$

The parameter  $\tau'_0$  stands for the propagation delay of the LOS component. The symbols  $f_0$  and  $\theta_0$  denote the Doppler frequency and phase shift of the LOS component, respectively. It is assumed that the phase shift  $\theta_0$  is unknown and will consequently be modelled as a random variable with uniform distribution over  $(0, 2\pi]$ . The parameter  $c_R$  in (B.12) is the Rice factor, thus, the distribution of the channel envelope can follow the Rice distribution. The Rice factor  $c_R$  is defined as a ratio between the power of LOS path and the power of scattered paths (i.e., DA and UA eigenrays). The Doppler frequency  $f_0$  is given by

$$f_0 = f_{\max}^T \cos(\beta_0 - \alpha_v^T) + f_{\max}^R \cos(\alpha_0 - \alpha_v^R) \quad (\text{B.13})$$

where  $f_{\max}^T$  ( $f_{\max}^R$ ) indicates the maximum Doppler frequency associated with  $T_x$  ( $R_x$ ), which is given by  $f_{\max}^T = v_T f_c / c_{k_T}$  ( $f_{\max}^R = v_R f_c / c_{k_R}$ ). Therein,  $v_T = |\vec{v}_T|$  ( $v_R = |\vec{v}_R|$ ) stands for the speed of the transmitter  $T_x$  (receiver  $R_x$ ). The symbol  $f_c$  denotes the carrier frequency (in Hz), and  $c_{k_T}$  ( $c_{k_R}$ ) is the speed of sound (in m/s) within the water layer  $k_T$  ( $k_R$ ). With reference to Fig. B.4, the AOD  $\beta_0$  and the AOA  $\alpha_0$  can be computed by using

$$\beta_0 = \begin{cases} \frac{3\pi}{2} + \varphi_0(k_T), & \text{if } k_T < k_R \\ \arctan\left(\frac{y_1^T - y_1^R}{D}\right), & \text{if } k_T = k_R \\ \frac{\pi}{2} - \varphi_0(k_T), & \text{if } k_T > k_R \end{cases} \quad (\text{B.14})$$

and

$$\alpha_0 = \begin{cases} \frac{\pi}{2} + \varphi_0(k_R) = \frac{\pi}{2} + \arcsin\left(\frac{c_{k_R}}{c_{k_T}} \sin(\varphi_0(k_T))\right), & \\ \quad \text{if } k_T < k_R \\ \pi + \beta_0, & \\ \quad \text{if } k_T = k_R \\ \frac{3\pi}{2} - \varphi_0(k_R) = \frac{3\pi}{2} - \arcsin\left(\frac{c_{k_R}}{c_{k_T}} \sin(\varphi_0(k_T))\right), & \\ \quad \text{if } k_T > k_R \end{cases} \quad (\text{B.15})$$

respectively. The total distance  $D_0$  in (B.12) which the LOS component travels between  $T_x$  and  $R_x$  is given by

$$D_0 = \begin{cases} \sum_{k=k_T}^{k_R} D_{0(k)} = \frac{\Delta y_2^T}{\cos(\varphi_0(k_T))} + \sum_{k=k_T+1}^{k_R-1} \frac{\Delta y}{\cos(\varphi_0(k))} + \frac{\Delta y_1^R}{\cos(\varphi_0(k_R))}, & \text{if } k_T < k_R \\ \sqrt{D^2 + (y_1^T - y_1^R)^2}, & \text{if } k_T = k_R \\ \sum_{k=k_R}^{k_T} D_{0(k)} = \frac{\Delta y_1^T}{\cos(\varphi_0(k_T))} + \sum_{k=k_R+1}^{k_T-1} \frac{\Delta y}{\cos(\varphi_0(k))} + \frac{\Delta y_2^R}{\cos(\varphi_0(k_R))}, & \text{if } k_T > k_R. \end{cases} \quad (\text{B.16})$$

The parameter  $D_{0(k)}$  stands for the distance that the LOS component travels in the

layer  $k$ . The propagation delay  $\tau'_0$  can be expressed by

$$\tau'_0 = \begin{cases} \sum_{k=k_T}^{k_R} \frac{D_{0(k)}}{c_k}, & \text{if } k_T < k_R \\ \frac{D_0}{c_{k_T}}, & \text{if } k_T = k_R \\ \sum_{k=k_R}^{k_T} \frac{D_{0(k)}}{c_k}, & \text{if } k_T > k_R. \end{cases} \quad (\text{B.17})$$

The AOIs  $\varphi_{0(\cdot)}$  in (B.15) and (B.16) can be computed by using Snell's law (B.1) as

$$\varphi_{0(k)} = \arcsin \left( \frac{c_k}{c_{k_T}} \sin \varphi_{0(k_T)} \right) \begin{cases} \text{for } k = k_T + 1, \dots, k_R \text{ if } k_T < k_R \\ \text{for } k = k_R + 1, \dots, k_T \text{ if } k_T > k_R. \end{cases} \quad (\text{B.18})$$

The functions  $A_s(\cdot)$  and  $A_a(\cdot)$  presented in (B.12) denote the propagation loss coefficients due to geometrical spreading and absorption, respectively. The loss as a result of geometrical spreading is divided into two categories: spherical spreading and cylindrical spreading. The spherical spreading normally occurs in long-range UWA communications in shallow/deep water; while cylindrical spreading occurs in short-range UWA communications in shallow water [27]. In this paper, long-range UWA communications are assumed, thus, spherical spreading is considered in analytical derivations. It is assumed that the transmitter is equipped with an omnidirectional hydrophone and generates spherical waveforms in a shallow water environment. The propagation loss coefficient due to the spherical spreading can be written as [13, Eq. (2.16)]

$$A_s(d) = \frac{1}{d} \quad (\text{B.19})$$

where the variable  $d$  denotes the total propagation distance (in m). The absorption loss coefficient  $A_a(\cdot)$  is expressed by [32, Eq. (4)]

$$A_a(d) = 10^{-\frac{d\beta}{20000}}. \quad (\text{B.20})$$

In (B.20), the parameter  $\beta$  is given by [3, Eq. (1.3.1)]

$$\beta = 8.68 \times 10^3 \left( \frac{S_a f_T f_c^2 A}{f_T^2 + f_c^2} + \frac{B f_c^2}{f_T} \right) \times (1 - 6.54 \times 10^{-4} P) \quad (\text{dB/km}) \quad (\text{B.21})$$

where  $A = 2.34 \cdot 10^{-6}$  and  $B = 3.38 \cdot 10^{-6}$ . The symbol  $S_a$  stands for the salinity (in parts per thousand),  $f_c$  is the carrier frequency (in kHz),  $f_T$  denotes the relaxation frequency (in kHz). The symbol  $P$  stands for the hydrostatic pressure (in kg/cm<sup>2</sup>), which is determined by  $P = 1.01 \cdot (1 + 0.1h)$ , where  $h$  denotes the water depth (in m). It needs to be emphasised that (B.21) is suitable for carrier frequencies  $f_c$  between 3 and 500 kHz [3, p. 10].

The second part  $h^{\text{DA}}(\tau', t)$  and the third part  $h^{\text{UA}}(\tau', t)$  of the TVCIR  $h(\tau', t)$  in (B.10) are given by

$$h^{\text{DA}}(\tau', t) = \sum_{s=1}^{N_S} \sum_{\check{b}=s-1}^s \sum_{n=1}^{N_{s\check{b}}} c_{s\check{b}n}^{\text{DA}} e^{j(2\pi f_{s\check{b}n}^{\text{DA}} t + \theta_{s\check{b}n}^{\text{DA}})} \delta(\tau' - \tau'_{s\check{b}n}^{\text{DA}}) \quad (\text{B.22})$$

and

$$h^{\text{UA}}(\tau', t) = \sum_{b=1}^{N_B} \sum_{\check{s}=b-1}^b \sum_{m=1}^{M_{b\check{s}}} c_{b\check{s}m}^{\text{UA}} e^{j(2\pi f_{b\check{s}m}^{\text{UA}} t + \theta_{b\check{s}m}^{\text{UA}})} \delta(\tau' - \tau'_{b\check{s}m}^{\text{UA}}) \quad (\text{B.23})$$

respectively. The gains  $c_{s\check{b}n}^{\text{DA}}$  and  $c_{b\check{s}m}^{\text{UA}}$  can be expressed by

$$c_{s\check{b}n}^{\text{DA}} = \sqrt{\frac{\eta_S}{2N_S N_{s\check{b}}(1 + c_R)}} A_s(D_{s\check{b}n}^{\text{DA}}) A_a(D_{s\check{b}n}^{\text{DA}}) A_b(\varphi_{s\check{b}n(K)}^{\text{DA}})^{\check{b}} \quad (\text{B.24})$$

and

$$c_{b\check{s}m}^{\text{UA}} = \sqrt{\frac{\eta_B}{2N_B M_{b\check{s}}(1 + c_R)}} A_s(D_{b\check{s}m}^{\text{UA}}) A_a(D_{b\check{s}m}^{\text{UA}}) A_b(\varphi_{b\check{s}m(K)}^{\text{UA}})^b \quad (\text{B.25})$$

respectively. The symbols  $\eta_S$  in (B.24) and  $\eta_B$  in (B.25) are used to balance the contribution of the DA and UA macro-eigenrays to the total power of the UWA channel model such that  $\eta_S + \eta_B = 1$ . Furthermore, each DA (UA) macro-eigenray is represented as an average of  $N_{s\check{b}}$  DA ( $M_{b\check{s}}$  UA) micro-eigenrays. The symbols  $D_{s\check{b}n}^{\text{DA}}$  and  $D_{b\check{s}m}^{\text{UA}}$  denote the total distances which the DA and UA micro-eigenrays travel from  $T_x$  to  $R_x$  given  $(s, \check{b})$  and  $(\check{s}, b)$  surface-bottom interactions, respectively. These two quantities can be computed as (B.55) and (B.56) (see (B.55) and (B.56) in the Appendix A). The propagation delays  $\tau'_{s\check{b}n}^{\text{DA}}$  and  $\tau'_{b\check{s}m}^{\text{UA}}$  can be expressed as (B.57) and (B.58), respectively (see (B.57) and (B.58) in the Appendix A). The parameters  $\varphi_{s\check{b}n(K)}^{\text{DA}}$  and  $\varphi_{b\check{s}m(K)}^{\text{UA}}$  stand for the AOIs of DA and UA micro-eigenrays at layer  $k$ . The phase shifts  $\theta_{s\check{b}n}^{\text{DA}}$  in (B.22) and  $\theta_{b\check{s}m}^{\text{UA}}$  in (B.23) are modelled by independent and identically distributed (i.i.d.) random variables, which are supposed to be uniformly

distributed over the interval  $(-\pi, \pi]$ . The function  $A_b(\cdot)$  in (B.24) and (B.25), which denotes the impedance mismatch between the ocean water and the ocean bed, can be expressed by [3, Eq. (3.1.14)]

$$A_b(\varphi) = \left| \frac{(\rho_b/\rho_K) \cos(\varphi) - \sqrt{(c_K/c_b)^2 - \sin^2(\varphi)}}{(\rho_b/\rho_K) \cos(\varphi) + \sqrt{(c_K/c_b)^2 - \sin^2(\varphi)}} \right| \quad (\text{B.26})$$

where  $\rho_K$  ( $\rho_b$ ) and  $c_K$  ( $c_b$ ) stand for the density of the  $K$ th layer of the ocean water (ocean bed) and the speed of sound in the  $K$ th layer of the ocean water (ocean bed), respectively. The symbol  $\varphi$  in (B.26) denotes the AOI of the eigenrays at the ocean bottom, which can be replaced by  $\varphi_{sbn(K)}^{\text{DA}}$  and  $\varphi_{b\check{s}m(K)}^{\text{UA}}$ .

### B. AOD, AOA, and Doppler frequencies

In this section, the analytical expressions for the AODs  $\beta_{sbn}^{\text{DA}}$  ( $\beta_{b\check{s}m}^{\text{UA}}$ ) and the AOAs  $\alpha_{sbn}^{\text{DA}}$  ( $\alpha_{b\check{s}m}^{\text{UA}}$ ), which are necessary to compute the Doppler frequencies of the micro-eigenrays are derived. The Doppler frequencies  $f_{sbn}^{\text{DA}}$  and  $f_{b\check{s}m}^{\text{UA}}$  presented in (B.22) and (B.23), respectively, can be computed by using (B.13), if we replace there  $\beta_0$  by  $\beta_{sbn}^{\text{DA}}$  ( $\beta_{b\check{s}m}^{\text{UA}}$ ) and  $\alpha_0$  by  $\alpha_{sbn}^{\text{DA}}$  ( $\alpha_{b\check{s}m}^{\text{UA}}$ ) which results in

$$f_{sbn}^{\text{DA}} = f_{\max}^T \cos(\beta_{sbn}^{\text{DA}} - \alpha_v^T) + f_{\max}^R \cos(\alpha_{sbn}^{\text{DA}} - \alpha_v^R) \quad (\text{B.27})$$

and

$$f_{b\check{s}m}^{\text{UA}} = f_{\max}^T \cos(\beta_{b\check{s}m}^{\text{UA}} - \alpha_v^T) + f_{\max}^R \cos(\alpha_{b\check{s}m}^{\text{UA}} - \alpha_v^R) \quad (\text{B.28})$$

respectively. With reference to Figs. B.4 and B.5, the general expressions for the AODs  $\beta_{sbn}^{\text{DA}}$  and  $\beta_{b\check{s}m}^{\text{UA}}$  can be written as

$$\beta_{sbn}^{\text{DA}} = \left( \check{b} - s + \frac{3}{2} \right) \pi + (-1)^{(s-\check{b})} \varphi_{sbn(k_T)}^{\text{DA}} \quad (\text{B.29})$$

and

$$\beta_{b\check{s}m}^{\text{UA}} = \left( b - \check{s} + \frac{1}{2} \right) \pi - (-1)^{(b-\check{s})} \varphi_{b\check{s}m(k_T)}^{\text{UA}} \quad (\text{B.30})$$

respectively. Similarly, the general solutions for the AOAs  $\alpha_{sbn}^{\text{DA}}$  and  $\alpha_{b\check{s}m}^{\text{UA}}$  can be found to be equal to

$$\alpha_{sbn}^{\text{DA}} = \frac{\pi}{2} + \varphi_{sbn(k_R)}^{\text{DA}} \quad (\text{B.31})$$

and

$$\alpha_{b\check{s}m}^{\text{UA}} = \frac{3\pi}{2} - \varphi_{b\check{s}m(k_R)}^{\text{UA}} \quad (\text{B.32})$$

respectively. By substituting (B.29) and (B.31) in (B.27), we obtain a new expression for the Doppler frequency  $f_{sb\check{n}}^{\text{DA}}$  as

$$f_{sb\check{n}}^{\text{DA}} = f_{\text{max}}^T \sin\left(\varphi_{sb\check{n}(k_T)}^{\text{DA}} - \alpha_v^T\right) - f_{\text{max}}^R \sin\left(\varphi_{sb\check{n}(k_R)}^{\text{DA}} - \alpha_v^R\right). \quad (\text{B.33})$$

Analogously, by substituting (B.30) and (B.32) in (B.54), the Doppler frequency  $f_{b\check{s}m}^{\text{UA}}$  can be expressed by

$$f_{b\check{s}m}^{\text{UA}} = f_{\text{max}}^T \sin\left(\varphi_{b\check{s}m(k_T)}^{\text{UA}} - \alpha_v^T\right) - f_{\text{max}}^R \sin\left(\varphi_{b\check{s}m(k_R)}^{\text{UA}} - \alpha_v^R\right). \quad (\text{B.34})$$

### C. TVCTF

The TVCTF  $H(f', t)$  can be computed by taking the Fourier transform of the TVCIR  $h(\tau', t)$  w.r.t the propagation delay  $\tau'$ . From (B.10), (B.11), (B.22), and (B.23), the TVCTF  $H(f', t)$  can obviously be written as

$$H(f', t) = H^{\text{LOS}}(f', t) + H^{\text{DA}}(f', t) + H^{\text{UA}}(f', t). \quad (\text{B.35})$$

The function  $H^{\text{LOS}}(f', t)$  represents the LOS part of the TVCTF  $H(f', t)$ , which can be written as

$$H^{\text{LOS}}(f', t) = c_0 e^{j[2\pi(f_0 t - f' \tau'_0) + \theta_0]}. \quad (\text{B.36})$$

The second part  $H^{\text{DA}}(f', t)$  and the third part  $H^{\text{UA}}(f', t)$  of the TVCTF  $H(f', t)$  are given by

$$H^{\text{DA}}(f', t) = \sum_{s=1}^{N_S} \sum_{\check{b}=s-1}^s \sum_{n=1}^{N_{s\check{b}}} c_{sb\check{n}}^{\text{DA}} e^{j[2\pi(f_{sb\check{n}}^{\text{DA}} t - f' \tau_{sb\check{n}}^{\text{DA}}) + \theta_{sb\check{n}}^{\text{DA}}]} \quad (\text{B.37})$$

and

$$H^{\text{UA}}(f', t) = \sum_{b=1}^{N_B} \sum_{\check{s}=b-1}^b \sum_{m=1}^{M_{b\check{s}}} c_{b\check{s}m}^{\text{UA}} e^{j[2\pi(f_{b\check{s}m}^{\text{UA}} t - f' \tau_{b\check{s}m}^{\text{UA}}) + \theta_{b\check{s}m}^{\text{UA}}]} \quad (\text{B.38})$$

respectively. For ease of reference, the most important parameters presented in Section III are listed in Table B.1.

Table B.1: Definition and selected values of the channel model parameters.

Parameters	Definitions	Figs. 8–14	Figs. 18
$D_{sbn}^{DA}, D_{b\check{s}m}^{UA}$	Total distances that the DA and UA micro-eigenrays travel from $T_x$ to $R_x$	-	-
$\varphi_{sbn(k)}^{DA}, \varphi_{b\check{s}m(k)}^{UA}$	AOIs of the DA and UA micro-eigenrays at layer $k$	-	-
$\mu_{sb(k_T)}^{DA}, \mu_{b\check{s}(k_T)}^{UA}$	Average of the AOI distributions for the DA and UA micro-eigenrays transmitted from $T_x$	-	-
$y_1^T$	Distance between $T_x$ and the ocean surface	35 m	46 m
$y_2^T$	Distance between $T_x$ and the ocean bottom	65 m	34 m
$y_1^R$	Distance between $R_x$ and the ocean surface	55 m	29 m
$y_2^R$	Distance between $R_x$ and the ocean bottom	45 m	51 m
$h$	Water depth	100 m	80 m
$D$	Total distance between $T_x$ and $R_x$ along the x-axis	5000 m	2000 m
$K$	Number of water layers	1, 3, 6, 10, 20, and 30	16
$\rho_K$	Density of the $K$ th layer of the ocean water	1000 kg/m <sup>3</sup>	1000 kg/m <sup>3</sup>
$\rho_b$	Density of the ocean bed	1500 kg/m <sup>3</sup>	1500 kg/m <sup>3</sup>
$c_s$	Speed of sound for the case of isovelocity ocean environment	1500 m/s	1500 m/s
$c_b$	Speed of sound in the ocean bed	1600 m/s	1600 m/s
$\alpha_v^T$	Angle-of-motion of the transmitter	180°	-
$\alpha_v^R$	Angle-of-motion of the receiver	0°	-
$f_c$	Carrier frequency	10 kHz	17 kHz
$f_{\max}^T$	Maximum Doppler frequency associated with the transmitter $T_x$	20 Hz	0 Hz
$f_{\max}^R$	Maximum Doppler frequency associated with the receiver $R_x$	20 Hz	0 Hz
$c_R$	Rice factor	0.2 (arbitrary)	0.3
$\eta_S$	Ratio of the power of DA macro-eigenrays to the total power of the UWA channel model	0.5	0.5
$\eta_B$	Ratio of the power of UA macro-eigenrays to the total power of the UWA channel model	0.5	0.5
$k_T$	Transmitter layer index	4 if $K = 10$	10
$k_R$	Receiver layer index	6 if $K = 10$	6
$\Delta y_1^T$	Transmitter position in the layer with index $k_T$	5 m if $K = 10$	1 m for $K = 16$
$\Delta y_2^T$	Transmitter position in the layer with index $k_T$	5 m if $K = 10$	4 m for $K = 16$
$\Delta y_1^R$	Receiver position in the layer with index $k_R$	5 m if $K = 10$	4 m for $K = 16$
$\Delta y_2^R$	Receiver position in the layer with index $k_R$	5 m if $K = 10$	1 m for $K = 16$
$N_S$	Maximum number of interactions between each DA macro-eigenray and the ocean surface	2	1
$N_B$	Maximum number of interactions between each UA macro-eigenray and the ocean bottom	2	1
$N_{s\check{b}}$	Number of DA micro-eigenrays	1000	23
$M_{b\check{s}}$	Number of UA macro-eigenrays	1001	24

#### IV. STATISTICAL PROPERTIES OF THE UWA CHANNEL MODEL

In this section, we study the statistical properties of the developed UWA channel model including the temporal ACF, FCF, and the PDP by means of the TVCTF.

##### A. Temporal ACF

By having the TVCTF  $H(f', t)$ , we can compute the temporal ACF and FCF of the channel. Assuming that the geometry-based UWA channel model is WSS in time  $t$ , the temporal ACF  $r_{HH}(\tau)$  can be obtained by using the TVCTF  $H(f', t)$  as

$$r_{HH}(\tau) = E\{H^*(f', t)H(f', t + \tau)\} \quad (\text{B.39})$$

where  $(\cdot)^*$  represents the complex conjugate operation and  $E\{\cdot\}$  is the statistical expectation operator. The symbol  $\tau$  denotes the time separation variable. After averaging over the random phases  $\theta_0$ ,  $\theta_{sbn}^{\text{DA}}$ , and  $\theta_{b\check{s}m}^{\text{UA}}$ , the temporal ACF  $r_{HH}(\tau)$  of the proposed UWA channel model is obtained as

$$\begin{aligned} r_{HH}(\tau) = c_0^2 e^{j2\pi f_0 \tau} &+ \sum_{s=1}^{N_S} \sum_{\check{b}=s-1}^s \sum_{n=1}^{N_{s\check{b}}} E_{\varphi_{sbn}^{\text{DA}}(k_T)} \left\{ [c_{sbn}^{\text{DA}}]^2 e^{j2\pi f_{sbn}^{\text{DA}} \tau} \right\} \\ &+ \sum_{b=1}^{N_B} \sum_{\check{s}=b-1}^b \sum_{m=1}^{M_{b\check{s}}} E_{\varphi_{b\check{s}m}^{\text{UA}}(k_T)} \left\{ [c_{b\check{s}m}^{\text{UA}}]^2 e^{j2\pi f_{b\check{s}m}^{\text{UA}} \tau} \right\} \end{aligned} \quad (\text{B.40})$$

The operator  $E_{\varphi}\{\cdot\}$  is the statistical expectation operator w.r.t the random variable  $\varphi$ . Note that the sets of random variables  $\{c_{sbn}^{\text{DA}}, f_{sbn}^{\text{DA}}\}$  and  $\{c_{b\check{s}m}^{\text{UA}}, f_{b\check{s}m}^{\text{UA}}\}$  can be expressed as functions of the random AOIs  $\varphi_{sbn}^{\text{DA}}(k_T)$  and  $\varphi_{b\check{s}m}^{\text{UA}}(k_T)$ , respectively. Recall that the random AOIs  $\varphi_{sbn}^{\text{DA}}(k_T)$  and  $\varphi_{b\check{s}m}^{\text{UA}}(k_T)$  are characterized by the von Mises distributions  $p_{\varphi_{sbn}^{\text{DA}}(k_T)}(\varphi_{sbn}^{\text{DA}}(k_T))$  and  $p_{\varphi_{b\check{s}m}^{\text{UA}}(k_T)}(\varphi_{b\check{s}m}^{\text{UA}}(k_T))$  presented in (B.6) and (B.7), respectively. By averaging over the random AOIs  $\varphi_{sbn}^{\text{DA}}(k_T)$  and  $\varphi_{b\check{s}m}^{\text{UA}}(k_T)$ , the temporal ACF  $r_{HH}(\tau)$  can be expressed as

$$\begin{aligned} r_{HH}(\tau) = c_0^2 e^{j2\pi f_0 \tau} &+ \frac{1}{2\pi I_0(\kappa)} \left[ \sum_{s=1}^{N_S} \sum_{\check{b}=s-1}^s \sum_{n=1}^{N_{s\check{b}}} \int_0^{2\pi} [c_{sbn}^{\text{DA}}]^2 e^{[j2\pi f_{sbn}^{\text{DA}} \tau + \kappa \cos(\varphi_{sbn}^{\text{DA}}(k_T) - \mu_{sbn}^{\text{DA}}(k_T))]} d\varphi_{sbn}^{\text{DA}}(k_T) \right. \\ &\left. + \sum_{b=1}^{N_B} \sum_{\check{s}=b-1}^b \sum_{m=1}^{M_{b\check{s}}} \int_0^{2\pi} [c_{b\check{s}m}^{\text{UA}}]^2 e^{[j2\pi f_{b\check{s}m}^{\text{UA}} \tau + \kappa \cos(\varphi_{b\check{s}m}^{\text{UA}}(k_T) - \mu_{b\check{s}m}^{\text{UA}}(k_T))]} d\varphi_{b\check{s}m}^{\text{UA}}(k_T) \right] \end{aligned} \quad (\text{B.41})$$

In general, the integral in (B.41) has to be solved numerically. However, a closed-form approximation for the temporal ACF  $r_{HH}(\tau)$  can be derived by replacing the random gains  $c_{sbn}^{\text{DA}}(c_{b\check{s}m}^{\text{UA}})$  by the gains  $c_{sb}^{\text{DA}}(c_{b\check{s}}^{\text{UA}})$ . To compute the gains  $c_{sb}^{\text{DA}}(c_{b\check{s}}^{\text{UA}})$ , the random AOIs  $\varphi_{sbn(k_T)}^{\text{DA}}(\varphi_{b\check{s}m(k_T)}^{\text{UA}})$  have to be replaced by their mean values  $\mu_{sb(k_T)}^{\text{DA}}(\mu_{b\check{s}(k_T)}^{\text{UA}})$  of the von Mises distributions. In other words, the gains  $c_{sb}^{\text{DA}}$  and  $c_{b\check{s}}^{\text{UA}}$  are functions of  $\mu_{sb(k_T)}^{\text{DA}}$  and  $\mu_{b\check{s}(k_T)}^{\text{UA}}$ , respectively, i.e.,  $c_{sb}^{\text{DA}} = c_{sbn}^{\text{DA}}(\mu_{sb(k_T)}^{\text{DA}})$  and  $c_{b\check{s}}^{\text{UA}} = c_{b\check{s}m}^{\text{UA}}(\mu_{b\check{s}(k_T)}^{\text{UA}})$ . The closed-form approximation  $r_{HH}^{\text{AP}}(\tau)$  of the temporal ACF  $r_{HH}(\tau)$  in (B.41) can be obtained as

$$r_{HH}^{\text{AP}}(\tau) = c_0^2 e^{j2\pi f_0 \tau} + \frac{1}{I_0(\kappa)} \left[ \sum_{s=1}^{N_S} \sum_{\check{s}=s-1}^s N_{s\check{s}} [c_{s\check{s}}^{\text{DA}}]^2 I_0 \left( \sqrt{[x_{s\check{s}}^{\text{DA}}]^2 + [y_{s\check{s}}^{\text{DA}}]^2} \right) + \sum_{b=1}^{N_B} \sum_{\check{s}=b-1}^b M_{b\check{s}} [c_{b\check{s}}^{\text{UA}}]^2 I_0 \left( \sqrt{[x_{b\check{s}}^{\text{UA}}]^2 + [y_{b\check{s}}^{\text{UA}}]^2} \right) \right] \quad (\text{B.42})$$

in which the functions  $x_{sb}^{\text{DA}}$ ,  $y_{sb}^{\text{DA}}$ ,  $x_{b\check{s}}^{\text{UA}}$ , and  $y_{b\check{s}}^{\text{UA}}$  are, respectively, given by

$$x_{sb}^{\text{DA}} = j2\pi\tau \left( f_{\max}^R \sin \alpha_v^R - f_{\max}^T \sin \alpha_v^T \right) + \kappa \cos \mu_{sb(k_T)}^{\text{DA}} \quad (\text{B.43})$$

$$y_{sb}^{\text{DA}} = j2\pi\tau \left( f_{\max}^T \cos \alpha_v^T - f_{\max}^R (c_{k_R}/c_{k_T}) \cos \alpha_v^R \right) + \kappa \sin \mu_{sb(k_T)}^{\text{DA}} \quad (\text{B.44})$$

$$x_{b\check{s}}^{\text{UA}} = j2\pi\tau \left( f_{\max}^R \sin \alpha_v^R - f_{\max}^T \sin \alpha_v^T \right) + \kappa \cos \mu_{b\check{s}(k_T)}^{\text{UA}} \quad (\text{B.45})$$

and

$$y_{b\check{s}}^{\text{UA}} = j2\pi\tau \left( f_{\max}^T \cos \alpha_v^T - f_{\max}^R (c_{k_R}/c_{k_T}) \cos \alpha_v^R \right) + \kappa \sin \mu_{b\check{s}(k_T)}^{\text{UA}}. \quad (\text{B.46})$$

The proof to the expression (B.42) is provided in Appendix B. The quality of the approximation  $r_{HH}(\tau) \approx r_{HH}^{\text{AP}}(\tau)$  depends on the concentration parameter  $\kappa$  that controls the spread of the von Mises distributions in (B.6) and (B.7). To measure the approximation error as a function of  $\kappa$ , we consider the following error function

$$E(\kappa) = \frac{1}{\tau_{\max}} \int_0^{\tau_{\max}} |r_{HH}(\tau) - r_{HH}^{\text{AP}}(\tau)|^2 d\tau \quad (\text{B.47})$$

where  $\tau_{\max}$  defines an appropriate time-lag interval  $[0, \tau_{\max}]$  over which the approximation of  $r_{HH}(\tau)$  is of importance. The evaluation of the error function  $E(\kappa)$  will be discussed in the next section.

## B. FCF

The geometry-based UWA channel model is also assumed to be WSS w.r.t. fre-

quency  $f'$ . Thus, we can compute the FCF  $r_{HH}(\nu')$  of the TVCTF  $H(f', t)$  by using

$$r_{HH}(\nu') = E\{H^*(f', t)H(f' + \nu', t)\} \quad (\text{B.48})$$

where the symbol  $\nu'$  stands for the frequency separation variable. After averaging over the random phases  $\theta_0$ ,  $\theta_{sbn}^{\text{DA}}$ , and  $\theta_{b\check{s}m}^{\text{UA}}$ , the FCF  $r_{HH}(\nu')$  of the proposed UWA channel model results in

$$\begin{aligned} r_{HH}(\nu') = & c_0^2 e^{-j2\pi\nu'\tau'_0} + \sum_{s=1}^{N_S} \sum_{\check{b}=s-1}^s \sum_{n=1}^{N_{s\check{b}}} E_{\varphi_{sbn}^{\text{DA}}(k_T)} \left\{ [c_{sbn}^{\text{DA}}]^2 e^{-j2\pi\nu'\tau'_{sbn}^{\text{DA}}} \right\} \\ & + \sum_{b=1}^{N_B} \sum_{\check{s}=b-1}^b \sum_{m=1}^{M_{b\check{s}}} E_{\varphi_{b\check{s}m}^{\text{UA}}(k_T)} \left\{ [c_{b\check{s}m}^{\text{UA}}]^2 e^{-j2\pi\nu'\tau'_{b\check{s}m}^{\text{UA}}} \right\}. \end{aligned} \quad (\text{B.49})$$

Analogously to Section IV-A, by averaging over the random AOIs  $\varphi_{sbn}^{\text{DA}}(k_T)$  and  $\varphi_{b\check{s}m}^{\text{UA}}(k_T)$ , the FCF  $r_{HH}(\nu')$  can be written as

$$\begin{aligned} r_{HH}(\nu') = & c_0^2 e^{-j2\pi\nu'\tau'_0} \\ & + \frac{1}{2\pi I_0(\kappa)} \left[ \sum_{s=1}^{N_S} \sum_{\check{b}=s-1}^s \sum_{n=1}^{N_{s\check{b}}} \int_0^{2\pi} [c_{sbn}^{\text{DA}}]^2 e^{\left[-j2\pi\nu'\tau'_{sbn}^{\text{DA}} + \kappa \cos\left(\varphi_{sbn}^{\text{DA}}(k_T) - \mu_{sbn}^{\text{DA}}(k_T)\right)\right]} d\varphi_{sbn}^{\text{DA}}(k_T) \right. \\ & \left. + \sum_{b=1}^{N_B} \sum_{\check{s}=b-1}^b \sum_{m=1}^{M_{b\check{s}}} \int_0^{2\pi} [c_{b\check{s}m}^{\text{UA}}]^2 e^{\left[-j2\pi\nu'\tau'_{b\check{s}m}^{\text{UA}} + \kappa \cos\left(\varphi_{b\check{s}m}^{\text{UA}}(k_T) - \mu_{b\check{s}m}^{\text{UA}}(k_T)\right)\right]} d\varphi_{b\check{s}m}^{\text{UA}}(k_T) \right]. \end{aligned} \quad (\text{B.50})$$

### C. PDP

The PDP  $S_{\tau'}(\tau')$  can be obtained by taking the inverse Fourier transform of the FCF  $r_{HH}(\nu')$  w.r.t. the variable  $\nu'$ , i.e.,  $S_{\tau'}(\tau') = \text{IFT}\{r_{HH}(\nu')\}$ . The PDP  $S_{\tau'}(\tau')$  also enables us to compute the average delay  $B_{\tau'}^{(1)}$ , the delay spread  $B_{\tau'}^{(2)}$ , and the coherence bandwidth  $B_C$  of the channel. These characteristic quantities can be expressed in closed form by means of the FCF. The average delay  $B_{\tau'}^{(1)}$  and the delay spread  $B_{\tau'}^{(2)}$  are defined by the first moment and the square root of the second central moment of the PDP  $S_{\tau'}(\tau')$ , respectively, i.e., [18, Eqs. (7.39)–(7.40)]

$$B_{\tau'}^{(1)} = \frac{\int_{-\infty}^{+\infty} \tau' S_{\tau'}(\tau') d\tau'}{\int_{-\infty}^{+\infty} S_{\tau'}(\tau') d\tau'} = -\frac{1}{2\pi j} \cdot \left. \frac{\dot{r}_{HH}(\nu')}{r_{HH}(\nu')} \right|_{\nu'=0} \quad (\text{B.51})$$

and

$$B_{\tau'}^{(2)} = \sqrt{\frac{\int_{-\infty}^{+\infty} (\tau' - B_{\tau'}^{(1)})^2 S_{\tau'}(\tau') d\tau'}{\int_{-\infty}^{+\infty} S_{\tau'}(\tau') d\tau'}} = \frac{1}{2\pi} \sqrt{\left(\frac{\dot{r}_{HH}(\nu')}{r_{HH}(\nu')}\right)^2 - \frac{\ddot{r}_{HH}(\nu')}{r_{HH}(\nu')}} \Bigg|_{\nu'=0} \quad (\text{B.52})$$

where  $\dot{r}_{HH}(\nu')$  and  $\ddot{r}_{HH}(\nu')$  are the first and second time derivative of the FCF  $r_{HH}(\nu')$  w.r.t. the variable  $\nu'$ . The frequency separation interval  $\nu' = B_C$  which fulfils the condition  $|r_{HH}(B_C)| = |r_{HH}(0)|/2$  is called coherence bandwidth. The coherence bandwidth  $B_C$  of the channel is also approximately the reciprocal of the delay spread  $B_{\tau'}^{(2)}$ , i.e.,  $B_C \approx 1/B_{\tau'}^{(2)}$  [18, p. 350].

## V. NUMERICAL RESULTS

In this section, we illustrate how the UWA channel model behaves in non-isovelocity ocean environments. The main objective is to show the influence of the non-isovelocity condition on the statistical properties of the UWA channel model. The results are compared with those of the isovelocity UWA channel models presented in [5, 32].

In our simulation setup, we set the carrier frequency  $f_c$  to 10 kHz and assume that the transmitter  $T_x$  and the receiver  $R_x$  are moving at the same speed of 3 m/s. This results in equal maximum Doppler frequencies of  $f_{\max}^T = f_{\max}^R = 20$  Hz. The transmitter  $T_x$  and the receiver  $R_x$  are moving in opposite directions determined by the AOMs  $\alpha_v^T = 180^\circ$  and  $\alpha_v^R = 0^\circ$ . The position parameters of the transmitter  $T_x$  and receiver  $R_x$  are set as follows:  $y_1^T = 35$  m,  $y_2^T = 65$  m,  $y_1^R = 55$  m,  $y_2^R = 45$  m, and  $D = 5$  km. The shallow water depth is assumed to be  $h = 100$  m with different number of layers  $K$  and consequently different layer depth  $\Delta y$ . For instance, if  $K = 10$  layers is considered in the ocean water, this results in the layer depth of  $\Delta y = h/K = 10$  m. With reference to (B.3), the SSP is modeled as  $c_k = c_s + g \cdot k \cdot \Delta y = 1500 + 4 \cdot k$  (for  $k = 1, 2, \dots, 10$ , if  $K = 10$ ) in which the speed gradient  $g$  is set to  $0.4 \text{ s}^{-1}$ . In our simulation setup, we have considered nine macro-eigenrays, including one LOS macro-eigenray, four DA macro-eigenrays, and four UA macro-eigenrays by assuming  $N_S = N_B = 2$ . The mean values  $\mu_{sb(k_T)}^{\text{DA}}$  of the AOIs  $\varphi_{sbn(k_T)}^{\text{DA}}$  (if  $K = 10$ ) associated with the DA micro-eigenrays are chosen as  $\mu_{10(k_T)}^{\text{DA}} = 84.4^\circ$  and  $\mu_{11(k_T)}^{\text{DA}} = \mu_{21(k_T)}^{\text{DA}} = 79.5^\circ$ , and  $\mu_{22(k_T)}^{\text{DA}} = 79.8^\circ$ . Similarly, for UA micro-eigenrays, the mean values  $\mu_{bs(k_T)}^{\text{UA}}$  of the AOIs  $\varphi_{bsm(k_T)}^{\text{UA}}$  are set as follows:  $\mu_{10(k_T)}^{\text{UA}} = \mu_{21(k_T)}^{\text{UA}} = 79.7^\circ$  and  $\mu_{11(k_T)}^{\text{UA}} = \mu_{22(k_T)}^{\text{UA}} = 78.6^\circ$ . The optimization algorithm for obtaining the mean values  $\mu_{sb(k_T)}^{\text{DA}}$  and  $\mu_{bs(k_T)}^{\text{UA}}$  has been explained in

Appendix C. The remaining parameters of the UWA channel model are listed in the third column of Table B.1.

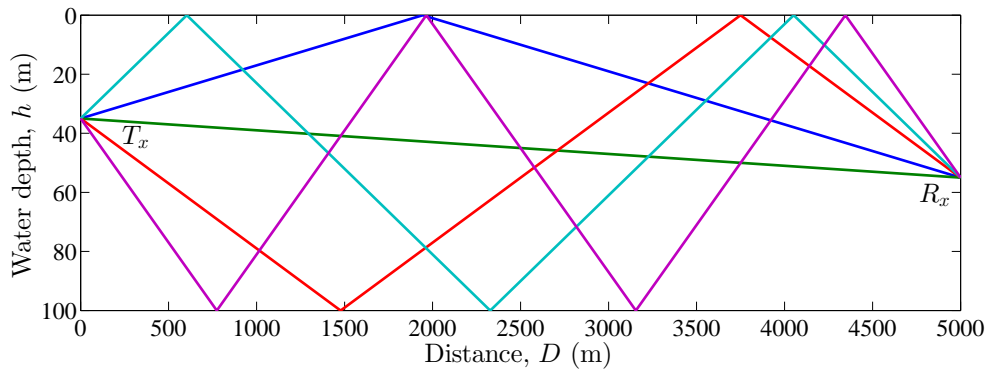


Figure B.6: LOS and DA macro-eigenrays in an *isovelocity* ocean environment ( $c_s = 1500$  m/s).

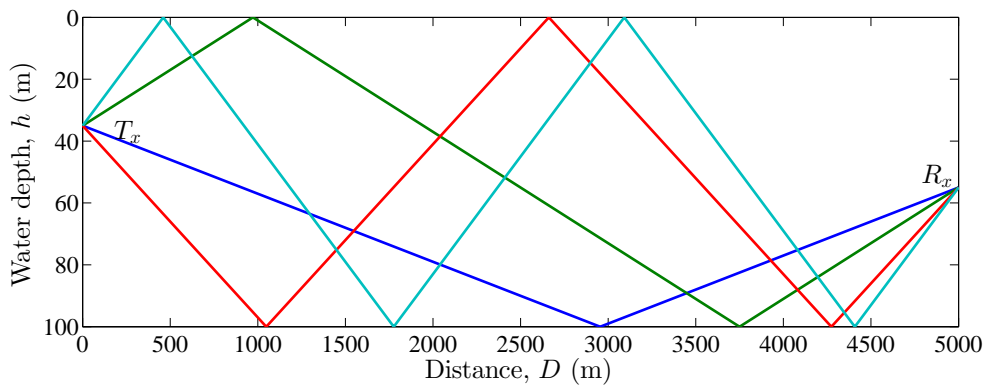


Figure B.7: UA macro-eigenrays in an isovelocity ocean environment ( $c_s = 1500$  m/s).

Figs. B.6 and B.7 display the propagation of acoustic waves in an isovelocity UWA ocean environment for LOS and DA macro-eigenrays (Fig. B.6) and UA macro-eigenrays (Fig. B.7), respectively. As can be seen in these figures, the acoustic rays travel along straight lines. However, this phenomenon differs from the propagation in non-isovelocity environments where the acoustic rays bend in the water as illustrated in Figs. B.8 and B.9. In these two figures, two different parameter sets are assumed. Fig. B.8 assumes  $K = 10$  layers and  $g = 0.4 \text{ s}^{-1}$ , and Fig. B.9 assumes  $K = 30$  layers and  $g = 0.2 \text{ s}^{-1}$ . As can be seen from these two figures, by increasing the number of layers  $K$  and decreasing the gradient  $g$  eigenrays bend smoothly and realistically. Moreover, by decreasing the gradient  $g$  from  $0.4 \text{ s}^{-1}$  to  $0.2 \text{ s}^{-1}$ , the overlap of eigenrays decreases. Note that eigenrays are more distinguishable in reality as the x-axis, in this scenario, should be 50 times larger than

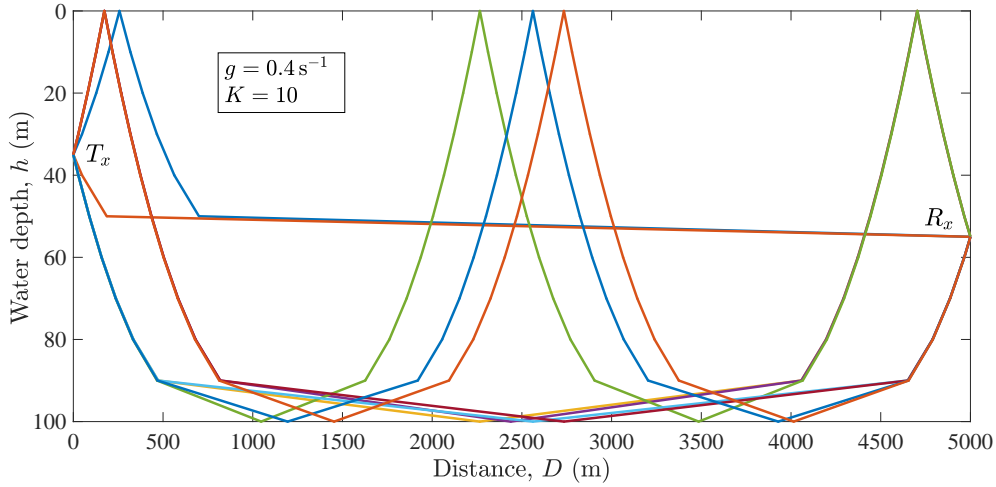


Figure B.8: Macro-eigenrays in a *non-isovelocity* ocean environment modeled by  $K = 10$  layers and  $g = 0.4 \text{ s}^{-1}$  ( $c_s = 1500 \text{ m/s}$ ).

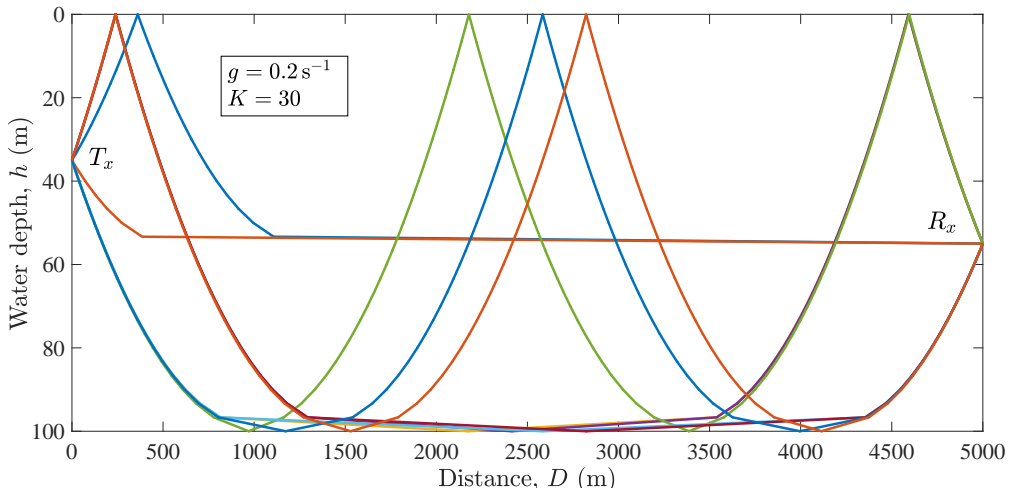


Figure B.9: Macro-eigenrays in a *non-isovelocity* ocean environment modeled by  $K = 30$  layers and  $g = 0.2 \text{ s}^{-1}$  ( $c_s = 1500 \text{ m/s}$ ).

y-axis.

Fig. B.10 depicts a comparison between the absolute value of the normalized temporal ACF  $r_{HH}(\tau)$  of the proposed non-isovelocity UWA channel model for the gradient  $g = 0.4 \text{ s}^{-1}$  and different numbers of layers  $K = 6, 10, 20,$  and  $30$  with that of the isovelocity channel model presented in [5, 32]. As can be observed in Fig. B.10, the temporal ACF of the non-isovelocity UWA channel model decays faster than the isovelocity one. The time interval  $\tau = T_C$  which fulfils the condition  $|r_{HH}(T_C)| = |r_{HH}(0)|/2$  is called coherence time [18, p. 351]. Thus, it can be observed from this figure that the coherence time  $T_C$  is significantly smaller in the non-isovelocity model than that of the isovelocity one. The same phenomena can be observed in Fig. B.11 where the gradient  $g$  equals  $0.2 \text{ s}^{-1}$ . As can be seen, there is a

good match between the theoretical results and the experimental simulation results. The experimental simulation results have been obtained from the simulation of a single sample function of the TVCTF  $H(f', t)$  of the UWA channel model presented in (B.35) by fixing the random phases  $\theta_0$ ,  $\theta_{sbm}^{DA}$ , and  $\theta_{bsm}^{UA}$ .

The effect of the gradient  $g$  on the correlation functions of the UWA channel model has been examined with two different values for the gradient  $g$  of  $0.2 \text{ s}^{-1}$  and  $0.4 \text{ s}^{-1}$ . The obtained numerical results, presented in Figs. B.10 and B.11 show that the correlation functions correspond to the a large gradient ( $g = 0.4 \text{ s}^{-1}$ ) decay rapidly compared to the small one ( $g = 0.2 \text{ s}^{-1}$ ). The reason of decaying rapidly for the greater parameter  $g$  is the influence of this parameter on the AOAs (makes them more similar) and channel gains (causes a increase of the total distances that eigenrays travel between the transmitter and receiver) of the eigenrays.

By comparing the graphs in Fig. B.10, we can conclude that the approximate temporal ACF  $r_{HH}^{AP}(\tau)$  (see (B.42)) fits to the exact results obtained by solving (B.41) numerically for  $\kappa = 160$ . From the evaluation results of the error function  $E(\kappa)$  (see (B.47)) illustrated in Fig. B.12, we can conclude that the parameter  $\kappa$  of the von Mises distribution has to be larger than 150 to keep  $E(\kappa)$  below 0.008; otherwise, we have to compute the temporal ACF  $r_{HH}(\tau)$  of the proposed UWA channel model by solving the integral in (B.41) numerically. Thus, in the simulation setup, the parameter  $\kappa$  is set to 160.

Comparison between the absolute value of the normalized FCFs  $r_{HH}(\nu')$  of the proposed UWA channel in non-isovelocity ocean environments and that of the isovelocity case for  $g = 0.4 \text{ s}^{-1}$  and different values of the layer  $K \in \{6, 10, 20, \text{ and } 30\}$  is illustrated in Figs. B.13 (where  $g = 0.4 \text{ s}^{-1}$ ) and Fig. B.14 (where  $g = 0.2 \text{ s}^{-1}$ ). As can be seen in these figures, the FCFs  $r_{HH}(\nu')$  of the non-isovelocity case decay faster than that of the isovelocity one with increasing values of the frequency separation  $\nu'$ . With reference to these figure, the coherence bandwidth  $B_C$  of the non-isovelocity model is notably smaller than that of the isovelocity one. Figs. B.13 and B.14 also demonstrate that the experimental simulation results of the FCF match very well with the theoretical results.

Converging correlation functions depends on the number of layers, SSP, and the water depth. In our numerical results assuming that the water depth  $h = 100 \text{ m}$ , correlation functions, presented in Figs. B.10–B.14 are very similar to each other for higher values of the number of layers  $K$  (here  $K = 20$  and  $K = 30$ ). This phenomena is more visible for the FCFs.

The PDPs  $S_{\tau'}(\tau')$  of the UWA channel model for isovelocity and non-isovelocity (for  $K = 10$ ) ocean environments have been shown in Figs. B.15 and B.16, respec-

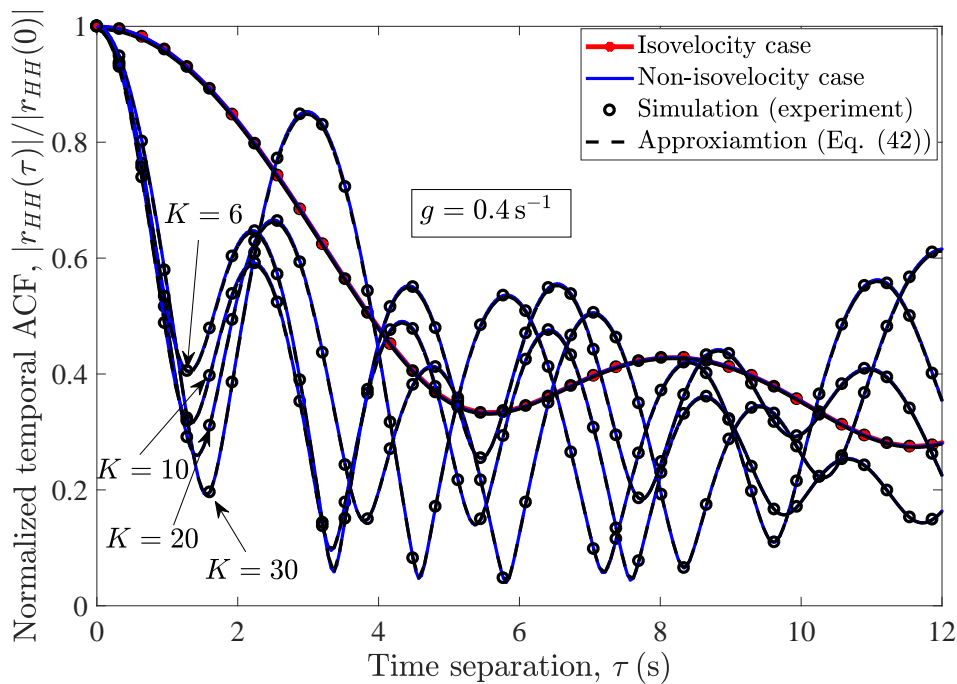


Figure B.10: Absolute value of the normalized temporal ACF  $|r_{HH}(\tau)|/|r_{HH}(0)|$  of the UWA channel model ( $\kappa = 160$ ).

tively. It needs to be mentioned that in Figs. B.15 and B.16 only macro-eigenrays, obtained by averaging over microeigenrays, are considered. From the inspection of Figs. B.15 and B.16, we can conclude that in non-isovelocity environments the strongest ray is not necessarily the first ray which arrives at the receiver.

## VI. COMPARISON WITH MEASUREMENT DATA

In this section, the main theoretical results introduced in Sections III and IV are verified by measurement data. The comparison is assessed in terms of the FCF  $r_{HH}(\nu')$ , PDP  $S_{\tau'}(\tau')$ , average delay  $B_{\tau'}^{(1)}$ , delay spread  $B_{\tau'}^{(2)}$ , and the coherence bandwidth  $B_C$  of the UWA channel.

The experimental data, which was first presented in [33], was collected near the New Jersey shore in May 2009 by a team from Naval Research LAB. The water depth was about 80 m and the fixed transmitter was about 46 m below the surface float ( $y_1^T = 46$  m). The fixed receiver was located at 29 m depth ( $y_1^R = 29$  m). The receiver was 2000 m away from the transmitter. The UWA channel measurements were performed at a carrier frequency of 17 kHz and a signal bandwidth of 4 kHz. More details regarding the communication system, the signals that have been sent and received, and the type of equipment (transducer and hydrophone) are available

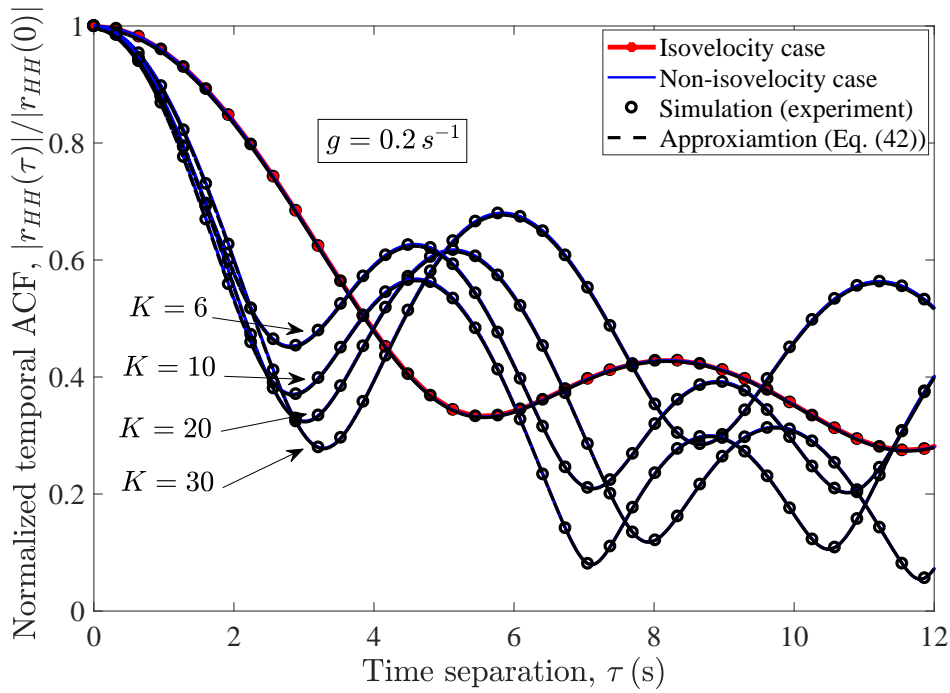


Figure B.11: Absolute value of the normalized temporal ACF  $|r_{HH}(\tau)|/|r_{HH}(0)|$  of the UWA channel model ( $g = 0.2 \text{ s}^{-1}$  and  $\kappa = 160$ ).

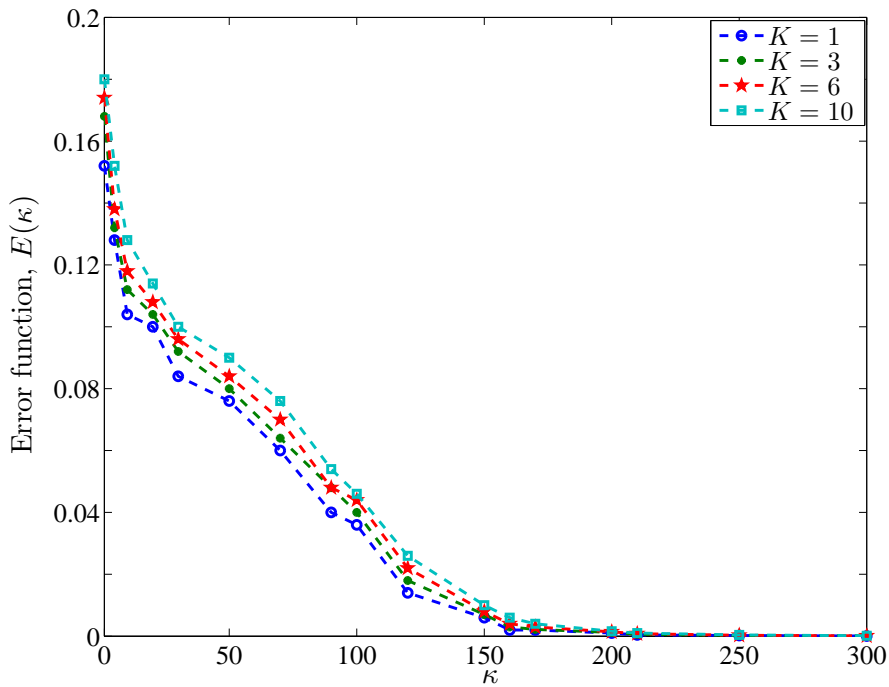


Figure B.12: Evaluation of the error function  $E(\kappa)$  in (B.47) for the various values of the number of layers  $K$ .



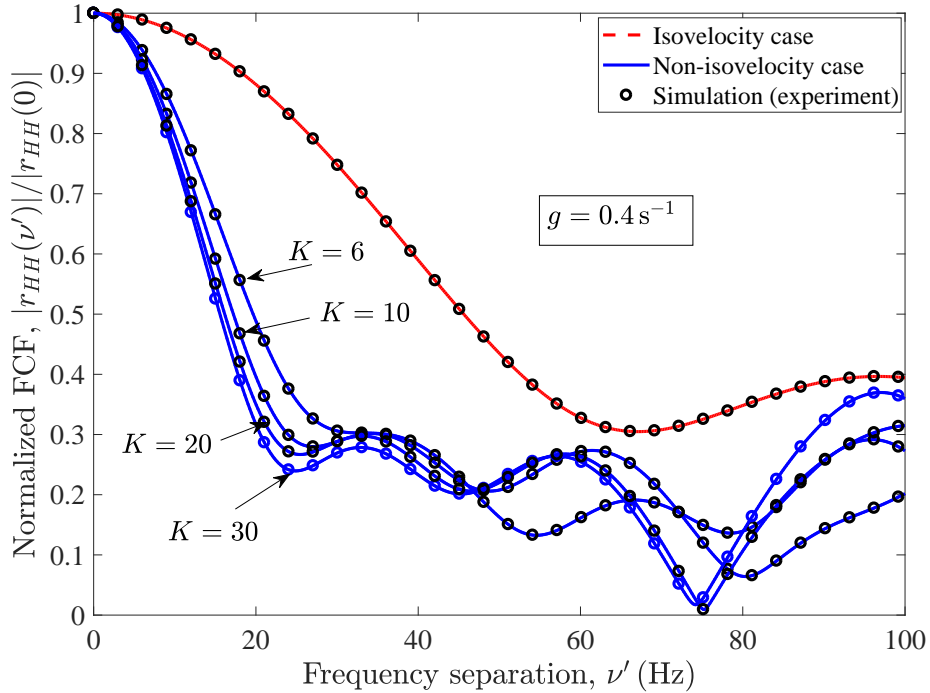


Figure B.13: Absolute value of the normalized FCF  $|r_{HH}(\nu')|/|r_{HH}(0)|$  of the UWA channel model.

in [33].

The SSP of the New Jersey shore has been reported in [4]. The model parameters based on the measurement scenario have been set as follows. The number of layers  $K$  has been set to 16 with the corresponding layer width of  $\Delta y = 5$  m. Thus, the transmitter and receiver are located in the layers with layer numbers  $k_T = 10$  and  $k_R = 6$ , respectively. The quantized form of the given SSP, obtained by means of the interpolation technique in [21], is illustrated in Fig. B.17. The values of the other channel model parameters describing the measurement scenario are listed in the fourth column of Table B.1.

The measured TVCIR  $\check{h}(\tau', t)$ , illustrated in Fig. B.18, has been obtained by  $M = 50$  samples in the time domain over a time range of  $T_{\text{mes}} = 20$  s. Thus, the sampling interval  $\Delta t$  in the time domain is equal to  $\Delta t = T_{\text{mes}}/M = 0.4$  s. In the delay domain, the measurement equipment allows a path resolution of  $\Delta\tau' = 0.125$  ms. The number of samples in the delay domain was  $L = 100$  allowing to measure propagation paths with a maximum path delay of  $\tau'_{\text{max}} = 12.5$  ms. In other words, the TVCIR  $\check{h}(\tau', t)$  has been measured at discrete time instances  $t_m = m\Delta t \in [0, T_{\text{mes}})$ ,  $m = 0, 1, \dots, M-1$ , and at discrete delay intervals  $\tau'_l = l\Delta\tau' \in [0, \tau'_{\text{max}})$ ,  $l = 0, 1, \dots, L-1$ . Consequently, the measured TVCIR  $\check{h}(\tau', t)$  can be

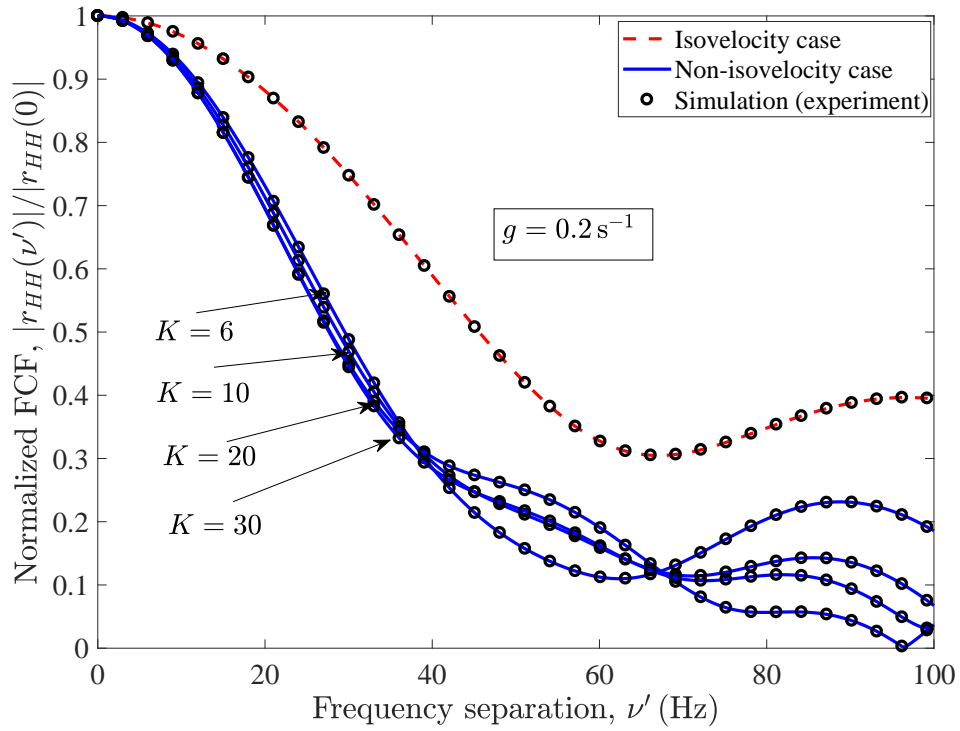


Figure B.14: Absolute value of the normalized FCF  $|r_{HH}(\nu')|/|r_{HH}(0)|$  of the UWA channel model ( $g = 0.2 \text{ s}^{-1}$  and  $\kappa = 160$ ).

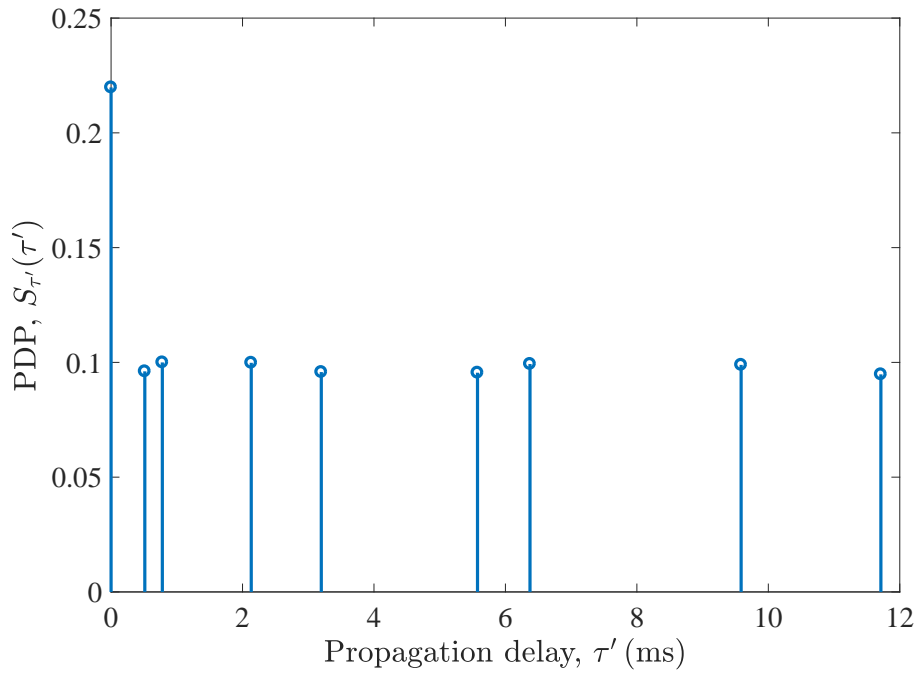


Figure B.15: The PDP  $S_{\tau'}(\tau')$  of the UWA channel model for the isovelocity case ( $c_s = 1500 \text{ m/s}$ ) by considering only macro-eigenrays.

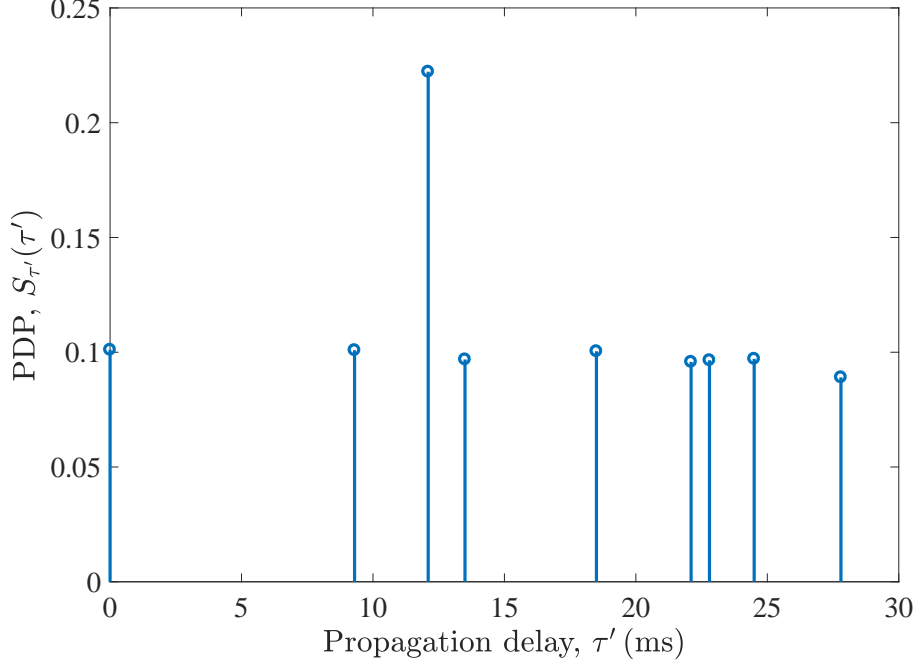


Figure B.16: The PDP  $S_{\tau'}(\tau')$  of the UWA channel model for the non-isovelocity case by considering only macro-eigenrays.

represented as a discrete TVCIR  $\check{h}[\tau'_l, t_m]$ .

As the eigenrays with delays larger than 12.5 ms are not observed in the measurement data (see Fig.B.18), we have to consider only double bounce scattering (i.e.,  $N_S = N_B = 1$ ) on the surface and bottom of the ocean. Thus, the parameters  $\eta_S$  and  $\eta_B$  are set to 0.5, i.e.,  $\eta_S = \eta_B = 0.5$ . The discrete TVCTF  $\check{H}[f'_q, t_m]$  of the measurement data can be obtained by taking the discrete Fourier transform of the TVCIR  $\check{h}[\tau'_l, t_m]$  with respect to delays  $\tau'_l$ . The discrete frequencies  $f'_q$  are given by  $f'_q = -B/2 + q\Delta f' \in [-B/2, B/2)$ ,  $q = 0, 1, \dots, Q - 1$  and  $B$  denotes the measurement bandwidth. The discrete FCF  $\check{r}_{HH}[\nu']$  can be obtained from the discrete TVCTF  $\check{H}[f'_q, t_m]$  as follows

$$\check{r}_{HH}[\nu'] = \frac{1}{M} \sum_{m=0}^{M-1} \check{H}[f'_q, t_m] \check{H}^*[f'_q + \nu', t_m]. \quad (\text{B.53})$$

Note that a deterministic simulation model can be computed from the realization of a sample function of the TVCTF  $H(f', t)$  of the UWA channel model presented in (B.35) by fixing the random AOI  $\varphi_{sbn}^{\text{DA}}$  and  $\varphi_{bsm}^{\text{UA}}$  and the random phases  $\theta_0$ ,  $\theta_{sbn}^{\text{DA}}$ , and  $\theta_{bsm}^{\text{UA}}$ . For parametrization of the deterministic simulation model, we apply the  $L_p$ -norm method (LPNM) [18, pp.189]. The application of the LPNM on the given

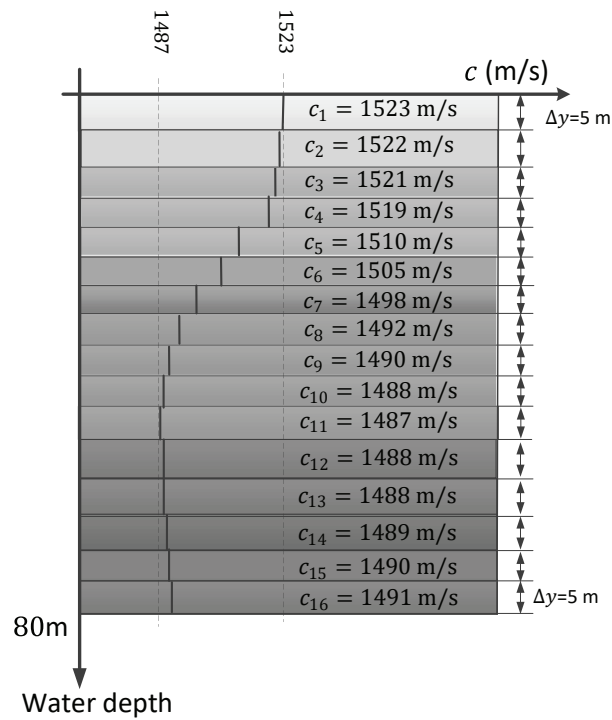


Figure B.17: The quantized form of the given SSP.

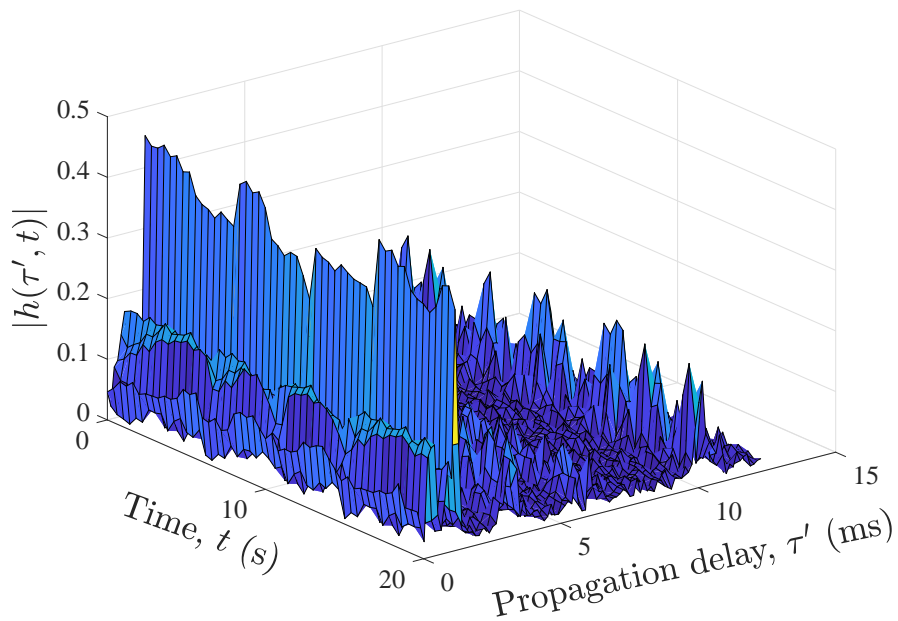


Figure B.18: Absolute value of the measured TVCIR  $|h(\tau', t)|$ .

parametrization problem requires the minimization of the following error function

$$E_p(\varphi) = \left[ \frac{1}{\nu'_{\max}} \int_0^{\nu'_{\max}} |\check{r}_{HH}[\nu'] - \tilde{r}_{HH}(\nu')|^p d\nu' \right]^{\frac{1}{p}} \quad (\text{B.54})$$

where  $\nu'_{\max}$  defines an appropriate frequency-lag interval  $[0, \nu'_{\max}]$  over which the approximation of  $\check{r}_{HH}(\nu')$  is of importance. The function  $\tilde{r}_{HH}(\nu')$  is the FCF of the deterministic simulation model. By minimizing of  $E_p(\varphi)$  using numerical optimization techniques, we obtain a set of optimized values of the AOIs  $\varphi$  and the parameters  $N_{s\check{b}}$  and  $M_{b\check{s}}$ .

The discrete PDP  $\check{S}_{\tau'}[\tau'_l]$  can be obtained by computing the inverse Fourier transform of the discrete FCF  $\check{r}_{HH}[\nu']$  with respect to  $\nu'$ . The average delay  $\check{B}_{\tau'}^{(1)}$  and the delay spread  $\check{B}_{\tau'}^{(2)}$  of the measured channel can be computed by replacing the continuous PDP  $S_{\tau'}(\tau')$  in (B.51) and (B.52), respectively, by the discrete PDP  $\check{S}_{\tau'}[\tau'_l]$ . The coherence bandwidth  $\check{B}_c$  of the measured channel can be obtained from the delay spread  $\check{B}_{\tau'}^{(2)}$  by using  $\check{B}_c \approx 1/\check{B}_{\tau'}^{(2)}$  (see Section IV-C). The Rice factor  $c_R$  of the measured TVCIR  $\check{h}[\tau'_l, t_m]$  is obtained by using the moment method presented in [10].

Table B.2 provides a comparison between the proposed channel model and the real-world UWA channel in terms of the characteristic quantities including the average delay, delay spread and the coherence bandwidth, where  $\check{B}_{\tau'}^{(1)}$  ( $\check{B}_{\tau'}^{(1)}$ ) and  $\check{B}_{\tau'}^{(2)}$  ( $\check{B}_{\tau'}^{(2)}$ ) denote the average delay and the delay spread of the simulation model (measured UWA channel), respectively. The quantity  $\check{B}_c$  ( $\check{B}_c$ ) is the coherence bandwidth of the simulation model (measured UWA channel). As can be seen in Table B.2, a good agreement has been achieved between the simulation model and the measured UWA channel w.r.t. the aforementioned characteristic quantities.

Fig. B.19 illustrates the FCF  $\check{r}_{HH}[\nu']$  of the measured UWA channel in comparison with FCF  $\tilde{r}_{HH}(\nu')$  of the simulation model. The discrete FCF  $\check{r}_{HH}[\nu']$  is computed by using (B.53). The values of the simulation model parameters are defined in the fourth column of Table B.1. This figure shows that a good fitting between the simulation model and the measured channel has been obtained. The PDP  $\check{S}_{\tau'}(\tau')$  of the measured channel and PDP  $\tilde{S}_{\tau'}(\tau')$  of the simulation model are shown in Figs. B.20 and B.21, respectively.

## VII. CONCLUSION

In this paper, a new geometry-based UWA channel model has been developed under the assumption that the ocean surface and bottom are rough. In addition, the ocean

Table B.2: Characteristic quantities of the measured UWA channel and the corresponding simulation model.

Characteristic quantities	Measured UWA channel	Simulation model
Average delay	$\check{B}_{\tau'}^{(1)} = 3$ ms	$\tilde{B}_{\tau'}^{(1)} = 3.05$ ms
Delay spread	$\check{B}_{\tau'}^{(2)} = 3.3$ ms	$\tilde{B}_{\tau'}^{(2)} = 3.304$ ms
Coherence bandwidth	$\check{B}_C \approx 303$ Hz	$\tilde{B}_C \approx 300$ Hz

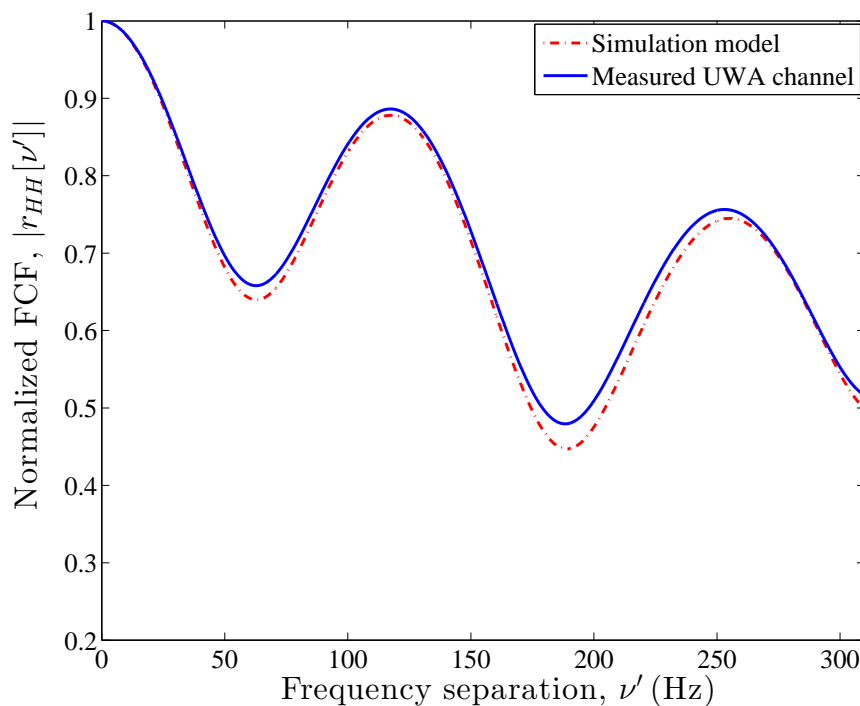


Figure B.19: The absolute value of the normalized FCF of the measured UWA channel compared to that of the simulation model.

water is assumed to be non-isovelocity. The influence of the non-isovelocity propagation conditions on the statistical properties of the UWA channel has been studied. The numerical results show that the non-isovelocity condition has a noticeable impact on the properties of the UWA channel model. For instance, the coherence bandwidth and the coherence time of the non-isovelocity UWA channel model are considerably smaller than those of the isovelocity channel model. Moreover, it has been shown that by taking these conditions into account, the UWA channel model becomes more realistic. The validity of the main analytical results has been confirmed by measurement data.

B

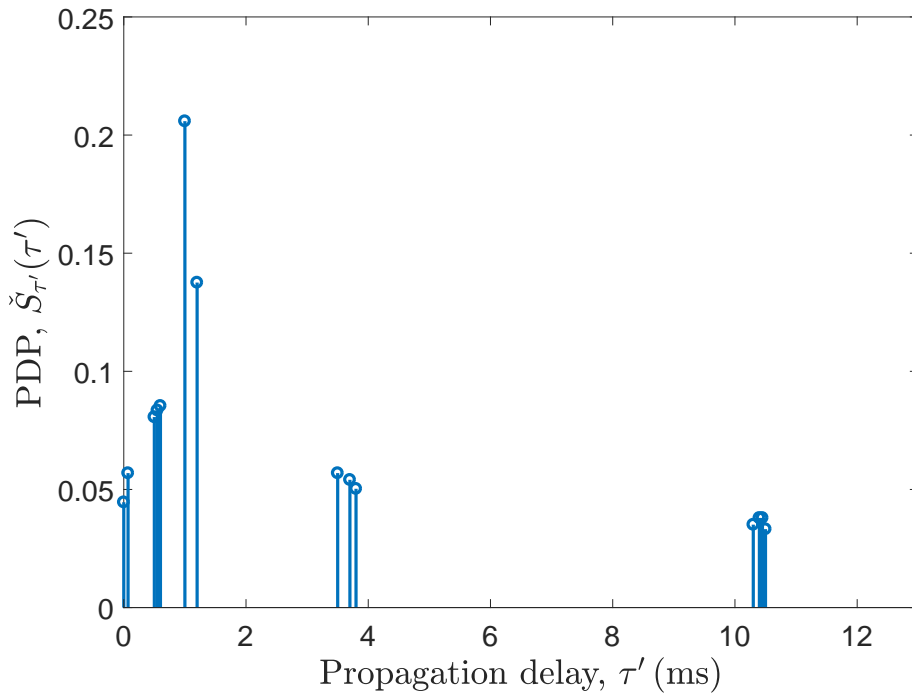


Figure B.20: The PDP  $\check{S}_{\tau'}(\tau')$  of the measured UWA channel.

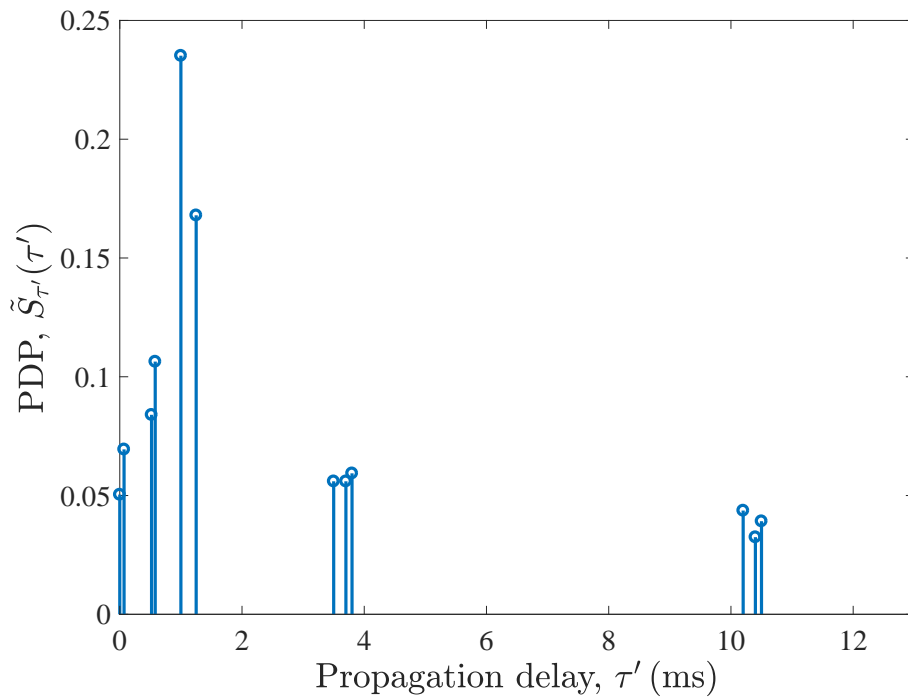


Figure B.21: The PDP  $\check{S}_{\tau'}(\tau')$  of the simulation model.

**APPENDIX A: THE TOTAL DISTANCES  $D_{s\check{b}n}^{\text{DA}}$  AND  $D_{b\check{s}m}^{\text{UA}}$  AND PROPAGATION DELAYS  $\tau'_{s\check{b}n}{}^{\text{DA}}$  AND  $\tau'_{b\check{s}m}{}^{\text{UA}}$**

The total distances  $D_{s\check{b}n}^{\text{DA}}$  and  $D_{b\check{s}m}^{\text{UA}}$  which the DA and UA micro-eigenrays travel from  $T_x$  to  $R_x$  given  $(s, \check{b})$  and  $(\check{s}, b)$  surface-bottom interactions, respectively, can be computed as

$$\begin{aligned}
 D_{s\check{b}n}^{\text{DA}} = & (s - \check{b}) \left[ \frac{\Delta y_1^T}{\cos(\varphi_{s\check{b}n(k_T)}^{\text{DA}})} + \sum_{k=1}^{k_T-1} \frac{\Delta y}{\cos(\varphi_{s\check{b}n(k)}^{\text{DA}})} \right] \\
 & + (\check{b} - s + 1) \left[ \frac{\Delta y_2^T}{\cos(\varphi_{s\check{b}n(k_T)}^{\text{DA}})} + \sum_{k=k_T+1}^K \frac{\Delta y}{\cos(\varphi_{s\check{b}n(k)}^{\text{DA}})} \right] \\
 & + \sum_{k=1}^K \frac{(s + \check{b} - 1)\Delta y}{\cos(\varphi_{s\check{b}n(k)}^{\text{DA}})} + \sum_{k=1}^{k_R-1} \frac{\Delta y}{\cos(\varphi_{s\check{b}n(k)}^{\text{DA}})} + \frac{\Delta y_1^R}{\cos(\varphi_{s\check{b}n(k_R)}^{\text{DA}})} \quad (\text{B.55})
 \end{aligned}$$

and

$$\begin{aligned}
 D_{b\check{s}m}^{\text{UA}} = & (b - \check{s}) \left[ \frac{\Delta y_2^T}{\cos(\varphi_{b\check{s}m(k_T)}^{\text{UA}})} + \sum_{k=k_T+1}^K \frac{\Delta y}{\cos(\varphi_{b\check{s}m(k)}^{\text{UA}})} \right] \\
 & + (\check{s} - b + 1) \left[ \frac{\Delta y_1^T}{\cos(\varphi_{b\check{s}m(k_T)}^{\text{UA}})} + \sum_{k=1}^{k_T-1} \frac{\Delta y}{\cos(\varphi_{b\check{s}m(k)}^{\text{UA}})} \right] \\
 & + \sum_{k=1}^K \frac{(b + \check{s} - 1)\Delta y}{\cos(\varphi_{b\check{s}m(k)}^{\text{UA}})} + \sum_{k=k_R+1}^K \frac{\Delta y}{\cos(\varphi_{b\check{s}m(k)}^{\text{UA}})} + \frac{\Delta y_2^R}{\cos(\varphi_{b\check{s}m(k_R)}^{\text{UA}})}. \quad (\text{B.56})
 \end{aligned}$$

The propagation delays  $\tau'_{s\check{b}n}{}^{\text{DA}}$  and  $\tau'_{b\check{s}m}{}^{\text{UA}}$  can be expressed as

$$\begin{aligned}
 \tau'_{s\check{b}n}{}^{\text{DA}} = & (s - \check{b}) \left[ \frac{\Delta y_1^T}{c_{k_T} \cos(\varphi_{s\check{b}n(k_T)}^{\text{DA}})} + \sum_{k=1}^{k_T-1} \frac{\Delta y}{c_k \cos(\varphi_{s\check{b}n(k)}^{\text{DA}})} \right] \\
 & + (\check{b} - s + 1) \left[ \frac{\Delta y_2^T}{c_{k_T} \cos(\varphi_{s\check{b}n(k_T)}^{\text{DA}})} + \sum_{k=k_T+1}^K \frac{\Delta y}{c_k \cos(\varphi_{s\check{b}n(k)}^{\text{DA}})} \right] \\
 & + \sum_{k=1}^K \frac{(s + \check{b} - 1)\Delta y}{c_k \cos(\varphi_{s\check{b}n(k)}^{\text{DA}})} + \sum_{k=1}^{k_R-1} \frac{\Delta y}{c_k \cos(\varphi_{s\check{b}n(k)}^{\text{DA}})} + \frac{\Delta y_1^R}{c_{k_R} \cos(\varphi_{s\check{b}n(k_R)}^{\text{DA}})} \quad (\text{B.57})
 \end{aligned}$$

for  $s = 1, 2, \dots, N_S$ , and  $\check{b} \in [s - 1, s]$  and

$$\tau'_{b\check{s}m}{}^{\text{UA}} = (b - \check{s}) \left[ \frac{\Delta y_2^T}{c_{k_T} \cos(\varphi_{b\check{s}m(k_T)}^{\text{UA}})} + \sum_{k=k_T+1}^K \frac{\Delta y}{c_k \cos(\varphi_{b\check{s}m(k)}^{\text{UA}})} \right]$$

$$\begin{aligned}
 & + (\check{s} - b + 1) \left[ \frac{\Delta y_1^T}{c_{k_T} \cos(\varphi_{b\check{s}m(k_T)}^{\text{UA}})} + \sum_{k=1}^{k_T-1} \frac{\Delta y}{c_k \cos(\varphi_{b\check{s}m(k)}^{\text{UA}})} \right] \\
 & + \sum_{k=1}^K \frac{(b + \check{s} - 1)\Delta y}{c_k \cos(\varphi_{b\check{s}m(k)}^{\text{UA}})} + \sum_{k=k_R+1}^K \frac{\Delta y}{c_k \cos(\varphi_{b\check{s}m(k)}^{\text{UA}})} + \frac{\Delta y_2^R}{c_{k_R} \cos(\varphi_{b\check{s}m(k_R)}^{\text{UA}})}
 \end{aligned} \tag{B.58}$$

for  $b = 1, 2, \dots, N_B$ , and  $\check{s} \in [b - 1, b]$ .

### APPENDIX B: DERIVATION OF (B.42)

This appendix presents the proof of (B.42). First, we replace the AOIs  $\varphi_{sb\check{n}(k_R)}^{\text{DA}}$  and  $\varphi_{b\check{s}m(k_R)}^{\text{UA}}$  in (B.33) and (B.34), respectively, by equivalent ones obtained by using (B.8) and (B.9). Then, by means of trigonometric transformations, such as  $\sin(a \pm b) = \sin(a) \cos(b) \pm \cos(a) \sin(b)$  and  $\cos(a \pm b) = \cos(a) \cos(b) \mp \sin(a) \sin(b)$ , we can express  $f_{sb\check{n}}^{\text{DA}}$  and  $f_{b\check{s}m}^{\text{UA}}$  as

$$\begin{aligned}
 f_{sb\check{n}}^{\text{DA}} & = f_{\max}^T \left[ \sin \varphi_{sb\check{n}(k_T)}^{\text{DA}} \cos \alpha_v^T - \cos \varphi_{sb\check{n}(k_T)}^{\text{DA}} \sin \alpha_v^T \right] \\
 & - f_{\max}^R \left[ (c_{k_R}/c_{k_T}) \sin \varphi_{sb\check{n}(k_T)}^{\text{DA}} \cos \alpha_v^R - \cos \varphi_{sb\check{n}(k_T)}^{\text{DA}} \sin \alpha_v^R \right]
 \end{aligned} \tag{B.59}$$

$$\begin{aligned}
 f_{b\check{s}m}^{\text{UA}} & = f_{\max}^T \left[ \sin \varphi_{b\check{s}m(k_T)}^{\text{UA}} \cos \alpha_v^T - \cos \varphi_{b\check{s}m(k_T)}^{\text{UA}} \sin \alpha_v^T \right] \\
 & - f_{\max}^R \left[ (c_{k_R}/c_{k_T}) \sin \varphi_{b\check{s}m(k_T)}^{\text{UA}} \cos \alpha_v^R - \cos \varphi_{b\check{s}m(k_T)}^{\text{UA}} \sin \alpha_v^R \right].
 \end{aligned} \tag{B.60}$$

The closed-form approximation for the temporal ACF  $r_{HH}(\tau)$  in (B.41) can be derived by replacing the random gains  $c_{sb\check{n}}^{\text{DA}}(c_{b\check{s}m}^{\text{UA}})$ , which are functions of random AOIs  $\varphi_{sb\check{n}(k_T)}^{\text{DA}}(\varphi_{b\check{s}m(k_T)}^{\text{UA}})$ , by the gains  $c_{sb}^{\text{DA}}(c_{b\check{s}}^{\text{UA}})$ . To compute the gains  $c_{sb}^{\text{DA}}(c_{b\check{s}}^{\text{UA}})$ , the random AOIs  $\varphi_{sb\check{n}(k_T)}^{\text{DA}}(\varphi_{b\check{s}m(k_T)}^{\text{UA}})$  have to be replaced by their mean values  $\mu_{sb\check{n}(k_T)}^{\text{DA}}(\mu_{b\check{s}(k_T)}^{\text{UA}})$ . Then, by substituting (B.59) and (B.60) in (B.41), the temporal ACF  $r_{HH}(\tau)$  can be written as

$$\begin{aligned}
 r_{HH}(\tau) & = c_0^2 e^{j2\pi f_0 \tau} \\
 & + \frac{1}{2\pi I_0(\kappa)} \left[ \sum_{s=1}^{N_S} \sum_{\check{b}=s-1}^s [c_{s\check{b}}^{\text{DA}}]^2 \sum_{n=1}^{N_{s\check{b}}} \int_0^{2\pi} e^{[x_{s\check{b}}^{\text{DA}} \cos \varphi_{s\check{b}n(k_T)}^{\text{DA}} + y_{s\check{b}}^{\text{DA}} \sin \varphi_{s\check{b}n(k_T)}^{\text{DA}}]} d\varphi_{s\check{b}n(k_T)}^{\text{DA}} \right. \\
 & \left. + \sum_{b=1}^{N_B} \sum_{\check{s}=b-1}^b [c_{b\check{s}}^{\text{UA}}]^2 \sum_{m=1}^{M_{b\check{s}}} \int_0^{2\pi} e^{[x_{b\check{s}}^{\text{UA}} \cos \varphi_{b\check{s}m(k_T)}^{\text{UA}} + y_{b\check{s}}^{\text{UA}} \sin \varphi_{b\check{s}m(k_T)}^{\text{UA}}]} d\varphi_{b\check{s}m(k_T)}^{\text{UA}} \right].
 \end{aligned} \tag{B.61}$$

The expressions of  $x_{sb}^{\text{DA}}$ ,  $y_{sb}^{\text{DA}}$ ,  $x_{b\check{s}}^{\text{UA}}$ , and  $y_{b\check{s}}^{\text{UA}}$  represented in (B.61), can be found in

(B.43)–(50). By exploiting the equality  $\int_0^{2\pi} e^{[a \sin(c) + b \cos(c)]} dc = 2\pi I_0(\sqrt{a^2 + b^2})$  [9, Eq. (3.338-4)], (B.61) can be simplified to (B.42).

### APPENDIX C: COMPUTATION OF THE MEAN VALUES $\mu_{s\check{b}(k_T)}^{\text{DA}}$ AND $\mu_{b\check{s}(k_T)}^{\text{UA}}$

This appendix presents the approach to optimize the mean value  $\mu_{s\check{b}(k_T)}^{\text{DA}}$  and  $\mu_{b\check{s}(k_T)}^{\text{UA}}$  of the AOIs associated with DA and UA micro-eigenrays, respectively. To find the optimized values of  $\mu_{s\check{b}(k_T)}^{\text{DA}}$  and  $\mu_{b\check{s}(k_T)}^{\text{UA}}$ , we need to minimize the error function

$$E_p(\mu) = |R - D|^2 \quad (\text{B.62})$$

where the parameter  $D$  stands for the distance between  $T_x$  and  $R_x$  along the x-axis. The parameter  $R$  denotes the range of the distance that macro-eigenrays travel on the x-axis, which can be replaced by ranges  $R_{s\check{b}}^{\text{DA}}$  and  $R_{b\check{s}}^{\text{UA}}$  corresponding to DA and UA micro-eigenrays. The ranges  $R_{s\check{b}}^{\text{DA}}$  and  $R_{b\check{s}}^{\text{UA}}$  are given by

$$\begin{aligned} R_{s\check{b}}^{\text{DA}} &= (s - \check{b}) \left[ \Delta y_1^T \tan(\mu_{s\check{b}(k_T)}^{\text{DA}}) + \sum_{k=1}^{k_T-1} \Delta y \tan(\mu_{s\check{b}(k)}^{\text{DA}}) \right] \\ &+ (\check{b} - s + 1) \left[ \Delta y_2^T \tan(\mu_{s\check{b}(k_T)}^{\text{DA}}) + \sum_{k=k_T+1}^K \Delta y \tan(\mu_{s\check{b}(k)}^{\text{DA}}) \right] \\ &+ \sum_{k=1}^K (s + \check{b} - 1) \Delta y \tan(\mu_{s\check{b}(k)}^{\text{DA}}) + \sum_{k=1}^{k_R-1} \Delta y \tan(\mu_{s\check{b}(k)}^{\text{DA}}) + \Delta y_1^R \tan(\mu_{s\check{b}(k_R)}^{\text{DA}}) \end{aligned} \quad (\text{B.63})$$

$$\begin{aligned} R_{b\check{s}}^{\text{UA}} &= (b - \check{s}) \left[ \Delta y_2^T \tan(\mu_{b\check{s}(k_T)}^{\text{UA}}) + \sum_{k=k_T+1}^K \Delta y \tan(\mu_{b\check{s}(k)}^{\text{UA}}) \right] \\ &+ (\check{s} - b + 1) \left[ \Delta y_1^T \tan(\mu_{b\check{s}(k_T)}^{\text{UA}}) + \sum_{k=1}^{k_T-1} \Delta y \tan(\mu_{b\check{s}(k)}^{\text{UA}}) \right] \\ &+ \sum_{k=1}^K (b + \check{s} - 1) \Delta y \tan(\mu_{b\check{s}(k)}^{\text{UA}}) + \sum_{k=k_R+1}^K \Delta y \tan(\mu_{b\check{s}(k)}^{\text{UA}}) + \Delta y_2^R \tan(\mu_{b\check{s}(k_R)}^{\text{UA}}). \end{aligned} \quad (\text{B.64})$$

Note that the mean values  $\mu_{s\check{b}(k)}^{\text{DA}}$  ( $\mu_{b\check{s}(k)}^{\text{UA}}$ ) for  $k = 1, 2, \dots, K$  and  $k \neq k_T$ , can be obtained as functions of  $\mu_{s\check{b}(k_T)}^{\text{DA}}$  ( $\mu_{b\check{s}(k_T)}^{\text{UA}}$ ) by using (B.8) ((B.9)). In other words,  $\varphi_{s\check{b}n(k_T)}^{\text{DA}}$  and  $\varphi_{s\check{b}n(k)}^{\text{DA}}$  in (B.8) have to be replaced by  $\mu_{s\check{b}(k_T)}^{\text{DA}}$  and  $\mu_{s\check{b}(k)}^{\text{DA}}$ , respectively. Analogously,  $\varphi_{b\check{s}m(k_T)}^{\text{UA}}$  and  $\varphi_{b\check{s}m(k)}^{\text{UA}}$  in (B.9) have to be replaced by  $\mu_{b\check{s}(k_T)}^{\text{UA}}$  and  $\mu_{b\check{s}(k)}^{\text{UA}}$ , respectively.

## PAPER B: REFERENCES

- [1] A. C. Arruda, M. W. Roeckel, and J. Wakeley. A raytracing approach to underwater reverberation modeling. Technical report, Pennsylvania State University, Applied Research Laboratory, <http://www.dtic.mil/dtic/tr/fulltext/u2/a209410.pdf>, Jun. 1989.
- [2] P. A. Bello. Characterization of randomly time-variant linear channels. *IEEE Trans. Commun. syst.*, 11:360–393, December 1963.
- [3] L. M. Brekhovskikh and Y. P. Lysanov. *Fundamentals of Ocean Acoustics*. New York, NY, USA: Springer, 3rd edition, 2002.
- [4] W. Carey, J. Doutt, and L. M. Dillman. Shallow-water transmission measurements taken on the New Jersey continental shelf. Technical report, Naval Undersea Warfare Center Detachment, <http://www.dtic.mil/dtic/tr/fulltext/u2/a251417.pdf>, Apr. 1992.
- [5] M. Chitre. A high-frequency warm shallow water acoustic communications channel model and measurements. *J. Acoust. Soc. Amer.*, 122(5):2580–2586, November 2007.
- [6] H. S. Dol, M. E. G. D. Colin, M. A. Ainslie, P. A. van Walree, and J. Janmaat. Simulation of an underwater acoustic communication channel characterized by wind-generated surface waves and bubbles. *IEEE J. Ocean. Eng.*, 38(4):642–654, Oct. 2013.
- [7] P. C. Etter. Review of ocean-acoustic models. In *Proc. IEEE Oceans*, pages 1–6, Biloxi, Mississippi, USA, Oct. 2009.
- [8] P. C. Etter. Advanced applications for underwater acoustic modeling. *Advances in Acoustics and Vibration*, 2012, Article ID 214839:1–28, 2012.
- [9] I. S. Gradshteyn and I. M. Ryzhik. *Table of Integrals, Series, and Products*. Burlington: Academic Press, 7th edition, 2007.
- [10] I. S. Greenstein, D. G. Michelson, and V. Erceg. Moment-method estimation of the Ricean K-factor. *IEEE Commun. Lett.*, 3(6):175–176, Jun. 1999.
- [11] J. M. Hovem. Ray trace modeling of underwater sound propagation: Modeling and measurement methods for acoustic waves and for acoustic microdevices. In *Modeling and Measurement Methods for Acoustic Waves and for Acoustic Microdevices*, chapter 23, pages 573–598. InTech, Aug. 2013.

## PAPER B: REFERENCES

- [12] T. Jenserud and S. Ivansson. Measurements and modeling of effects of out-of-plane reverberation on the power delay profile for underwater acoustic channels. *IEEE J. Ocean. Eng.*, 40(4):807–821, Oct. 2015.
- [13] X. Lurton. *An Introduction to Underwater Acoustics: Principles and Applications*. Heidelberg, Germany: Springer, 2nd edition, 2010.
- [14] H. Medwin and C. S. Clay. *Fundamentals of acoustical oceanography*. San Diego: Academic Press, 1997.
- [15] M. Naderi, M. Pätzold, R. Hicheri, and N. Youssef. A geometry-based underwater acoustic channel model allowing for sloped ocean bottom conditions. *IEEE Trans. Wireless Commun.*, 16(4):2394–2408, Apr. 2017.
- [16] M. Naderi, M. Pätzold, and A. G. Zajić. A geometry-based channel model for shallow underwater acoustic channels under rough surface and bottom scattering conditions. In *Proc. 5th Int. Conf. Commun. and Electron. (ICCE)*, pages 112–117, DaNang, Vietnam, Jul./Aug. 2014.
- [17] R. Otnes, P. A. van Walree, and T. Jenserud. Validation of replaybased underwater acoustic communication channel simulation. *IEEE J. Ocean. Eng.*, 38:689–700, Oct. 2013.
- [18] M. Pätzold. *Mobile Fading Channels*. Chichester, U.K.: John Wiley & Sons, 2nd edition, 2011.
- [19] J. C. Peterson and M. B. Porter. Ray/beam tracing for modeling the effects of ocean and platform dynamics. *IEEE J. Ocean. Eng.*, 38(4):655–665, Oct. 2013.
- [20] M. B. Porter. The KRAKEN normal mode program (draft). Technical report, Washington, DC: Naval Res. Lab., <http://www.dtic.mil/dtic/tr/fulltext/u2/a252409.pdf>, May 1992.
- [21] M. B. Porter. The BELLHOP manual and user’s guide: Preliminary draft. Technical report, Heat, Light, and Sound Research, Inc., <http://oalib.hlsresearch.com/Rays/HLS-2010-1.pdf>, Jan. 2011.
- [22] M. B. Porter and H. P. Bucker. Gaussian beam tracing for computing ocean acoustic fields. *J. Acoust. Soc. Amer.*, 82(4):1349–1359, Oct. 1987.

## PAPER B: REFERENCES

- [23] P. Qarabaqi and M. Stojanovic. Statistical characterization and computationally efficient modeling of a class of underwater acoustic communication channels. *IEEE J. Ocean. Eng.*, 38(4):701–717, Oct. 2013.
- [24] M. Siderius and M. B. Porter. Modeling broadband ocean acoustic transmissions with time-varying sea surfaces. *J. Acoust. Soc. Amer.*, 124(1):137–150, Jul. 2008.
- [25] F.-X. Socheleau, C. Laot, and J. M. Passerieux. Stochastic replay of non-WSSUS underwater acoustic communication channels recorded at sea. *IEEE Trans. Signal Process.*, 59(10):4838–4849, Oct. 2011.
- [26] M. Stojanovic. *Acoustic (Underwater) Communications*. in Encyclopedia of Telecommunications, John G. Proakis (Ed.), New York: John Wiley & Sons, 2003.
- [27] R. J. Urick. *Principles of Underwater Sound*. Los Altos, California: Peninsula Publishing, 3rd edition, 1983.
- [28] P. A. van Walree, T. Jenserud, and M. Smedsrud. A discrete-time channel simulator driven by measured scattering functions. *IEEE J. Sel. Areas Commun.*, 26(9):1628–1637, Dec. 2008.
- [29] P. A. van Walree and R. Otnes. Ultrawideband underwater acoustic communication channels. *IEEE J. Ocean. Eng.*, 38(4):678–688, Oct. 2013.
- [30] T. C. Yang. A study of spatial processing gain in underwater acoustic communications. *IEEE J. Ocean. Eng.*, 32(3):689–709, Jul. 2007.
- [31] T. C. Yang. Toward continuous underwater acoustic communications. In *Proc. IEEE OCEANS*, pages 1–6, Quebec City, QC, Canada, Sep. 2008.
- [32] A. G. Zajić. Statistical modeling of MIMO mobile-to-mobile underwater channels. *IEEE Trans. Veh. Technol.*, 60(4):1337–1351, May 2011.
- [33] A. G. Zajić and G. F. Edelmann. Feasibility study of underwater acoustic communications between buried and bottom-mounted sensor network nodes. *IEEE J. Ocean. Eng.*, 38(1):109–116, Jan. 2013.

# Paper C

---

**Title:** A Geometry-Based Underwater Acoustic Channel Model Allowing for Sloped Ocean Bottom Conditions

**Authors:** Meisam Naderi<sup>1</sup>, Matthias Pätzold<sup>1</sup>, Rym Hicheri<sup>2</sup>, and Néji Youssef<sup>2</sup>

**Affiliation:** <sup>1</sup> Faculty of Engineering and Science, University of Agder, P.O. Box 509, 4879 Grimstad, Norway  
<sup>2</sup> Ecole Supérieure des Communications de Tunis, Ariana 2083, Tunisia

**Journal:** *IEEE Trans. Wireless Commun.*, vol. 16, no. 4, pp. 2394–2408, Apr. 2017, DOI: 10.1109/TWC.2017.2664829

**Copyright ©:** IEEE

---



## A Geometry-Based Underwater Acoustic Channel Model Allowing for Sloped Ocean Bottom Conditions

Meisam Naderi, Matthias Pätzold, Rym Hicheri, and Néji Youssef

**Abstract** — This paper proposes a new geometry-based channel model for shallow-water ocean environments in which the ocean bottom can slope gently down/up. The need for developing such an underwater acoustic (UWA) channel model is driven by the fact that the standard assumption of a flat ocean bottom does not hold in many realistic scenarios. Starting from a geometrical model, we develop a stochastic channel model for wideband single-input single-output vehicle-to-vehicle UWA channels using the ray theory assuming smooth ocean surface and bottom. We investigate the effect of the ocean-bottom slope angle on the distribution of the channel envelope, instantaneous channel capacity, temporal autocorrelation function, frequency correlation function, Doppler power spectral density, and the power delay profile. Theoretical and simulation results show that even a relatively small slope angle influences considerably the statistical properties of UWA channels. The validation of the proposed UWA channel model has been performed by fitting its main characteristic quantities (average delay, delay spread, and coherence bandwidth) to measurement data. In comparison with the conventional UWA channel model, which has been developed on the assumption of a flat ocean bottom, it is shown that the proposed UWA channel model enables the modelling of measured channels with higher precision.

**Keywords**—Shallow underwater acoustic channels, instantaneous channel capacity, Doppler power spectral density, power delay profile, temporal correlation function.

---

Manuscript received April 14, 2016; revised September 8, 2016 and December 16, 2016; accepted January 31, 2017. Date of publication March 13, 2017; date of current version April 7, 2017. The associate editor coordinating the review of this paper and approving it for publication was G. D. Durgin.

M. Naderi and M. Pätzold are with the Faculty of Engineering and Science, University of Agder, 4887 Grimstad, Norway (e-mail: meisam.naderi@uia.no; matthias.paetzold@uia.no).

R. Hicheri and N. Youssef are with the Ecole Supérieure des Communications de Tunis, Ariana 2083, Tunisia (e-mail: rym.hicheri@supcom.tn; neji.youssef@supcom.rnu.tn).

Color versions of one or more of the figures in this paper are available online at <http://ieeexplore.ieee.org>.

Digital Object Identifier 10.1109/TWC.2017.2664829

## I. INTRODUCTION

In recent years, underwater acoustic (UWA) communication systems have received considerable attention. UWA networks have been studied in various areas due to their potential applications in oceanography that involve the exploration of the ocean [3], support for underwater robots [22], offshore oil industry exploration [7], and pollution monitoring [24], just to name a few examples. Owing to the fact that electromagnetic waves and laser beams suffer from high path loss in ocean water, acoustic signals are being used, especially, in medium- and long-range underwater communications. For the design, test, and performance analysis of UWA communication systems, realistic channel models are required. This calls for the statistical analysis of UWA channels in terms of the channel envelope distribution, instantaneous channel capacity, correlation functions, Doppler power spectral density (PSD), and power delay profile (PDP).

UWA wave propagation in the ocean is described by the wave equation, but the development of a proper propagation model by solving the wave equation is well known to be a difficult problem [6]. To circumvent this problem, approximations by means of the ray theory are often used to model the acoustic wave propagation phenomena in ocean environments [5]. By invoking the ray theory, the energy of sound propagates in shallow-water environments along straight lines like light rays, where the speed of sound is assumed to be constant (isovelocity assumption) [6, 8, 26].

Moreover, several stochastic channel models have been developed for UWA communication systems under the assumption that the ocean bottom is flat [1, 6, 14, 19, 20, 30]. For example, in [6] and [30], the total distances that *macro-eigenrays* travel between the transmitter and the receiver have been computed by using the *method of image projections*, which has first been introduced in [5]. In both aforementioned papers, the reference channel models have been developed by combining the deterministic ray-tracing concept with statistical methods to account for the randomness of the propagation environment. However, the ocean bottom is not necessarily flat and most parts of the ocean bottom slope gradually from the shore to the high and deep ocean. This natural feature motivated us to develop a new geometrical model which we call the sloped-ocean-bottom (SOB) model. The objective of this paper is to start from the geometrical SOB model and to develop a general stochastic UWA channel model that accounts for SOB conditions. It is shown that the flat-ocean-bottom (FOB) model, which is widely used in the literature [1, 6, 14, 19, 20, 30], can be obtained as a special case of the proposed model if the slope angle is zero.

In this context, several studies have been conducted to investigate the probability density functions (PDFs) of the UWA channel gains and the corresponding instantaneous capacity [4, 11, 21]. The study of these statistical characteristics is of great importance as it allows us to gain a deeper insight into the dynamical and temporal behavior of UWA channels.

In this paper, we develop a geometry-based UWA channel model assuming ray propagation in shallow-water ocean environments by taking *macro-scattering* effects, which are caused by specular reflections at the surface and bottom of the ocean, into account. The randomness of the UWA channel as a result of *micro-scattering* (diffuse scattering) effects will not be discussed in this paper. Starting from the geometrical SOB model, we derive the time-variant channel impulse response (TVCIR) of the UWA channel model. Expressions are derived for the total distances that the macro-eigenrays travel from the transmitter to the receiver by assuming multiple-bounce scattering in shallow-water environments. We also study the angles-of-departure (AODs) and the angles-of-arrival (AOAs) of the macro-eigenrays. Furthermore, we investigate the effect of the ocean-bottom slope angle on the PDF of the UWA channel envelope and the PDF of the instantaneous channel capacity. Moreover, the statistical quantities of the proposed SOB-UWA channel model, such as the temporal autocorrelation function (ACF), frequency correlation function (FCF), Doppler PSD, and the PDP, are compared with those of the FOB-UWA channel model. The influence of the slope angle on the Doppler spread, average Doppler shift, coherence time, average delay, delay spread, and the coherence bandwidth of the UWA channel model are also studied. It is shown that the ocean-bottom slope angle considerably influences the statistical properties of UWA channels. The key theoretical results are illustrated by computer simulations.

In addition, the main statistical properties of the proposed UWA channel model, such as the FCF, average delay, delay spread, and the coherence bandwidth have been matched to real-world measurement data of UWA channels. The observed excellent agreement between model prediction and experimental measurement confirms the validity of the proposed SOB-UWA model. Moreover, the superiority of the SOB model over the FOB model is shown regarding the modelling of characteristic quantities (such as the delay spread and coherence bandwidth) of the measurement data, which are useful quantities for designing UWA communication systems, especially when orthogonal frequency division multiplexing (OFDM) techniques are used.

The rest of this paper is organized as follows. In Section II, the geometrical UWA channel model is presented. Section III studies the stochastic UWA channel

model from the geometrical UWA model. Section IV focuses on the statistical properties of the proposed UWA channel model. The numerical results are illustrated in Section V. The validation of the main theoretical results through measurement data is outlined in Section VI. Finally, the conclusions are drawn in Section VII.

## II. THE GEOMETRICAL SOB-UWA MODEL

In this section, we present a new geometrical model for a wideband single-input single-output (SISO) shallow-water ocean environment under the assumption that the ocean surface and ocean bottom are smooth. In addition, it is assumed that the ocean bottom declines (inclines) with a slope angle denoted by  $\phi$ . The shallow-water ocean environment is considered as an isovelocity environment. This paper considers medium- and long-range shallow UWA communication links under line-of-sight (LOS) propagation conditions. The UWA channel is also assumed to be wide-sense stationary in time and frequency.

Fig. C.1 presents the geometrical model of a SOB-UWA channel in a shallow-water ocean environment. As can be seen, the two-dimensional geometrical SOB model is bounded by the ocean surface and bottom. These natural boundaries act as reflectors for acoustic waves such that several macro-eigenrays can travel from the transmitter  $T_x$  to the receiver  $R_x$ . With reference to Fig. C.1, there are three kinds of macro-eigenrays. They can be grouped into downward arriving (DA) macro-eigenrays, upward arriving (UA) macro-eigenrays, and a LOS macro-eigenray. Each of the DA macro-eigenrays for which the last reflection originates from the ocean surface can have a different number of  $s$  surface reflections and  $\check{b}$  bottom reflections. Let  $N_S$  be the maximum number of surface interactions that a DA macro-eigenray can have with the ocean surface, then  $s$  and  $\check{b}$  are limited by  $1 \leq s \leq N_S$  and  $s - 1 \leq \check{b} \leq s$ , respectively. At any time instance  $t$ , the receiver  $R_x$  receives  $2N_S$  DA macro-eigenrays. The UA macro-eigenrays for which the last reflection originates from the ocean bottom can have a different number of  $b$  bottom reflections and  $\check{s}$  surface reflections. Analogously, let  $N_B$  denote the maximum number of bottom interactions that a UA macro-eigenray can have with the ocean bottom, then  $b$  and  $\check{s}$  are limited by  $1 \leq b \leq N_B$  and  $b - 1 \leq \check{s} \leq b$ , respectively. Similarly, at the time instance  $t$ , the receiver  $R_x$  receives  $2N_B$  UA macro-eigenrays. For instance, if a UA macro-eigenray has only one interaction with the ocean bottom, i.e.,  $N_B = 1$ , then there are two possible paths which this macro-eigenray can travel from the transmitter  $T_x$  to the receiver  $R_x$ . The first path arrives at  $R_x$  after a single bounce on the bottom of the ocean, i.e.,  $b = 1$ , and  $\check{s} = 0$ . The second path is a double-bounce path if a UA macro-eigenray starts upward. This means the macro-eigenray first interacts with the ocean surface and then, after interacting with

the ocean bottom, arrives at  $R_x$ , i.e.,  $b = 1$  and  $\check{s} = 1$ . It should be mentioned that experimental results obtained for medium- and long-range shallow UWA channels have shown that the number of macro-eigenrays arriving at  $R_x$  rarely exceeds 8, i.e.,  $2N_S + 2N_B = 8$  [6, 28–30].

The exact positions of the *macro-scatterers* are computable and depend on the waveguide geometry and the number of macro-eigenrays [5]. In [5], the total distances which macro-eigenrays travel in FOB models after their interactions with macro-scatterers, located at the ocean surface and bottom, have been derived by using the method of images. *Micro-scatterers*, which can be clustered around the positions of macro-scatterers will not be considered in our paper. In other words, we limit our study to the propagation of deterministic macro-eigenrays by considering only the specular (mirror-like) reflections of the ocean surface and bottom.

Moreover, we assume that the transmitter  $T_x$  and the receiver  $R_x$  are moving with velocities  $\vec{v}_T$  and  $\vec{v}_R$  in the directions determined by the angles-of-motion (AOMs)  $\alpha_v^T$  and  $\alpha_v^R$ , respectively. As shown in Figs. C.1 and C.2, the transmitter  $T_x$  (receiver  $R_x$ ) is located at the distances  $y_1^T$  ( $y_1^R$ ) and  $y_2^T$  ( $y_2^R$ ) from the ocean surface and ocean bottom, respectively. The distance along the x-axis between  $T_x$  and  $R_x$  is denoted by  $D$ . As can be seen in Fig. C.2, the symbol  $\beta_{sb}^{DA}$  ( $\alpha_{sb}^{DA}$ ) stands for the AODs (AOAs) of the DA macro-eigenrays associated with the number of surface interactions  $s$  and bottom interactions  $\check{b}$ . Analogously, the symbol  $\beta_{b\check{s}}^{UA}$  ( $\alpha_{b\check{s}}^{UA}$ ) also denotes the AODs (AOAs) of UA macro-eigenrays associated with the number of bottom interactions  $b$  and surface interactions  $\check{s}$ . The symbol  $\beta_0$  ( $\alpha_0$ ) stands for the AOD (AOA) of the LOS component.

### III. THE GEOMETRY-BASED SOB-UWA CHANNEL MODEL

In this section, we develop a mathematical model for the macro-eigenray propagation through shallow-water environments, where it is assumed that the ocean bottom slopes down or up. We first present the TVCIR of the proposed geometry-based channel model for a vehicle-to-vehicle (V2V) UWA wideband fading channel under LOS propagation conditions. Then, we derive the expressions of the total distances which macro-eigenrays travel from  $T_x$  to  $R_x$  after their interactions with the surface and bottom of the ocean. The AODs and the AOAs, which are required for computing the Doppler frequencies, are also studied. We show that the proposed UWA channel model includes the well-known model in [30], where the ocean bottom is flat, as a special case.

#### A. TVCIR

According to the geometrical model shown in Fig. C.2, the TVCIR  $h(\tau', t)$  can

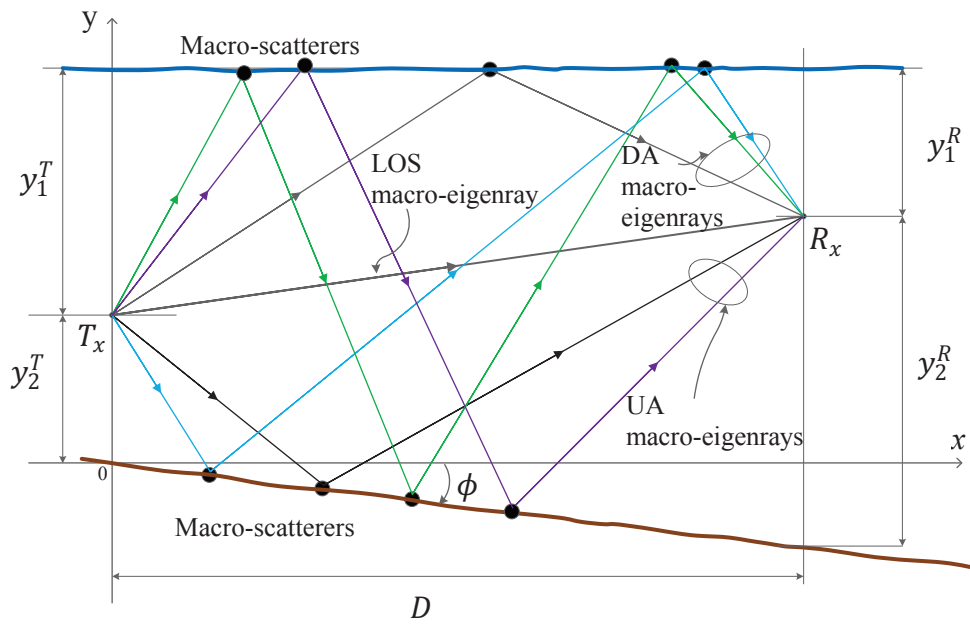


Figure C.1: Illustration of the LOS macro-eigenray and several DA and UA macro-eigenrays which travel from  $T_x$  to  $R_x$  in a shallow UWA channel ( $N_S = 2$ ,  $N_B = 1$ ) with the slope angle  $\phi < 0$ .

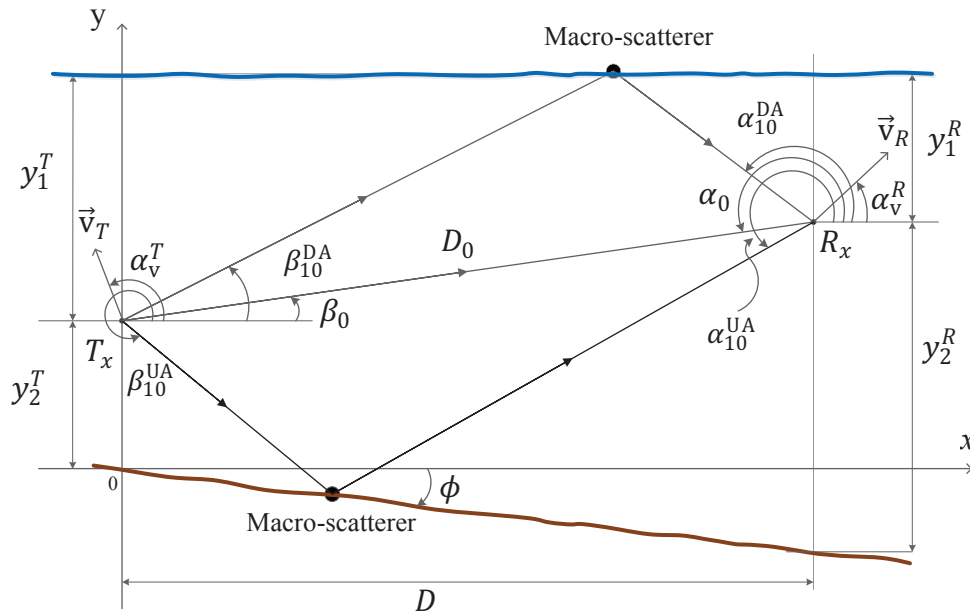


Figure C.2: The geometrical SOB model of a UWA channel in a shallow-water ocean environment with the slope angle  $\phi < 0$ .

be split into three parts. The first part  $h^{\text{LOS}}(\tau', t)$  describes the LOS component, whereas the second part  $h^{\text{DA}}(\tau', t)$  and the third part  $h^{\text{UA}}(\tau', t)$  comprise the DA macro-eigenrays and the UA macro-eigenrays, respectively. Hence, the TVCIR  $h(\tau', t)$  can be written as

$$h(\tau', t) = h^{\text{LOS}}(\tau', t) + h^{\text{DA}}(\tau', t) + h^{\text{UA}}(\tau', t). \quad (\text{C.1})$$

The LOS part  $h^{\text{LOS}}(\tau', t)$  of the TVCIR is described by the expression

$$h^{\text{LOS}}(\tau', t) = c_0 e^{j(2\pi f_0 t + \theta_0)} \delta(\tau' - \tau'_0) \quad (\text{C.2})$$

in which the gain  $c_0$  is given by

$$c_0 = \sqrt{c_R / (1 + c_R)} A_s(D_0) A_a(D_0). \quad (\text{C.3})$$

The parameter  $c_R$  is the Rice factor, and  $\tau'_0$  denotes the propagation delay of the LOS component. The symbols  $f_0$  and  $\theta_0$  represent the Doppler frequency and phase shift of the LOS component, respectively. The Doppler frequency  $f_0$  in (C.2) is defined by

$$f_0 = f_{\text{max}}^T \cos(\beta_0 - \alpha_v^T) + f_{\text{max}}^R \cos(\alpha_0 - \alpha_v^R) \quad (\text{C.4})$$

where  $f_{\text{max}}^T$  ( $f_{\text{max}}^R$ ) denotes the maximum Doppler frequency associated with the transmitter  $T_x$  (receiver  $R_x$ ), which is given by  $f_{\text{max}}^T = v_T f_c / c_s$  ( $f_{\text{max}}^R = v_R f_c / c_s$ ). Therein,  $v_T = |\vec{v}_T|$  ( $v_R = |\vec{v}_R|$ ) denotes the speed of the transmitter (receiver),  $f_c$  indicates the carrier frequency (in Hz), and  $c_s$  is the speed of sound in water, which is assumed to be 1500 m/s (isovelocity environment). With reference to Fig. C.2, the AOD  $\beta_0$  and the AOA  $\alpha_0$  of the LOS component can be computed by

$$\beta_0 = \arctan\left(\frac{y_1^T - y_1^R}{D}\right) \quad (\text{C.5})$$

and

$$\alpha_0 = \pi + \beta_0 \quad (\text{C.6})$$

respectively. The propagation delay  $\tau'_0$  can be expressed by

$$\tau'_0 = \frac{D_0}{c_s} \quad (\text{C.7})$$

where the total distance  $D_0$  between  $T_x$  and  $R_x$  is given by

$$D_0 = \sqrt{D^2 + (y_1^T - y_1^R)^2}. \quad (\text{C.8})$$

The functions  $A_s(\cdot)$  and  $A_a(\cdot)$  introduced in the gain  $c_0$  [see (C.3)] denote the propagation loss coefficients due to spherical spreading and absorption, respectively. We assume that the transmitter is equipped with an omnidirectional hydrophone, which generates spherical waveforms in the isovelocity environment. The propagation loss coefficient due to spherical spreading can be written as [13, Eq. (2.16)]

$$A_s(d) = \frac{1}{d} \quad (\text{C.9})$$

where the variable  $d$  stands for the total propagation distance in meters. The absorption loss coefficient  $A_a(\cdot)$  is given by [30, Eq. (4)]

$$A_a(d) = 10^{-\frac{d\beta}{20000}}. \quad (\text{C.10})$$

In (C.10), which is suitable for carrier frequencies between 3 and 500 kHz, the parameter  $\beta$  (in dB/km) is computed as follows [5, Eq. (1.3.1)]

$$\beta = 8.68 \times 10^3 \left( \frac{S_a f_T f_c^2 A}{f_T^2 + f_c^2} + \frac{B f_c^2}{f_T} \right) \times (1 - 6.54 \times 10^{-4} P) \quad (\text{C.11})$$

where  $A = 2.34 \times 10^{-6}$  and  $B = 3.38 \times 10^{-6}$ . The symbol  $S_a$  denotes the salinity (in parts per thousand),  $f_c$  is the carrier frequency (in kHz),  $f_T$  is the relaxation frequency (in kHz) determined by  $f_T = 21.9 \times 10^6 - (1520/(T+273))$ , and the quantity  $T$  denotes the water temperature (in °C). The symbol  $P$  stands for the hydrostatic pressure (in kg/cm<sup>2</sup>), which is determined by  $P = 1.01 \times (1 + 0.1h)$ , where  $h$  denotes the water depth (in m).

The second part  $h^{\text{DA}}(\tau', t)$  and the third part  $h^{\text{UA}}(\tau', t)$  of the TVCIR  $h(\tau', t)$  in (C.1) are given by

$$h^{\text{DA}}(\tau', t) = \sum_{s=1}^{N_S} \sum_{\check{b}=s-1}^s c_{s\check{b}}^{\text{DA}} e^{j(2\pi f_{s\check{b}}^{\text{DA}} t + \theta_{s\check{b}}^{\text{DA}})} \delta(\tau' - \tau_{s\check{b}}^{\text{DA}}) \quad (\text{C.12})$$

and

$$h^{\text{UA}}(\tau', t) = \sum_{b=1}^{N_B} \sum_{\check{s}=b-1}^b c_{b\check{s}}^{\text{UA}} e^{j(2\pi f_{b\check{s}}^{\text{UA}} t + \theta_{b\check{s}}^{\text{UA}})} \delta(\tau' - \tau_{b\check{s}}^{\text{UA}}) \quad (\text{C.13})$$

respectively. The gains  $c_{sb}^{\text{DA}}$  and  $c_{b\check{s}}^{\text{UA}}$  are expressed by

$$c_{sb}^{\text{DA}} = \sqrt{\frac{\eta_S}{2N_S(1+c_R)}} A_s(D_{sb}^{\text{DA}}) A_a(D_{sb}^{\text{DA}}) A_b(\varphi_{sb}^{\text{DA}} + (2\check{b}-1)\phi)^{\check{b}} \quad (\text{C.14})$$

and

$$c_{b\check{s}}^{\text{UA}} = \sqrt{\frac{\eta_B}{2N_B(1+c_R)}} A_s(D_{b\check{s}}^{\text{UA}}) A_a(D_{b\check{s}}^{\text{UA}}) A_b(\varphi_{b\check{s}}^{\text{UA}})^{(b-1)} A_b(\varphi_{b\check{s}}^{\text{UA}} + 2(b-1)\phi) \quad (\text{C.15})$$

respectively. The propagation delays  $\tau_{sb}^{\text{DA}}$  and  $\tau_{b\check{s}}^{\text{UA}}$  are determined by  $\tau_{sb}^{\text{DA}} = D_{sb}^{\text{DA}}/c_s$  ( $s = 1, 2, \dots, N_S$  and  $\check{b} \in [s-1, s]$ ) and  $\tau_{b\check{s}}^{\text{UA}} = D_{b\check{s}}^{\text{UA}}/c_s$  ( $b = 1, 2, \dots, N_B$  and  $\check{s} \in [b-1, b]$ ), respectively. The symbols  $D_{sb}^{\text{DA}}$  and  $D_{b\check{s}}^{\text{UA}}$  denote the total distances which the DA and UA macro-eigenrays travel from  $T_x$  to  $R_x$  given  $(s, \check{b})$  and  $(\check{s}, b)$  surface-bottom interactions, respectively. It is shown in the Appendix that the total distances  $D_{sb}^{\text{DA}}$  and  $D_{b\check{s}}^{\text{UA}}$  can be computed by using the method of images which results in

$$D_{sb}^{\text{DA}} = \sqrt{(D - f^{\text{DA}}(\phi))^2 + ((2s-1)g^{\text{DA}}(\phi)y_1^T + 2\check{b}h^{\text{DA}}(\phi)y_2^T + y_1^R)^2} \quad (\text{C.16})$$

$$D_{b\check{s}}^{\text{UA}} = \sqrt{(D/\cos(\phi) - f^{\text{UA}}(\phi))^2 + (2\check{s}g^{\text{UA}}(\phi)y_1^T + (2b-1)h^{\text{UA}}(\phi)y_2^T + y_2^R \cos(\phi))^2} \quad (\text{C.17})$$

The functions  $f^{\text{DA}}(\phi)$  ( $f^{\text{UA}}(\phi)$ ),  $g^{\text{DA}}(\phi)$  ( $g^{\text{UA}}(\phi)$ ), and  $h^{\text{DA}}(\phi)$  ( $h^{\text{UA}}(\phi)$ ) in (C.16) ((C.17)) are presented in the Appendix.

The symbols  $\eta_S$  in (C.14) and  $\eta_B$  in (C.15) are used to balance the contribution of the DA and UA macro-eigenrays to the total power of the UWA channel model, respectively, such that  $\eta_S + \eta_B = 1$ . The phase shifts  $\theta_{sb}^{\text{DA}}$  in (C.12) and  $\theta_{b\check{s}}^{\text{UA}}$  in (C.13) are modelled by independent and identically distributed (i.i.d.) random variables, which are supposed to be uniformly distributed over the interval  $(-\pi, \pi]$ .

The function  $A_b(\cdot)$  in (C.14) and (C.15) denotes the reflection coefficient due to the impedance mismatch between the ocean water and the ocean bed. It should be mentioned that the impedance mismatch between the ocean water and air causes the sea surface to be a very good reflector. If the sea surface is smooth, the reflection coefficient has a magnitude that is close to one but the phase shift is  $\pi$  radians, i.e., the reflection coefficient is close to  $-1$  [2, 5, 6]. In the area of underwater acoustic channel modelling, the ocean bed is definitely the most complex bound-

ary, exhibiting vastly different reflectivity characteristics in different geographical locations [9, 12]. The impedance mismatch between the ocean water and ocean bed causes the ocean bed to reflect some parts of an incident wave. For a smooth ocean bed, the reflection coefficient  $A_b(\cdot)$  is given by [5, Eq. (3.1.12)]

$$A_b(\varphi) = \left| \frac{(\rho_b/\rho_s) \cos(\varphi) - \sqrt{(c_s/c_b)^2 - \sin^2(\varphi)}}{(\rho_b/\rho_s) \cos(\varphi) + \sqrt{(c_s/c_b)^2 - \sin^2(\varphi)}} \right| \quad (\text{C.18})$$

where  $\rho_s$  ( $\rho_b$ ) and  $c_s$  ( $c_b$ ) stand for the density of the ocean water (ocean bed) and the speed of sound in the ocean water (ocean bed), respectively. The symbol  $\varphi$  in (C.18) denotes the angle-of-incidence (AOI) of the macro-eigenrays of the specular reflections at the ocean bottom.

### B. Derivation of the AOD and AOA

In this section, we derive analytical expressions for the AODs  $\beta_{sb}^{\text{DA}}$  ( $\beta_{bs}^{\text{UA}}$ ) and the AOAs  $\alpha_{sb}^{\text{DA}}$  ( $\alpha_{bs}^{\text{UA}}$ ), which are necessary to compute the Doppler frequencies of the macro-eigenrays. The Doppler frequencies  $f_{sb}^{\text{DA}}$  and  $f_{bs}^{\text{UA}}$  presented in (C.12) and (C.13), respectively, can be computed by using (C.4), if we replace  $\beta_0$  by  $\beta_{sb}^{\text{DA}}$  ( $\beta_{bs}^{\text{UA}}$ ) and  $\alpha_0$  by  $\alpha_{sb}^{\text{DA}}$  ( $\alpha_{bs}^{\text{UA}}$ ). Note that the slope angle  $\phi$  influences in our model the AOIs at the ocean surface and bottom as shown in Figs. C.3 and C.4. This is in contrast for the FOB environment, where the AOIs at the ocean bottom are fixed for each macro-eigenray. With reference to Figs. C.3 and C.4, the general solutions for the AODs  $\beta_{sb}^{\text{DA}}$  and  $\beta_{bs}^{\text{UA}}$  can be obtained as

$$\beta_{sb}^{\text{DA}} = \left( \check{b} - s + \frac{3}{2} \right) \pi + (-1)^{(s-\check{b})} \left( \varphi_{sb}^{\text{DA}} + 2\check{b}\phi \right) \quad (\text{C.19})$$

and

$$\beta_{bs}^{\text{UA}} = \left( b - \check{s} + \frac{1}{2} \right) \pi - (-1)^{(b-\check{s})} \left[ \varphi_{bs}^{\text{UA}} + (2b-1)\phi \right] \quad (\text{C.20})$$

respectively. Similarly, the general-form expressions for the AOAs  $\alpha_{sb}^{\text{DA}}$  and  $\alpha_{bs}^{\text{UA}}$  can be written as

$$\alpha_{sb}^{\text{DA}} = \frac{\pi}{2} + \varphi_{sb}^{\text{DA}} \quad (\text{C.21})$$

and

$$\alpha_{bs}^{\text{UA}} = \frac{3\pi}{2} - (\varphi_{bs}^{\text{UA}} - \phi) \quad (\text{C.22})$$

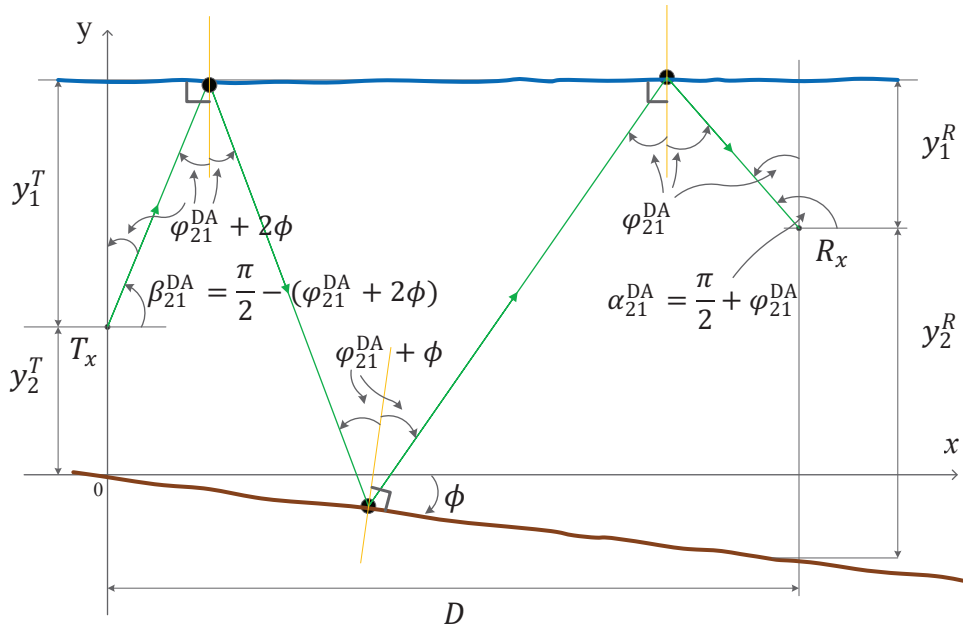


Figure C.3: The effect of the slope angle  $\phi < 0$  on the AOIs  $\varphi_{sb}^{\text{DA}}$  of the DA macro-eigenray at the ocean surface/bottom for  $s = 2$  and  $\check{b} = 1$ .

respectively. According to Figs. C.3 and C.4, the AOIs  $\varphi_{sb}^{\text{DA}}$  and  $\varphi_{bs}^{\text{UA}}$  at  $R_x$  play a key role in the determination of the AODs and AOAs presented in (C.19)–(C.22). The AOIs  $\varphi_{sb}^{\text{DA}}$  and  $\varphi_{bs}^{\text{UA}}$  can be expressed by

$$\varphi_{sb}^{\text{DA}} = \arctan \left( \frac{D - f^{\text{DA}}(\phi)}{(2s - 1)g^{\text{DA}}(\phi)y_1^T + 2\check{b}h^{\text{DA}}(\phi)y_2^T + y_1^R} \right) \quad (\text{C.23})$$

and

$$\varphi_{bs}^{\text{UA}} = \arctan \left( \frac{D / \cos(\phi) - f^{\text{UA}}(\phi)}{2\check{s}g^{\text{UA}}(\phi)y_1^T + (2b - 1)h^{\text{UA}}(\phi)y_2^T + y_2^R \cos(\phi)} \right) \quad (\text{C.24})$$

respectively. The proof of the expression in (C.23) is presented in the Appendix.

### C. FOB Case

In this section, we will show that the proposed geometry-based SOB-UWA channel model includes the FOB-UWA model as a special case if  $\phi = 0$ . Recall that the FOB model has been widely used in the literature on UWA channel modelling [1, 6, 14, 19, 20, 30]. From now on, we underline the symbols, which are

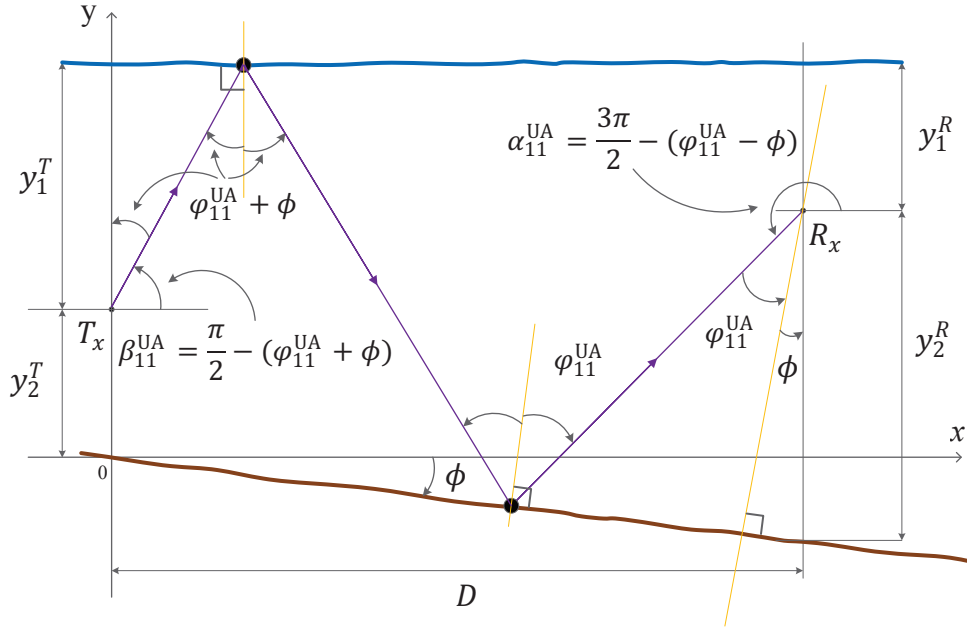


Figure C.4: The effect of the slope angle  $\phi < 0$  on the AOIs  $\varphi_{b\check{s}}^{\text{UA}}$  of the UA macro-eigenray at the ocean surface/bottom for  $b = \check{s} = 1$ .

specific for the FOB model. The TVCIR  $\underline{h}(\tau', t)$  in (C.1) will be written as

$$\underline{h}(\tau', t) = h^{\text{LOS}}(\tau', t) + \underline{h}^{\text{DA}}(\tau', t) + \underline{h}^{\text{UA}}(\tau', t) \quad (\text{C.25})$$

where the first part  $h^{\text{LOS}}(\tau', t)$  is the same as in (C.2), whereas the second part  $\underline{h}^{\text{DA}}(\tau', t)$  and the third part  $\underline{h}^{\text{UA}}(\tau', t)$  of  $\underline{h}(\tau', t)$  are given by

$$\underline{h}^{\text{DA}}(\tau', t) = \sum_{s=1}^{N_S} \sum_{\check{b}=s-1}^s \underline{c}_{s\check{b}}^{\text{DA}} e^{j(2\pi f_{s\check{b}}^{\text{DA}} t + \theta_{s\check{b}}^{\text{DA}})} \delta(\tau' - \tau_{s\check{b}}^{\text{DA}}) \quad (\text{C.26})$$

and

$$\underline{h}^{\text{UA}}(\tau', t) = \sum_{b=1}^{N_B} \sum_{\check{s}=b-1}^b \underline{c}_{b\check{s}}^{\text{UA}} e^{j(2\pi f_{b\check{s}}^{\text{UA}} t + \theta_{b\check{s}}^{\text{UA}})} \delta(\tau' - \tau_{b\check{s}}^{\text{UA}}) \quad (\text{C.27})$$

respectively. The gains  $\underline{c}_{s\check{b}}^{\text{DA}}$  and  $\underline{c}_{b\check{s}}^{\text{UA}}$  can be expressed by

$$\underline{c}_{s\check{b}}^{\text{DA}} = \sqrt{\frac{\eta_S}{2N_S(1+c_R)}} A_s(\underline{D}_{s\check{b}}^{\text{DA}}) A_a(\underline{D}_{s\check{b}}^{\text{DA}}) A_b(\varphi_{s\check{b}}^{\text{DA}})^{\check{b}} \quad (\text{C.28})$$

and

$$c_{b\check{s}}^{\text{UA}} = \sqrt{\frac{\eta_B}{2N_B(1+c_R)}} A_s(\underline{D}_{b\check{s}}^{\text{UA}}) A_a(\underline{D}_{b\check{s}}^{\text{UA}}) A_b(\underline{\varphi}_{b\check{s}}^{\text{UA}})^b \quad (\text{C.29})$$

respectively. The phase shifts  $\underline{\theta}_{s\check{b}}^{\text{DA}}$  and  $\underline{\theta}_{b\check{s}}^{\text{UA}}$  are again modelled by i.i.d. random variables, which are uniformly distributed over the interval  $(-\pi, \pi]$ . For  $\phi = 0$ , the total distances  $\underline{D}_{s\check{b}}^{\text{DA}}$  and  $\underline{D}_{b\check{s}}^{\text{UA}}$  in (C.16) and (C.17), respectively reduce to that in [5, Eq. (5.1.7)], namely

$$\underline{D}_{s\check{b}}^{\text{DA}} = \sqrt{D^2 + ((2s-1)y_1^T + 2\check{b}y_2^T + y_1^R)^2} \quad (\text{C.30})$$

$$\underline{D}_{b\check{s}}^{\text{UA}} = \sqrt{D^2 + (2\check{s}y_1^T + (2b-1)y_2^T + y_2^R)^2}. \quad (\text{C.31})$$

The propagation delays  $\underline{\tau}_{s\check{b}}^{\text{DA}}$  in (C.26) and  $\underline{\tau}_{b\check{s}}^{\text{UA}}$  in (C.27) can be computed by  $\underline{\tau}_{s\check{b}}^{\text{DA}} = \underline{D}_{s\check{b}}^{\text{DA}}/c_s$  ( $s = 1, 2, \dots, N_S$  and  $\check{b} \in [s-1, s]$ ) and  $\underline{\tau}_{b\check{s}}^{\text{UA}} = \underline{D}_{b\check{s}}^{\text{UA}}/c_s$  ( $b = 1, 2, \dots, N_B$  and  $\check{s} \in [b-1, b]$ ), respectively. Similar to Section III-A, the Doppler shifts  $\underline{f}_{s\check{b}}^{\text{DA}}$  and  $\underline{f}_{b\check{s}}^{\text{UA}}$  can be computed by using (C.4), if we replace there  $\beta_0$  by  $\underline{\beta}_{s\check{b}}^{\text{DA}}$  ( $\underline{\beta}_{b\check{s}}^{\text{UA}}$ ) and  $\alpha_0$  by  $\underline{\alpha}_{s\check{b}}^{\text{DA}}$  ( $\underline{\alpha}_{b\check{s}}^{\text{UA}}$ ). The expressions of the AODs  $\underline{\beta}_{s\check{b}}^{\text{DA}}$  and  $\underline{\beta}_{b\check{s}}^{\text{UA}}$  in (C.19) and (C.20) reduce to

$$\underline{\beta}_{s\check{b}}^{\text{DA}} = \left( \check{b} - s + \frac{3}{2} \right) \pi + (-1)^{(s-\check{b})} \underline{\varphi}_{s\check{b}}^{\text{DA}} \quad (\text{C.32})$$

and

$$\underline{\beta}_{b\check{s}}^{\text{UA}} = \left( b - \check{s} + \frac{1}{2} \right) \pi - (-1)^{(b-\check{s})} \underline{\varphi}_{b\check{s}}^{\text{UA}} \quad (\text{C.33})$$

respectively. The corresponding AOA  $\underline{\alpha}_{s\check{b}}^{\text{DA}}$  and  $\underline{\alpha}_{b\check{s}}^{\text{UA}}$  are given by

$$\underline{\alpha}_{s\check{b}}^{\text{DA}} = \frac{\pi}{2} + \underline{\varphi}_{s\check{b}}^{\text{DA}} \quad (\text{C.34})$$

and

$$\underline{\alpha}_{b\check{s}}^{\text{UA}} = \frac{3\pi}{2} - \underline{\varphi}_{b\check{s}}^{\text{UA}} \quad (\text{C.35})$$

respectively. By means of (C.30) and (C.31), the AOIs  $\underline{\varphi}_{s\check{b}}^{\text{DA}}$  and  $\underline{\varphi}_{b\check{s}}^{\text{UA}}$  can be deter-

mined as

$$\underline{\varphi}_{s\check{b}}^{\text{DA}} = \arctan \left( \frac{D}{(2s-1)y_1^T + 2\check{b}y_2^T + y_1^R} \right) \quad (\text{C.36})$$

and

$$\underline{\varphi}_{b\check{s}}^{\text{UA}} = \arctan \left( \frac{D}{2\check{s}y_1^T + (2b-1)y_2^T + y_2^R} \right) \quad (\text{C.37})$$

respectively. Note that the special solutions in (C.36) and (C.37) are identical with the known results in [30, Eqs. (11) and (12)].

#### IV. STATISTICAL PROPERTIES OF THE SOB-UWA CHANNEL MODEL

In this section, we study the statistical properties of the developed SOB-UWA channel model including the distribution of the channel envelope, instantaneous channel capacity, temporal ACF, FCF, Doppler PSD, and PDP.

##### A. Distribution of the Channel Envelope

Starting from the TVCIR  $h(\tau', t)$ , we can obtain the time-variant channel transfer function (TVCTF)  $H(f', t)$  by computing the Fourier transform of the TVCIR  $h(\tau', t)$  with respect to the propagation delay  $\tau'$ . From (C.1), (C.2), (C.12), and (C.13), it follows that the TVCTF  $H(f', t)$  can be written as

$$H(f', t) = H^{\text{LOS}}(f', t) + H^{\text{DA}}(f', t) + H^{\text{UA}}(f', t) \quad (\text{C.38})$$

where the function  $H^{\text{LOS}}(f', t)$  represents the LOS part of the TVCTF  $H(f', t)$ , which is given by

$$H^{\text{LOS}}(f', t) = c_0 e^{j[2\pi(f_0 t - f' \tau'_0) + \theta_0]}. \quad (\text{C.39})$$

The second part  $H^{\text{DA}}(f', t)$  and third part  $H^{\text{UA}}(f', t)$  of the TVCTF  $H(f', t)$  can be represented as

$$H^{\text{DA}}(f', t) = \sum_{s=1}^{N_S} \sum_{\check{b}=s-1}^s c_{s\check{b}}^{\text{DA}} e^{j[2\pi(f_{s\check{b}}^{\text{DA}} t - f' \tau'_{s\check{b}}^{\text{DA}}) + \theta_{s\check{b}}^{\text{DA}}]} \quad (\text{C.40})$$

and

$$H^{\text{UA}}(f', t) = \sum_{b=1}^{N_B} \sum_{\check{s}=b-1}^b c_{b\check{s}}^{\text{UA}} e^{j[2\pi(f_{b\check{s}}^{\text{UA}} t - f' \tau'_{b\check{s}}^{\text{UA}}) + \theta_{b\check{s}}^{\text{UA}}]} \quad (\text{C.41})$$

respectively. Using the results presented in [18] regarding the statistics of the envelope of sum-of-cisoids (SOC)-based multipath fading channel models, the PDF  $p_{|H|}(z)$  of the channel envelope  $|H(f', t)|$  can be written as

$$p_{|H|}(z) = 4\pi^2 z \int_0^\infty \left[ \prod_{n=1}^N J_0(2\pi|c_n|x) \right] J_0(2\pi zx) J_0(2\pi c_0 x) x dx \quad (\text{C.42})$$

where  $(c_1, \dots, c_N) = (c_{1,0}^{\text{DA}}, c_{1,1}^{\text{DA}}, c_{2,1}^{\text{DA}}, c_{2,2}^{\text{DA}}, \dots, c_{N_S, N_S-1}^{\text{DA}}, c_{N_S, N_S}^{\text{DA}}, c_{1,0}^{\text{UA}}, c_{1,1}^{\text{UA}}, c_{2,1}^{\text{UA}}, c_{2,2}^{\text{UA}}, \dots, c_{N_B, N_B-1}^{\text{UA}}, c_{N_B, N_B}^{\text{UA}})$  and  $N = 2N_S + 2N_B$ .

### B. Distribution of the Instantaneous Channel Capacity

According to E. Telatar [27] and G. E. Shannon [23], the channel capacity  $C(f', t)$  can be written as

$$C(f', t) = \log_2 \left( 1 + \frac{S(f')}{N(f')} |H(f', t)|^2 \right) \quad (\text{C.43})$$

where  $f'$  is a tone frequency within the bandwidth of the transmit signal. In (C.43),  $S(f')$  is the PSD of the transmit signal and  $N(f')$  represents the PSD of the total underwater coloured noise component, which is given by

$$N(f') = N_t(f') + N_s(f') + N_w(f') + N_{th}(f'). \quad (\text{C.44})$$

Here,  $N_t(f')$ ,  $N_s(f')$ ,  $N_w(f')$ , and  $N_{th}(f')$  are the noise PSDs resulting from the turbulence, shipping, waves, and thermal noise, respectively [25]. It should be pointed out that the noise in underwater propagation environments is strongly frequency dependent. This characteristic is usually taken into account for the selection of appropriate frequency bands for UWA communications. From (C.43), the instantaneous channel capacity  $C(t)$  can be obtained by integrating over the frequency variable  $f'$  within the transmit bandwidth  $B$ , i.e.,

$$C(t) = \int_{f_c - \frac{B}{2}}^{f_c + \frac{B}{2}} \log_2 \left( 1 + \frac{S(f')}{N(f')} |H(f', t)|^2 \right) df'. \quad (\text{C.45})$$

The PDF  $p_C(r)$  of the instantaneous channel capacity  $C(t)$  can be directly obtained from the PDF  $p_{|H|}(z)$  of the channel envelope  $|H(f', t)|$  in (C.42) by applying the

concept of transformation of random variables [16, pp. 130], which results in

$$p_C(r) = \frac{2^{r-1} \log(2)}{\gamma} \sqrt{\frac{\gamma}{2^r - 1}} P_{|H|} \left( \sqrt{\frac{2^r - 1}{\gamma}} \right) \quad (\text{C.46})$$

where  $\gamma$  is the average signal-to-noise ratio (SNR) viewed at the receive-hydrophone side.

### C. Temporal ACF, FCF, Doppler PSD, and PDP

In the following, we study the temporal ACF, FCF, Doppler PSD, and the PDP of the proposed UWA channel model. The knowledge of the TVCTF  $H(f', t)$  enables us to compute the time-frequency correlation function (TFCF) of the channel. Assuming that the geometry-based SOB-UWA channel model is wide-sense stationary in time  $t$  and frequency  $f'$ , we can compute the TFCF  $r_{HH}(\nu', \tau)$  of the TVCTF  $H(f', t)$  by using

$$r_{HH}(\nu', \tau) = E\{H^*(f', t)H(f' + \nu', t + \tau)\} \quad (\text{C.47})$$

where  $(\cdot)^*$  represents the complex conjugate operation, and  $E\{\cdot\}$  is the statistical expectation operator. The symbols  $\nu'$  and  $\tau$  denote the frequency and the time separation variables, respectively. After averaging over the random phases  $\theta_{sb}^{\text{DA}}$  and  $\theta_{b\check{s}}^{\text{UA}}$ , the TFCF  $r_{HH}(\nu', \tau)$  of the proposed UWA channel model results in

$$\begin{aligned} r_{HH}(\nu', \tau) = c_0^2 e^{j2\pi(f_0\tau - \nu'\tau_0)} &+ \sum_{s=1}^{N_S} \sum_{\check{b}=s-1}^s [c_{s\check{b}}^{\text{DA}}]^2 e^{j2\pi(f_{s\check{b}}^{\text{DA}}\tau - \nu'\tau'_{s\check{b}})} \\ &+ \sum_{b=1}^{N_B} \sum_{\check{s}=b-1}^b [c_{b\check{s}}^{\text{UA}}]^2 e^{j2\pi(f_{b\check{s}}^{\text{UA}}\tau - \nu'\tau'_{b\check{s}})}. \end{aligned} \quad (\text{C.48})$$

It should be noted that the temporal ACF  $r_{HH}(\tau)$  and the FCF  $r_{HH}(\nu')$  are obtained from the TFCF  $r_{HH}(\nu', \tau)$  by setting  $\nu'$  and  $\tau$  to zero, respectively, can be computed by

$$\begin{aligned} r_{HH}(\tau) = r_{HH}(0, \tau) = c_0^2 e^{j2\pi f_0\tau} &+ \sum_{s=1}^{N_S} \sum_{\check{b}=s-1}^s [c_{s\check{b}}^{\text{DA}}]^2 e^{j2\pi f_{s\check{b}}^{\text{DA}}\tau} \\ &+ \sum_{b=1}^{N_B} \sum_{\check{s}=b-1}^b [c_{b\check{s}}^{\text{UA}}]^2 e^{j2\pi f_{b\check{s}}^{\text{UA}}\tau} \end{aligned} \quad (\text{C.49})$$

$$\begin{aligned}
 r_{HH}(\nu') = r_{HH}(\nu', 0) = c_0^2 e^{-j2\pi\nu'\tau'_0} &+ \sum_{s=1}^{N_S} \sum_{\check{b}=s-1}^s [c_{s\check{b}}^{\text{DA}}]^2 e^{-j2\pi\nu'\tau'_{s\check{b}}} \\
 &+ \sum_{b=1}^{N_B} \sum_{\check{s}=b-1}^b [c_{b\check{s}}^{\text{UA}}]^2 e^{-j2\pi\nu'\tau'_{b\check{s}}}. \quad (\text{C.50})
 \end{aligned}$$

From (C.48), we can obtain the total power  $\sigma_{HH}^2$  of the UWA channel model as  $\sigma_{HH}^2 = r_{HH}(0, 0)$ . Moreover, the Doppler PSD  $S_{HH}(f)$  can be obtained by computing the Fourier transform of the temporal ACF  $r_{HH}(\tau)$  in (C.49) with respect to the variable  $\tau$ . The PDP  $S_{\tau'}(\tau')$  can be obtained by taking the inverse Fourier transform of the FCF  $r_{HH}(\nu')$  in (C.50) with respect to the variable  $\nu'$ .

#### D. Characteristic Quantities

The Doppler PSD  $S_{HH}(f)$  enables us to compute the average Doppler shift  $B_{HH}^{(1)}$ , the Doppler spread  $B_{HH}^{(2)}$ , and the coherence time  $T_C$  of the channel. These characteristic quantities can also be expressed in closed form by using the temporal ACF  $r_{HH}(\tau)$ . The average Doppler shift  $B_{HH}^{(1)}$  and the Doppler spread  $B_{HH}^{(2)}$  are defined by the first moment and the square root of the second central moment of the Doppler PSD  $S_{HH}(f)$ , respectively, i.e., [17, Eqs. (3.28) and (3.29)]

$$B_{HH}^{(1)} = \frac{\int_{-\infty}^{+\infty} f S_{HH}(f) df}{\int_{-\infty}^{+\infty} S_{HH}(f) df} = \frac{1}{2\pi j} \left. \frac{\dot{r}_{HH}(\tau)}{r_{HH}(\tau)} \right|_{\tau=0} \quad (\text{C.51})$$

and

$$\begin{aligned}
 B_{HH}^{(2)} &= \sqrt{\frac{\int_{-\infty}^{+\infty} (f - B_{HH}^{(1)})^2 S_{HH}(f) df}{\int_{-\infty}^{+\infty} S_{HH}(f) df}} \\
 &= \frac{1}{2\pi} \sqrt{\left( \frac{\dot{r}_{HH}(\tau)}{r_{HH}(\tau)} \right)^2 - \frac{\ddot{r}_{HH}(\tau)}{r_{HH}(\tau)}} \Bigg|_{\tau=0}, \quad (\text{C.52})
 \end{aligned}$$

where  $\dot{r}_{HH}(\tau)$  and  $\ddot{r}_{HH}(\tau)$  are the first and second time derivative of the temporal ACF  $r_{HH}(\tau)$  with respect to the variable  $\tau$ . The coherence time  $T_C$  of the channel is approximately the reciprocal of the Doppler spread  $B_{HH}^{(2)}$ , i.e.,  $T_C \approx 1/B_{HH}^{(2)}$ .

Analogously, the PDP  $S_{\tau'}(\tau')$  enables us to compute the average delay  $B_{\tau'}^{(1)}$ , the delay spread  $B_{\tau'}^{(2)}$ , and the coherence bandwidth  $B_C$  of the channel. These characteristic quantities can be expressed in closed form by means of the FCF. The

average delay  $B_{\tau'}^{(1)}$  and the delay spread  $B_{\tau'}^{(2)}$  are defined by the first moment and the square root of the second central moment of the PDP  $S_{\tau'}(\tau')$ , respectively, i.e., [17, Eqs. (7.39)–(7.40)]

$$B_{\tau'}^{(1)} = \frac{\int_{-\infty}^{+\infty} \tau' S_{\tau'}(\tau') d\tau'}{\int_{-\infty}^{+\infty} S_{\tau'}(\tau') d\tau'} = -\frac{1}{2\pi j} \cdot \frac{\dot{r}_{HH}(\nu')}{r_{HH}(\nu')} \Bigg|_{\nu'=0} \quad (\text{C.53})$$

and

$$\begin{aligned} B_{\tau'}^{(2)} &= \sqrt{\frac{\int_{-\infty}^{+\infty} (\tau' - B_{\tau'}^{(1)})^2 S_{\tau'}(\tau') d\tau'}{\int_{-\infty}^{+\infty} S_{\tau'}(\tau') d\tau'}} \\ &= \frac{1}{2\pi} \sqrt{\left(\frac{\dot{r}_{HH}(\nu')}{r_{HH}(\nu')}\right)^2 - \frac{\ddot{r}_{HH}(\nu')}{r_{HH}(\nu')}} \Bigg|_{\nu'=0}, \end{aligned} \quad (\text{C.54})$$

where  $\dot{r}_{HH}(\nu')$  and  $\ddot{r}_{HH}(\nu')$  are the first and second time derivative of the FCF  $r_{HH}(\nu')$  with respect to the variable  $\nu'$ . The coherence bandwidth  $B_C$  of the channel is approximately the reciprocal of the delay spread  $B_{\tau'}^{(2)}$ , i.e.,  $B_C \approx 1/B_{\tau'}^{(2)}$ .

## V. NUMERICAL RESULTS

In this section, we illustrate the theoretical results presented in the previous sections. One of our main objectives is to show how much the slope angle  $\phi$  influences the statistical properties of UWA channels. Note that the ocean-bottom slope angle  $\phi = -1^\circ$  ( $\phi = 1^\circ$ ) results in an increase (or decrease) of the water depth of 17.4 meter per kilometer. In our simulation setup, we set the carrier frequency  $f_c$  to 10 kHz and assume that the transmitter  $T_x$  and the receiver  $R_x$  are moving at the same speed of 3 m/s, which results in maximum Doppler frequencies of 20 Hz (i.e.,  $f_{\max}^T = f_{\max}^R = 20$  Hz). The transmitter  $T_x$  and the receiver  $R_x$  are moving in opposite directions determined by  $\alpha_v^T = 180^\circ$  and  $\alpha_v^R = 0^\circ$ . The  $T_x$  and  $R_x$  location parameters have been set as follows:  $y_1^T = 40$  m,  $y_2^T = 60$  m,  $y_1^R = 15$  m, and  $D = 1.6$  km. The remaining parameters of the UWA channel model are listed in the third column of Table C.1.

Fig. C.5 displays the PDF  $p_{|H|}(z)$  of the UWA channel model envelope  $|H(f', t)|$  for slope angles  $\phi = -3^\circ, \dots, 0^\circ, \dots, 3^\circ$ . A good fitting between theory and simulation can be observed. Moreover, this figure shows that the average and the spread of the UWA channel model envelope distribution decrease if  $\phi$  decreases. Fig. C.6 illustrates the effect of the slope angle  $\phi$  on the PDF  $p_C(r)$  of the instantaneous

capacity of the UWA channel model for an average SNR  $\gamma$  set to 17 dB. In fact, a relatively small decrease of  $\phi$  results in a considerable decrease of both the average and the spread of the instantaneous capacity of the UWA channel model. For example, compared to the FOB case ( $\phi = 0^\circ$ ), a slope angle  $\phi$  of  $-3^\circ$  results approximately in an average capacity loss of 0.15 bits/s/Hz. Here again, a good agreement between the theoretical results and the corresponding simulation results can be seen.

Figs. C.7 and C.8 show the influence of the slope angle  $\phi$  on the absolute value of the normalized temporal ACF  $|r_{HH}(\tau)|$  and FCF  $|r_{HH}(\nu')|$  of the UWA channel model, respectively. The results illustrate that both quantities decay rapidly with  $\tau$  and  $\nu'$  by decreasing the value of  $\phi$  from  $+3^\circ$  to  $-3^\circ$ . It can be seen from Fig. C.7 that the slope angle  $\phi$  influences significantly the curvature of the temporal ACF  $|r_{HH}(\tau)|$  at the origin. From this figure we notice that the graph that corresponds to the slope angle  $\phi = -3^\circ$  descends at a faster rate than other graphs. The same results are obtained for the FCF  $|r_{HH}(\nu')|$  shown in Fig. C.8. As can be seen in Figs. C.7 and C.8, there is a good match between the theoretical results and the corresponding simulation results.

Fig. C.9 depicts the Doppler PSD  $S_{HH}(f)$  of the UWA channel model for the FOB case. The Doppler PSD  $S_{HH}(f)$  of the UWA channel model for the SOB case has been illustrated in Fig. C.10 by assuming slope angles  $\phi$  of  $+3^\circ$  and  $-3^\circ$ . From the inspection of Figs. C.9 and C.10, we can conclude that the path gains are influenced by the slope angle  $\phi$ , and that its effect is also noticeable in the range of the Doppler frequencies. It is obvious that the slope angle  $\phi$  remarkably affects the AOAs and consequently the Doppler frequencies.

Figs. C.11 and C.12 show the PDP  $S_{\tau'}(\tau')$  of the UWA channel model for the FOB and SOB cases, respectively. Based on the results depicted in Figs. C.11 and C.12, the time range in the propagation delay axis is extended by decreasing the value of  $\phi$  from  $+3$  to  $-3$ . The only reason for the extension is the effect of the slope angle  $\phi$  on increasing the total distance which each macro-eigenray travels from the transmitter to the receiver.

The effect of the slope angle  $\phi$  on the average Doppler shift  $B_{HH}^{(1)}$ , Doppler spread  $B_{HH}^{(2)}$ , and the coherence time  $T_C$  of the UWA channel model is shown in Fig. C.13. According to the results, one can conclude that the slope angle  $\phi$  does have a considerable impact on the average Doppler shift and Doppler spread of the UWA channel model. Moreover, the coherence time  $T_C$  of the UWA channel model is almost quadrupled by increasing  $\phi$  from  $-3^\circ$  to  $3^\circ$ .

Fig. C.14 shows the influence of the slope angle  $\phi$  on the average delay  $B_{\tau'}^{(1)}$ , delay spread  $B_{\tau'}^{(2)}$ , and the coherence bandwidth  $B_C$  of the UWA channel model.

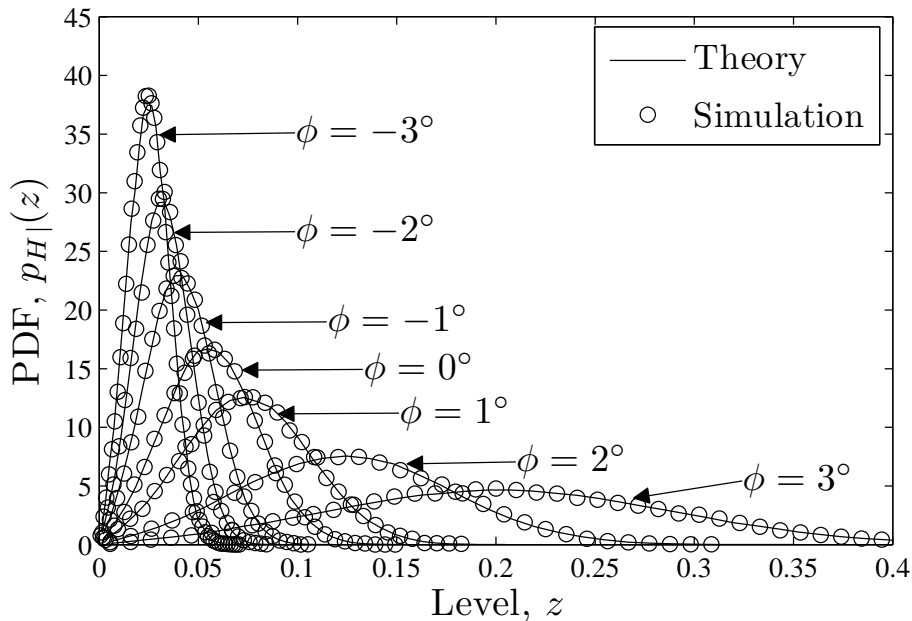


Figure C.5: The PDF of the channel envelope.

It can be seen from this figure how the aforementioned characteristic functions of the UWA channel model vary w.r.t. the slope angle  $\phi$ . According to Fig. C.14, by increasing  $\phi$  from  $-3^\circ$  to  $3^\circ$ , the average delay  $B_{\tau'}^{(1)}$  decreases from 25 ms to 3 ms, and also there is a noticeable fall in the delay spread  $B_{\tau'}^{(2)}$  of the UWA channel model from 22 ms to 3 ms. The coherence bandwidth  $B_C$  experiences a remarkable rise from 45 Hz to 335 Hz by increasing  $\phi$ . For ease of reference, some parameters presented in Section III and associated values used for the computer simulations are defined in Table C.1.

According to the simulation results, a gradual slope in the ocean bottom changes the statistical properties of the UWA channel, thus, this parameter plays a key role in the modelling of UWA channels. Notice that the proposed UWA channel model has been studied by only considering the deterministic macro-eigenrays.

## VI. COMPARISON WITH MEASUREMENT DATA

In this section, the main theoretical results presented in Sections III and IV are verified by measurement data, which was first presented in [15]. The comparison is assessed in terms of the FCF  $r_{HH}(\nu')$ , average delay  $B_{\tau'}^{(1)}$ , delay spread  $B_{\tau'}^{(2)}$ , and the coherence bandwidth  $B_C$  of the UWA channel.

The experimental data was collected near the New Jersey shore in May 2009 by a team from Naval Research LAB. The water depth was about 80 m and the

Table C.1: Definition and selected values of the channel parameters.

Parameters	Definitions	Figs. 5–14	Figs. 16–19
$D_{sb}^{DA}, D_{bs}^{UA}$	Total distances that the DA and UA macro-eigenrays travel from $T_x$ to $R_x$	-	-
$\varphi_{sb}^{DA}, \varphi_{bs}^{UA}$	AOIs of the DA and UA macro-eigenrays at the receiver $R_x$	-	-
$y_1^T$	Distance between $T_x$ and the ocean surface	40 m	45.5 m
$y_1^R$	Distance between $R_x$ and the ocean surface	15 m	44 m
$y_1^T + y_2^T$	Water depth at the transmitter side	100 m	80 m
$D$	Total distance between $T_x$ and $R_x$ along the x-axis	1600 m	1500 m
$\phi$	Ocean-bottom slope angle	Various	Fig. 16: $0^\circ$ Figs. 17–18: Various Fig. 19: $0^\circ$ and $-0.2^\circ$
$\rho_s$	Density of the ocean water	1000 kg/m <sup>3</sup>	1000 kg/m <sup>3</sup>
$\rho_b$	Density of the ocean bed	1500 kg/m <sup>3</sup>	1500 kg/m <sup>3</sup>
$c_s$	Speed of sound in the ocean water	1500 m/s	1440 m/s
$c_b$	Speed of sound in the ocean bed	1600 m/s	1600 m/s
$\alpha_v^T$	Angle of motion of the transmitter	$180^\circ$	-
$\alpha_v^R$	Angle of motion of the receiver	$0^\circ$	-
$f_c$	Carrier frequency	10 kHz	17 kHz
$f_{\max}^T$	Maximum Doppler frequency associated with the transmitter $T_x$	20 Hz	0 Hz
$f_{\max}^R$	Maximum Doppler frequency associated with the receiver $R_x$	20 Hz	0 Hz
$c_R$	Rice factor	0.2	0.3
$\eta_S$	Ratio of the power of DA macro-eigenrays to the total power	0.5	0.5
$\eta_B$	Ratio of the power of UA macro-eigenrays to the total power	0.5	0.5
$N_S$	Maximum number of interactions between each DA macro-eigenray and the ocean surface	2	2 in Fig. 16, 1 in Figs. 17–19
$N_B$	Maximum number of interactions between each UA macro-eigenray and the ocean bottom	2	2 in Fig. 16, 1 in Figs. 17–19

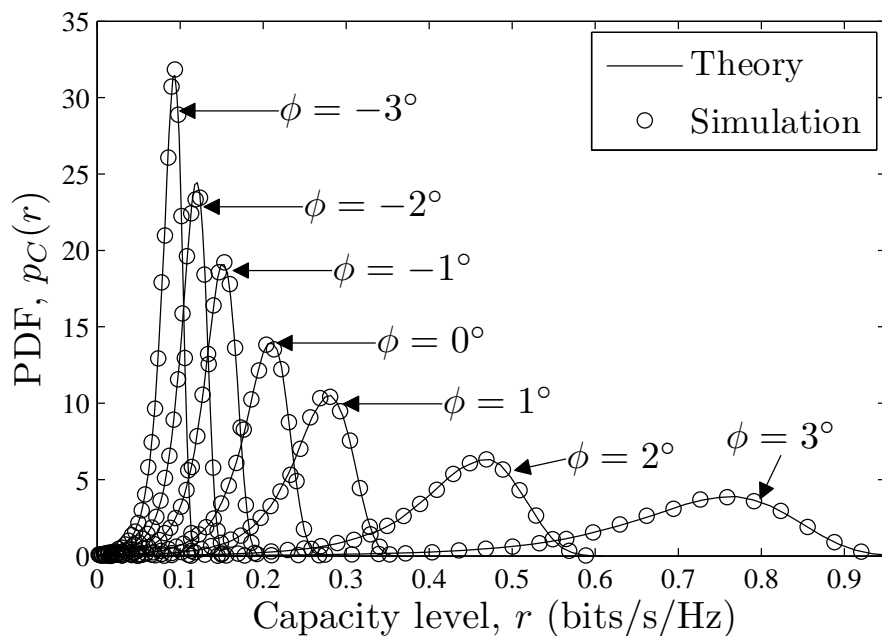


Figure C.6: The PDF of the instantaneous channel capacity.

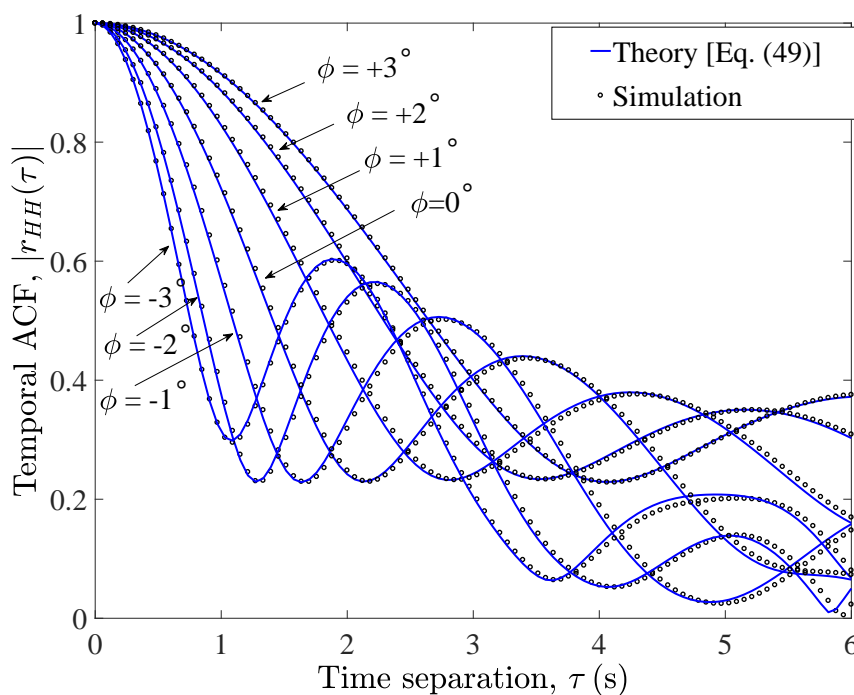


Figure C.7: Absolute value of the normalized temporal ACF  $|r_{HH}(\tau)|$  of the UWA channel model.

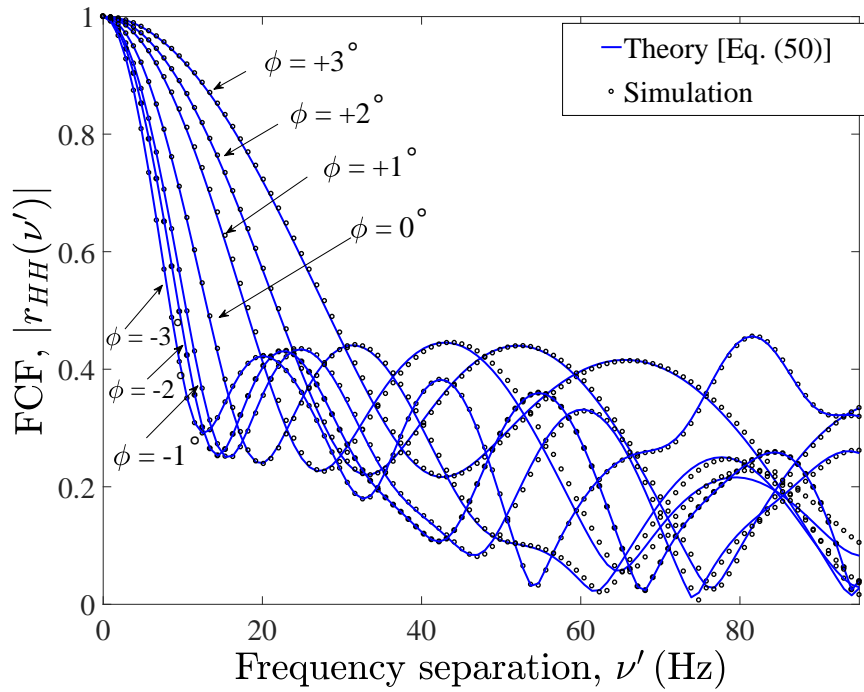


Figure C.8: Absolute value of the normalized FCF  $|r_{HH}(\nu')|$  of the UWA channel model.

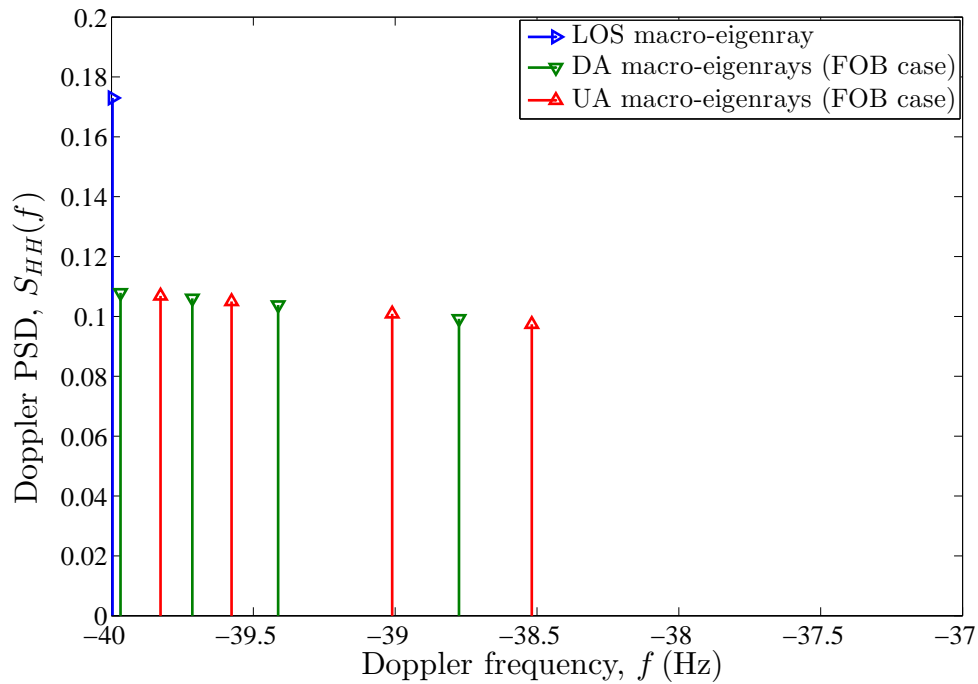


Figure C.9: The Doppler PSD  $S_{HH}(f)$  of the UWA channel model for the FOB case.

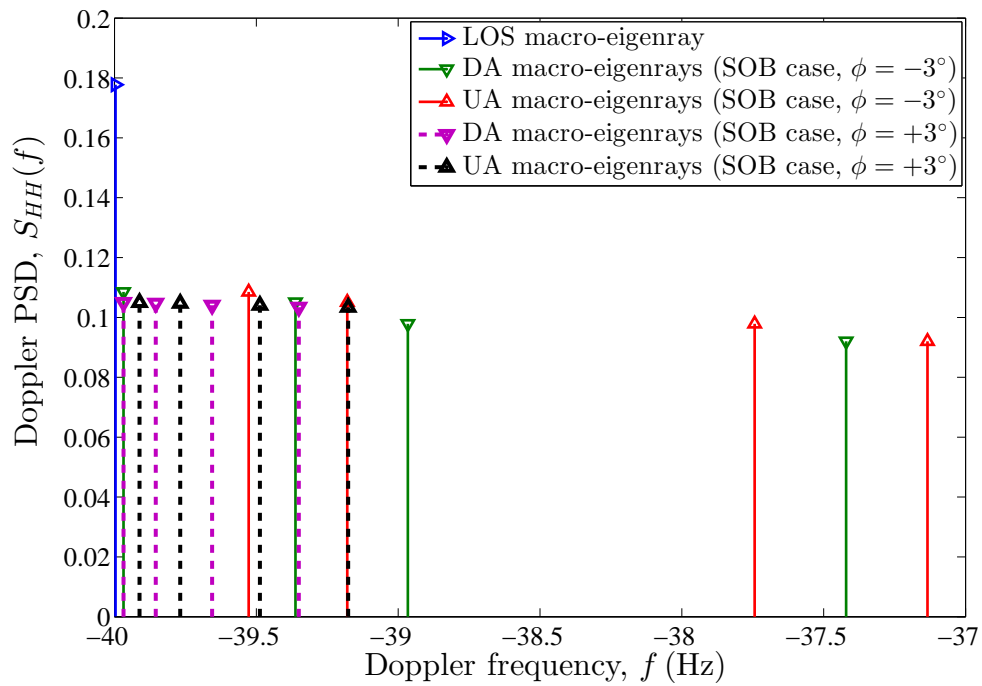


Figure C.10: The Doppler PSD  $S_{HH}(f)$  of the UWA channel model for the SOB case (slope angles  $\phi = 3^\circ$  and  $\phi = -3^\circ$ ).

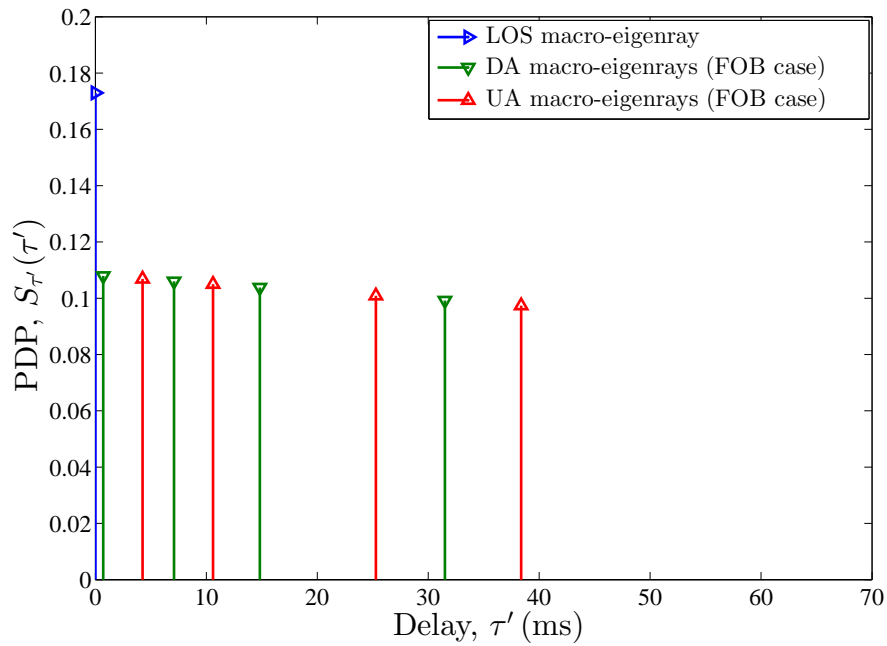


Figure C.11: The PDP  $S_{\tau'}(\tau')$  of the UWA channel model for the FOB case.

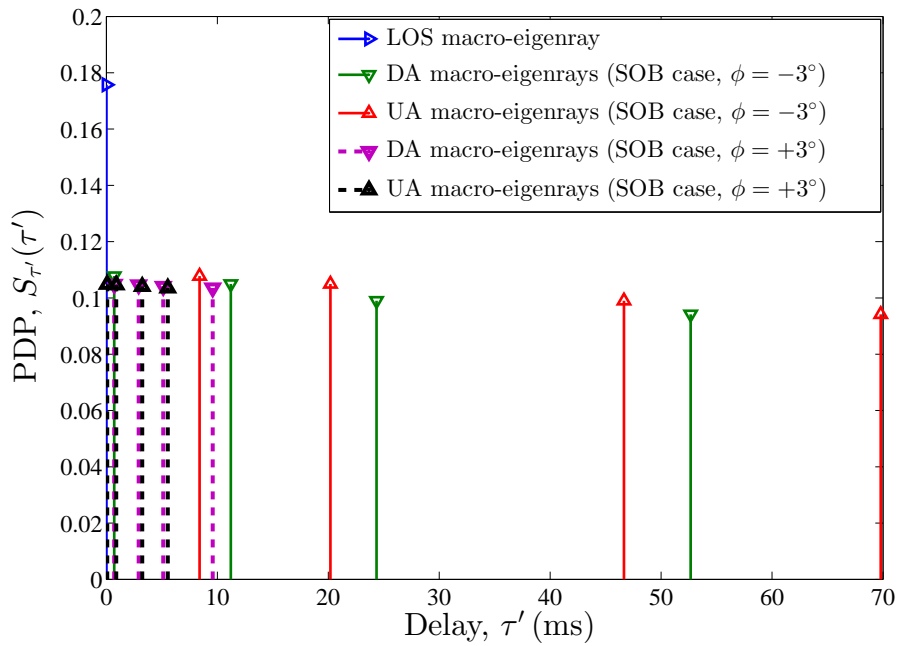


Figure C.12: The PDP  $S_{\tau'}(\tau')$  of the UWA channel model or the SOB case (slope angles  $\phi = 3^\circ$  and  $\phi = -3^\circ$ ).

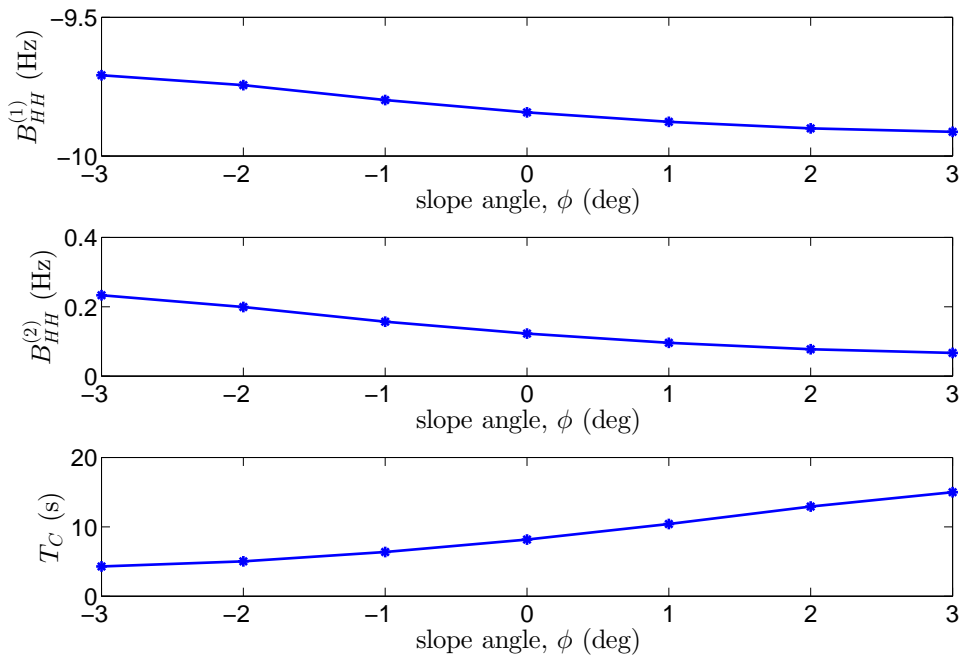


Figure C.13: The effect of the slope angle  $\phi$  on the average Doppler shift  $B_{HH}^{(1)}$ , Doppler spread  $B_{HH}^{(2)}$ , and the coherence time  $T_C$  of the UWA channel model.

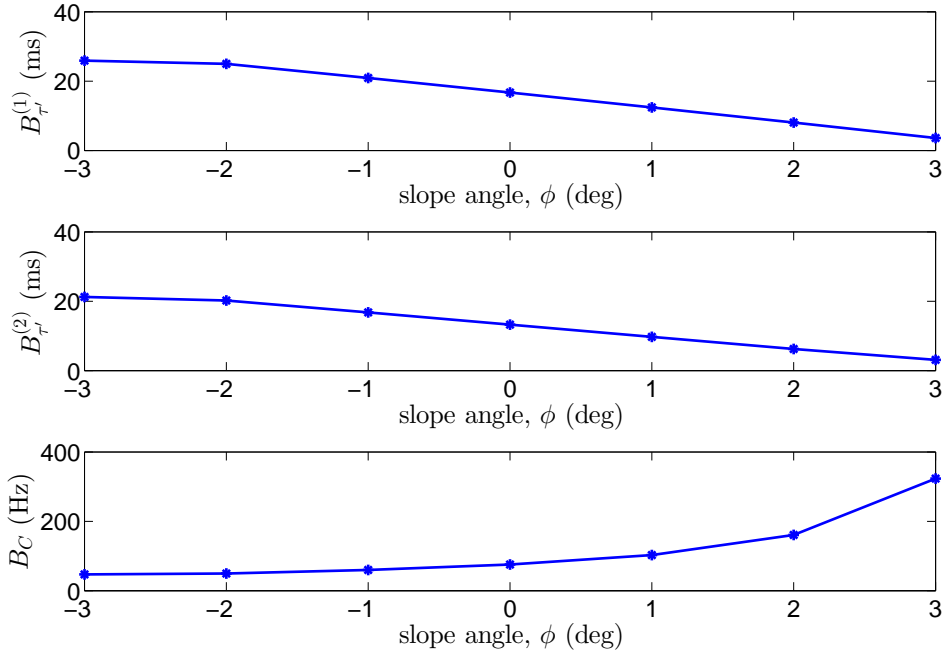


Figure C.14: The effect of the slope angle  $\phi$  on the average delay  $B_{\tau}^{(1)}$ , delay spread  $B_{\tau}^{(2)}$ , and the coherence bandwidth  $B_C$  of the UWA channel model.

sediment was a silty clay. The fixed transmitter was about 45.5 m below the surface float ( $y_1^T = 45.5$  m). The fixed receiver hydrophone was located at 44 m depth ( $y_1^R = 44$  m). The receiver was 1500 m away from the transmitter. Fig. C.15 demonstrates the measurement scenario of the underwater propagation scenario. The speed of sound in that shallow water environment was about 1440 m/s and the weather was rainy and windy. The channel measurements were performed at a carrier frequency of 17 kHz and a signal bandwidth of 4 kHz. More details regarding the communication system, what was sent and received, and the type of equipment (transducer and hydrophone) can be found in [31].

We start from the measured TVCIR  $\check{h}(\tau', t)$  which has been obtained by  $M = 20$  samples in the time domain over a time range of  $T_{\text{mes}} = 8$  s. Hence, the sampling interval  $\Delta t$  in the time domain is  $\Delta t = T_{\text{mes}}/M = 0.4$  s. In the delay domain, the measurement equipment allows a path resolution of  $\Delta\tau' = 0.125$  ms. The number of samples in the delay domain was equal to  $L = 90$ . In other words, the TVCIR  $\check{h}(\tau', t)$  has been measured at discrete time instances  $t_m = m\Delta t \in [0, T_{\text{mes}})$ ,  $m = 0, 1, \dots, M - 1$ , and at the discrete delay interval  $\tau'_l = l\Delta\tau'$ ,  $l = 0, 1, \dots, L - 1$ . Consequently, the measured TVCIR  $\check{h}(\tau', t)$  can be represented as a discrete TVCIR  $\check{h}[\tau'_l, t_m]$ . The discrete TVCTF  $\check{H}[f'_q, t_m]$  can be obtained by computing the

discrete Fourier transform of the TVCIR  $\check{h}[\tau'_l, t_m]$  with respect to delays  $\tau'_l$ . The discrete frequencies  $f'_q$  are given by  $f'_q = -B/2 + q\Delta f' \in [-B/2, B/2)$ ,  $q = 0, 1, \dots, Q - 1$  and  $B$  denotes the measurement bandwidth. The discrete FCF  $\check{r}_{HH}[\nu']$  can be obtained from the discrete TVCTF  $\check{H}[f'_q, t_m]$  as follows

$$\check{r}_{HH}[\nu'] = \frac{1}{M} \sum_{m=0}^{M-1} \check{H}[f'_q, t_m] \check{H}^*[f'_q + \nu', t_m]. \quad (\text{C.55})$$

The discrete PDP  $\check{S}_{\tau'}[\tau'_l]$  of the measurement data can be computed by taking the inverse Fourier transform of the discrete FCF  $\check{r}_{HH}[\nu']$  with respect to  $\nu'$ . The average delay  $\check{B}_{\tau'}^{(1)}$  and the delay spread  $\check{B}_{\tau'}^{(2)}$  of the measured channel can be computed by replacing the Continuous PDP  $S_{\tau'}(\tau')$  in (C.53) and (C.54), respectively, by the discrete PDP  $\check{S}_{\tau'}[\tau'_l]$ . As mentioned in Section IV-C, the coherence bandwidth  $\check{B}_c$  of the measured channel can be obtained from the channel delay spread  $\check{B}_{\tau'}^{(2)}$ , which is determined by  $\check{B}_c \approx 1/\check{B}_{\tau'}^{(2)}$ . The Rice factor  $c_R$  of the measured TVCIR  $\check{h}[\tau'_l, t_m]$  is obtained by using the moment method presented in [10].

In our simulation setup, we have considered nine macro-eigenrays including one LOS macro-eigenray, four DA macro-eigenrays, and four UA macro-eigenrays by assuming  $N_S = N_B = 2$ . Other model parameters based on the measurement scenario are defined in the fourth column of Table C.1. Fig. C.16 illustrates the PDP  $\check{S}_{\tau'}[\tau'_l]$  of the measured UWA channel and that of the simulation model. Note that in case of the simulation model seen in Fig. C.16, four macro-eigenrays which reach the receiver with delays of more than 10 ms, correspond to triple- and quadruple-bounced macro-eigenrays on the surface and bottom of the ocean. Such delayed macro-eigenrays are unobserved in the measurement data. Therefore, in our simulation model, we should consider only macro-eigenrays with single and double bounces on the surface and bottom of the ocean (i.e.,  $N_S = N_B = 1$ ). With reference to Fig. C.16, the number of macro-eigenrays captured from the measured UWA channel for single- and double-bounced macro-eigenrays is higher than those for the simulation model. Therefore, matching the PDP of the simulation model to that of the measured UWA channel is meaningless. For comparison purposes, we choose other statistical properties of the UWA channel, such as the FCF, average delay, delay spread, and the coherence bandwidth. Our proposed channel model has the ocean slope angle  $\phi$  as an extra degree of freedom compared with the FOB model. This feature can help us to achieve a better fitting between our proposed UWA channel model and the measurement data w.r.t. the statistical properties of the UWA channel. To find the optimum value of the ocean slope angle  $\phi$ , we con-

sider the error function

$$E(\phi) = w_1 \left| \check{\tilde{B}}_{\tau'}^{(1)} - \tilde{B}_{\tau'}^{(1)} \right|^2 + w_2 \left| \check{\tilde{B}}_{\tau'}^{(2)} - \tilde{B}_{\tau'}^{(2)} \right|^2 \quad (\text{C.56})$$

where  $\check{\tilde{B}}_{\tau'}^{(1)}$  ( $\check{\tilde{B}}_{\tau'}^{(1)}$ ) and  $\check{\tilde{B}}_{\tau'}^{(2)}$  ( $\check{\tilde{B}}_{\tau'}^{(2)}$ ) denote the average delay and the delay spread of the deterministic simulation model (measured UWA channel), respectively. Note that the deterministic simulation model can be computed from the realization of a sample function of the TVCTF  $H(f', t)$  of the UWA channel model presented in (C.38) by fixing the random phases  $\theta_0$ ,  $\theta_{sb}^{\text{DA}}$ , and  $\theta_{bs}^{\text{UA}}$ . The parameters  $w_1$  and  $w_2$  are weighting factors for the normalization which have been set to 0.5, i.e.,  $w_1 = w_2 = 0.5$ . The values of other channel model parameters are listed in the fourth column of Table C.1. We have also considered another error function to optimize the parameter  $\phi$  for the coherence bandwidth  $B_C$ , which is given by

$$E_{B_C}(\phi) = \left| \check{\tilde{B}}_C - \tilde{B}_C \right|^2 \quad (\text{C.57})$$

where  $\check{\tilde{B}}_C$  ( $\check{\tilde{B}}_C$ ) is the coherence bandwidth of the deterministic simulation model (measured UWA channel). From the results shown in Figs. C.17 and C.18, we can conclude that the minima of the error functions  $E(\phi)$  and  $E_{B_C}(\phi)$  are reached at  $\phi = -0.2^\circ$ . As can be seen in Figs. C.17 and C.18, the error functions  $E(\phi)$  and  $E_{B_C}(\phi)$  at the slope angle  $\phi = 0^\circ$  result in  $0.09 \times 10^{-3}$  and 1.21, respectively.

Table C.2 provides a comparison between the proposed channel model and the real-world UWA channel in terms of the average delay, delay spread, and the coherence bandwidth. With reference to Table C.2, a good agreement has been achieved between the simulation model (if  $\phi = -0.2^\circ$ ) and the measured UWA channel w.r.t. the aforementioned characteristic quantities. As our available measurement data was obtained in a mild SOB environment, where the slope angle  $\phi$  was low, the obtained characteristic quantities associated with the SOB model (with  $\phi = -0.2^\circ$ ) are close to those of the FOB model (with  $\phi = 0^\circ$ ). The superiority of the SOB case over the FOB case is more distinguishable under harsh SOB ocean conditions as discussed in Section V.

Fig. C.19 illustrates the FCF of the measured UWA channel in comparison with those of the simulation model for the FOB case and the SOB case by assuming  $\phi = -0.2^\circ$ . The values of the remaining channel model parameters are defined in the fourth column of Table C.1. As can be seen from Fig. C.19, three curves are similar to each other in terms of the curvature at the origin and trend. However, the SOB case demonstrates a better performance in approximating the FCF of the measurement data. It should be mentioned that the superiority of the SOB model

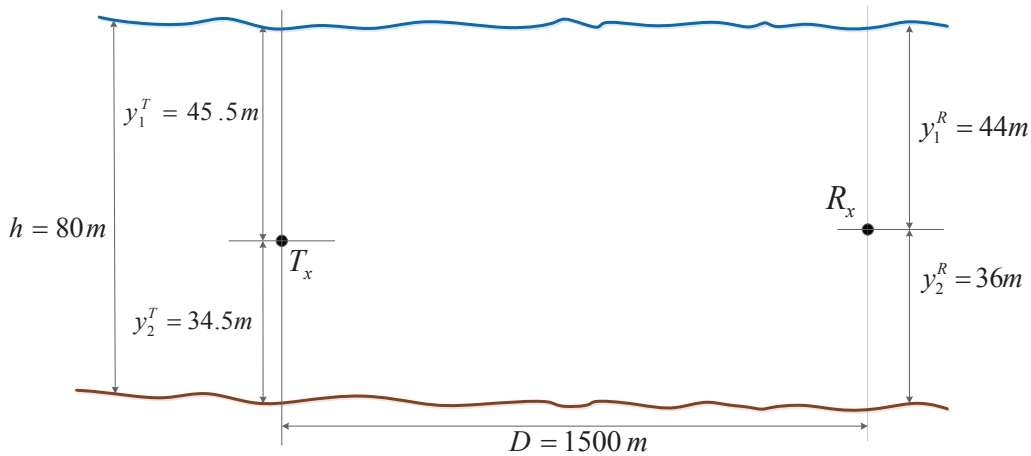


Figure C.15: The measurement scenario of the experiment.

Table C.2: Characteristic quantities of the measured UWA channel and the corresponding simulation model.

Characteristic quantities	Measured UWA channel	Simulation model ( $\phi = -0.2^\circ$ )	Simulation model ( $\phi = 0^\circ$ )
Average delay	$\check{B}_{\tau'}^{(1)} = 1.5$ ms	$\tilde{B}_{\tau'}^{(1)} = 1.495$ ms	$\tilde{B}_{\tau'}^{(1)} = 1.491$ ms
Delay spread	$\check{B}_{\tau'}^{(2)} = 2.4$ ms	$\tilde{B}_{\tau'}^{(2)} = 2.405$ ms	$\tilde{B}_{\tau'}^{(2)} = 2.41$ ms
Coherence bandwidth	$\check{B}_C = 416$ Hz	$\tilde{B}_C = 415.8$ Hz	$\tilde{B}_C = 414.9$ Hz

(over the FOB model) in approximating the FCF of the measurement data should be even more evident for ocean environments with considerable slope angles. To obtain a better fitting, we can consider clusters of micro-scatterers around macro-scatterers which results in having different eigenrays like the PDP of the measured UWA channel shown in Fig. C.16. In other words, to make the proposed channel model more realistic, it should be developed by taking micro-scattering effects into account.

## VII. CONCLUSION

In this paper, a new geometry-based UWA channel model has been developed under the assumption that the ocean surface and bottom are smooth and also that the ocean bottom slopes gently up/down. We have studied the waveguide model in the general form by considering the SOB case. The influence of the ocean-bottom slope angle on the statistical properties of the UWA channel model has been studied. The validity of the main analytical results is confirmed by measurement data. It has been shown that the slope angle has a considerable impact on the quantities of the UWA channel and has to be considered in the area of UWA channel modelling.

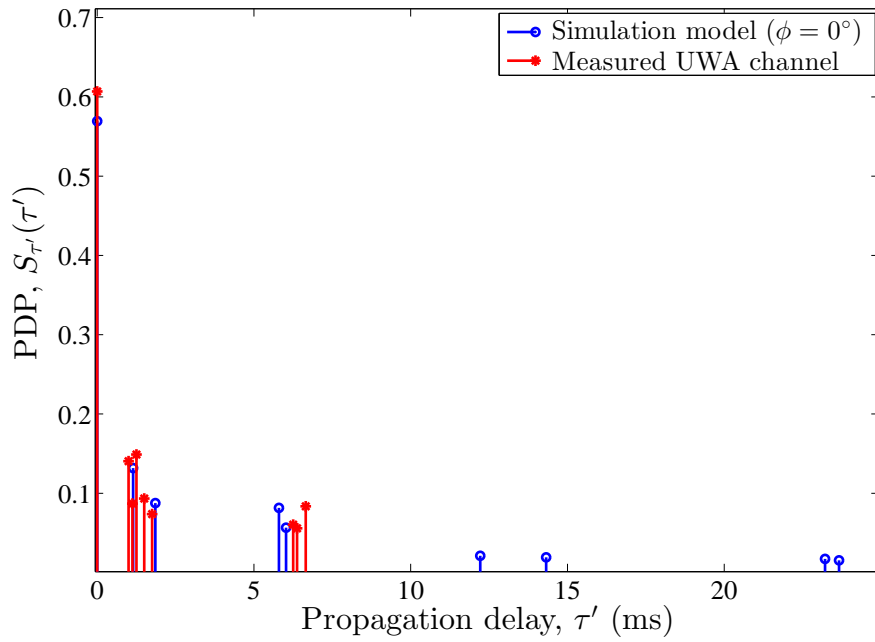


Figure C.16: The PDP of measured UWA channel in comparison with that of the simulation model.

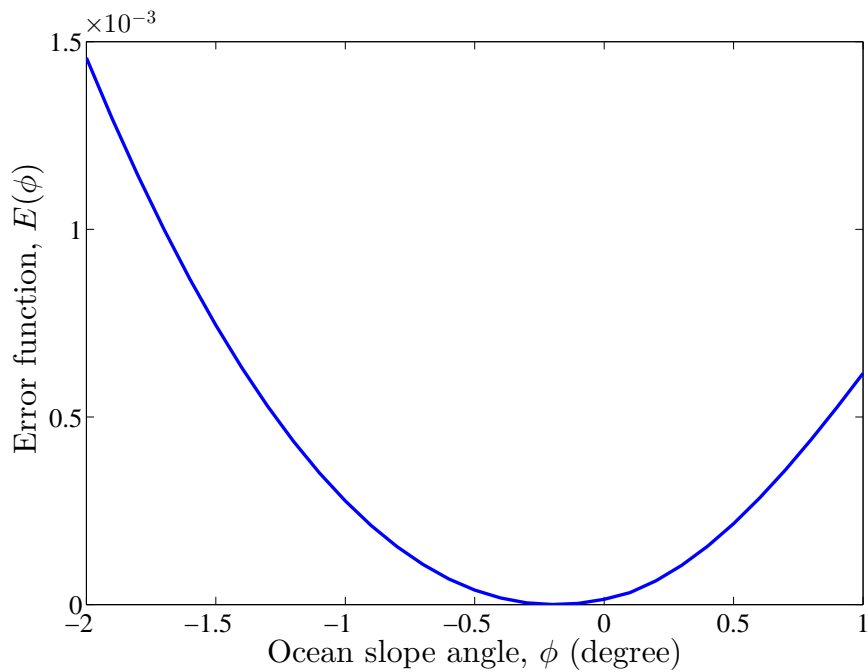


Figure C.17: Evaluation of the error function  $E(\phi)$  in (C.56) to find the optimum value of the slope angle  $\phi$ .

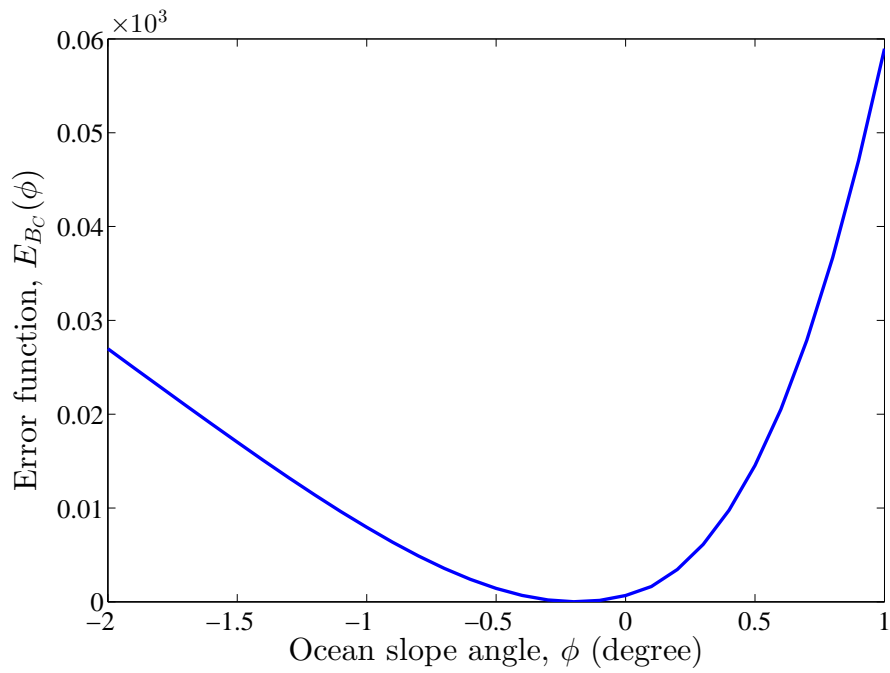


Figure C.18: Evaluation of the error function  $E_{BC}(\phi)$  in (C.57) to find the optimum value of the slope angle  $\phi$ .

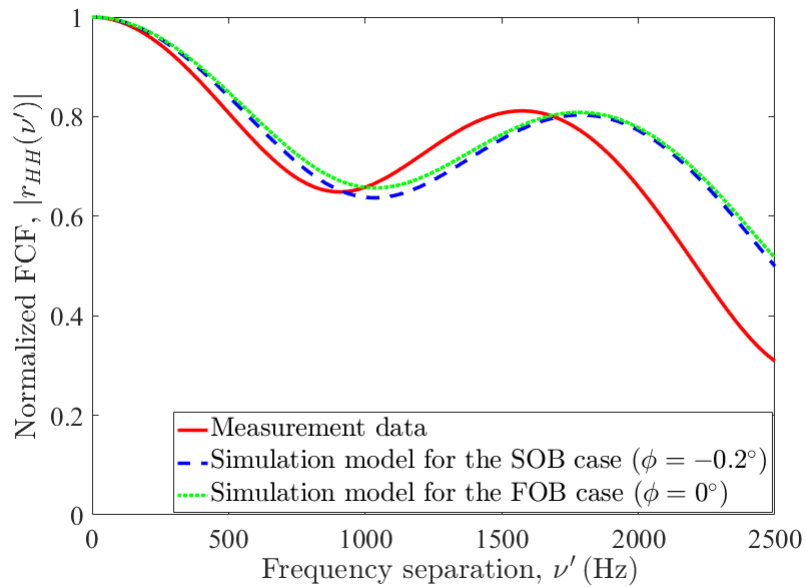


Figure C.19: The absolute value of the normalized FCF of the measured UWA channel against to those of the simulation model.

## APPENDIX

This appendix presents the proofs of (C.16) and (C.23). For brevity, we only focus on the double-bounce scattering scenario shown in Fig. C.20, in which the DA macro-eigenray arrives at the transmitter  $R_x$  after a single bounce on the bottom followed by a single bounce on the surface of the ocean, i.e.,  $N_S = 1$ ,  $s = 1$ , and  $\check{b} = 1$ . According to Fig. C.20, the transmitter  $T_x$  and the receiver  $R_x$  are located at the points  $T$  and  $R$ , respectively. As can be seen, the reflected macro-eigenray may be considered as emitted from the image source  $T'_x$  located at the point  $T'$  obtained by the specular reflection of the source  $T_x$  at the ocean bottom. In Fig. C.20, we also observe the image source  $T''_x$  at the point  $T''$ , which is obtained by the specular reflection of the image source  $T'_x$  at the ocean surface. The total distance that the DA macro-eigenray travels from  $T_x$  to  $R_x$  is thus equal to the side length  $T''R$ , which can be computed from the side lengths  $RI$  and  $T''I$  by

$$T''R = \sqrt{(RI)^2 + (T''I)^2}. \quad (\text{C.58})$$

Thus, we need to compute the lengths of the sides  $RI$  and  $T''I$  as a function of the parameters of the geometrical channel model, namely  $y_1^T, y_2^T, y_1^R, y_2^R, \phi$ , and  $D$ . The length of the left side  $T''I$  is  $T''I = T''F + FI$ , where  $FI = y_1^R$  and  $T''F = FT'$ . The length of  $FT'$  is given by  $FT' = y_1^T + ET'$ , where  $ET'$  is the right side of the triangle  $ETT'$ . Thus,  $ET' = TT' \cos(\phi)$ , where the side  $TT'$  is the left side of the triangle  $TT'B$ . With  $TT' = TB \cos(\phi)$  and  $TB = 2y_2^T$  it then follows  $ET' = 2y_2^T \cos^2(\phi)$ . Now, the length of the side  $T''I$  in (C.58) can be expressed by  $T''I = y_1^T + 2y_2^T \cos^2(\phi) + y_1^R$ . With reference to Fig. C.20, the length of the right side  $RI$  is equal to  $RG + GI$ , where  $RG = D$  and  $GI = TE$ . The side  $TE$  is given by  $TE = TT' \sin(\phi)$ , where  $TT' = 2y_2^T \cos(\phi)$ . Thus,  $TE = 2y_2^T \cos(\phi) \sin(\phi)$ . Now, the side  $RI$  can be obtained as  $RI = D + 2y_2^T \cos(\phi) \sin(\phi)$ . Finally, the total distance  $T''R$  can be computed by substituting the obtained expressions for  $T''I$  and  $RI$  in (C.58) as

$$T''R = \sqrt{(D + 2y_2^T \cos(\phi) \sin(\phi))^2 + (y_1^T + 2y_2^T \cos^2(\phi) + y_1^R)^2}. \quad (\text{C.59})$$

Notice that the same results follows from (C.16), if we set there  $s = 1$  and  $\check{b} = 1$ , i.e.,  $D_{11}^{\text{DA}} = T''R$ . The AOI  $\varphi_{11}^{\text{DA}}$  at  $R_x$  can be computed by applying the tangent law to the triangle  $T''IR$ , which results in

$$\varphi_{11}^{\text{DA}} = \arctan \left( \frac{D + 2y_2^T \cos(\phi) \sin(\phi)}{y_1^T + 2y_2^T \cos^2(\phi) + y_1^R} \right). \quad (\text{C.60})$$

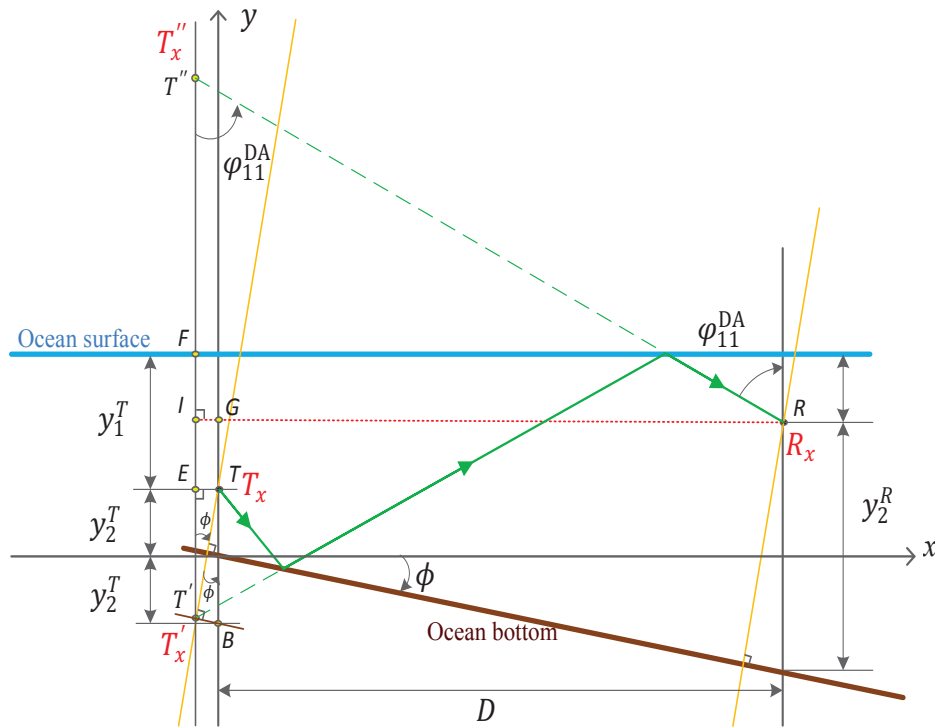


Figure C.20: Double-bounce scattering scenario for a DA macro-eigenray ( $N_S = 1$ ,  $s = 1$ , and  $\check{b} = 1$ ).

The expression above is exactly the same as the result obtained by setting  $s = 1$  and  $\check{b} = 1$  in (C.23). Similarly, we can compute all total distances  $D_{sb}^{\text{DA}}$  and  $D_{bs}^{\text{UA}}$  and the corresponding AOIs  $\varphi_{sb}^{\text{DA}}$  and  $\varphi_{bs}^{\text{UA}}$  by using the same procedure for all values of  $s$ ,  $\check{b}$ ,  $b$ , and  $\check{s}$ . The total distances  $D_{sb}^{\text{DA}}$  and  $D_{bs}^{\text{UA}}$  can be computed as

$$D_{sb}^{\text{DA}} = \sqrt{(D - f^{\text{DA}}(\phi))^2 + ((2s - 1)g^{\text{DA}}(\phi)y_1^T + 2\check{b}h^{\text{DA}}(\phi)y_2^T + y_1^R)^2} \quad (\text{C.61})$$

$$D_{bs}^{\text{UA}} = \sqrt{(D/\cos(\phi) - f^{\text{UA}}(\phi))^2 + (2\check{s}g^{\text{UA}}(\phi)y_1^T + (2b - 1)h^{\text{UA}}(\phi)y_2^T + y_2^R \cos(\phi))^2} \quad (\text{C.62})$$

respectively. The functions  $f^{\text{DA}}(\phi)$ ,  $g^{\text{DA}}(\phi)$ , and  $h^{\text{DA}}(\phi)$  in (C.61) are given by

$$f^{\text{DA}}(\phi) = \left\{ 4(s - 1)y_1^T + 2\check{b} [2 \cos^4(\phi)]^{(1 + \check{s}\check{b} - s - \check{b})} y_2^T \right\} \times \cos(\phi) \sin(\phi) \quad (\text{C.63a})$$

$$g^{\text{DA}}(\phi) = \left[ \frac{4}{3} \cos^2(\phi) - \frac{1}{3} \right]^{(s-1)} \quad (\text{C.63b})$$

## PAPER C: REFERENCES

$$h^{\text{DA}}(\phi) = \cos^2(\phi) [2 \cos^2(\phi) - 1]^{(1+s\check{s}-s-\check{b})}. \quad (\text{C.63c})$$

The functions  $f^{\text{UA}}(\phi)$ ,  $g^{\text{UA}}(\phi)$ , and  $h^{\text{UA}}(\phi)$  in (C.62) can be expressed by

$$f^{\text{UA}}(\phi) = \left\{ 2\check{s} [2 \cos^2(\phi)]^{(1+b\check{s}-\check{s}-b)} y_1^T + [4 \cos^2(\phi) + 1]^{(b-1)} y_2^T - y_2^R \right\} \sin(\phi) \quad (\text{C.64a})$$

$$g^{\text{UA}}(\phi) = [2 \cos^2(\phi) - 1]^{(1+b\check{s}-b-\check{s})} \cos(\phi) \quad (\text{C.64b})$$

$$h^{\text{UA}}(\phi) = \left[ \frac{4}{3} \cos^2(\phi) - \frac{1}{3} \right]^{(b-1)} \cos(\phi). \quad (\text{C.64c})$$

## PAPER C: REFERENCES

- [1] A. Abdi and H. Guo. Signal correlation modeling in acoustic vector sensor arrays. *IEEE Trans. Signal Process.*, 57(3):892–903, Mar. 2009.
- [2] E. Baktash, M. J. Dehghani, M. R. F. Nasab, and M. Karimi. Shallow water acoustic channel modeling based on analytical second order statistics for moving transmitter/receiver. *IEEE Trans. Signal Process.*, 63(10):2533–2545, May 2015.
- [3] A. Baptista, B. Howe, J. Freire, D. Maier, and C. T. Silva. Scientific exploration in the era of ocean observatories. *Comput. Sci. Eng.*, 10(3):53–58, May 2008.
- [4] P. J. Bouvet and A. Loussert. Capacity analysis of underwater acoustic MIMO communications. In *Proc. IEEE OCEANS*, pages 1–8, Sydney, NSW, Australia, May 2010.
- [5] L. M. Brekhovskikh and Y. P. Lysanov. *Fundamentals of Ocean Acoustics*. New York, NY, USA: Springer, 3rd edition, 2002.
- [6] M. Chitre. A high-frequency warm shallow water acoustic communications channel model and measurements. *J. Acoust. Soc. Amer.*, 122(5):2580–2586, November 2007.
- [7] M. Dalbro et al. Wireless sensor networks for off-shore oil and gas installations. In *Proc. 2nd Int. Conf. Sensor Technol. and Appl. (SENSORCOMM)*, pages 258–263, Aug. 2008.

## PAPER C: REFERENCES

- [8] M. C. Domingo. Overview of channel models for underwater wireless communication networks. *Phys. Commun.*, 1(3):163 – 182, Sep. 2008.
- [9] P. C. Etter. *Underwater Acoustic Modeling and Simulation*. New York, NY, USA: CRC Press, 4th edition, 2013.
- [10] I. S. Greenstein, D. G. Michelson, and V. Erceg. Moment-method estimation of the Ricean K-factor. *IEEE Commun. Lett.*, 3(6):175–176, Jun. 1999.
- [11] R. Hicheri, M. Pätzold, B. Talha, and N. Youssef. A study on the distribution of the envelope and the capacity of underwater acoustic channels. In *IEEE Int. Conf. Commun. Syst. (ICCS)*, pages 394–399, Macau, China, Nov. 2014.
- [12] F. B. Jensen, W. A. Kuperman, M. B. Porter, and H. Schmidt. *Computational Ocean Acoustics*. New York, NY, USA: Springer, 2nd edition, 2011.
- [13] X. Lurton. *An Introduction to Underwater Acoustics: Principles and Applications*. Heidelberg, Germany: Springer, 2nd edition, 2010.
- [14] M. Naderi, M. Pätzold, and A. G. Zajić. A geometry-based channel model for shallow underwater acoustic channels under rough surface and bottom scattering conditions. In *Proc. 5th Int. Conf. Commun. and Electron. (ICCE)*, pages 112–117, DaNang, Vietnam, Jul./Aug. 2014.
- [15] M. Naderi, M. Pätzold, and A. G. Zajić. The design of measurement-based underwater acoustic channel simulators using the INLSA algorithm. In *Proc. IEEE OCEANS*, pages 1–6, Genova, Italy, May 2015.
- [16] A. Papoulis. *Probability, Random Variables, and Stochastic Processes*. New York, NY, USA: McGraw-Hill, 4rd edition, 2002.
- [17] M. Pätzold. *Mobile Fading Channels*. Chichester, U.K.: John Wiley & Sons, 2nd edition, 2011.
- [18] M. Pätzold and B. Talha. On the statistical properties of sum-of-cisoids-based mobile radio channel models. In *Proc. 10th Int. Symp. Wireless Pers. Multimedia Commun. (WPMC)*, pages 394–400, Jaipur, India, Dec. 2007.
- [19] P. Qarabaqi and M. Stojanovic. Statistical modeling of a shallow water acoustic communication channel. In *Proc. Underwater Acoust. Meas. Conf.*, pages 1341–1350, Nafplion, Greece, Jun. 2009.

## PAPER C: REFERENCES

- [20] P. Qarabaqi and M. Stojanovic. Statistical characterization and computationally efficient modeling of a class of underwater acoustic communication channels. *IEEE J. Ocean. Eng.*, 38(4):701–717, Oct. 2013.
- [21] A. Radošević, J. G. Proakis, and M. Stojanovic. Statistical characterization and capacity of shallow water acoustic channels. In *Proc. IEEE EUROPE OCEANS*, pages 1–8, Bremen, Germany, May 2009.
- [22] M. T. Rashid, A. A. Ali, R. S. Ali, L. Fortuna, M. Frasca, and M. G. Xibilia. Wireless underwater mobile robot system based on ZigBee. In *Proc. Int. Conf. Future Commun. Netw. (ICFCN)*, pages 117–122, Apr. 2012.
- [23] C. E. Shannon. A mathematical theory of communications. *Bell Syst. Tech. J.*, 27:379–423, Jul./Oct. 1948.
- [24] D. Shin, S. Y. Na, J. Kim, and S. J. Baek. Fish robots for water pollution monitoring using ubiquitous sensor networks with sonar localization. In *Proc. Int. Conf. Convergence Inf. Technol.*, pages 1298–1303, Nov. 2007.
- [25] M. Stojanovic. On the relationship between capacity and distance in an underwater acoustic communication channel. In *Proc. 1st ACM Int. Workshop Underwater Netw. (WUWNet)*, pages 41–47, Los Angeles, CA, USA, Sep. 2006.
- [26] M. Stojanovic. Underwater acoustic communications: Design considerations on the physical layer. In *Proc. 5th Annu. Conf. Wireless Demand Netw. Syst. Services (WONS)*, pages 1–10, Jan. 2008.
- [27] E. Telatar. Capacity of multi-antenna Gaussian channels. *Trans. Emerg. Telecommun. Technol.*, 10(6):585–595, 1999.
- [28] T. C. Yang. A study of spatial processing gain in underwater acoustic communications. *IEEE J. Ocean. Eng.*, 32(3):689–709, Jul. 2007.
- [29] T. C. Yang. Toward continuous underwater acoustic communications. In *Proc. IEEE OCEANS*, pages 1–6, Quebec City, QC, Canada, Sep. 2008.
- [30] A. G. Zajić. Statistical modeling of MIMO mobile-to-mobile underwater channels. *IEEE Trans. Veh. Technol.*, 60(4):1337–1351, May 2011.
- [31] A. G. Zajić and G. F. Edelmann. Feasibility study of underwater acoustic communications between buried and bottom-mounted sensor network nodes. *IEEE J. Ocean. Eng.*, 38(1):109–116, Jan. 2013.

## PAPER C: REFERENCES

---

## **PAPER C: REFERENCES**

# Paper D

---

**Title:** The Design of Measurement-Based Underwater Acoustic Channel Simulators Using the INLSA Algorithm

**Authors:** Meisam Naderi<sup>1</sup>, Matthias Pätzold<sup>1</sup>, and Alenka G. Zajic<sup>2</sup>

**Affiliation:** <sup>1</sup> Faculty of Engineering and Science, University of Agder, P.O. Box 509, 4879 Grimstad, Norway

<sup>2</sup> School of Electrical and Computer Engineering, Georgia Institute of Technology, Atlanta, GA 30332-0280 USA

**Conference:** *Proc. IEEE OCEANS*, Genova, Italy, May 2015, pp. 1-6, DOI: 10.1109/OCEANS-Genova.2015.7271396

**Copyright ©:** IEEE

---

D



## **The Design of Measurement-Based Underwater Acoustic Channel Simulators Using the INLSA Algorithm**

Meisam Naderi, Matthias Pätzold, and Alenka G. Zajic

***Abstract*** — This paper utilizes the iterative nonlinear least square approximation (INLSA) algorithm for designing measurement-based wideband shallow underwater acoustic (UWA) channel simulators. Measurement-based channel simulators are essential for the test, optimization, and performance analysis of UWA communication systems. The aim is to fit the time-variant channel impulse response (TVCIR) of the simulation model to that of the measured UWA channel. The performance of the designed UWA channel simulator is assessed by comparing the time-frequency correlation function (TFCF), the power delay profile (PDP), and the probability density function (PDF) of the channel envelope with the corresponding quantities of the measured channel. The results of the assessment show an excellent match between the statistical properties of the UWA channel simulator, designed by the INLSA method, and those of the real-world UWA channel. It is also shown that the distribution of the channel envelope of our measurement data, which is collected from a shallow-water environment, follows closely the Rayleigh distribution.

***Keywords***—Measurement-based channel modelling, shallow underwater acoustic channels, iterative optimization, underwater acoustic communications, wideband channels, power delay profile, time-frequency correlation function.

## I. INTRODUCTION

Underwater acoustic (UWA) communication systems have been receiving noticeable attention in the past decade. UWA networks have been studied in various areas due to their potential applications in oceanography. For the design, test, and performance analysis of UWA communication systems, realistic channel models are required. This calls for the statistical analysis of UWA channels in terms of correlation functions, distribution of the channel envelope, and power delay profiles (PDPs). For the performance analysis of UWA communication systems, one usually resorts to computer simulations, which provide a powerful means to assess the system performance. They can also be used to confirm the correctness of theoretical results obtained analytically.

Recently, some few reference models for UWA channel have been developed in [8, 11, 16], however, none of them can precisely capture all physical properties of UWA channels. For instance, a stochastic reference channel model for wide-band MIMO mobile-to-mobile (M2M) UWA channels has been proposed in [16]. Therein, the reference model has been developed by combining the deterministic ray-tracing concept with statistical methods to account for the randomness of the propagation environment. In the absence of a standardized model for UWA channels, measurement-based channel modelling is an alternative approach to model the behavior of real-world UWA channels. However, it is a scenario-specific approach. For the design of a measurement-based channel simulator, we need to estimate the model parameters, including the path gains, Doppler frequencies, propagation delays, and phase shifts. Hence, sophisticated and efficient parameter computation methods are required to precisely estimate these model parameters from real-world measurement data. In the literature, many powerful parameter computation methods have been proposed. For example, an application of the estimation of signal parameters via rotational invariance techniques (ESPRIT) algorithm to design a measurement-based wideband channel model is presented in [6]. The space-alternating generalized expectation-maximization (SAGE) algorithm is another parameter computation method, which is widely used because of its high performance [5]. Furthermore, the iterative nonlinear least square approximation (INLSA) algorithm has been proposed in [15] to design measurement-based wide-band channel simulators. Therein, the authors showed that the INLSA algorithm has lower complexity and better performance compared with the SAGE algorithm. The INLSA has further been developed and refined in [1, 2, 4]. It has been shown in [3] that the INLSA outperforms the SAGE and ESPRIT algorithms with respect to their fitting accuracy to the autocorrelation function (ACF) of a given reference

model.

There are numerous studies focussing on the modelling of UWA channels, which are based on measured acoustic channel data collected in specific scenarios. For example, the probability density function (PDF) of the UWA channel envelope has been shown to be Rayleigh distributed in [13], [7]; while the authors of [10], [12] have reported that the envelope follows the Rice distribution. Besides these distributions, the channel envelope may also follow the lognormal distribution or the  $K$ -distribution as claimed in [14] and [17], respectively. These controversial studies demonstrate that there is a need for a realistic UWA channel simulator.

In this paper, we propose a sum-of-cisoids uncorrelated scattering (SOCUS) channel simulator based on shallow UWA measurement data. To obtain the experiment data, we launched a campaign to measure a shallow UWA channel. The measured data was used as a starting point for computing the TVCIR of the UWA channel. The objective is to design a channel simulator that emulates the TVCIR of the measured channel. Starting from the measurement-based channel simulator, we derive the time-variant channel transfer function (TVCTF), time-frequency correlation function (TFCF), PDP, and the channel envelope PDF. To determine the parameters of the simulation model, we employ the INLSA method developed in [4]. It needs to mention that the INLSA algorithm has not been applied to UWA communications. We will present a procedure that allows us to easily use it for the area of measurement-based UWA channel modelling. It will be shown that the INLSA algorithm estimates precisely the simulation model parameters and results in an excellent match to the statistical properties of real-world channels. Our numerical results show that a good fitting between the measured channel and the simulation model can be achieved with respect to the TVCIR, TFCF, PDP, and the channel envelope distribution.

The rest of this paper is organized as follows. In Section II, the wideband SOCUS channel simulation model is presented. Section III describes the utilized parameter computation method. Sections IV and V focus on the measurement scenario and the measurement results, respectively. The numerical results are illustrated in Section VI. Finally, the conclusions are drawn in Section VII.

## II. THE WIDEBAND CHANNEL SIMULATION MODEL

A measured UWA TVCIR  $\check{h}(\tau', t)$  of a single snapshot measurement scenario is usually limited in the time domain and the delay domain. Given a measured UWA TVCIR  $\check{h}(\tau', t)$ , our aim is to develop a channel simulation model such that the statistical properties of the simulation model are as close as possible to those of the

measured real-world channel.

### A. TVCIR

In this section, we adopt a channel simulation model with TVCIR  $\tilde{h}(\tau', t)$  based on the SOCUS model, which is an appropriate model for a large class of wideband measured channels under non-isotropic scattering conditions. The TVCIR  $\tilde{h}(\tau', t)$  of the SOCUS model is given by [9, Eq. (7.138)]

$$\tilde{h}(\tau', t) = \sum_{l=0}^{L-1} \sum_{n=1}^{N_l} c_{n,l} e^{j(2\pi f_{n,l}t + \theta_{n,l})} \delta(\tau' - \tau'_l) \quad (\text{D.1})$$

where  $L$  stands for the number of propagation paths which experience different propagation delays  $\tau'_l$ . It should be mentioned that the propagation delays  $\tau'_l$  and the number of paths  $L$  are obtained directly from the measured data. The symbol  $N_l$  denotes the number of paths having the same propagation delay. The  $n$ th component of the  $l$ th path is characterized by its path gain  $c_{n,l}$ , Doppler frequency  $f_{n,l}$ , and phase shift  $\theta_{n,l}$ . Since the propagation delays  $\tau'_l$  are achieved from the measured TVCIR  $\tilde{h}(\tau', t)$ , we need to determine the set of parameters  $\mathcal{P} = \{N_l, c_{n,l}, f_{n,l}, \theta_{n,l}\}$ . In this case, instead of computing the TVCIR  $\tilde{h}(\tau', t)$ , we compute the model parameters of the time-variant complex channel gains  $\tilde{\mu}_l(t)$  having the form

$$\tilde{\mu}_l(t) = \sum_{n=1}^{N_l} \tilde{\mu}_{n,l}(t) = \sum_{n=1}^{N_l} c_{n,l} e^{j(2\pi f_{n,l}t + \theta_{n,l})} \quad (\text{D.2})$$

where  $\tilde{\mu}_{n,l}(t)$  denotes the complex channel gain of the  $n$ th path corresponding to the delay  $\tau'_l$ .

### B. TVCTF

To analyze the performance of the channel simulator, we need to compare the statistical properties of the channel simulator, such as the TFCF, PDP, and the channel envelope PDF with those of the measured channel. For the computation of the TFCF, we first need to derive the TVCTF  $\tilde{H}(f', t)$ , which is obtained by taking the Fourier transform of the TVCIR  $\tilde{h}(\tau', t)$  with respect to propagation delays  $\tau'$ . This results in

$$\tilde{H}(f', t) = \sum_{l=0}^{L-1} \sum_{n=1}^{N_l} \tilde{\mu}_{n,l}(t) e^{-j2\pi f' \tau'_l} = \sum_{l=0}^{L-1} \tilde{\mu}_l(t) e^{-j2\pi f' \tau'_l}. \quad (\text{D.3})$$

### C. TFCF

As discussed in the previous section, the TVCTF enables us to compute the TFCF. Under the assumption that the UWA channel simulator is wide-sense stationary in frequency  $f'$  and time  $t$ , the TFCF  $\tilde{r}_{HH}(\nu', \tau)$  is given by [9, Eq. (7.145)]

$$\tilde{r}_{HH}(\nu', \tau) = \sum_{l=0}^{L-1} \sum_{n=1}^{N_l} c_{n,l}^2 e^{j2\pi(f_{n,l}\tau - \nu'\tau'_l)} \quad (\text{D.4})$$

where the symbols  $\nu'$  and  $\tau$  denote the frequency and time separation variables, respectively.

### D. PDP

The PDP  $\tilde{S}_{\tau'}(\tau')$  of the SOCUS channel simulator can be expressed by [9, Eq. (7.151)]

$$\tilde{S}_{\tau'}(\tau') = \sum_{l=0}^{L-1} \sum_{n=1}^{N_l} c_{n,l}^2 \delta(\tau' - \tau'_l). \quad (\text{D.5})$$

Note that the behavior of the PDP  $\tilde{S}_{\tau'}(\tau')$  is fully determined by the model parameters  $L$ ,  $N_l$ ,  $c_{n,l}$ , and  $\tau'_l$ . The average delay  $\tilde{B}_{\tau'}^{(1)}$  and the delay spread  $\tilde{B}_{\tau'}^{(2)}$  are defined by the first moment of the PDP  $\tilde{S}_{\tau'}(\tau')$  and the square root of the second central moment of the PDP  $\tilde{S}_{\tau'}(\tau')$ , respectively. According to [9, Eqs. (7.152) and (7.153)], the average delay  $\tilde{B}_{\tau'}^{(1)}$  and the delay spread  $\tilde{B}_{\tau'}^{(2)}$  of the SOCUS channel simulation model are given by

$$\tilde{B}_{\tau'}^{(1)} = \frac{\sum_{l=0}^{L-1} \sum_{n=1}^{N_l} c_{n,l}^2 \tau'_l}{\sum_{l=0}^{L-1} \sum_{n=1}^{N_l} c_{n,l}^2} \quad (\text{D.6})$$

and

$$\tilde{B}_{\tau'}^{(2)} = \sqrt{\frac{\sum_{l=0}^{L-1} \sum_{n=1}^{N_l} (c_{n,l} \tau'_l)^2}{\sum_{l=0}^{L-1} \sum_{n=1}^{N_l} c_{n,l}^2} - \left(\tilde{B}_{\tau'}^{(1)}\right)^2} \quad (\text{D.7})$$

respectively. The coherence bandwidth  $\tilde{B}_C$  of the channel simulator is approximately reciprocally proportional to the delay spread  $\tilde{B}_{\tau'}^{(2)}$ , i.e.,  $\tilde{B}_C \approx 1/\tilde{B}_{\tau'}^{(2)}$  [9, p. 350].

### E. PDF of the Channel Envelope

In this section, we analyze the PDF  $p_{|H|}(x)$  of the absolute value of the TVCTF  $|\tilde{H}(f', t)|$ . Following the analytics in [9, Sect. (4.5.2)], it can be shown that the PDF of the envelope process  $|\tilde{H}(f', t)| = |\sum_{l=0}^{L-1} \sum_{n=1}^{N_l} \tilde{\mu}_{n,l}(t) e^{-j2\pi f' \tau'_l}|$  of the SOCUS channel simulator is completely determined by the number of cisoids  $L \times N_l$  and the choice of the gains  $c_{n,l}$  according to

$$\tilde{p}_{|H|}(x) = (2\pi)^2 x \int_0^\infty \left[ \prod_{l=0}^{L-1} \prod_{n=1}^{N_l} J_0(2\pi |c_{n,l}| y) \right] J_0(2\pi x y) y dy \quad (\text{D.8})$$

where  $J_0(\cdot)$  denotes the zeroth-order Bessel function of the first kind.

### III. THE UTILIZED PARAMETER COMPUTATION METHOD

In this section, we briefly explain the parameter computation method used in this paper. For the parametrization of the channel simulator, the latest version of INLSA algorithm is used, as described in [4]. According to [4, Eq. (4)], the channel parameters are computed in  $L$  independent steps, each of which corresponds to the estimation of the parameters of the channel gain  $\tilde{\mu}_l(t)$  by minimizing the following error norm

$$\varepsilon_l = |\check{\mu}_l(t) - \tilde{\mu}_l(t)| \quad \forall l = 0, 1, \dots, L-1 \quad (\text{D.9})$$

where  $\check{\mu}_l(t)$  is the  $l$ th channel gain of the measured TVCIR  $\check{h}(\tau', t)$  at  $\tau' = \tau'_l$ , i.e.,  $\check{\mu}_l(t) = \check{h}(\tau'_l, t)$ . To solve each of the  $L$  minimization problems formulated by (D.9), the authors of [4] proposed an iterative parameter computation method according to the following steps

- Step 1: Set the iteration index  $q$  to zero.
- Step 2: Select the initial values  $c_{n,l}^{(0)}$ ,  $f_{n,l}^{(0)}$ , and  $\theta_{n,l}^{(0)}$  for all  $l = 0, 1, \dots, L-1$  and  $n = 1, 2, \dots, N_l$ .
- Step 3: Compute the auxiliary error function  $y_{n,l}^{(q)}(t_m)$  as

$$y_{n,l}^{(q)}(t_m) = \check{\mu}_l(t_m) - \sum_{p=1, p \neq n}^{N_l} c_{p,l}^{(q)} e^{j(2\pi f_{p,l}^{(q)} t_m + \theta_{p,l}^{(q)})} \quad (\text{D.10})$$

where  $t_m = m\Delta t$  ( $m = 0, 1, \dots, M-1$ ) is the discrete time, and  $\Delta t$  is the measurement time sampling interval.

- Step 4: Determine the value of gain  $c_{n,l}^{(q+1)}$  as follows

$$c_{n,l}^{(q+1)} = \frac{\operatorname{Re} \left\{ \mathbf{y}_{n,l}^{(q)} \right\}^T \operatorname{Re} \left\{ \mathbf{s}_{n,l}^{(q)} \right\} + \operatorname{Im} \left\{ \mathbf{y}_{n,l}^{(q)} \right\}^T \operatorname{Im} \left\{ \mathbf{s}_{n,l}^{(q)} \right\}}{\left( \mathbf{s}_{n,l}^{(q)} \right)^H \mathbf{s}_{n,l}^{(q)}} \quad (\text{D.11})$$

where the column vectors  $\mathbf{y}_{n,l}^{(q)}$  and  $\mathbf{s}_{n,l}^{(q)}$  contain the stacked values of  $y_{n,l}^{(q)}(t_m)$  and the exponential function  $e^{j(2\pi f_{n,l}^{(q)}t + \theta_{n,l}^{(q)})}$ , respectively. The operators  $\{\cdot\}^T$  and  $\{\cdot\}^H$  denote the transpose and the complex-conjugate transpose, respectively.

- Step 5: The Doppler frequency  $f_{n,l}^{(q+1)}$  is obtained as follows

$$f_{n,l}^{(q+1)} = \arg \min_{f_{n,l}} \left\| \mathbf{y}_{n,l}^{(q)} - c_{n,l}^{(q+1)} \mathbf{s}_{n,l}^{(q)} \right\|_2^2. \quad (\text{D.12})$$

- Step 6: The phase  $\theta_{n,l}^{(q+1)}$  can be computed as

$$\theta_{n,l}^{(q+1)} = \arg \min_{\theta_{n,l}} \left\| \mathbf{y}_{n,l}^{(q)} - c_{n,l}^{(q+1)} \mathbf{s}_{n,l}^{(q)} \right\|_2^2. \quad (\text{D.13})$$

The parameter computation procedure defined in Steps 3–6 is applied to each of the  $N_l$  paths, which corresponds to one iteration. The error norm  $\varepsilon_l$  in (D.9) is re-evaluated at the end of each iteration. In case of a noticeable change of  $\varepsilon_l$ , the iteration index  $q$  is increased by one, i.e.,  $q + 1 \rightarrow q$ . The parameter computation procedure is carried out again starting from Step 3. The iteration algorithm is terminated if the relative change in the error norm  $\varepsilon_l$  is below a given threshold  $\epsilon$ , i.e.,  $|\varepsilon_l^{(q+1)} - \varepsilon_l^{(q)}| < \epsilon$ .

#### IV. MEASUREMENT SCENARIO

The experimental data was collected near the New Jersey shore in May 2009 by a team from the School of Electrical and Computer Engineering at the Georgia Institute of Technology. The water depth was about 80 m and the sediment was a silty clay. Two stationary vertical arrays were placed near the water column. The stationary vertical transmit array named ASRA was about 45.57 m below the surface float ( $y_1^T = 45.57$  m). However, only the highest hydrophone had been used for transmission. On the receiver side, an acoustic communications and data storage (ACDS) stationary array named ACDS3, equipped with eight hydrophones with an aperture of 2.06 m was used. The first hydrophone was at 41.96 m depth ( $y_1^R = 41.96$  m), and all other hydrophones were lower with a hydrophone spacing of 2.06 m. The ACDS3 receiver was 1500 m away from the ASRA transmitter. The speed of sound in that shallow water environment was about 1440 m/s and the weather was rainy

and windy. The  $1 \times 8$  single-input multiple-output (SIMO) channel measurements were performed at a carrier frequency of 17 kHz and a signal bandwidth of 4 kHz. The signal, used for channel sounding, was an inverse linear frequency modulation (LFM) chirp. Fig. D.1 demonstrates the measurement configuration of the underwater propagation scenario.

## V. MEASUREMENT RESULTS

In this section, we analyse the measured data by computing the statistical properties of the measured UWA channel.

### A. Measured TVCIR

We start from the TVCIR  $\check{h}(\tau', t)$  which has been measured by  $M = 20$  samples in the time domain over a time range of  $T_{\text{mes}} = 8$  s. Hence, the sampling interval  $\Delta t$  in the time domain is  $\Delta t = T_{\text{mes}}/M = 0.4$  s. In the delay domain, the measurement equipment allows a path resolution of  $\Delta\tau' = 0.125$  ms. The number of samples in the delay domain was equal to  $L = 90$ . In other words, one can say that the TVCIR  $\check{h}(\tau', t)$  has been measured at discrete time instances  $t_m = m\Delta t \in [0, T_{\text{mes}})$ ,  $m = 0, 1, \dots, M-1$ , and at the discrete delay interval  $\tau'_l = l\Delta\tau'$ ,  $l = 0, 1, \dots, L-1$ . Consequently, the TVCIR  $\check{h}(\tau', t)$  can be represented as a discrete TVCIR  $\check{h}[\tau'_l, t_m]$ .

### B. Measured TVCTF

The discrete TVCTF  $\check{H}[f'_k, t_m]$  can be obtained by computing the discrete Fourier transform of the TVCIR  $\check{h}[\tau'_l, t_m]$  with respect to  $\tau'$ , which results in

$$\check{H}[f'_k, t_m] = \sum_{l=0}^{L-1} \check{h}[\tau'_l, t_m] e^{-j2\pi\tau'_l f'_k} \quad (\text{D.14})$$

where the discrete frequencies  $f'_k$  are given by  $f'_k = -B/2 + k\Delta f' \in [-B/2, B/2)$ ,  $k = 0, 1, \dots, K-1$  and  $B$  stands for the measurement bandwidth.

### C. Measured TFCF

The discrete TFCF  $\check{r}_{HH}[\nu'_p, \tau_q]$  can be obtained from the discrete TVCTF  $\check{H}[f'_k, t_m]$  and can be expressed by

$$\check{r}_{HH}[\nu', \tau] = \frac{1}{MK} \sum_{k=0}^{K-1} \sum_{m=0}^{M-1} \check{H}[f'_k, t_m] \check{H}^*[f'_k + \nu', t_m + \tau] \quad (\text{D.15})$$

where the discrete frequency separation  $\nu'$  and the discrete time separation  $\tau$  are given by  $\nu' = 0, \Delta f', \dots, (K-1)\Delta f'$ , and  $\tau = 0, \Delta t, \dots, (M-1)\Delta t$ , respec-

tively.

#### D. Measured PDP

The discrete PDP  $\check{S}_{\tau'}[\tau'_l]$  of the measurement data can be computed from the discrete TVCIR  $\check{h}[\tau'_l, t_m]$  as follows

$$\check{S}_{\tau'}[\tau'_l] = \frac{1}{M} \sum_{m=0}^{M-1} |\check{h}[\tau'_l, t_m]|^2. \quad (\text{D.16})$$

The average delay  $\check{B}_{\tau'}^{(1)}$  is defined by the first moment of the PDP  $\check{S}_{\tau'}[\tau'_l]$ , and the delay spread  $\check{B}_{\tau'}^{(2)}$  is defined by the square root of the second central moment of the PDP  $\check{S}_{\tau'}[\tau'_l]$  which are given by [9, p. 348]

$$\check{B}_{\tau'}^{(1)} = \frac{\sum_{l=0}^{L-1} \check{p}_{\tau'}[\tau'_l] \tau'_l}{\sum_{l=0}^{L-1} \check{p}_{\tau'}[\tau'_l]} \quad (\text{D.17})$$

and

$$\check{B}_{\tau'}^{(2)} = \sqrt{\frac{\sum_{l=0}^{L-1} \check{p}_{\tau'}[\tau'_l] \tau'^2_l}{\sum_{l=0}^{L-1} \check{p}_{\tau'}[\tau'_l]} - \left(\check{B}_{\tau'}^{(1)}\right)^2} \quad (\text{D.18})$$

respectively. As mentioned in Section II-D, the coherence bandwidth  $\check{B}_c$  of the measured channel can be obtained from the channel delay spread  $\check{B}_{\tau'}^{(2)}$ , which is determined by  $\check{B}_c \approx 1/\check{B}_{\tau'}^{(2)}$ .

#### E. PDF of the Measured Channel Envelope

The PDF  $\check{p}_{|H|}(x)$  of the measured channel envelope  $|\check{H}(f', t)|$  can be obtained first by using the command *hist* in MATLAB<sup>®</sup>, which creates a histogram containing a number of equally spaced bins. Then, the histogram is normalized by dividing the number of events in each bin by the total number of events. The candidate distributions can then be fitted to the obtained PDF  $\check{p}_{|H|}(x)$  of the measured channel envelope by means of the command *fitdist*.

## VI. NUMERICAL RESULTS

In this section, we illustrate and verify the simulation results presented in the previous sections. For brevity, we focus here only on the single-input single-output (SISO) case. The performance of the channel simulator has been compared with that of the measured channel by analyzing the TVCIR and the statistical properties, including the TFCF, PDP, and the PDF of the channel envelope. After implementing the INLSA algorithm in MATLAB<sup>®</sup> and determining the UWA simulation model

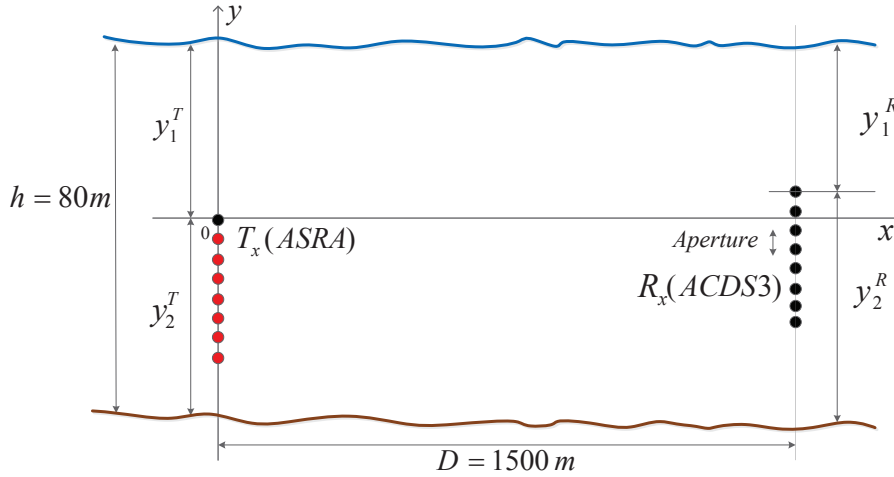


Figure D.1: The measurement configuration of the experiment for SIMO fixed-to-fixed (F2F) communication.

parameter set  $\mathcal{P} = \{N_l, c_{n,l}, f_{n,l}, \theta_{n,l}\}$ , we are able to compute the channel gains  $\tilde{\mu}_l(t)$ . The TVCIR  $\tilde{h}(\tau', t)$  of the simulation model can be computed by taking into account that the corresponding propagation delay  $\tau'_l$  of each channel gain  $\tilde{\mu}_l(t)$  and the number of the Paths  $L$  are obtained directly from the measurement data.

Figs. D.2 and D.3 show the absolute value of the baseband measurement TVCIR  $|\check{h}(\tau', t)|$  and the resulting TVCIR  $|\tilde{h}(\tau', t)|$  of the simulation model, represented in (D.1), respectively. As can be seen, there is an excellent match between these two figures. This excellent match can be expected for other statistical properties of the UWA channel. Fig. D.4 depicts the absolute value of the normalized TFCF  $|\check{r}_{HH}(\nu', \tau)|$  of the measured channel. The absolute value of the normalized TFCF  $|\tilde{r}_{HH}(\nu', \tau)|$  of the simulation model is shown in Fig. D.5. From the inspection of Figs. D.4 and D.5, we can conclude that the TFCF of the simulation model is well fitted to that of the measurement data.

Fig. D.6 depicts a comparison between the PDP  $\check{S}_{\tau'}(\tau')$  of the measurement data and the corresponding PDP  $\tilde{S}_{\tau'}(\tau')$  of the simulation model designed by using the INLSA algorithm. As can be seen, a good match can be achieved between the measurement data and the simulation model. Table D.1 shows the characteristic quantities of the UWA channel obtained from the measurement data and the simulation model. With reference to Table D.1, there is a good match between the values obtained from the real-world data and the simulation model by using the INLSA parameter computation method. According to the simulation results, the value of the coherence bandwidth is about 420Hz, which is very small compared to terrestrial wireless channels. This small value is caused by the large value of the UWA channel delay spread, which is common for UWA channels.

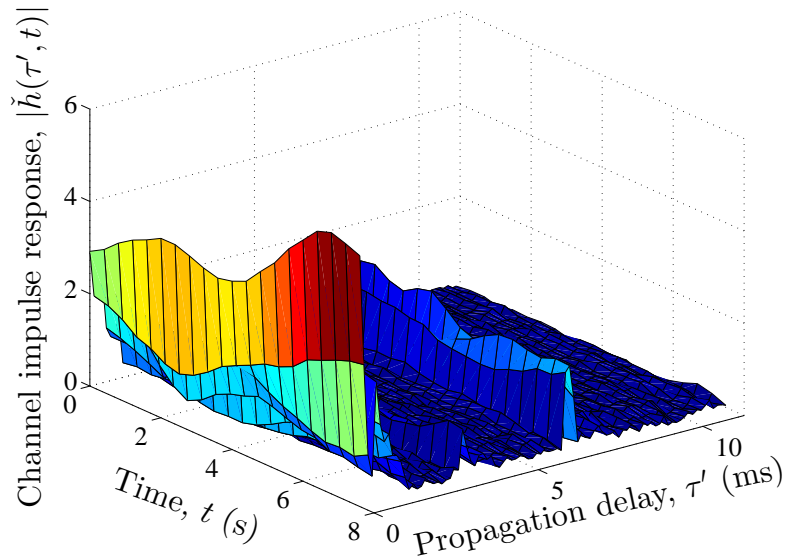

 Figure D.2: Absolute value of the TVCIR  $|\check{h}(\tau', t)|$  of the measured UWA channel.

Table D.1: Characteristic quantities of the UWA channel.

$R$	Channel parameter	Measured channel	Simulation model
1	Average delay $B_{\tau'}^{(1)}$	1.5 ms	1.46 ms
2	Delay spread $B_{\tau'}^{(2)}$	2.4 ms	2.35 ms
3	Coherence bandwidth $B_C$	$\approx 416$ Hz	$\approx 424$ Hz

Fig. D.7 illustrates a comparison between the channel envelope PDF by using the approaches represented in Sections II-E and V-E. The results show that there is a good fitting between the channel envelope PDF of the measurement data provided by numerical computations and that of the analytical results represented in (D.8). We can also observe that all distributions follow the Rayleigh distribution.

## VII. CONCLUSION

In this paper, we have used the latest version of the INLSA algorithm for designing measurement-based UWA channel simulators. The algorithm has been applied to UWA measurement data to estimate the parameters of the channel simulator. The TVCIR, TFCF, PDP, and the channel envelope distribution of the channel simulator have been matched to corresponding quantities of the measured channel. It has been shown that the INLSA algorithm precisely estimates the channel model parameters and provides an excellent fitting to measured UWA channels. We have also shown that the distribution of the UWA channel envelope follows closely the Rayleigh distribution.

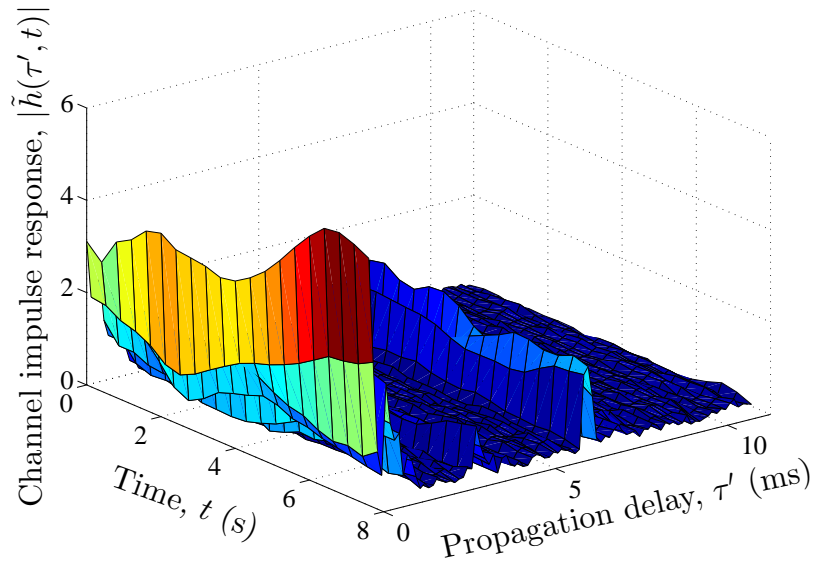


Figure D.3: Absolute value of the TVCIR  $|\tilde{h}(\tau', t)|$  of the simulation model.

D

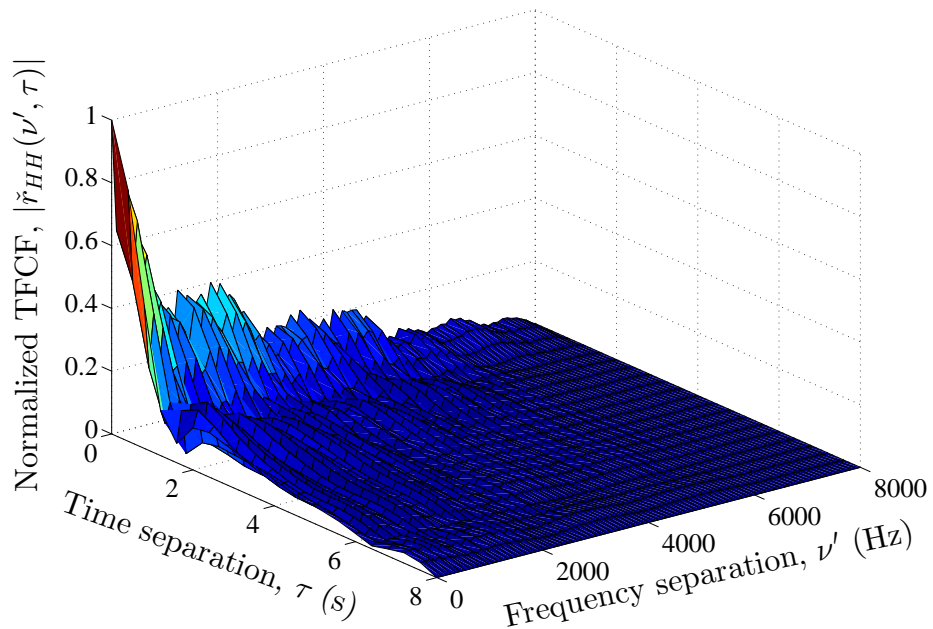


Figure D.4: Absolute value of the normalized TFCF  $|\tilde{r}_{HH}(\nu', \tau)|$  of the measured UWA channel.

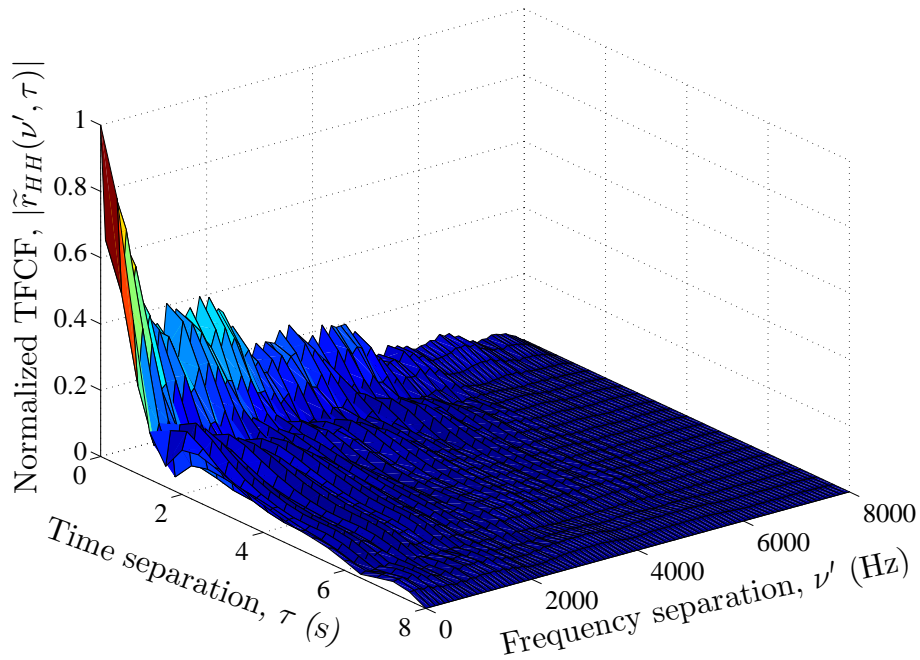


Figure D.5: Absolute value of the normalized TFCF  $|\tilde{r}_{HH}(\nu', \tau)|$  of the simulation model.

D

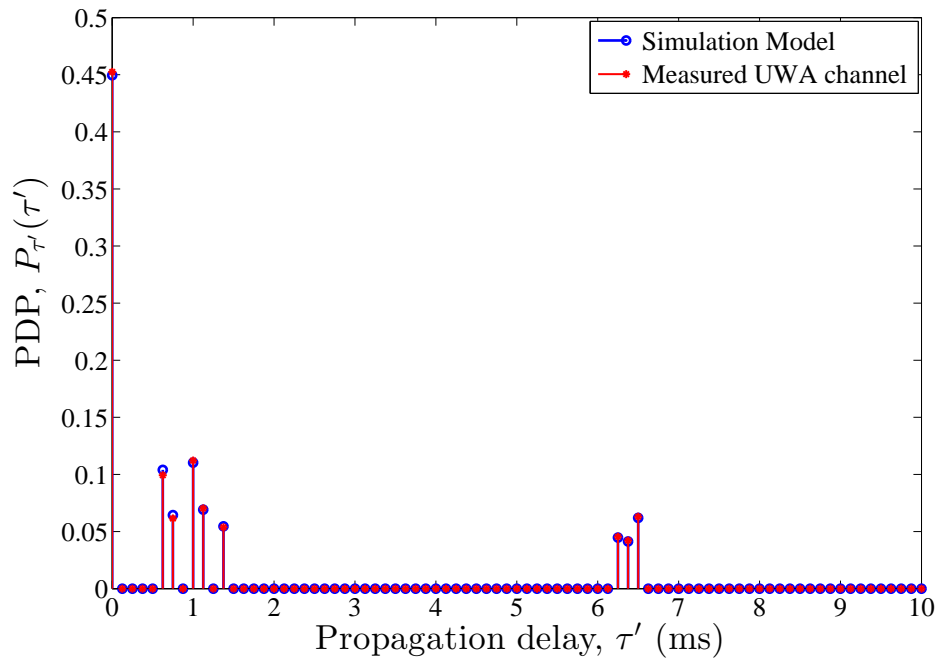


Figure D.6: The PDP  $\tilde{S}_{\tau'}(\tau')$  of the UWA measured channel compared to the PDP  $\tilde{S}_{\tau'}(\tau')$  of the simulation model.

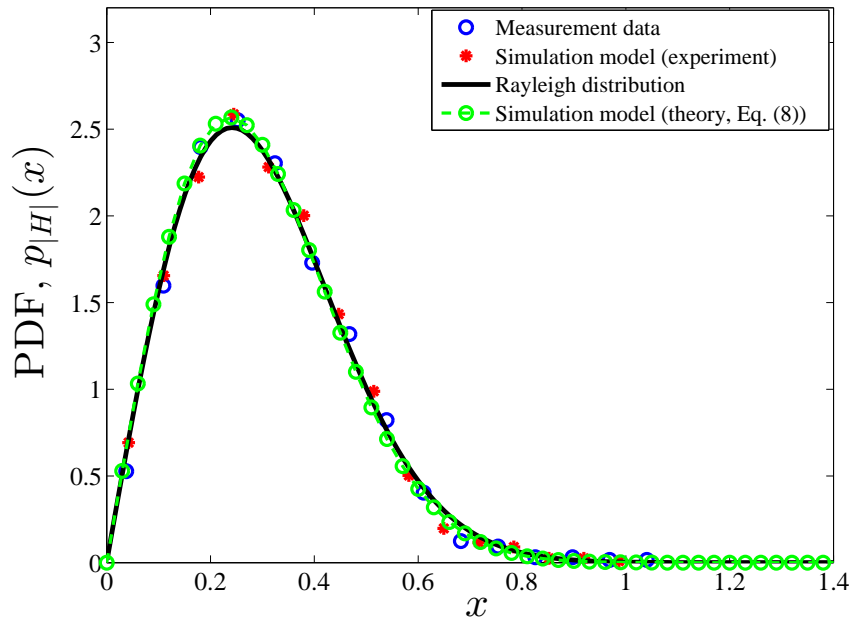


Figure D.7: The PDF of the UWA channel envelope .

#### PAPER D: REFERENCES

- [1] A. Fayziyev and M. Pätzold. An improved iterative nonlinear least square approximation method for the design of measurement-based wideband mobile radio channel simulators. In *Proc. Int. Conf. Adv. Technolo. for Commun. (ATC)*, pages 106–111, Danang, Vietnam, Aug. 2011.
- [2] A. Fayziyev and M. Pätzold. An improved iterative nonlinear least square approximation method for the design of SISO wideband mobile radio channel simulators. *REV J. Electron. Commun.*, 2(1–2):19–25, Jan./Jun. 2012.
- [3] A. Fayziyev and M. Pätzold. The performance of the INLSA in comparison with the SAGE and ESPRIT algorithms. In *Proc. Int. Conf. Adv. Technol. for Commun. (ATC)*, Hanoi, Vietnam, Oct. 2014.
- [4] A. Fayziyev, M. Pätzold, E. Masson, Y. Cocheril, and M. Berbineau. A measurement-based channel model for vehicular communications in tunnels. In *Proc. IEEE Conf. Wireless Commun. and Netw. (WCNC)*, pages 128–133, Istanbul, Turkey, Apr. 2014.
- [5] B. H. Fleury, M. Tschudin, R. Heddergott, D. Dahlhaus, and K. I. Pedersen. Channel parameter estimation in mobile radio environments using the SAGE algorithm. *IEEE J. Sel. Areas Commun.*, 17(3):434–450, Mar. 1999.

## PAPER D: REFERENCES

- [6] J. Fuhl, J. P. Rossi, and E. Bonek. High-resolution 3-D direction-of-arrival determination for urban mobile radio. *IEEE Antennas Propag. Mag.*, 45(4):672–682, April 1997.
- [7] R. Galvin and R. F. W. Coats. A stochastic underwater acoustic channel model. In *Proc. IEEE OCEANS Prospects for the 21st Century*, volume 1, pages 203–210, Sep. 1996.
- [8] M. Naderi, M. Pätzold, and A. G. Zajić. A geometry-based channel model for shallow underwater acoustic channels under rough surface and bottom scattering conditions. In *Proc. 5th Int. Conf. Commun. and Electron. (ICCE)*, pages 112–117, DaNang, Vietnam, Jul./Aug. 2014.
- [9] M. Pätzold. *Mobile Fading Channels*. Chichester, U.K.: John Wiley & Sons, 2nd edition, 2011.
- [10] P. Qarabaqi and M. Stojanovic. Statistical modeling of a shallow water acoustic communication channel. In *Proc. Underwater Acoust. Meas. Conf.*, pages 1341–1350, Nafplion, Greece, Jun. 2009.
- [11] P. Qarabaqi and M. Stojanovic. Statistical characterization and computationally efficient modeling of a class of underwater acoustic communication channels. *IEEE J. Ocean. Eng.*, 38(4):701–717, Oct. 2013.
- [12] A. Radosevic, J. G. Proakis, and M. Stojanovic. Statistical characterization and capacity of shallow water acoustic channels. In *Proc. IEEE EUROPE OCEANS*, pages 1–8, Bremen, Germany, May 2009.
- [13] F.-X. Socheleau, J. M. Passerieux, and C. Laot. Characterisation of time-varying underwater acoustic communication channel with application to channel capacity. In *Proc. Underwater Acoust. Meas. Conf.*, Nafplion, Greece, June 2009.
- [14] B. Tomasi, P. Casari, L. Badia, and M. Zorzi. A study of incremental redundancy hybrid ARQ over Markov channel models derived from experimental data. In *Proc. 5th ACM Int. Workshop on UnderWater Networks (WUWNet)*, pages 1–8, Massachusetts, USA, Sep./Oct. 2010.
- [15] D. Umansky and M. Pätzold. Design of measurement-based wideband mobile radio channel simulators. In *Proc. 4th IEEE Int. Symp. Wireless Commun. Syst. (ISWCS)*, pages 229–235, Trondheim, Norway, Oct. 2007.

## PAPER D: REFERENCES

- [16] A. G. Zajić. Statistical modeling of MIMO mobile-to-mobile underwater channels. *IEEE Trans. Veh. Technol.*, 60(4):1337–1351, May 2011.
- [17] J. Zhang, J. Cross, and Y. R. Zheng. Statistical channel modeling of wireless shallow water acoustic communications from experiment data. In *Proc. Conf. Military Commun. (MILCOM)*, pages 2412–2416, Oct. 2010.

# Paper E

---

**Title:** Modelling the Doppler Power Spectrum of Non-Stationary Underwater Acoustic Channels Based on Doppler Measurements

**Authors:** Meisam Naderi<sup>1</sup>, Do Viet Ha<sup>2</sup>, Van Duc Nguyen<sup>2</sup>, and Matthias Pätzold<sup>1</sup>

**Affiliation:** <sup>1</sup> Faculty of Engineering and Science, University of Agder, P.O. Box 509, 4879 Grimstad, Norway

<sup>2</sup> School of Electronics and Telecommunications, Hanoi University of Science and Technology, Hanoi, Vietnam

**Conference:** *Proc. IEEE OCEANS*, Aberdeen, Scotland (accepted), Jun. 2017, DOI: ...

**Copyright ©:** IEEE

---



# **Modelling the Doppler Power Spectrum of Non-Stationary Underwater Acoustic Channels Based on Doppler Measurements**

Meisam Naderi, Do Viet Ha, Van Duc Nguyen, and Matthias Pätzold

**Abstract** — This paper proposes a non-stationary time-continuous simulation model for wideband shallow underwater acoustic (UWA) channels based on measured Doppler power spectrums (DPSs). Measurement-based channel simulators are essential for the test, optimization, and performance analysis of UWA communication systems. The aim is to fit the DPS of the simulation model to that of the measured UWA channel. The performance of the designed UWA channel simulator is assessed by comparing the average Doppler shift and Doppler spread of the channel simulator with the corresponding quantities of the measured UWA channel. The results of the assessment show a good match between the statistical quantities of the UWA channel simulator and those of the real-world UWA channel.

*Keywords*—Measurement-based channel modelling, shallow underwater acoustic channels, underwater acoustic communications, wideband channels, Doppler power spectrum, Doppler spread.

## **I. INTRODUCTION**

Underwater acoustic (UWA) communication systems have been widely used in various applications in oceanography. For the test, design, and performance analysis of UWA communication systems, the statistical properties of UWA channels in terms of correlation functions, Doppler power spectrum (DPS), and power delay profile (PDP) play an important role. For the performance analysis of UWA communication systems, one usually resorts to computer simulations, which provide a cost-effective and powerful tool to assess the system performance. They can also be used to confirm the correctness of theoretical results obtained analytically.

While many researchers are concerned with the PDPs, the DPS have been less developed for UWA channels [12, 13]. This motivates us to analyze and model the DPS of UWA channels based on Doppler measurements. The Doppler effect in UWA channels is more severe than that in mobile radio channels due to the low speed of sound (1500 m/s), large Doppler frequency shifts with respect to the carrier

frequency, and the time-variant characteristics of the surface motion [9]. Therefore, the Doppler effect is indeed a critical issue that affects the performance of UWA communication systems.

In the absence of a standardized model for UWA channels, measurement-based channel modelling is an alternative approach to model the behavior of real-world UWA channels. However, it is a scenario-specific approach. There are a large number of studies related to the modelling of measurement-based UWA channels. For instance, the distribution of a UWA channel envelope has been reported in [2, 8] to match the Rayleigh distribution, while in [6, 7], it has been shown that the envelope follows the Rice distribution. In addition, the channel envelope may also follow the lognormal distribution as claimed in [10]. These controversial studies show that a realistic UWA channel simulator is necessarily required.

Under the standard assumption of wide-sense stationary uncorrelated scattering (WSSUS), the DPS of UWA channels can be computed by taking the Fourier transform of the autocorrelation function (ACF) of the received signal [1, 11]. However, the WSSUS assumption may not be valid due to the non-stationary behavior of UWA channels [12].

This paper presents a non-stationary time-continuous simulation model for UWA channels with given DPS obtained from measurements. To obtain the experimental data, we launched a campaign to measure a shallow UWA channel, which was used as a starting point for computing the DPS. The proposed channel simulator has been developed such that its statistical properties (average Doppler shift and Doppler spread) match as close as possible those of the measured real-world channel. For the design of measurement-based channel simulators, we need to determine the model parameters, including the path gains, Doppler frequencies, and phase shifts. Our numerical results show that a good fitting between the measured channel and the simulation model can be achieved with respect to the DPS, average Doppler shifts and Doppler spread.

The rest of this paper is organized as follows. In Section II, the time-continuous channel simulation model is presented. Section III describes the measurement scenario. The numerical results are illustrated in Section IV. Finally, the conclusions are drawn in Section V.

## **II. NON-STATIONARY TIME-CONTINUOUS CHANNEL SIMULATION MODEL**

In this section, we develop a non-stationary time-continuous simulation model for UWA channels using a given DPS. First, the given DPS is presented and then the

complex channel gain of the channel simulator is proposed.

#### A. Given DPS

In the measurement, we assume that the received signal has been stored after each snapshot interval. It is also assumed that the UWA channel is quasi-stationary during each snapshot interval. For the  $k$ th snapshot interval of duration  $T_s$ , the DPS  $\check{S}_{yy}^{(k)}(f, t)$  of the measured UWA channel can be computed as

$$\check{S}_{yy}^{(k)}(f, t) = \sum_{n=1}^N [c_n^{(k)}]^2 \delta(f - f_n^{(k)}) \quad (\text{E.1})$$

for  $t \in [t_k, t_{k+1})$  and  $k = 0, 1, 2, \dots, K - 1$ . The time interval  $t_k$  is defined as  $t_k = t_0 + kT_s$  and  $t_0$  equals  $T_s/2$ . The parameter  $K$  denotes the number of snapshots intervals, and thus, the measurement duration  $T_{\text{mes}}$  is determined by  $T_{\text{mes}} = KT_s$ . The parameters  $c_n^{(k)}$  and  $f_n^{(k)}$  denote, respectively, the path gain and Doppler shift of the  $n$ th received multipath component for the  $k$ th snapshot. The quantity  $N$  stands for the number of multipath components in each snapshot. The proof of (E.1) is provided in the Appendix.

#### B. Complex Channel Gain

In this paper, we adopt a channel simulation model with complex channel gain  $\tilde{\mu}(t)$  based on a sum-of-cisoids uncorrelated scattering (SOCUS) model [4], which is an appropriate channel model for a large class of wideband measured channels under non-isotropic scattering conditions. However, unlike the conventional SOCUS model, the channel gains are time-variant. In the proposed simulation model, for each Doppler shift  $f_n$ , we compute time-continuous gains  $c_n^{(k)}(t)$  between two consecutive snapshot intervals. The complex channel gain  $\tilde{\mu}(t)$  of the non-stationary simulation model can be obtained by  $\tilde{\mu}(t) = \sum_{k=0}^{K-1} \tilde{\mu}^{(k)}(t)$ , where the  $k$ th complex channel gain  $\tilde{\mu}^{(k)}(t)$  is given by

$$\tilde{\mu}^{(k)}(t) = \sum_{n=1}^{N'} c_n^{(k)}(t) e^{j(2\pi f_n t + \theta_n)} \quad (\text{E.2})$$

for  $t \in [t_k, t_{k+1})$ , where the range of Doppler frequencies  $f_n$  are obtained from the measurement data, and the phase shifts  $\theta_n$  are unknown and will consequently be modelled as random variables with uniform distribution over  $(0, 2\pi]$ . The parameter  $N'$  denotes the number of cisoids in the simulation model. The time-variant path gain  $c_n^{(k)}(t)$  corresponds to the  $k$ th snapshot and interpolates the values between two consecutive and constant gains  $c_n^{(k)}$  and  $c_n^{(k+1)}$ , which can be computed by [3, Eq.

(6.207)]

$$c_n^{(k)}(t) = \frac{c_n^{(k)} + c_n^{(k+1)}}{2} + \frac{c_n^{(k)} - c_n^{(k+1)}}{2} \cos\left(\frac{\pi(t - t_k)}{T_s}\right) \quad (\text{E.3})$$

for  $t \in [t_k, t_{k+1})$ . Note that if  $t = t_k$ , then  $c_n^{(k)}(t) = c_n^{(k)}$  and if  $t = t_{k+1}$ , then  $c_n^{(k)}(t) = c_n^{(k+1)}$ .

### C. The Spectrogram of the Simulation Model

The spectrogram  $\tilde{S}_{yy}(f, t)$  of the simulation model can be obtained by applying the concept of the spectrogram presented in [5]. The spectrogram has been widely used for analyzing time-variant signals and both stationary and non-stationary processes. In addition, the spectrogram provides variation of the spectral density of a signal (or stochastic process) over time. The spectrogram of a time-varying signal is computed by dividing the signal into overlapping shorter signals and then computing the squared absolute value of the Fourier transform of the short-time signal. However, the spectrogram suffers from a term named cross-term, which is time-variant and depends on the phases. More detailed analysis of the spectrogram can be found in [5]. Let  $h(t)$  denote an even and positive window function of the form

$$h(t) = \frac{1}{\sqrt{T}} \text{rect}\left(\frac{t}{T}\right) = \begin{cases} \frac{1}{\sqrt{T}}, & \text{if } -\frac{T}{2} \leq t \leq \frac{T}{2}, \\ 0, & \text{otherwise,} \end{cases} \quad (\text{E.4})$$

where the parameter  $T$  stands for the window length and the function  $\text{rect}(\cdot)$  is the rectangular function. The energy of the window function  $h(t)$  has been normalized to unity, i.e.,  $\int_{-\infty}^{\infty} h^2(t) dt = 1$ . The short-time Fourier transform (STFT)  $\tilde{Y}(f, t)$  of  $\tilde{y}(t', t) = \tilde{\mu}(t')h(t' - t)$  is given by

$$\begin{aligned} \tilde{Y}(f, t) &= \int_{-\infty}^{\infty} \tilde{y}(t', t) e^{-j2\pi f t'} dt' = \int_{-\infty}^{\infty} \tilde{\mu}(t') h(t' - t) e^{-j2\pi f t'} dt' \\ &= \frac{1}{\sqrt{T}} \int_{-\infty}^{\infty} \sum_{k=0}^{K-1} \sum_{n=1}^{N'} c_n^{(k)}(t') e^{-j[2\pi(f-f_n)t' - \theta_n]} \text{rect}\left(\frac{t' - t}{T}\right) dt' \\ &= \sqrt{T} \sum_{k=0}^{K-1} \sum_{n=1}^{N'} c_n^{(k)}(f) * \text{sinc}[(f - f_n)T] e^{-j[2\pi(f-f_n)t - \theta_n]} \end{aligned} \quad (\text{E.5})$$

in which the function  $\text{sinc}(\cdot)$  is the sinc function and the symbol  $(*)$  denotes the convolutional operator. Note that the window function  $h(t')$  is centred at time  $t$ .

The spectrogram  $\tilde{S}_{yy}(f, t)$  of the simulation model is finally obtained as

$$\begin{aligned} \tilde{S}_{yy}(f, t) &= \left| \tilde{Y}(f, t) \right|^2 = T \sum_{k=0}^{K-1} \sum_{n=1}^{N'} [c_n^{(k)}(f)]^2 * \text{sinc}^2[(f - f_n)T] \\ &+ T \sum_{k=0}^{K-1} \sum_{n=1}^{N'} \sum_{\substack{l=1 \\ l \neq k}}^{K-1} \sum_{m=1}^{N'} c_n^{(k)}(f) c_m^{(l)}(f) * \text{sinc}[(f - f_n)T] \\ &\cdot \text{sinc}[(f - f_m)T] e^{-j[2\pi(f_n - f_m)t + \theta_n - \theta_m]} \end{aligned} \quad (\text{E.6})$$

The spectrogram  $\tilde{S}_{yy}(f, t)$  in (E.6) reduces to [5, Eq. (11)] if  $T \rightarrow \infty$  and channel gains are constant, i.e.,  $c_n^{(k)}(t) = c_n$ .

#### D. Characteristic Quantities

In analogy to [3, Eqs. (7.155) and (7.156)], the time-variant average Doppler shift  $\tilde{B}_{yy}^{(1)}(t)$  and the time-variant delay spread  $\tilde{B}_{yy}^{(2)}(t)$  of the SOCUS simulation model are defined by the first moment of the spectrogram  $\tilde{S}_{yy}(f, t)$  and the square root of the second central moment of the spectrogram  $\tilde{S}_{yy}(f, t)$  as

$$\tilde{B}_{yy}^{(1)}(t) = \frac{\int_{-\infty}^{\infty} f \tilde{S}_{yy}(f, t) df}{\int_{-\infty}^{\infty} \tilde{S}_{yy}(f, t) df} \quad (\text{E.7})$$

and

$$\tilde{B}_{yy}^{(2)}(t) = \sqrt{\frac{\int_{-\infty}^{\infty} f^2 \tilde{S}_{yy}(f, t) df}{\int_{-\infty}^{\infty} \tilde{S}_{yy}(f, t) df} - \left( \tilde{B}_{yy}^{(1)}(t) \right)^2} \quad (\text{E.8})$$

respectively. Analogously, the time-variant average Doppler shift  $\check{B}_{yy}^{(1)}(t)$  and the time-variant delay spread  $\check{B}_{yy}^{(2)}(t)$  of the measured UWA channel can be computed by

$$\check{B}_{yy}^{(1)}(t) = \frac{\sum_{n=1}^N f_n^{(k)} [c_n^{(k)}]^2}{\sum_{n=1}^N [c_n^{(k)}]^2} \quad (\text{E.9})$$

and

$$\check{B}_{yy}^{(2)}(t) = \sqrt{\frac{\sum_{n=1}^N \left[ f_n^{(k)} c_n^{(k)} \right]^2}{\sum_{n=1}^N \left[ c_n^{(k)} \right]^2} - \left( \check{B}_{yy}^{(1)}(t) \right)^2} \quad (\text{E.10})$$

respectively for  $t \in [t_k, t_{k+1})$ . To study the influence of the parameter  $N'$  on the performance of the channel simulator, two error functions  $E^{(1)}(N')$  and  $E^{(2)}(N')$  are considered as

$$E^{(1)}(N') = \frac{1}{T_{\text{mes}}} \int_0^{T_{\text{mes}}} \left| \check{B}_{yy}^{(1)}(t) - \check{B}_{yy}^{(1)}(t) \right|^2 dt \quad (\text{E.11})$$

and

$$E^{(2)}(N') = \frac{1}{T_{\text{mes}}} \int_0^{T_{\text{mes}}} \left| \check{B}_{yy}^{(2)}(t) - \check{B}_{yy}^{(2)}(t) \right|^2 dt \quad (\text{E.12})$$

respectively.

### III. MEASUREMENT SCENARIO

To obtain the experimental data, we launched a measurement campaign in West Lake, Hanoi, Vietnam, in June 2016. The measured data was used as a starting point for computing the time-variant DPS  $\check{S}_{yy}(f, t)$  of UWA channel. The water depth was about 2.5 m and the transducer and hydrophone were secured at a depth of 1.5 m. The single-input single-output (SISO) channel measurements were performed at a carrier frequency of 12 kHz and a signal bandwidth of 4 kHz. The measurement data was collected for two different scenarios. In the first measurement scenario, the initial distance between the receiver and the transmitter was 50 m. Then, the receiver moved away from the fixed transmitter at a speed of about  $v_R = 0.5$  m/s and stopped after travelling 50 m. In the second measurement scenario, the receiver was 100 m away from the fixed transmitter. Then, the receiver moved towards the transmitter at a speed of about  $v_R = 0.5$  m/s and stopped after passing 50 m.

### IV. NUMERICAL RESULTS

In this section, we analyse the statistical properties of the measured UWA channel. Our aim is to develop a non-stationary channel simulation model based on measured

DPSs. The performance of the channel simulator has been analyzed by comparing its statistical quantities, including the time-variant average Doppler shift and time-variant Doppler spread, with the corresponding statistical quantities of the measured UWA channel.

The UWA channel has been measured by  $K = 20$  snapshots for the first scenario with a snapshot interval of  $T_s = 5$  s. Hence, the measurement duration  $T_{\text{mes}}$  of the first scenario was 100 s. In the second scenario, the channel was measured by  $K = 24$  snapshots, each one again with the snapshot interval of  $T_s = 5$  s, i.e., the measurement duration was equal to  $T_{\text{mes}} = 120$  s.

From the results shown in Figs. E.1 and E.2, we can conclude that by increasing the number of cisoids  $N'$ , the error functions in (E.11) and (E.12) decrease. As a trade-off between complexity and accuracy, the number of cisoids  $N'$  in the simulation setup has been set to 80. The window size  $T$  of the spectrogram has been set to 5 s.

Fig. E.3 shows the obtained DPS  $\check{S}_{\mu\mu}(f, t) = \sum_{k=0}^{K-1} \check{S}_{\mu\mu}^{(k)}(f, t)$  of the first scenario, where negative Doppler frequencies can be observed as expected, because the receiver moves away from the transmitter. As can be seen in this figure, there are strong variations of the gains  $c_n^{(k)}$  from one snapshot interval to the next. To address this non-stationary behavior, as stated in Sect. II-B, we propose time-continuous channel gains for the simulation model. Fig. E.4 shows the spectrogram  $\tilde{S}_{\mu\mu}(f, t)$  of the non-stationary time-continuous simulation model for the first scenario, where a similar trend as for the DPS  $\check{S}_{\mu\mu}(f, t)$  of the measured UWA channel can be observed. Similar results have been achieved by comparing the DPS of the measured UWA channel and the spectrogram of the simulation model of the second scenario, which have been presented in Figs. E.5 and E.6, respectively, where positive Doppler shifts can be observed.

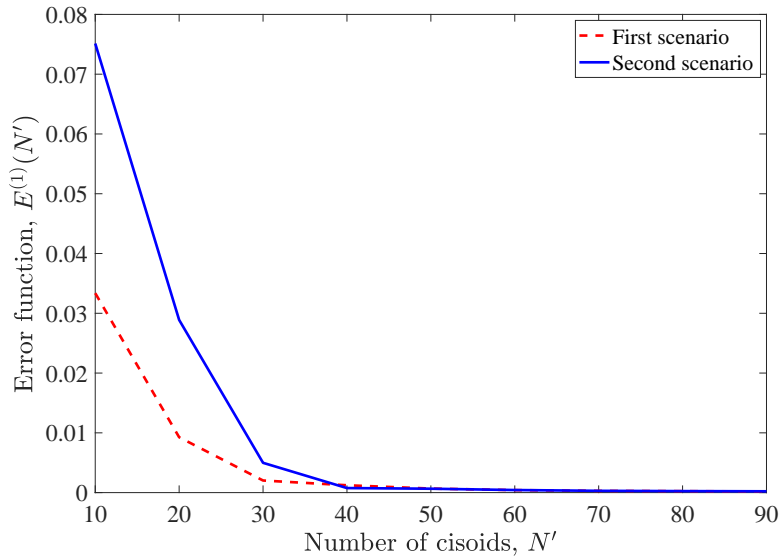


Figure E.1: Evaluation of the error function  $E^{(1)}(N')$  in (E.11) as a function of the number of cisoids  $N'$ .

E

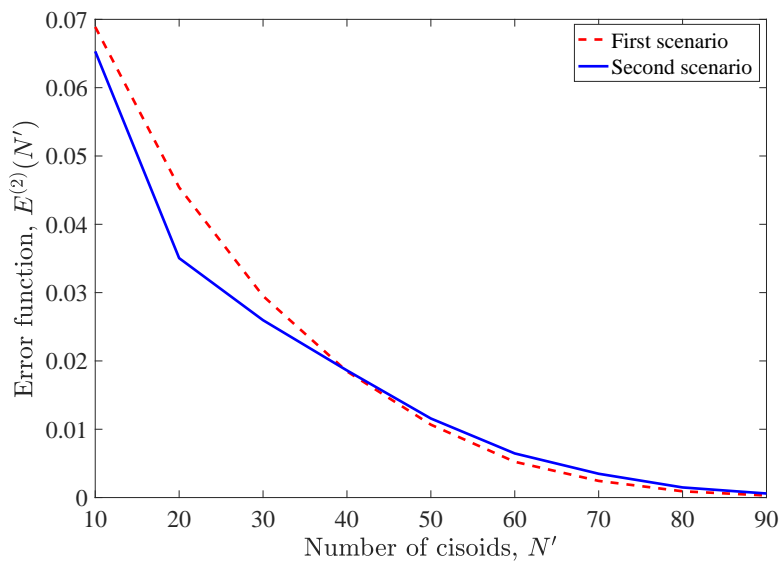


Figure E.2: Evaluation of the error function  $E^{(2)}(N')$  in (E.12) as a function of the number of cisoids  $N'$ .

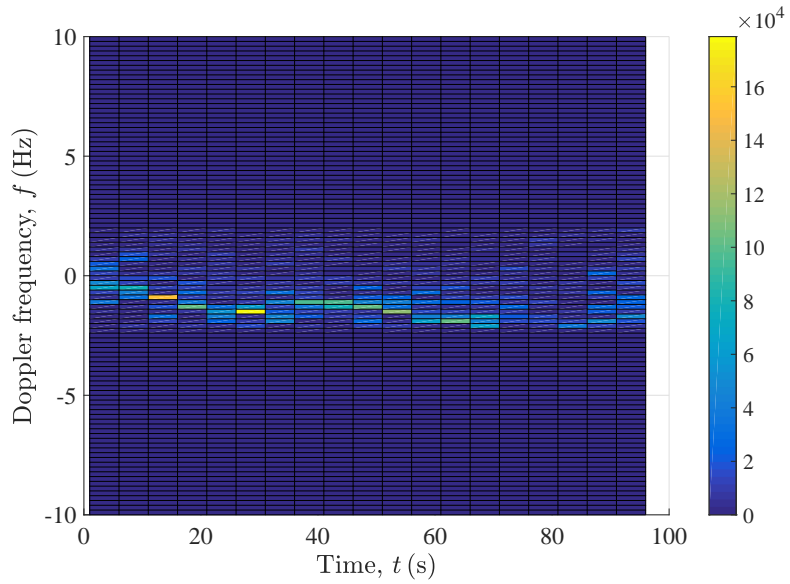


Figure E.3: Time-variant DPS  $\check{S}_{\mu\mu}(f, t)$  of the measured UWA channel (first scenario).

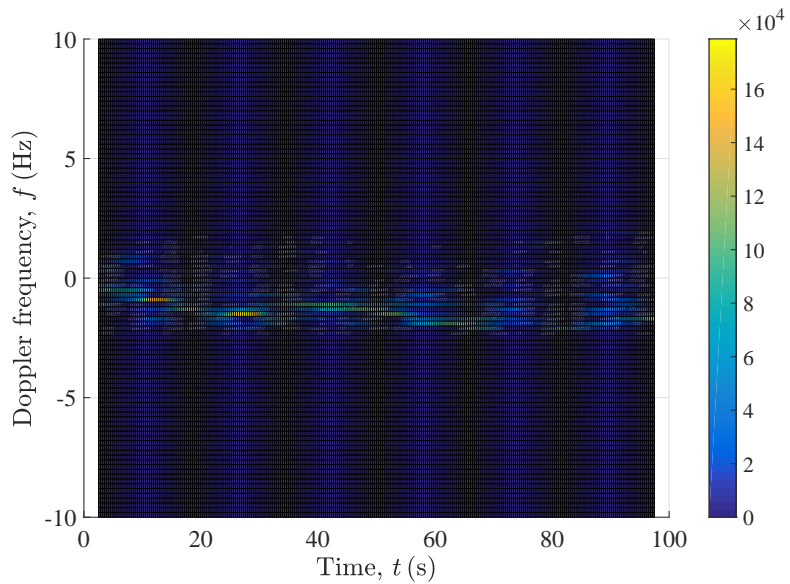


Figure E.4: The spectrogram  $\tilde{S}_{\mu\mu}(f, t)$  of the simulation model (first scenario).

E

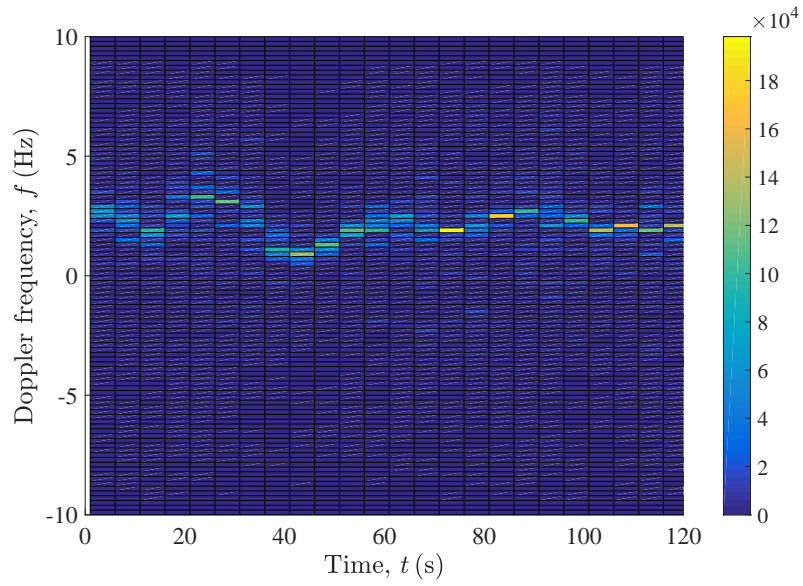


Figure E.5: Time-variant DPS  $\check{S}_{\mu\mu}(f, t)$  of the measured UWA channel (second scenario).

E

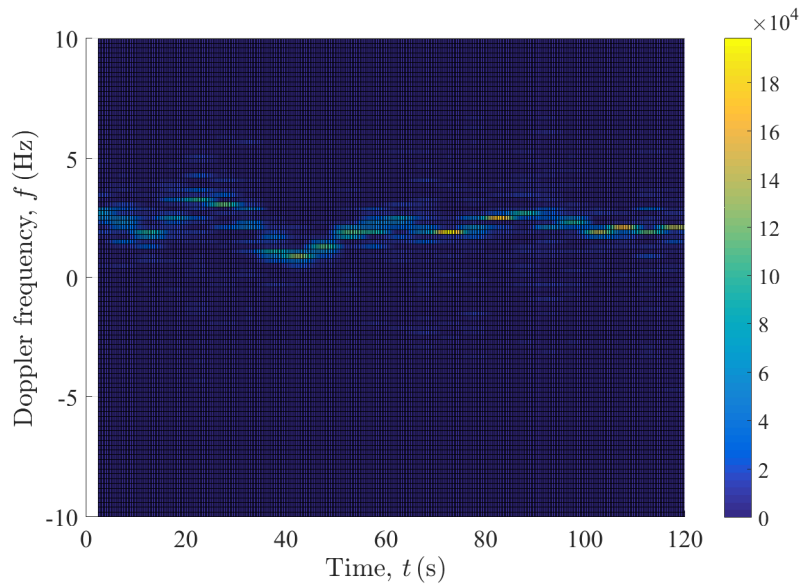


Figure E.6: The spectrogram  $\tilde{S}_{\mu\mu}(f, t)$  of the simulation model (second scenario).

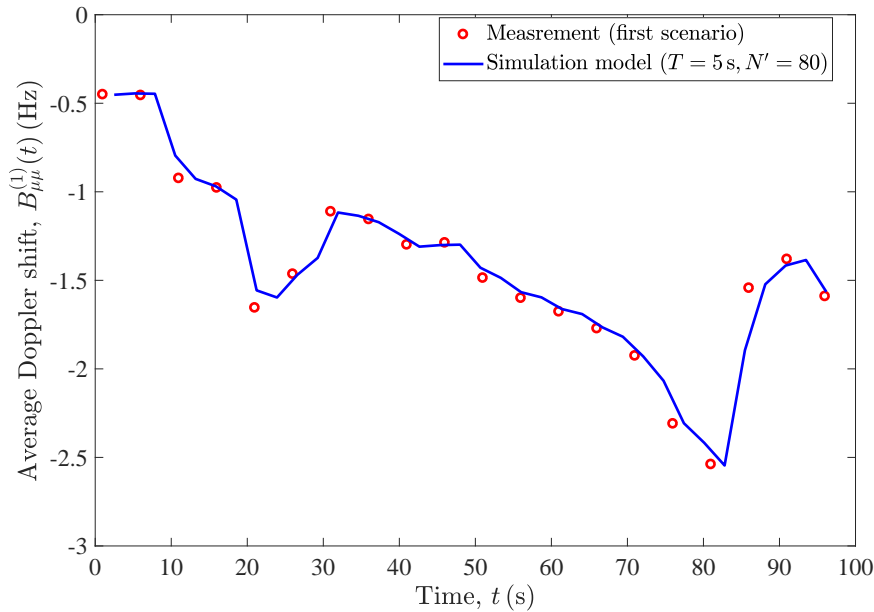


Figure E.7: Time-variant average Doppler shift (first scenario).

The results of the assessment show an excellent match between the measured UWA channel and the corresponding simulation model with respect to the time-variant average Doppler shifts  $B_{yy}^{(1)}(t)$  obtained for the first scenario and second scenario, as illustrated in Figs. E.7 and E.8, respectively. As can be seen, unlike stationary channels, the average Doppler shifts change considerably during the measurement duration  $T_{\text{mes}}$ .

Fig. E.9 shows a comparison between the time-variant Doppler spread  $\tilde{B}_{yy}^{(2)}(t)$  of the simulation model and that of the measured UWA channel of the first scenario according to (E.8) and (E.10), respectively. With reference to this figure, the time-variant Doppler spread of the simulation model follows closely that of the measured UWA channel.

We also analysed the time-variant Doppler spread of the UWA channel for the second scenario as depicted in Fig. E.10. As can be seen, a good match has been achieved between the measured UWA channel and the simulation model.

## V. CONCLUSION

In this paper, we have presented a non-stationary time-continuous simulation model for UWA channels by means of measured DPS. We have used an approach to compute time-continuous path gains for the simulation model. The DPS, time-variant average Doppler shift, and time-variant Doppler spread of the channel simulator have been matched to the corresponding quantities of the measured UWA channel.

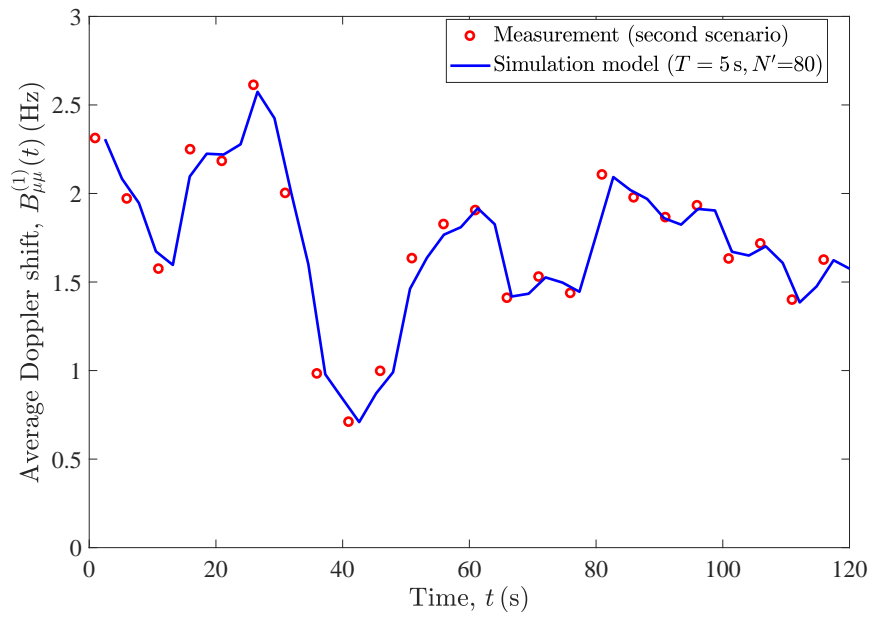


Figure E.8: Time-variant average Doppler shift (second scenario).

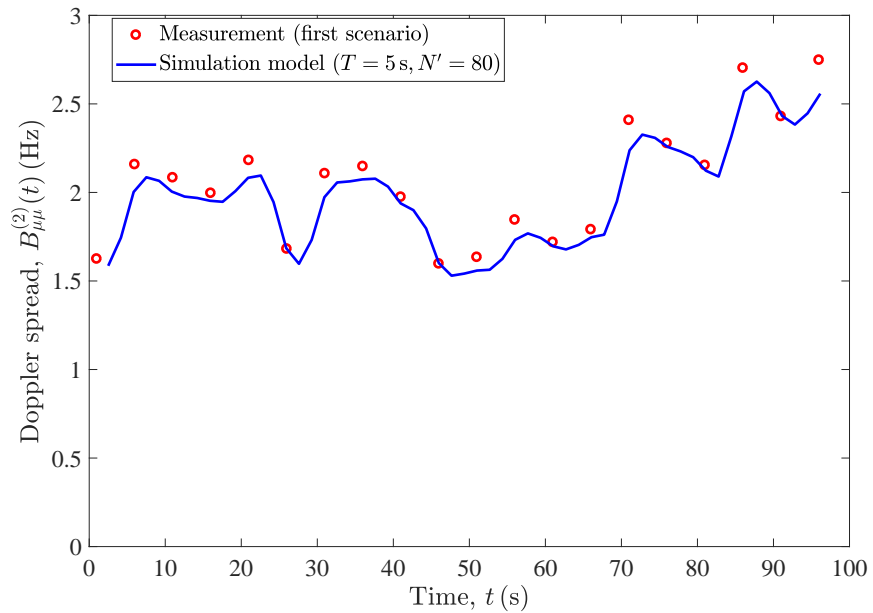


Figure E.9: Time-variant Doppler spread (first scenario).

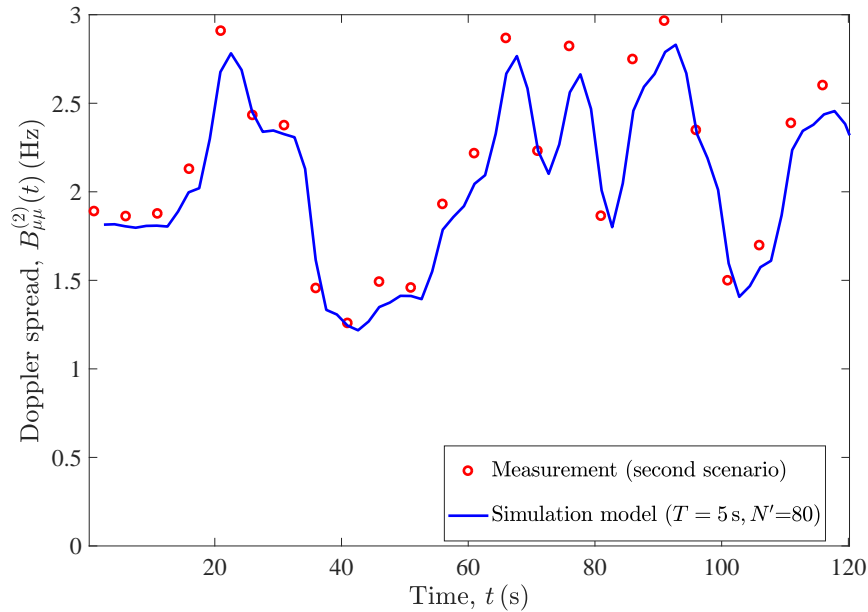


Figure E.10: Time-variant Doppler spread (second scenario).

It has been shown that the new channel model provides an excellent fit to measured UWA channels.

## APPENDIX A

This Appendix presents the proof of (E.1). The UWA channel is excited by the signal  $x(t)$  described by an amplitude  $A$ , a carrier frequency  $f_c$ , and a phase  $\theta$  as

$$x(t) = Ae^{j(2\pi f_c t + \theta)}. \quad (\text{E.13})$$

We assume that the UWA channel is quasi-stationary during each snapshot, and its time-variant channel impulse response  $\check{h}^{(k)}(\tau', t)$  can be presented by

$$\check{h}^{(k)}(\tau', t) = \sum_{n=1}^N c_n^{(k)} e^{j(2\pi f_n^{(k)} t + \theta_n)} \delta(\tau' - \tau_n') \quad (\text{E.14})$$

for  $k = 0, 1, \dots, K - 1$ . The parameter  $\tau_n'$  stands for the propagation delay of the  $n$ th received component. The received signal  $y^{(k)}(t)$  of the  $k$ th snapshot can be computed as

$$y^{(k)}(t) = \int_0^{\infty} x(t - \tau') \check{h}^{(k)}(\tau', t) d\tau'$$

$$\begin{aligned}
&= A \int_0^{\infty} e^{j[2\pi f_c(t-\tau')+\theta]} \sum_{n=1}^N c_n^{(k)} e^{j(2\pi f_n^{(k)}t+\theta_n)} \delta(\tau' - \tau'_n) d\tau' \\
&= A e^{j(2\pi f_c t + \theta)} \sum_{n=1}^N c_n^{(k)} e^{j(2\pi f_n^{(k)}t + \theta_n)} \int_0^{\infty} e^{-j2\pi f_c \tau'} \delta(\tau' - \tau'_n) d\tau' \\
&= x(t) \cdot \sum_{n=1}^N c_n^{(k)} e^{j(2\pi f_n^{(k)}t + \theta_n)} e^{-j2\pi f_c \tau'_n}. \tag{E.15}
\end{aligned}$$

The ACF  $\check{r}_{yy}^{(k)}(\tau)$  of  $y^{(k)}(t)$  can be computed by

$$\begin{aligned}
\check{r}_{yy}^{(k)}(\tau) &= \langle y^{(k)*}(t) y^{(k)}(t + \tau) \rangle \\
&= \langle x^*(t) x(t + \tau) \cdot \sum_{n=1}^N c_n^{(k)} e^{-j(2\pi f_n^{(k)}t + \theta_n)} e^{+j2\pi f_c \tau'_n} \\
&\quad \times \sum_{m=1}^N c_m^{(k)} e^{j[2\pi f_m^{(k)}(t+\tau) + \theta_m]} e^{-j2\pi f_c \tau'_m} \rangle \tag{E.16}
\end{aligned}$$

where the operator  $\langle \cdot \rangle$  denotes the time average operator. If  $n \neq m$ , then the ACF  $\check{r}_{yy}^{(k)}(\tau) = 0$ , and if  $n = m$ , then the ACF  $\check{r}_{yy}^{(k)}(\tau)$  can be obtained as

$$\check{r}_{yy}^{(k)}(\tau) = |A|^2 e^{j2\pi f_c \tau} \sum_{n=1}^N [c_n^{(k)}]^2 e^{j2\pi f_n^{(k)}\tau} = |A|^2 \sum_{n=1}^N [c_n^{(k)}]^2 e^{j2\pi(f_c + f_n^{(k)})\tau}. \tag{E.17}$$

The DPS  $\check{S}_{yy}^{(k)}(f)$  of the measured channel of the  $k$ th snapshot can be obtained by taking the Fourier transform of the ACF  $\check{r}_{yy}^{(k)}(\tau)$  with respect to  $\tau$  which results in

$$\check{S}_{yy}^{(k)}(f) = |A|^2 \sum_{n=1}^N [c_n^{(k)}]^2 \delta(f - f_c - f_n^{(k)}). \tag{E.18}$$

Finally, the time-variant DPS of the measured UWA channel after normalizing with respect to the amplitude squared  $|A|^2$  and the carrier frequency  $f_c$  can be presented by

$$\check{S}_{yy}^{(k)}(f, t) = \sum_{n=1}^N [c_n^{(k)}]^2 \delta(f - f_n^{(k)}) \tag{E.19}$$

for  $t \in [t_k, t_{k+1})$ .

## PAPER E: REFERENCES

### PAPER E: REFERENCES

- [1] H. Lasota and I. Kochańska. Transmission parameters of underwater communication channels. *Hydroacoustics*, 14:119–126, 2011.
- [2] M. Naderi, M. Pätzold, and A. G. Zajić. The design of measurement-based underwater acoustic channel simulators using the INLSA algorithm. In *Proc. IEEE OCEANS*, pages 1–6, Genova, Italy, May 2015.
- [3] M. Pätzold. *Mobile Fading Channels*. Chichester, U.K.: John Wiley & Sons, 2nd edition, 2011.
- [4] M. Pätzold and B. Talha. On the statistical properties of sum-of-cisoids-based mobile radio channel models. In *Proc. 10th Int. Symp. Wireless Pers. Multimedia Commun. (WPMC)*, pages 394–400, Jaipur, India, Dec. 2007.
- [5] M. Pätzold and N. Youssef. Spectrogram analysis of multipath fading channels. In *Proc. 26th IEEE Personal, Indoor and Mobile Radio Communications (PIMRC)*, pages 2214–2219, Hong Kong, China, August/September 2015.
- [6] P. Qarabaqi and M. Stojanovic. Statistical modeling of a shallow water acoustic communication channel. In *Proc. Underwater Acoust. Meas. Conf.*, pages 1341–1350, Nafplion, Greece, Jun. 2009.
- [7] A. Radosevic, J. G. Proakis, and M. Stojanovic. Statistical characterization and capacity of shallow water acoustic channels. In *Proc. IEEE EUROPE OCEANS*, pages 1–8, Bremen, Germany, May 2009.
- [8] F.-X. Socheleau, J. M. Passerieux, and C. Laot. Characterisation of time-varying underwater acoustic communication channel with application to channel capacity. In *Proc. Underwater Acoust. Meas. Conf.*, Nafplion, Greece, June 2009.
- [9] M. Stojanovic. Underwater acoustic communications: Design considerations on the physical layer. In *Proc. 5th Annu. Conf. Wireless Demand Netw. Syst. Services (WONS)*, pages 1–10, Jan. 2008.
- [10] B. Tomasi, P. Casari, L. Badia, and M. Zorzi. A study of incremental redundancy hybrid ARQ over Markov channel models derived from experimental data. In *Proc. 5th ACM Int. Workshop on UnderWater Networks (WUWNet)*, pages 1–8, Massachusetts, USA, Sep./Oct. 2010.

## PAPER E: REFERENCES

- [11] C. C. Tsimenidis, B. S. Sharif, O. R. Hinton, and A. E. Adams. Analysis and modelling of experimental doubly-spread shallow-water acoustic channels. In *Proc. Europe Oceans*, volume 2, pages 854–858, Jun. 2005.
- [12] P. A. van Walree, T. Jensenrud, and M. Smedsrud. A discrete-time channel simulator driven by measured scattering functions. *IEEE J. Sel. Areas Commun.*, 26(9):1628–1637, Dec. 2008.
- [13] S. Watts, L. Rosenberg, S. Bocquet, and M. Ritchie. Doppler spectra of medium grazing angle sea clutter; part 1: characterisation. *IET Radar, Sonar Navigation*, 10(1):24–31, 2016.

# Paper F

---

**Title:** Design and Analysis of a One-Dimensional Sea Surface Simulator Using the Sum-of-Sinusoids Principle

**Authors:** Meisam Naderi and Matthias Pätzold

**Affiliation:** Faculty of Engineering and Science, University of Agder, P.O. Box 509, 4879 Grimstad, Norway

**Conference:** *Proc. IEEE OCEANS*, Washington, USA, Oct. 2015, pp. 1-7, DOI: 10.23919/OCEANS.2015.7404478

---



# Design and Analysis of a One-Dimensional Sea Surface Simulator Using the Sum-of-Sinusoids Principle

Meisam Naderi and Matthias Pätzold

**Abstract** — Simulators for sea surface waves are useful for many practical applications, such as the construction of offshore structures and ocean surface animations. This paper studies three methods for the design of one-dimensional sea surface waves simulators with given wave spectra using the sum-of-sinusoids (SOS) principle. The wave spectrum provides insight into important statistical properties of the sea surface waves, such as the autocorrelation function (ACF) of the sea surface waves, significant wave height, and the moments of the spectrum. The sea surface simulator is designed by applying the concept of deterministic channel modelling on two main classical wave spectra, namely the Pierson-Moskowitz (PM) model and JOint North Sea WAve Project (JONSWAP) model. For the parametrization of the sea surface simulator, we adopt three well-known parameter computation methods: the  $L_p$ -norm method (LPNM), method of equal distances (MED), and the method of equal areas (MEA). A good match between the given sea surface models and the corresponding simulation model is achieved with respect to the main statistical properties of the sea surface waves. It is shown that for a given number of sinusoids, the LPNM and the MEA have almost the same performance, whereas the MED results in a sea surface waves simulator that suffers from a relatively small period.

**Keywords**—Sea surface modelling, Pierson-Moskowitz spectrum, JONSWAP spectrum, sea surface waves simulator, spectral moments.

## I. INTRODUCTION

Sea surface simulation is a popular research topic in ocean engineering [10] and computer graphics [5]. Sea surface waves greatly enhance the flux of energy and momentum between the atmosphere and the sea. A detailed knowledge of the statistics of the sea waves is important for the construction of coastal works like offshore structures [9] and for animating games and movies [7]. Thus, a realistic simulation model for sea surface waves is of great interest.

Moreover, the temporal elevation of the sea surface causes backscatterer signals influencing the Doppler frequency spectrum of acoustic underwater waves. To design more realistic channel models for acoustic underwater communications, accurate simulation models for the sea surface dynamics are required, which capture the temporal elevation of the sea surface. A proper approach is to model the sea surface waves by a random process with a specified wave spectrum, such as the Pierson-Moskowitz (PM) spectrum [17] and JOint North Sea WAve Project (JONSWAP) spectrum [6].

The kinetic energy of random waves is represented by the wave spectrum, which plays a key role in the analysis of the statistical properties of sea surface wave processes. The energy contained in the waves is defined by the energy density per unit area of the horizontal sea surface. The wave spectrum is of central importance for the characterization of ocean waves and gives insight into the distribution of the wave energy as a function of the wave frequencies. One source of irregularity of sea surface waves is the local wind. The wind-generated waves mix with the swell on the sea surface, which can be identified in the wave spectrum.

A few approaches exist in the literature to simulate the sea surface waves. The approaches can be classified as physical and parametric/spectral methods. In general, physical approaches (e.g., [1,4,21]) aiming to solve the wave equations are too complex to find analytical solutions. In contrast, parametric/spectral approaches (e.g., [3,5]) are appropriate to model the periodic motion of the sea surface elevation in deep water environments.

In [5], a method has been presented in which an adaptive spectrum sampling technique has been applied for determining the sea surface model parameters. This study considered only a limited frequency range and selected waves that are the most typical representatives of the wave spectrum. A real-time additive sound synthesis method applied to the sea surface wave modelling has been described in [20]. In this paper, the sea waves have been considered as partials of a sound by transposing the frequency and time domains to the wavenumber domain. In [8], a real-time simulation model has been proposed based on the sum-of-sinusoids (SOS) principle for the simulation of sea surface waves characterized by a given wave spectrum.

In this paper, we present three methods to design a one-dimensional sea surface waves simulator based on the SOS principle. This paper aims to exploit some techniques used in the area of the mobile radio channel modelling for simulating sea surface waves. For the design of a sea surface simulator, we need to compute the model parameters, which are the wave amplitudes, wave frequencies, and phase shifts. In this paper, parameters of the sea surface waves simulator have been deter-

mined by means of the  $L_p$ -norm method (LPNM) [15], method of equal distances (MED) [14], and the method of equal areas (MEA) [14]. Assuming the PM and JONSWAP spectra, the main statistical properties of the sea surface waves reference model are compared with those of the sea surface waves simulator. A good fitting between the reference model and the simulation model has been achieved with respect to the ACF, distribution of the sea surface elevation, and the moments of the PM and JONSWAP spectra.

The rest of this paper is organized as follows. In Section II, the PM and JONSWAP spectra are presented. Section III describes the proposed simulation model for sea surface waves. The statistical properties of the reference model and the simulation model are derived in Section IV. In Section V, the utilized parameter computation methods are briefly reviewed and applied on the PM and JONSWAP spectra. The numerical results are illustrated in Section VI. Finally, the conclusions are drawn in Section VII.

## II. PARAMETRIC SEA SURFACE SPECTRA

The PM and JONSWAP models are two non-symmetric parametric models of the sea surface spectrum. From systems theory, it follows that the sea surface spectrum must be real and even, i.e.,  $S_{\mu\mu}(\omega) = S_{\mu\mu}^*(-\omega)$  to obtain real-valued sea surface waves. However, non-symmetric spectra are preferred in experimental practice [11]. In this paper, we introduce a symmetrical PM (JONSWAP) spectrum by mirroring the original PM (JONSWAP) model with respect to the y-axis. To have the same energy level as the one for the non-symmetric spectra, we divide the symmetrical spectra by two.

In the PM model, the wave spectrum is a function of the wind speed and the wave frequency. For a fully-developed sea, the symmetrical PM spectrum model is given by

$$S_{\mu\mu}(\omega) = \frac{\alpha g^2}{2|\omega|^5} e^{-\beta\left(\frac{g}{\omega U}\right)^4}, \quad -\infty < \omega < +\infty \quad (\text{F.1})$$

where  $\alpha = 0.0081$ ,  $\beta = 0.74$  and the symbol  $\omega$  stands for the sea wave frequency (in rad·Hz). The parameters  $U$  and  $g$  denote the wind speed (in m/s) and the gravity acceleration (in m/s<sup>2</sup>), respectively. Fig. F.1 illustrates the PM spectrum for positive frequencies  $\omega$  in terms of different wind speeds.

The JONSWAP spectrum is an empirical model, which was established during the joint research project called the joint north sea wave project. The JONSWAP

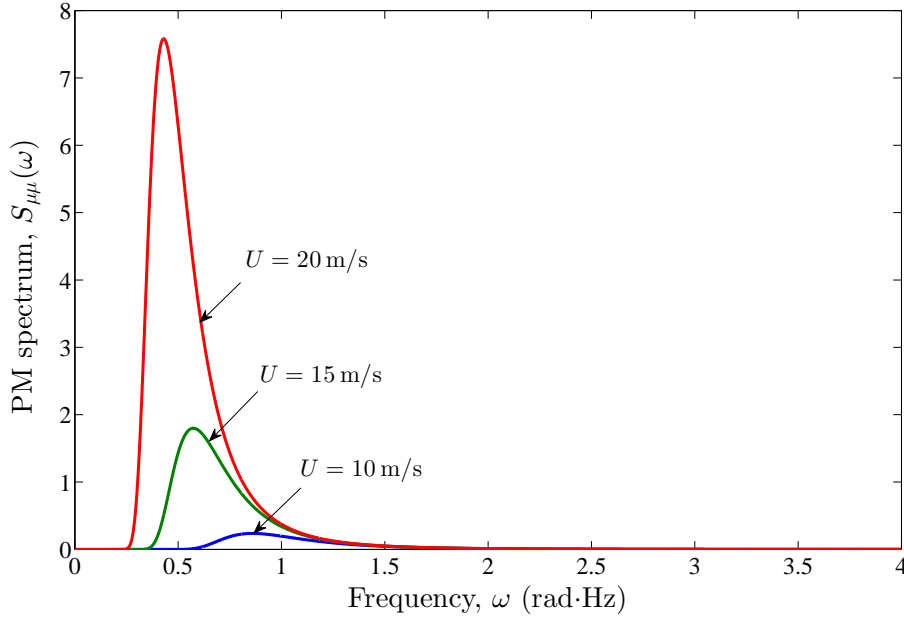


Figure F.1: The symmetrical PM spectrum  $S_{\mu\mu}(\omega)$  for  $\omega > 0$ .

spectrum is an extension of the PM spectrum for fetch-limited seas. The symmetrical JONSWAP spectrum is given by

$$S_{\mu\mu}(\omega) = \frac{\alpha_J g^2}{2 |\omega|^5} e^{-\frac{5}{4} \left(\frac{\omega_p}{\omega}\right)^4} \gamma e^{-\frac{(|\omega| - \omega_p)^2}{2\sigma_J^2 \omega_p^2}}, \quad -\infty < \omega < +\infty \quad (\text{F.2})$$

where  $\alpha_J = 0.076 (U^2/Fg)^{0.22}$ , in which  $F$  is the fetch defined as the distance over which the wind blows with constant velocity. The symbol  $\omega_p = 22 (g^2/FU)^{1/3}$  is the peak wave frequency, which is also called the modal frequency. The parameter  $\gamma$  is the so-called peak enhancement factor. Its default value is  $\gamma = 3.3$ . The symbol  $\sigma_J$  is a measure of the width of the spectral peak. Typical values of the parameter  $\sigma_J$  are 0.07 on the low frequency side ( $|\omega| \leq \omega_p$ ) and 0.09 on the high side ( $|\omega| > \omega_p$ ). The JONSWAP spectrum is shown in Fig. F.2 for different wind speeds.

From systems theory, it follows that the sea surface spectrum must be real and even, i.e.,  $S_{\mu\mu}(\omega) = S_{\mu\mu}^*(-\omega)$  to obtain real-valued sea surface waves. However, non-symmetric spectra are preferred in experimental practice [11].

### III. PROPOSED SEA SURFACE MODEL

By using Rice's SOS [18, 19], the sea surface waves can be modeled as a superposition of sine waves. In this paper, we propose a simulation model for sea surface

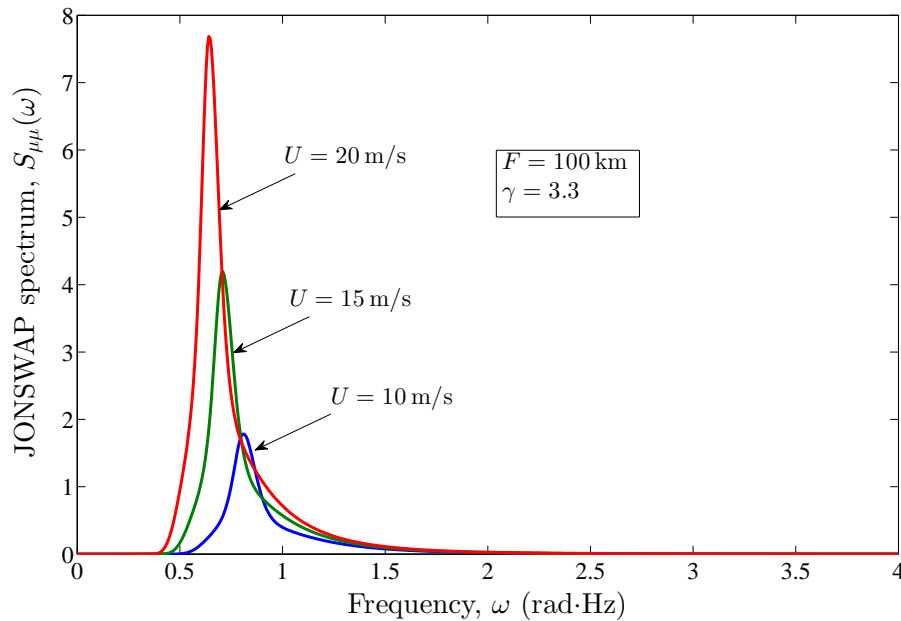


Figure F.2: The symmetrical JONSWAP spectrum  $S_{\mu\mu}(\omega)$  for  $\omega > 0$ .

waves described by a stochastic SOS process  $\hat{\mu}(t)$  of the form

$$\hat{\mu}(t) = \sum_{n=1}^N c_n \cos(\omega_n t + \theta_n) \quad (\text{F.3})$$

where  $N$  is the number of sinusoids. The symbol  $c_n$  stands for the  $n$ th wave amplitude (in m). The symbols  $\omega_n$  and  $\theta_n$  denote the wave frequency (in rad·Hz) and the phase shift of the  $n$ th sea surface wave, respectively. In Section. V, three methods are described for the computation of constant values for the wave amplitudes  $c_n$  and the wave frequencies  $\omega_n$ . The phase shifts  $\theta_n$  are modelled by independent and identically distributed (i.i.d.) random variables, which are supposed to be uniformly distributed over the interval  $(0, 2\pi]$ .

#### IV. THE STATISTICAL PROPERTIES OF THE SEA SURFACE WAVES

In this section, we study the main statistical properties of the PM and JONSWAP spectra, which serve as reference models, and those of the corresponding simulation model.

##### A. Statistical Properties of the Reference Model

The ACF  $r_{\mu\mu}(\tau)$  is obtained by taking the inverse Fourier transform of the (sym-

metrical) spectrum  $S_{\mu\mu}(\omega)$  with respect to the wave frequency  $\omega$ , i.e.,

$$r_{\mu\mu}(\tau) = \frac{1}{\pi} \int_0^{\infty} S_{\mu\mu}(\omega) \cos(\omega\tau) d\omega \quad (\text{F.4})$$

where the symbol  $\tau$  denotes the time separation variable. In this paper, the sea surface sea process is considered to be a narrowband process, meaning that the energy of the waves spectrum is concentrated within a narrow frequency range. In analogy to [12], the symmetrical PM spectrum can be formulated as

$$S_{\mu\mu}(\omega) = \frac{A}{2|\omega|^5} e^{-\frac{B}{\omega^4}}, \quad -\infty < \omega < +\infty \quad (\text{F.5})$$

where  $A = \alpha g^2$  and  $B = \beta(g/U)^4$ . By using the wave spectrum given in (F.5), the moments  $m_j$  can be expressed by

$$m_j = \int_{-\infty}^{\infty} \omega^j S_{\mu\mu}(\omega) d\omega \quad (\text{F.6a})$$

$$m_0 = \frac{A}{4B} \quad (\text{F.6b})$$

$$m_1 = 0 \quad (\text{F.6c})$$

$$m_2 = \frac{\sqrt{\pi}A}{4\sqrt{B}} \quad (\text{F.6d})$$

where the zeroth moment  $m_0$  is the area under the spectrum, which is related to the significant wave height  $H_s$ . For a narrowband spectrum, the significant wave height  $H_s$  is approximately four times the square root of the zeroth moment, i.e.,

$$H_s = 4\sqrt{m_0} = 2\sqrt{\frac{A}{B}}. \quad (\text{F.7})$$

For a narrowband spectrum, the maximum wave height  $H$  follows approximately the Rayleigh distribution [2]. Therefore, the distribution  $p_H(x)$  of the maximum wave height  $H$  can be approximated by [12, Eq. (2.71)]

$$p_H(x) = \frac{2x}{R} e^{-x^2/R}, \quad \text{if } x > 0 \quad (\text{F.8})$$

in which  $R = 8m_0$ . The average wave height  $\bar{H}$  can be determined as [12, Eq. (2.72)]

$$\bar{H} = \int_0^{\infty} x \left( \frac{2x}{R} e^{-x^2/R} \right) dx = \frac{\sqrt{\pi R}}{2}. \quad (\text{F.9})$$

Hence, by using  $R = 8m_0 = 2A/B$ , the average wave height  $\bar{H}$  equals  $\bar{H} = \sqrt{\pi A/(2B)}$ . The ratio of the significant wave  $H_s$  height to the average wave height  $\bar{H}$  can be computed as

$$H_s/\bar{H} = \sqrt{\frac{8}{\pi}} = 1.6. \quad (\text{F.10})$$

The modal frequency  $\omega_p$  of the PM spectrum is given by [12, Eq. (2.63)]

$$\omega_p = 0.4 \sqrt{\frac{g}{H_s}}. \quad (\text{F.11})$$

The JONSWAP spectrum cannot be formulated like the PM spectrum in (F.5). Thus, we have to compute the corresponding characteristic quantities numerically. The numerical results are presented in Table. F.2. However, the total energy of the JONSWAP spectrum can be expressed in closed form by

$$m_0 = 1.67 \times 10^{-7} \frac{U^2 F}{g}. \quad (\text{F.12})$$

### B. Statistical Properties of the Sea Surface Waves Simulator

The ACF  $\hat{r}_{\mu\mu}(\tau)$  of the stochastic SOS process  $\hat{\mu}(t)$  can be computed as

$$\hat{r}_{\mu\mu}(\tau) = E \{ \hat{\mu}^*(t) \hat{\mu}(t + \tau) \} = \sum_{n=1}^N \frac{c_n^2}{2} \cos(\omega_n \tau) \quad (\text{F.13})$$

where  $E\{\cdot\}$  denotes the expected value operator, which has to be applied on the random phases  $\theta_n$ . It should be noted that the ACF  $\hat{r}_{\mu\mu}(\tau)$  in (F.13) depends on the number of sinusoids  $N$ , the wave amplitudes  $c_n$ , and the wave frequencies  $\omega_n$ , but not on the phases  $\theta_n$ . The spectral density  $\hat{S}_{\mu\mu}(\omega)$  of the sea surface waves simulator is obtained computed by taking the Fourier transform of the ACF  $\hat{r}_{\mu\mu}(\tau)$  with respect to the variable  $\tau$ , which results in

$$\hat{S}_{\mu\mu}(\omega) = \frac{\pi}{2} \sum_{n=1}^N c_n^2 [\delta(\omega - \omega_n) + \delta(\omega + \omega_n)]. \quad (\text{F.14})$$

Analogously to (F.6a), the moments  $\hat{m}_j$  of the spectrum  $\hat{S}_{\mu\mu}(\omega)$  can be computed by using

$$\hat{m}_j = \int_{-\infty}^{\infty} \omega^j \hat{S}_{\mu\mu}(\omega) d\omega. \quad (\text{F.15})$$

For instance, the first three moments of the spectrum  $\hat{S}_{\mu\mu}(\omega)$  are given by

$$\hat{m}_0 = \pi \sum_{n=1}^N c_n^2 \quad (\text{F.16a})$$

$$\hat{m}_1 = 0 \quad (\text{F.16b})$$

$$\hat{m}_2 = \pi \sum_{n=1}^N (\omega_n c_n)^2. \quad (\text{F.16c})$$

By replacing  $m_0$  by  $\hat{m}_0$  in (F.7) and (F.9), the significant wave height  $\hat{H}_s$  and the average wave height  $\hat{H}$  of the sea surface simulator can be expressed as

$$\hat{H}_s = 4 \sqrt{\pi \sum_{n=1}^N c_n^2} \quad (\text{F.17})$$

and

$$\hat{H} = \sqrt{2 \pi^2 \sum_{n=1}^N c_n^2} \quad (\text{F.18})$$

respectively.

The distribution  $\hat{p}_\mu(x)$  of the stochastic process  $\hat{\mu}(t)$  with random phases  $\theta_n$  is given by [16, Eq. (32)]

$$\hat{p}_\mu(x) = 2 \int_0^\infty \left[ \prod_{n=1}^N J_0(2\pi c_n \nu) \right] \cos(2\pi \nu x) d\nu \quad (\text{F.19})$$

where  $J_0(\cdot)$  denotes the zeroth-order Bessel function of the first kind. It should be mentioned that the distribution  $\hat{p}_\mu(x)$  depends only on the number of sinusoids  $N$  and the gains  $c_n$ . If the gain  $c_n$  are chosen as  $c_n = \sqrt{m_0/(\pi N)}$ , then it follows from the central limit theorem that the distribution  $\hat{p}_\mu(x)$  approaches the normal distribution with zero mean and variance  $\hat{\sigma}^2 = \hat{m}_0/(2\pi)$  if  $N$  tends to infinity.

## V. THE UTILIZED PARAMETER COMPUTATION METHODS

In this section, we represent the three utilized parameter computation methods, namely the LPNM [15], MED [14], and the MEA [14]. The objective is to compute the wave amplitudes  $c_n$  and the wave frequencies  $\omega_n$  such that the ACF  $\hat{r}_{\mu\mu}(\tau)$  of the sea surface waves simulator matches the ACF  $r_{\mu\mu}(\tau)$  of the reference model

described by the PM and JONSWAP spectra.

### A. LPNM

For the parametrization of the sea surface waves simulator, we first apply the LPNM [15], which is widely used in the area of mobile radio channel modelling. The application of the LPNM on the given parametrization problem requires the minimization of the following error function

$$E_p = \left[ \frac{1}{\tau_{\max}} \int_0^{\tau_{\max}} |r_{\mu\mu}(\tau) - \hat{r}_{\mu\mu}(\tau)|^p d\tau \right]^{\frac{1}{p}} \quad (\text{F.20})$$

where  $p$  is a positive integer, and  $\tau_{\max}$  defines an appropriate time-lag interval  $[0, \tau_{\max}]$  over which the approximation of  $r_{\mu\mu}(\tau)$  is of interest. After the minimization of  $E_p$  by using numerical optimization techniques, we obtain a set  $\{\omega_n^{\text{opt}}\}$  of optimized wave frequencies. In the literature, the sea surface waves have been reported to follow a zero-mean Gaussian process in deep water [12]. For a given finite value of  $N$ , it was shown in [16] that the closest match to the Gaussian distribution can be achieved if all wave amplitudes  $c_n$  have the same value  $c_n = \sqrt{m_0/(\pi N)}$ . Therefore, we only need to compute the parameters  $\omega_n$  by substituting (F.4) and (F.13) in (F.20) and optimizing  $\omega_n$  such that the error norm  $E_p$  results in a minimum.

### B. MED

By using the MED [14], any pair of adjacent discrete wave frequencies  $\omega_n$  have the same Euclidean distance, which can be achieved by defining  $\omega_n$  as

$$\omega_n = \frac{\Delta\omega}{2} (2n - 1), \quad n = 1, 2, \dots, N \quad (\text{F.21})$$

where  $\Delta\omega = \omega_{\max}/N$  denotes the distance between two adjacent discrete wave frequencies, i.e.,  $\Delta\omega = \omega_n - \omega_{n-1}$  for  $n = 2, 3, \dots, N$ . The parameter  $\omega_{\max}$  stands for the maximum wave frequency, where the wave spectrum is unequal to zero. The wave amplitudes  $c_n$  are determined as

$$c_n = \sqrt{\frac{1}{\pi} \int_{\omega \in I_n} S_{\mu\mu}(\omega) d\omega} \quad (\text{F.22})$$

in which the frequency intervals  $I_n$  are defined as

$$I_n = \left[ \omega_n - \frac{\Delta\omega}{2}, \omega_n + \frac{\Delta\omega}{2} \right), \quad n = 1, 2, \dots, N. \quad (\text{F.23})$$

By substituting (F.22) in (F.13), one can easily prove that  $\hat{r}_{\mu\mu}(\tau) \rightarrow r_{\mu\mu}(\tau)$  holds as  $N \rightarrow \infty$ . Concerning the periodicity property of  $\hat{\mu}(t)$  [13, p. 151], we need to compute the greatest common divisor (gcd) of the discrete wave frequencies, which is equal to

$$\omega_0 = \text{gcd}\{\omega_n\}_{n=1}^N = \frac{\Delta\omega}{2} = \frac{\omega_{\max}}{2N}. \quad (\text{F.24})$$

Thus, by using the MED,  $\hat{\mu}(t)$  is periodic with period  $T_0 = 2\pi/\omega_0 = 4\pi N/\omega_{\max}$ . The fact that the period  $T_0$  is proportional to  $N$  is the major disadvantage of the MED.

### C. MEA

The MEA, which was first presented in [14], chooses the wave frequencies  $\omega_n$  such that the area under the wave spectrum  $S_{\mu\mu}(\omega)$  is equal to  $m_0/(2N)$  within the wave frequency range  $\omega_{n-1} < \omega \leq \omega_n$ , i.e.,

$$\int_{\omega_{n-1}}^{\omega_n} S_{\mu\mu}(\omega) d\omega = \frac{m_0}{2N} \quad \text{for } n = 1, 2, \dots, N \quad (\text{F.25})$$

where  $\omega_0 = 0$ . To compute the discrete wave frequencies  $\omega_n$ , we define an auxiliary function  $G_\mu(\omega_n)$  as

$$G_\mu(\omega_n) = \int_{-\infty}^{\omega_n} S_{\mu\mu}(\omega) d\omega. \quad (\text{F.26})$$

In the case of a symmetrical wave spectrum,  $G_\mu(\omega_n)$  can be expressed in the form

$$G_\mu(\omega_n) = \frac{m_0}{2} \left( 1 + \frac{n}{N} \right). \quad (\text{F.27})$$

If the inverse function of  $G_\mu$ , denoted by  $G_\mu^{-1}$ , exists, the wave frequencies  $\omega_n$  can be computed as

$$\omega_n = G_\mu^{-1} \left[ \frac{m_0}{2} \left( 1 + \frac{n}{N} \right) \right]. \quad (\text{F.28})$$

In [13, p. 205], it is shown that by replacing  $n$  by  $n - 1/2$ , we can improve the performance of the MEA. Thus, by applying the substitution  $n \rightarrow n - 1/2$ , we can rewrite (F.28) as

$$\omega_n = G_\mu^{-1} \left[ \frac{m_0}{2} \left( 1 + \frac{2n-1}{2N} \right) \right]. \quad (\text{F.29})$$

Like the LPNM, the wave amplitudes  $c_n$  have the same value, which are given by

$$c_n = \sqrt{m_0/(\pi N)}.$$

## VI. NUMERICAL RESULTS

In the following we compute the sets of the model parameter  $\mathcal{P} = \{c_n, \omega_n, N\}$  by applying the three parameter computation methods presented in Section V. In our simulation setup, the number of sinusoids has been set to  $N = 40$ . For the JONSWAP spectrum, the fetch  $F$  and the peak enhancement factor  $\gamma$  have been set to  $F = 100$  km and  $\gamma = 3.3$ , respectively.

Figs. F.3 and F.4 show the resulting ACFs  $\hat{r}_{\mu\mu}(\tau)$  of the sea surface waves simulator designed by the MEA for the symmetrical PM and JONSWAP spectra, respectively. As can be seen, there is an excellent fitting between the ACFs of the reference models and those of the simulation model.

Sample functions of the sea surface process  $\hat{\mu}(t)$ , which have been generated using the sea surface waves simulator designed by using the MEA for the PM and the JONSWAP spectra with  $U = 10$  m/s are illustrated in Figs. F.5 and F.6, respectively.

Figs. F.7 and F.8 show the distribution  $\hat{p}_\mu(x)$  of the sea surface wave process  $\hat{\mu}(t)$  designed by using the MEA for the given PM and JONSWAP spectra. Our results show that a good fitting between the analytical model and the simulation model can be achieved with respect to the distribution of the sea surface elevation. The individual curves can hardly be distinguished from each other in Figs. F.7 and F.8. As can be seen from both figures, the distribution of the simulated sea surface elevation follows closely the Gaussian distribution.

The distribution  $p_H(x)$  of the maximum wave height  $H$  of the sea surface waves simulator designed by using the MEA assuming the PM spectrum is shown in Fig. F.9. With reference to the results illustrated in Fig. F.9, one can see that the distribution  $p_H(x)$  of the maximum wave height  $H$  follows closely the Rayleigh distribution for large values of  $x$ . The reason for the poor fitting between theory and simulation for medium and low values of  $x$  is that the analytical expression presented in (F.8) is an approximation for the distribution of the maximum sea-wave heights.

In case of the PM spectrum, Table F.1 compares the statistical properties of the sea surface waves, such as the moments, significant wave height  $H_s$ , average wave height  $\bar{H}$ , and the period  $T_0$  of the reference model with the corresponding statistical quantities of the simulation model designed by the different parameter computation methods. The same comparison is shown in Table F.2 assuming the JONSWAP spectrum. Although all methods have a relatively good performance in terms of the metrics presented in the tables, they have some specific advantages and disadvantages. As mentioned in Section V-B, the relatively low period  $T_0$  of  $\hat{\mu}(t)$ ,

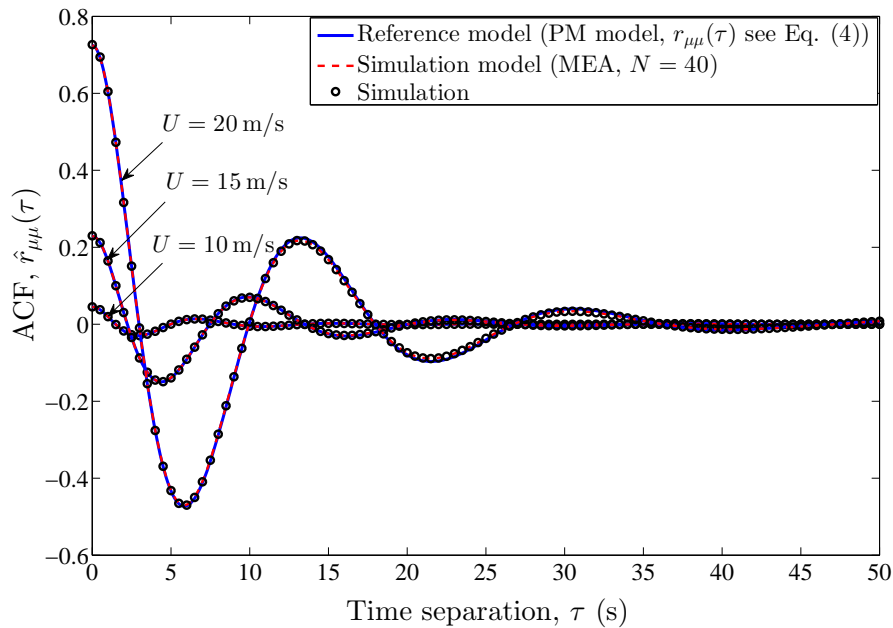


Figure F.3: The ACF  $\hat{r}_{\mu\mu}(\tau)$  of sea surface waves simulator assuming the PM spectrum designed by the MEA ( $N = 40$ ) in comparison with the ACF  $r_{\mu\mu}(\tau)$  of the reference model.

which increases linearly with  $N$ , is the main drawback of the MED. Nevertheless, it must be noted that the MED has a low computational complexity, and can be easily adopted to determine the sea surface model parameters. The main disadvantage of the MEA is the computation of the inverse function  $G_{\mu}^{-1}$  in (F.28), which does not exist for the PM and JONSWAP spectra. Thus, we have to determine the wave frequencies  $\omega_n$  numerically. As can be observed from the tables, the performance of the LPNM is slightly better than that of the other methods, but, the price to be paid for this achievement is a considerable increase in numerical complexity.

## VII. CONCLUSION

In this paper, we have proposed three methods for the design of a sea surface waves simulator based on the SOS concept. We have employed three well-known parameter computation methods, namely the LPNM, MED, and the MEA, which have widely been used in the area of mobile radio channel modelling. These methods have been applied to compute the parameters of a sea surface waves simulator for the case of the PM and JONSWAP spectra. The results of the assessment show an excellent agreement between the main statistical properties of the sea surface waves simulator designed by the three parameter computation methods and those of the given reference model. It has been shown that the LPNM and the MEA have almost

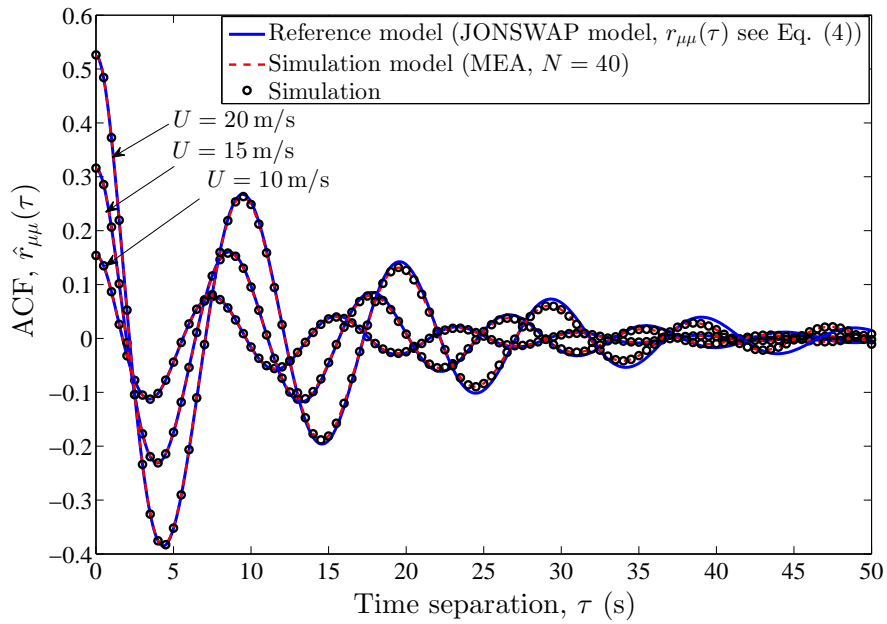


Figure F.4: The ACF  $\hat{r}_{\mu\mu}(\tau)$  of sea surface waves simulator assuming the JONSWAP spectrum designed by the MEA ( $N = 40$ ) in comparison with the ACF  $r_{\mu\mu}(\tau)$  of the reference model.

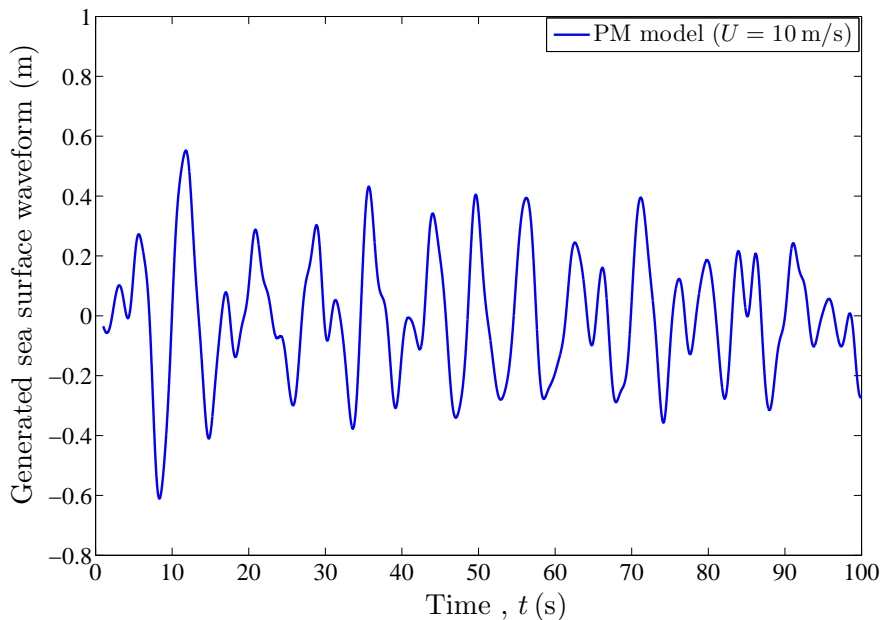


Figure F.5: Sample function of the sea surface waves process  $\hat{\mu}(t)$  designed by using the MEA ( $N = 40$ ) assuming the PM spectrum ( $U = 10$  m/s).

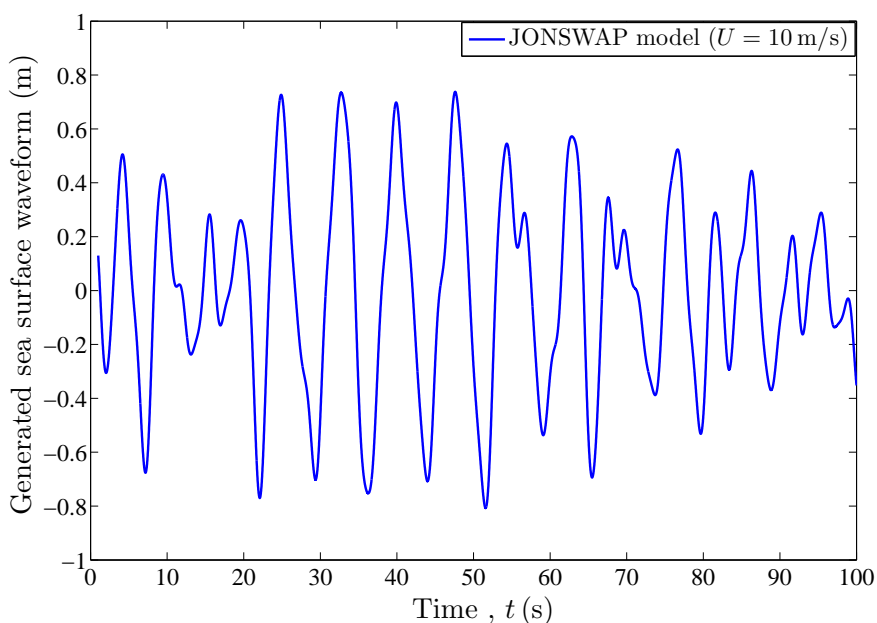


Figure F.6: Sample function of the sea surface waves process  $\hat{\mu}(t)$  designed by using the MEA ( $N = 40$ ) assuming the JONSWAP spectrum ( $U = 10$  m/s).

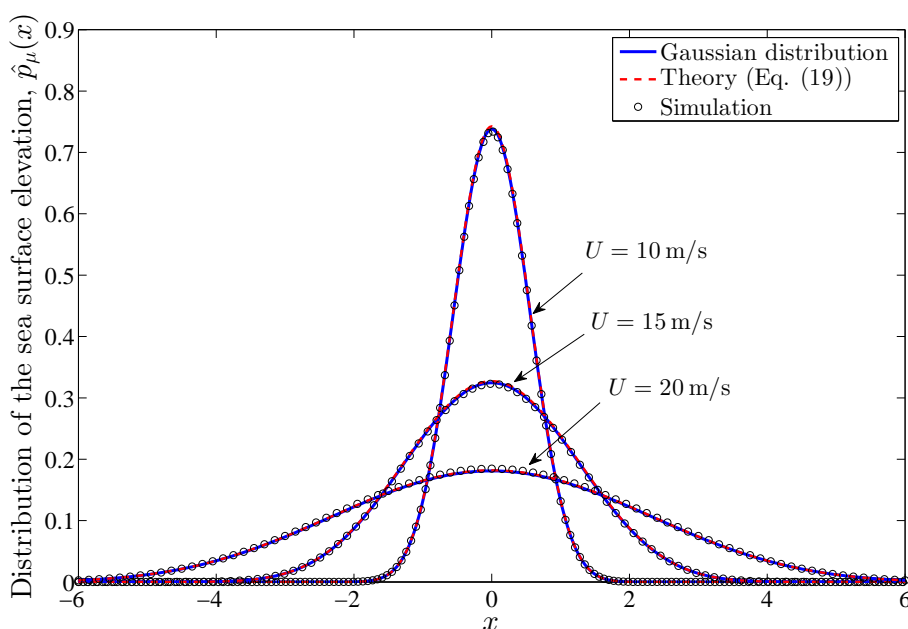


Figure F.7: The distribution  $\hat{p}_\mu(x)$  of the sea surface waves process  $\hat{\mu}(t)$  designed by using the MEA ( $N = 40$ ) assuming the PM spectrum in comparison with the Gaussian distribution.

F

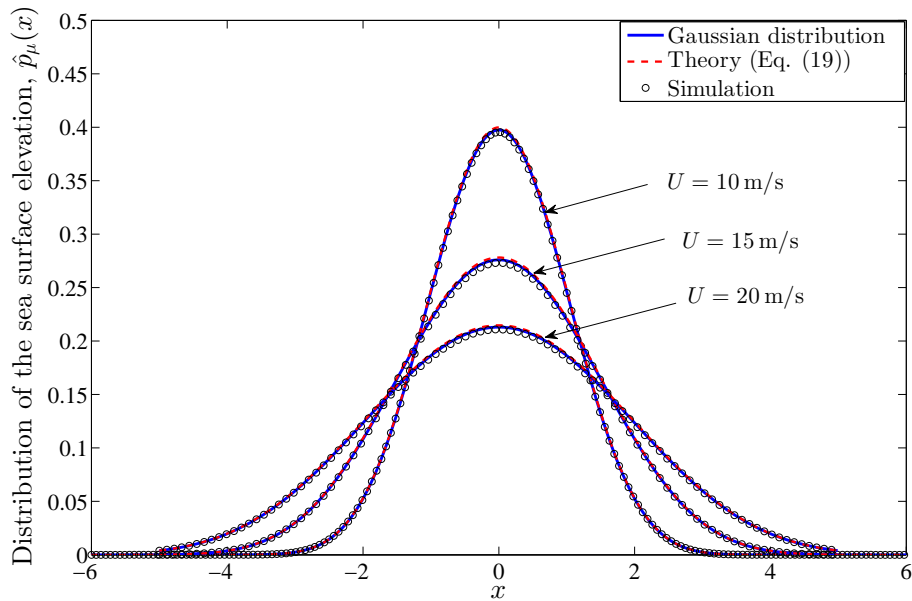


Figure F.8: The distribution  $\hat{p}_\mu(x)$  of the sea surface waves process  $\hat{\mu}(t)$  designed by using the MEA ( $N = 40$ ) assuming the JONSWAP spectrum in comparison with the Gaussian distribution.

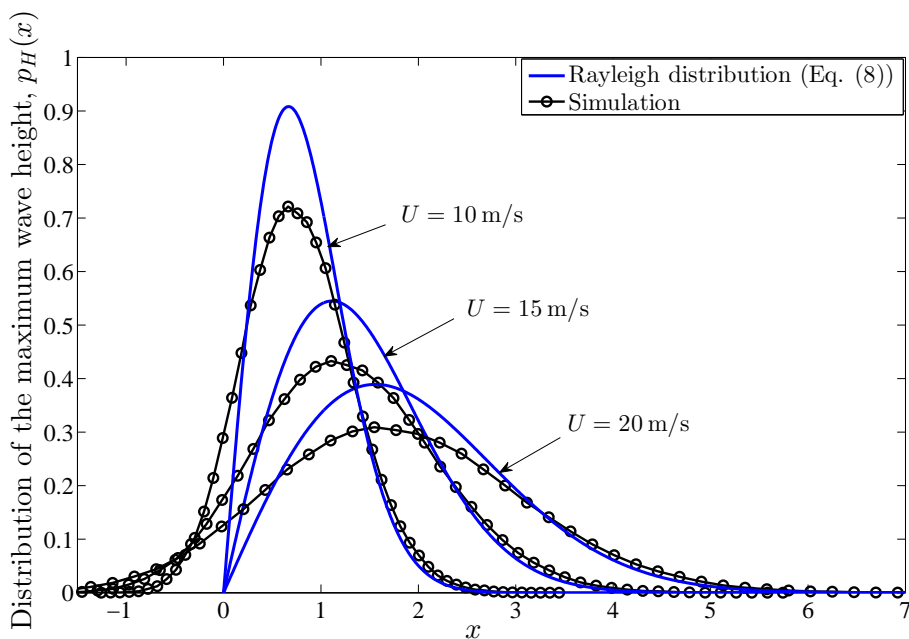


Figure F.9: The distribution  $p_H(x)$  of the maximum wave height  $H$  designed by using the MEA ( $N = 40$ ) assuming the PM spectrum in comparison with the Rayleigh distribution.

Table F.1: Comparison of the sea surface wave properties of the simulation model designed by the LPNM, MED, and MEA by using the PM spectrum ( $U = 15 \text{ m/s}$ ).

Parameters	PM spectrum	Simulation model, LPNM ( $N = 40$ )	Simulation model, MED ( $N = 40, \omega_{\max} = 8 \text{ rad}\cdot\text{Hz}$ )	Simulation model, MEA ( $N = 40$ )
Zeroth moment, $m_0$	1.4405	1.4405	1.4405	1.4405
First moment, $m_1$	0	0	0	0
Second moment, $m_2$	0.9388	0.9380	0.9366	0.9327
Forth moment, $m_4$	1.8970	1.8990	1.9149	1.9189
Significant wave height, $H_s$	4.8008 m	4.8008 m	4.8008 m	4.8008 m
Average wave height, $\bar{H}$	3.0084 m	3.0084 m	3.0084 m	3.008 m
Ratio of the significant wave height to the average wave height, $H_s/\bar{H}$	1.6	1.6	1.6	1.6
Modal frequency $\omega_p$	0.5717 rad·Hz	0.5717 rad·Hz	0.5717 rad·Hz	0.5717 rad·Hz
Period, $T_0$	$\infty$	Quasi $\infty$	$4\pi/\Delta\omega = 62.84 \text{ s}$	Quasi $\infty$

Table F.2: Comparison of the sea surface wave properties of the simulation model designed by the LPNM, MED, and MEA by using the JONSWAP spectrum ( $U = 15 \text{ m/s}$ ,  $F = 10 \text{ km}$ ,  $\gamma = 3.3$ ).

Parameters	JONSWAP spectrum	Simulation model, LPNM ( $N = 40$ )	Simulation model, MED ( $N = 40, \omega_{\max} = 8 \text{ rad}\cdot\text{Hz}$ )	Simulation model, MEA ( $N = 40$ )
Zeroth moment, $m_0$	1.9794	1.9794	1.9794	1.9794
First moment, $m_1$	0	0	0	0
Second moment, $m_2$	1.5882	1.5888	1.5894	1.5896
Forth moment, $m_4$	3.6413	3.6464	3.6626	3.6665
Significant wave height, $H_s$	5.6276 m	5.6276 m	5.6276 m	5.6276 m
Average wave height, $\bar{H}$	3.5266 m	3.5266 m	3.5266 m	3.5266 m
Ratio of the significant wave height to the average wave height, $H_s/\bar{H}$	1.6	1.6	1.6	1.6
Modal frequency $\omega_p$	0.7056 rad·Hz	0.7056 rad·Hz	0.7056 rad·Hz	0.7056 rad·Hz
Period, $T_0$	$\infty$	Quasi $\infty$	$4\pi/\Delta\omega = 62.84 \text{ s}$	Quasi $\infty$

## PAPER F: REFERENCES

the same performance, whereas the MED results in a sea surface waves simulator that has a relatively small period.

## PAPER F: REFERENCES

- [1] A. Arakawa and V. R. Lamb. A potential enstrophy and energy conserving scheme for the shallow water equations. *Monthly Weather Review*, 109(1):18–36, Jan. 1981.
- [2] D. E. Cartwright and M. S. Longuet-Higgins. The statistical distribution of the maxima of a random function. *Proc. Royal Society of London. Series A, Mathematical and Physical Sciences*, 237(1209):212–232, Oct. 1956.
- [3] E. Darles, B. Crespin, D. Ghazanfarpour, and J. C. Gonzato. A survey of ocean simulation and rendering techniques in computer graphics. *Computer Graphics Forum*, 30(1):43–60, 2011.
- [4] D. Enright, S. Marschner, and R. Fedkiw. Animation and rendering of complex water surfaces. *ACM Trans. Graph.*, 21(3):736–744, Jul. 2002.
- [5] J. Fréchet. Realistic simulation of ocean surface using wave spectra. In *Proc. 1st Int. Conf. Computer Graph. Theory and Appl. (GRAPP)*, pages 76–83, Seyúbal, Portugal, Feb. 2006.
- [6] K. Hasselmann et al. Measurement of wind wave growth and swell decay during the joint North Sea Wave Project (JONSWAP). *Deutsches Hydrographisches Institut*, 12:1–95, January 1973.
- [7] Y. Kryachko. Using vertex texture displacement for realistic water rendering. In *Proc. Int. Conf. GPU Gems*, pages 283–294, 2005.
- [8] L. M. Lachman. An open programming architecture for modeling ocean waves. In *Proc. IMAGE Conf.*, pages 1–13, Scottsdale, AZ, USA, Jul. 2007.
- [9] R. Luppez, B. Düz, H. J. L. Van Der Henri P. Van Der Plas, and A. E. p. Veldman. Numerical simulation of extreme wave impact on offshore platforms and coastal constructions. In *Proc. 5th Int. Conf. Comput. Methods in Marine Eng. (MARINE)*, pages 122–133, 2011.

## PAPER F: REFERENCES

- [10] X. Ma, Z. Chen, and G. Shi. Real-time ocean wave motion simulation based on statistic model and GPU programming. In *Proc. 2nd Int. Conf. Inform. Science and Eng. (ICISE)*, pages 3876–3880, Dec. 2010.
- [11] S. R. Massel. *Ocean Surface Waves: Their Physics and Prediction*, volume 11. World Scientific, 1st edition, 1996.
- [12] M. K. Ochi. *Ocean Waves: The Stochastic Approach*. New York: Cambridge University Press, 1st edition, 2005.
- [13] M. Pätzold. *Mobile Fading Channels*. Chichester, U.K.: John Wiley & Sons, 2nd edition, 2011.
- [14] M. Pätzold, U. Killat, and F. Laue. A deterministic model for a shadowed Rayleigh land mobile radio channel. In *Proc. 5th IEEE Int. Symp. Pers., Indoor and Mobile Radio Commun. (PIMRC)*, volume 4, pages 1202–1210, Hague, Netherlands, Sep. 1994.
- [15] M. Pätzold, U. Killat, F. Laue, and Y. Li. A new and optimal method for the derivation of deterministic simulation models for mobile radio channels. In *Proc. IEEE 46th Veh. Technol. Conf., (VTC)*, volume 3, pages 1423–1427, Atlanta, Georgia, USA, Apr./May 1996.
- [16] M. Pätzold, U. Killat, F. Laue, and Y. Li. On the statistical properties of deterministic simulation models for mobile fading channels. *IEEE Trans. Veh. Technol.*, 47(1):254–269, February 1998.
- [17] W. J. Pierson and L. Moskowitz. A proposed spectral form for fully developed wind seas. *J. of Geophysical Research*, 69:5181–5203, Oct. 1963.
- [18] S. O. Rice. Mathematical analysis of random noise. *Bell Syst. Tech. J.*, 23:282–332, Jul. 1944.
- [19] S. O. Rice. Mathematical analysis of random noise. *Bell Syst. Tech. J.*, 24:46–156, January 1945.
- [20] M. Robine and J. Fréchet. Fast additive sound synthesis for real-time simulation of ocean surface. In *Proc. Int. Conf. Syst., Signals and Image Process. (IWSSIP)*, pages 223–226, Budapest, Hungary, Sep. 2006.
- [21] R. Sadourny. The dynamics of finite-difference models of the shallow-water equations. *J. Atmos. Sci.*, 32(1):680–689, Apr. 1975.

# Paper G

---

**Title:** Performance Analysis of Alamouti-Coded OFDM Systems Over Spatio-Temporally Correlated Underwater Acoustic Channels

**Authors:** Meisam Naderi<sup>1</sup>, Gulzaib Rafiq<sup>2</sup>, and Matthias Pätzold<sup>1</sup>

**Affiliation:** <sup>1</sup> Faculty of Engineering and Science, University of Agder, P.O. Box 509, 4879 Grimstad, Norway

<sup>2</sup> ABB Corporate Research Center, Billingstad NO-1396, Norway

**Conference:** *Proc. International Conference on Communications (ICC)*, Paris, France (accepted), May 2017. DOI: ...

**Copyright ©:** IEEE

---



# Performance Analysis of Alamouti-Coded OFDM Systems Over Spatio-Temporally Correlated Underwater Acoustic Channels

Meisam Naderi, Gulzaib Rafiq, and Matthias Pätzold

**Abstract** — In this paper, we analyze the performance of Alamouti-coded orthogonal frequency division multiplexing (OFDM) systems over time-varying underwater acoustic (UWA) channels. A realistic UWA channel model has been considered, which can be correlated in either time or space or simultaneously in both domains. An exact analytical expression for the bit error probability (BEP) is necessary to analyze accurately the performance of Alamouti-coded OFDM systems over the spatio-temporally correlated UWA channel model. Hence, by using this UWA channel model, an expression has been derived for the BEP of Alamouti-coded OFDM systems assuming that the receiver knows perfectly the channel state information. The BEPs of two special cases are also studied, where the UWA channel is only correlated in either time or space. The performance of the Alamouti-coded OFDM system over UWA channels has been assessed for different maximum Doppler frequencies and antenna spacings. All theoretical results are validated by system simulations.

*Keywords*—Underwater acoustic channels, bit error probability, Alamouti scheme, orthogonal frequency division multiplexing, space time block coding.

## I. INTRODUCTION

Multiple-input multiple-output orthogonal frequency division multiplexing (MIMO OFDM) systems, which are very advantageous for band-limited underwater acoustic (UWA) channels, have been thoroughly investigated in recent years [6, 14]. Space-time block coding (STBC) techniques such as the Alamouti scheme [2] coupled with OFDM provides more reliable communications with high data rate transmissions [3]. The application of the simple Alamouti scheme in UWA communication systems has been extensively studied in the literature [4, 7, 16]. For example, in [7], a detection algorithm has been proposed for UWA communication systems exploiting the Alamouti STBC scheme. In contrast, two different detection algorithms have been proposed in [16] and [4] for UWA communication systems by employing Alamouti space-frequency block coding (SFBC) techniques.

---

Manuscript submitted March 21, 2016.

It is shown in [15] that the Alamouti scheme performs well if the channel remains constant over the duration of an Alamouti codeword. Owing to the fact that UWA channels cannot be assumed to be constant over the duration of two consecutive OFDM blocks [7], there is a need to study the degradation effect of the temporal correlation of UWA channels on the performance of Alamouti-coded OFDM systems for UWA communications. This effect has been investigated in [8–10] for mobile radio communications over Rayleigh fading channels. It has been shown in [8] by simulation and in [10] and [9] by theory that the performance of Alamouti STBC OFDM systems depends on both the temporal correlation and the spatial correlation of the 2-by-1 channel. For an accurate performance analysis of communication systems over spatio-temporally correlated UWA channels, the exact theoretical expression for the bit error probability (BEP) is required.

In this paper, we first extend the UWA channel model developed in [11] with respect to spatial selectivity. Then, we study the performance of Alamouti-coded OFDM systems over the proposed UWA channel model, which is correlated in time and space. The performance is assessed by taking into account that the UWA channel varies during two consecutive transmission time slots. Starting from the instantaneous output signal-to-interference-plus-noise ratio (SINR), we derive a general exact expression for the BEP. This expression is then used to study the performance for several specific cases, where the channel is correlated in time or space or even in both domains. The general expression is not limited to UWA channels. In fact, it can also be used for analyzing the performance of any time-varying multipath Rayleigh fading channel. It needs to mention that the detection scheme used in this paper is different from those of the aforementioned in [8–10]. The obtained results allow us to study the influence of the antenna spacing and maximum Doppler frequency on the system performance. It will be shown that the performance of Alamouti-coded OFDM systems depends greatly on the statistics of the UWA channel assessed at the antenna spacing and symbol duration.

The rest of this paper is structured as follows. Sections II and III represent the geometrical model and the therefrom derived UWA channel model, respectively. In Section IV, the Alamouti scheme and the symbol detection method are reviewed. The performance of Alamouti-coded OFDM systems over the proposed UWA channel model is studied in Section V. In Section VI, some numerical results are presented. Finally, the conclusions are drawn in Section VII.

## II. THE GEOMETRICAL UWA MODEL

In this paper, we first extend the 1-by-1 UWA channel model presented in [11] to a 2-by-1 channel to make it readily available for systems with two transmit

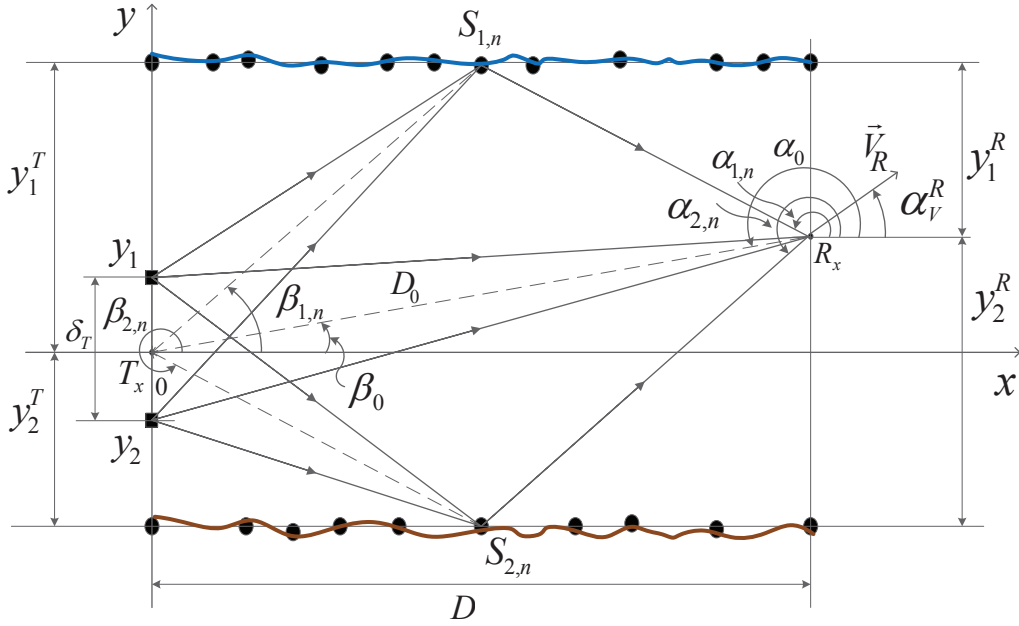


Figure G.1: A geometrical scattering model for a UWA channel with  $N_i^S$  randomly distributed scatterers  $S_{i,n}(\bullet)$  ( $n = 1, 2, \dots, N_i^S$ ) on the surface ( $i = 1$ ) and bottom ( $i = 2$ ) of the ocean.

antennas and one receiver antenna. Fig. G.1 presents the geometrical scattering model for UWA communication channels assuming that the scatterers  $S_{i,n}$  ( $n = 1, 2, \dots, N_i^S$  and  $i = 1, 2$ ) are uniformly distributed on the surface ( $i = 1$ ) and bottom ( $i = 2$ ) of the ocean between the transmitter and the receiver. Moreover, single-bounce scattering is assumed, i.e., each transmitted acoustic signal arrives at the receiver after a single bounce on the surface or bottom of the ocean. The fixed transmitter  $T_x$  is positioned at  $y_1^T$  and  $y_2^T$  seen from the surface and bottom of the ocean, respectively. Moreover, the transmitter  $T_x$  is equipped with two omnidirectional acoustic antennas separated by the antenna distance  $\delta_T$ . The single hydrophone receiver  $R_x$  is located at the distance  $y_1^R$  and  $y_2^R$  from the surface and bottom of the ocean, respectively. We assume that the receiver  $R_x$  is moving with constant velocity  $\vec{v}_R$  in the direction determined by the angle-of-motion (AOM)  $\alpha_v^R$ . According to Fig. G.1, the distance along the x-axis between  $T_x$  and  $R_x$  is denoted by  $D$ . The symbol  $\alpha_{i,n}$  ( $\beta_{i,n}$ ) denotes the angle-of-arrival (AOA) (angle-of-departure (AOD)) of the  $n$ th path associated with the ocean's surface ( $i = 1$ ) and the bottom ( $i = 2$ ). The symbol  $\alpha_0$  ( $\beta_0$ ) stands for the AOA (AOD) of the line-of-sight (LOS) component. Finally, the parameter  $D_0$  denotes the total distance which the LOS component travels from  $T_x$  to  $R_x$ .

### III. UWA CHANNEL MODEL

In this section, we present first the complex space-time variant channel transfer function (STVCTF) of the UWA channel model, and then we study the correlation functions of the UWA channel model required for the performance analysis of MIMO-OFDM UWA communication systems.

#### A. The STVCTF of the UWA Channel Model

The function  $H_{k1}(f', y_k, t_m)$  represents the STVCTF of the transmission link between the  $k$ th transmit antenna located at  $y_k$  ( $k = 1, 2$ ) and the single receive antenna at the time slot  $t_m$  ( $m = 1, 2$ ). We assume that the real and imaginary parts of  $H_{k1}(f', y_k, t_m)$  are uncorrelated, each having the variance  $\sigma_0^2$ . The STVCTFs  $H_{k1}(f', y_k, t_m)$  can be presented by their envelopes  $R_p = |H_{k1}(f', y_k, t_m)|$  and phases  $\Theta_p = \arg\{H_{k1}(f', y_k, t_m)\}$  for  $p = 1, 2, 3$ , and 4 as follows

$$\begin{aligned} H_{11}(f', y_1, t_1) &= R_1 e^{j\Theta_1}, & H_{11}(f', y_1, t_2) &= R_2 e^{j\Theta_2} \\ H_{21}(f', y_2, t_1) &= R_3 e^{j\Theta_3}, & H_{21}(f', y_2, t_2) &= R_4 e^{j\Theta_4}. \end{aligned} \quad (\text{G.1})$$

According to the geometrical model illustrated in Fig. G.1, the STVCTF  $H_{k1}(f', y_k, t_m)$  can be split into three parts. The first part  $H_{0,k}(f', y_k, t_m)$  is associated with the LOS component, whereas the second part  $H_{1,k}(f', y_k, t_m)$  and the third part  $H_{2,k}(f', y_k, t_m)$  are determined by the scattered components from the surface and bottom of the ocean, respectively. Thus, the STVCTF  $H_{k1}(f', y_k, t_m)$  can be expressed by

$$H_{k1}(f', y_k, t_m) = \sum_{i=0}^2 H_{i,k}(f', y_k, t_m) \quad (\text{G.2})$$

where  $k = 1, 2$  and  $m = 1, 2$ .

The LOS part  $H_{0,k}(f', y_k, t_m)$  of the STVCTF is given by

$$H_{0,k}(f', y_k, t_m) = \sqrt{\frac{c_R}{1 + c_R}} c_0 e^{j[2\pi(f_0 t_m - f' \tau'_0) + \theta_0]} e^{-j[\frac{2\pi}{\lambda} D_{0,k}]} \quad (\text{G.3})$$

in which  $c_R$  is the Rice factor, and the quantities  $c_0$ ,  $\tau'_0$ , and  $\theta_0$  denote the gain, delay, and the phase shift of the LOS component, respectively. The parameter  $\lambda$  designates the wavelength, which is determined by  $\lambda = c_s / f_c$ , where  $c_s$  and  $f_c$  are the speed of sound and the central carrier frequency, respectively. The symbol  $D_{0,k}$  stands for the total distance which the transmitted signal travels from the  $k$ th transmit acoustic antenna to the receiver hydrophone. This quantity is given by

$$D_{0,k} = D_0 - \frac{\delta_T(3 - 2k)}{2} \sin(\beta_0), \quad k = 1, 2. \quad (\text{G.4})$$

The Doppler frequency  $f_0$  in (G.3) is determined by

$$f_0 = f_{\max}^R \cos(\alpha_0 - \alpha_v^R) \quad (\text{G.5})$$

where  $f_{\max}^R$  is the maximum Doppler frequency associated with the receiver  $R_x$ .

The second part  $H_{1,k}(f', y_k, t_m)$  and the third part  $H_{2,k}(f', y_k, t_m)$  of the STVCTF  $H_{k1}(f', y_k, t_m)$  in (G.2) are given by

$$H_{i,k}(f', y_k, t_m) = \frac{1}{\sqrt{1 + c_R}} \sum_{n=1}^{N_i^S} c_{i,n} e^{j[2\pi(f_{i,n}t_m - f'\tau'_{i,n}) + \theta_{i,n}]} e^{-j[\frac{2\pi}{\lambda} D_{i,n,k}]} \quad (\text{G.6})$$

for  $i = 1, 2$ , where  $c_{i,n}$ ,  $f_{i,n}$ ,  $\tau'_{i,n}$  and  $\theta_{i,n}$ , denote, respectively, the gains, Doppler shifts, delays, and the phase shifts of the  $n$ th received component from the surface ( $i = 1$ ) and bottom ( $i = 2$ ) of the ocean. The parameter  $D_{i,n,k}$  stands for the total distance which the transmitted signal travels from the  $k$ th transmit antenna to the receive antenna after the interaction with the  $n$ th scatterer on the surface ( $i = 1$ ) and bottom ( $i = 2$ ) of the ocean. This parameter can be expressed by

$$D_{i,n,k} = \frac{(-1)^{(i-1)} y_i^T}{\sin(\beta_{i,n})} + \frac{(-1)^{(i-1)} y_i^R}{\sin(\alpha_{i,n})} - \frac{\delta_T(3 - 2k)}{2} \sin(\beta_{i,n}) \quad (\text{G.7})$$

for  $i, k = 1, 2$  and  $n = 1, 2, \dots, N_i^S$ .

### B. Correlation Functions of the UWA Channel Model

In this section, we define the correlation functions of the UWA channel model, such as the space-time cross-correlation function (CCF), temporal autocorrelation function (ACF), and the space CCF. The space-time CCF  $r_{HH}(\delta_T, \tau)$  of the sub-channels  $H_{11}(f', y_1, t_1)$  and  $H_{21}(f', y_2, t_2)$  is defined by

$$r_{HH}(\delta_T, \tau) = E\{H_{11}^*(f', y_1, t_1) \cdot H_{21}(f', y_2, t_2)\} \quad (\text{G.8})$$

where  $()^*$  and  $E\{\cdot\}$  represent the complex conjugate operation and the statistical expectation operator, respectively. The quantity  $\tau = t_2 - t_1$  denotes the time separation variable and  $\delta_T = y_2 - y_1$  denotes the antenna spacing. According to the generalized principle of deterministic channel modelling [13, pp. 418], a stochastic simulation model can be derived by using only a finite number of scatterers  $S_{i,n}$  and placing them at fixed positions on the surface ( $i = 1$ ) and the bottom ( $i = 2$ ) of the ocean. Without proof, we mention that the resulting space-time CCF  $\hat{r}_{HH}(\delta_T, \tau)$  of

the simulation UWA channel model can be computed as

$$\hat{r}_{HH}(\delta_T, \tau) = \frac{c_R}{1 + c_R} c_0^2 e^{j2\pi[f_0\tau - \frac{\delta_T}{\lambda} \sin(\beta_0)]} + \frac{1}{1 + c_R} \sum_{i=1}^2 \sum_{n=1}^{N_i^S} c_{i,n}^2 e^{j2\pi[f_{i,n}\tau - \frac{\delta_T}{\lambda} \sin(\beta_{i,n})]}. \quad (\text{G.9})$$

For the parametrization of the channel simulator, i.e., obtaining the channel simulator parameters including  $c_{i,n}$ ,  $f_{i,n}$ ,  $\beta_{i,n}$ , and  $\alpha_{i,n}$ , we employ the parameter computation method, which is called the method of equally spaced scatterers (MESS) [11]. It should be noted that the temporal ACF  $\hat{r}_{HH}(\tau)$  and the space CCF  $\hat{r}_{HH}(\delta_T)$  are obtained from the space-time CCF  $\hat{r}_{HH}(\delta_T, \tau)$  by setting  $\tau$  and  $\delta_T$  to zero, respectively, i.e.,  $\hat{r}_{HH}(\tau) = \hat{r}_{HH}(0, \tau)$  and  $\hat{r}_{HH}(\delta_T) = \hat{r}_{HH}(\delta_T, 0)$ .

#### IV. REVIEW OF THE ALAMOUTI-CODED OFDM SYSTEM

As mentioned in Section II, in this paper, an OFDM system equipped with two transmit antennas and one receive antenna is considered. A complex data symbol pair  $(S_1, S_2)$  is encoded first by means of the Alamouti scheme, and then it is transmitted over a UWA channel. The received symbols  $Y_1$  and  $Y_2$  at the time slots  $t_1$  and  $t_2$ , respectively, can be expressed in matrix form as

$$\begin{bmatrix} Y_1 \\ Y_2^* \end{bmatrix} = \begin{bmatrix} H_{11}(f', y_1, t_1) & H_{21}(f', y_2, t_1) \\ H_{21}^*(f', y_2, t_2) & -H_{11}^*(f', y_1, t_2) \end{bmatrix} \begin{bmatrix} S_1 \\ S_2 \end{bmatrix} + \begin{bmatrix} N_1 \\ N_2^* \end{bmatrix}. \quad (\text{G.10})$$

where  $N_m$  denotes a zero-mean additive underwater noise component at the time slot  $t_m$  ( $m = 1, 2$ ). Thus, we have equivalently

$$\mathbf{Y} = \mathbf{H}\mathbf{S} + \mathbf{N} \quad (\text{G.11})$$

in which  $\mathbf{H}$  denotes the 2-by-2 channel matrix, and  $\mathbf{N}$  is the noise vector. The symbol  $\mathbf{S}$  and  $\mathbf{Y}$  are the transmitted symbol vector and received symbol vector, respectively. Under the assumption that the receiver knows perfectly the channel state information and there is no synchronization error, the symbol vector  $\mathbf{S}$  can be estimated as [1]

$$\hat{\mathbf{S}} = \mathbf{H}^H \mathbf{Y} = \mathbf{H}^H \mathbf{H} \mathbf{S} + \mathbf{H}^H \mathbf{N} \quad (\text{G.12})$$

where  $\mathbf{H}^H$  is the conjugate transpose of the channel matrix  $\mathbf{H}$ . Thus, the estimated

symbols  $\hat{S}_1$  and  $\hat{S}_2$  at the output of the combiner can be expressed

$$\begin{aligned} \hat{S}_1 = & [|H_{11}(f', y_1, t_1)|^2 + |H_{21}(f', y_2, t_2)|^2]S_1 + [H_{11}^*(f', y_1, t_1)H_{21}(f', y_2, t_1) \\ & - H_{11}^*(f', y_1, t_2)H_{21}(f', y_2, t_2)]S_2 + H_{11}^*(f', y_1, t_1)N_1 + H_{21}(f', x_{T_2}, t_2)N_2^* \end{aligned} \quad (\text{G.13a})$$

$$\begin{aligned} \hat{S}_2 = & [|H_{11}(f', y_1, t_2)|^2 + |H_{21}(f', y_2, t_1)|^2]S_2 + [H_{11}(f', y_1, t_1)H_{21}^*(f', y_2, t_1) \\ & - H_{11}(f', y_1, t_2)H_{21}^*(f', y_2, t_2)]S_1 + H_{21}^*(f', y_2, t_1)N_1 - H_{11}(f', y_1, t_2)N_2^* \end{aligned} \quad (\text{G.13b})$$

As can be seen from (G.13a) and (G.13b), each estimated symbol experiences intersymbol-interference (ISI). But, due to the fact that the space CCFs

$E\{H_{11}^*(f', y_1, t_1)H_{21}(f', y_2, t_1)\}$  and  $E\{H_{11}^*(f', y_1, t_2)H_{21}(f', y_2, t_2)\}$  are equal, no diversity order is lost in the system [1].

## V. PERFORMANCE ANALYSIS OF ALAMOUTI-CODED OFDM SYSTEMS

In this section, we first analyze the instantaneous output SINR, and then we study the BEP of the Alamouti-coded OFDM system over UWA channels.

### A. The Instantaneous Output SINR

Due to the fact that the system model is symmetrical, the BEPs of  $S_1$  and  $S_2$  are equal. Thus, it is sufficient if we only focus on analyzing the BEP of  $S_1$ . From (G.13a), the instantaneous output SINR  $\gamma_\Sigma$  of  $S_1$  can be expressed as

$$\gamma_\Sigma = \frac{(R_1^2 + R_4^2)^2}{(R_1R_3)^2 + (R_2R_4)^2 - 2R_1R_2R_3R_4 \cos(\Theta_3 - \Theta_1 + \Theta_2 - \Theta_4) + 2\sigma_n^2 \cdot (R_1^2 + R_4^2)} \quad (\text{G.14})$$

in which  $2\sigma_n^2$  represents the variance of the noise.

### B. The Joint Probability Density Function of the Envelopes

An expression for the joint probability density function (PDF) of the envelopes  $R_1, R_2, R_3,$  and  $R_4$  is required for the performance analysis. In [9], the joint PDF  $p_{R_1R_2R_3R_4}(r_1, r_2, r_3, r_4)$  of four envelopes has been derived. The obtained expression (see [9, Eq. (16)]) is represented as

$$p_{R_1R_2R_3R_4}(r_1, r_2, r_3, r_4) = \frac{r_1r_2r_3r_4}{(2\pi)^2 E} e^{[-\frac{A}{2E}(r_1^2+r_2^2+r_3^2+r_4^2)]}$$

$$\int_0^{2\pi} \int_0^{2\pi} e^{-\frac{1}{E}[Br_3r_4 \cos(\varphi_2) + Cr_2r_4 \cos(\varphi_1 + \varphi_2) + Dr_2r_3 \cos(\varphi_1)]} I_0\left(\frac{r_1}{E} (B^2r_2^2 + C^2r_3^2 + D^2r_4^2 + 2[BCr_2r_3 \cos(\varphi_1) + BDr_2r_4 \cos(\varphi_1 + \varphi_2) + CDr_3r_4 \cos(\varphi_2)])^{(\frac{1}{2})}\right) d\varphi_1 d\varphi_2 \quad (\text{G.15})$$

where the symbols A, B, C, D, and E are given by [9, Eq. (13)]

$$A = 2\rho_T\rho_x\rho_{x,T} + \sigma_0^2(\sigma_0^4 - \rho_T^2 - \rho_x^2 - \rho_{x,T}^2), \quad (\text{G.16a})$$

$$B = 2\sigma_0^2\rho_x\rho_{x,T} - \rho_T(\sigma_0^4 - \rho_T^2 + \rho_x^2 + \rho_{x,T}^2), \quad (\text{G.16b})$$

$$C = 2\sigma_0^2\rho_T\rho_{x,T} - \rho_x(\sigma_0^4 + \rho_T^2 - \rho_x^2 + \rho_{x,T}^2), \quad (\text{G.16c})$$

$$D = 2\sigma_0^2\rho_T\rho_x - \rho_{x,T}(\sigma_0^4 + \rho_T^2 + \rho_x^2 - \rho_{x,T}^2), \quad (\text{G.16d})$$

$$E = (\sigma_0^4 - \rho_T^2)^2 + (\rho_x^2 - \rho_{x,T}^2)^2 - 2(\sigma_0^4 + \rho_T^2)(\rho_x^2 + \rho_{x,T}^2) + 8\sigma_0^2\rho_T\rho_x\rho_{x,T} \quad (\text{G.16e})$$

respectively, where  $\rho_T = r_{HH}(T_s)/2$ ,  $\rho_x = r_{HH}(\delta_T)/2$ , and  $\rho_{x,T} = r_{HH}(\delta_T, T_s)/2$ . The symbol  $T_s$  denotes the OFDM symbol duration.

### C. Derivation of the PDF of the Instantaneous Output SINR

It is shown in [10] that the differences between the phase changes  $\Theta_3 - \Theta_1$  and  $\Theta_4 - \Theta_2$  can be neglected, i.e.,  $\Theta_3 - \Theta_1 - (\Theta_4 - \Theta_2) \approx 0$ . This allows us to approximate the instantaneous output SINR  $\gamma_\Sigma$  as

$$\gamma_\Sigma \approx \frac{(R_1^2 + R_4^2)^2}{(R_1R_3 - R_2R_4)^2 + 2\sigma_n^2 \cdot (R_1^2 + R_4^2)}. \quad (\text{G.17})$$

To obtain the PDF  $p_{\gamma_\Sigma}(\gamma)$  of the instantaneous output SINR presented in (G.17), we define a system of equations as follows:

$$\begin{aligned} z_1 &= (r_1^2 + r_4^2)^2 \\ z_2 &= (r_1r_3 - r_2r_4)^2 + 2\sigma_n^2 \cdot (r_1^2 + r_4^2) \\ &= (z_3 - r_2r_4)^2 + 2\sigma_n^2 \cdot \sqrt{z_1} \\ z_3 &= r_1r_3, \quad z_4 = r_1^2. \end{aligned} \quad (\text{G.18})$$

This system of equations has the following real-valued solutions under the preconditions that  $z_3 > \sqrt{z_2 - 2\sigma_n^2 \cdot \sqrt{z_1}}$ ,  $z_4 < \sqrt{z_1}$ , and  $z_2 > 2\sigma_n^2 \cdot \sqrt{z_1}$ :

$$r_1 = \sqrt{z_4}, \quad r_2 = \frac{z_3 - \sqrt{z_2 - 2\sigma_n^2 \cdot \sqrt{z_1}}}{\sqrt{\sqrt{z_1} - z_4}}$$

$$r_3 = \frac{z_3}{\sqrt{z_4}}, \quad r_4 = \sqrt{\sqrt{z_1} - z_4}. \quad (\text{G.19})$$

The joint PDF of the random variables  $Z_1$ ,  $Z_2$ ,  $Z_3$ , and  $Z_4$  can be obtained by applying the concept of transformation of random variables [12, p. 244]. Thus,

$$p_{Z_1 Z_2 Z_3 Z_4}(z_1, z_2, z_3, z_4) = |J(z_1, z_2, z_3, z_4)| \cdot p_{R_1 R_2 R_3 R_4} \left( \sqrt{z_4}, \frac{z_3 - \sqrt{z_2 - 2\sigma_n^2 \cdot \sqrt{z_1}}}{\sqrt{\sqrt{z_1} - z_4}}, \frac{z_3}{\sqrt{z_4}}, \sqrt{\sqrt{z_1} - z_4} \right) \quad (\text{G.20})$$

where  $J(z_1, z_2, z_3, z_4)$  denotes the Jacobian determinant, which can be expressed as

$$J(z_1, z_2, z_3, z_4) = \frac{1}{16(z_1 z_4 - z_4^2 \sqrt{z_1}) \cdot \sqrt{z_2 - 2\sigma_n^2 \cdot \sqrt{z_1}}}. \quad (\text{G.21})$$

Now, integrating the joint PDF  $p_{Z_1 Z_2 Z_3 Z_4}(z_1, z_2, z_3, z_4)$  over the variables  $z_3$  and  $z_4$  results in the joint PDF  $p_{Z_1 Z_2}(z_1, z_2)$  of the random variables  $Z_1$  and  $Z_2$ , which is given by

$$p_{Z_1 Z_2}(z_1, z_2) = \int_{\sqrt{z_2 - 2\sigma_n^2 \cdot \sqrt{z_1}}}^{\infty} \int_0^{\sqrt{z_1}} \frac{1}{16(z_1 z_4 - z_4^2 \sqrt{z_1}) \cdot \sqrt{z_2 - 2\sigma_n^2 \cdot \sqrt{z_1}}} \cdot p_{R_1 R_2 R_3 R_4} \left( \sqrt{z_4}, \frac{z_3 - \sqrt{z_2 - 2\sigma_n^2 \cdot \sqrt{z_1}}}{\sqrt{\sqrt{z_1} - z_4}}, \frac{z_3}{\sqrt{z_4}}, \sqrt{\sqrt{z_1} - z_4} \right) dz_4 dz_3 \quad (\text{G.22})$$

By applying the rule presented in [12, Eq. (6-59)], the PDF of the random variable  $\gamma_\Sigma = Z_1/Z_2$  can be expressed in terms of the joint PDF  $p_{R_1 R_2 R_3 R_4}(r_1, r_2, r_3, r_4)$  as

$$p_{\gamma_\Sigma}(\gamma) = \frac{1}{16} \int_{4\sigma_0^4 \gamma / \bar{\gamma}^2}^{\infty} \int_{\zeta}^{\infty} \int_0^{\omega} \frac{z_2}{(\omega^2 z_4 - \omega z_4^2) \cdot \zeta} \cdot p_{R_1 R_2 R_3 R_4} \left( \sqrt{z_4}, \frac{z_3 - \zeta}{\sqrt{\omega - z_4}}, \frac{z_3}{\sqrt{z_4}}, \sqrt{\omega - z_4} \right) dz_4 dz_3 dz_2 \quad (\text{G.23})$$

where  $\zeta$  and  $\omega$  are defined as  $\zeta = \sqrt{z_2 - 2\sigma_0^2 \omega / \bar{\gamma}}$  and  $\omega = \sqrt{z_1} = \sqrt{\gamma z_2}$ , respectively. The variance  $2\sigma_n^2$  of the noise in (G.22) has been replaced by  $2\sigma_n^2 = 2\sigma_0^2 / \bar{\gamma}$  in which the parameter  $\bar{\gamma}$  stands for the average signal-to-noise ratio (SNR). As can

be seen in (G.23), the precondition  $z_2 > 2\sigma_n^2 \cdot \sqrt{z_1}$  results in  $z_2 > 4\sigma_0^4\gamma/\bar{\gamma}^2$ .

#### D. Derivation of the BEP

The instantaneous output BEP of the system can be obtained by using [5, Eq. (7.2)]

$$P_b = \int_0^\infty p_{\gamma\Sigma}(\gamma)P_{b|\gamma\Sigma}(\gamma)d\gamma \quad (\text{G.24})$$

where  $P_{b|\gamma\Sigma}(\gamma)$  denotes the conditional BEP of a digital modulation scheme for a specific value of  $\gamma$ . For example, for the binary phase shift keying (BPSK) modulation scheme,  $P_{b|\gamma\Sigma}(\gamma)$  is given by  $P_{b|\gamma\Sigma}(\gamma) = \text{erfc}(\sqrt{\gamma})/2$ , where  $\text{erfc}(x)$  denotes the complementary error function. Thus, the BEP  $P_b$  of the Alamouti-coded OFDM system can be computed using

$$P_b = \frac{1}{2} \int_0^\infty p_{\gamma\Sigma}(\gamma)\text{erfc}(\sqrt{\gamma})d\gamma. \quad (\text{G.25})$$

Now, by inserting (G.15) in (G.23), and then substituting  $p_{\gamma\Sigma}(\gamma)$  in (G.25), we obtain the desired exact solution of the BEP of BPSK Alamouti-coded OFDM systems as

$$\begin{aligned} P_b &= \frac{1}{128\pi^2 E} \int_0^\infty \int_{4\sigma_0^4\gamma/\bar{\gamma}^2}^\infty \int_\zeta^\omega \int_0^\omega \frac{z_2 z_3 (z_3 - \zeta)}{(\omega^2 z_4 - \omega z_4^2) \cdot \zeta} \cdot e^{-\frac{A}{2E} \left[ \frac{(z_3 - \zeta)^2}{\omega - z_4} + \omega + \frac{z_3^2}{z_4} \right]} \text{erfc}(\sqrt{\gamma}) \int_0^{2\pi} \int_0^{2\pi} \\ &I_0 \left( \frac{\sqrt{z_4}}{E} \left( B^2 \frac{(z_3 - \zeta)^2}{\omega - z_4} + C^2 \frac{z_3^2}{z_4} + D^2 (\omega - z_4) + 2[BC \frac{(z_3^2 - \zeta z_3)}{\sqrt{z_4 \omega - z_4^2}} \cos \varphi_1 \right. \right. \\ &\left. \left. + BD(z_3 - \zeta) \cos(\varphi_1 + \varphi_2) + CD \frac{z_3 \sqrt{\omega - z_4}}{\sqrt{z_4}} \cos \varphi_2] \right)^{(1/2)} \right) \\ &e^{-\frac{1}{E} [B \frac{z_3 \sqrt{\omega - z_4}}{\sqrt{z_4}} \cos \varphi_2 + C(z_3 - \zeta) \cos(\varphi_1 + \varphi_2) + D \frac{(z_3^2 - \zeta z_3)}{\sqrt{z_4 \omega - z_4^2}} \cos \varphi_1]} d\varphi_1 d\varphi_2 dz_4 dz_3 dz_2 d\gamma \quad (\text{G.26}) \end{aligned}$$

where the function  $I_0(\cdot)$  is the zeroth-order modified Bessel function of the first kind. In the following, we will discuss two special cases where the UWA channel is correlated either in time or space. If we set  $\rho_x = \rho_{x,T} = 0$  and  $\rho_T \neq 0$ , then the BEP in (G.26) reduces to

$$P_b = \frac{1}{32(\sigma_0^4 - \rho_T^2)} \int_0^\infty \int_{4\sigma_0^4\gamma/\bar{\gamma}^2}^\infty \int_\zeta^\omega \int_0^\omega \frac{z_2 z_3 (z_3 - \zeta)}{(\omega^2 z_4 - \omega z_4^2) \cdot \zeta} I_0 \left( \frac{\sqrt{z_4} (z_3 - \zeta) \rho_T}{\sqrt{\omega - z_4} (\sigma_0^4 - \rho_T^2)} \right)$$

$$\cdot I_0 \left( \frac{z_3 \sqrt{\omega - z_4} \rho_T}{\sqrt{z_4} (\sigma_0^4 - \rho_T^2)} \right) e^{-\frac{\sigma_0^2}{2(\sigma_0^4 - \rho_T^2)} \left[ \frac{(z_3 - \zeta)^2}{\omega - z_4} + \omega + \frac{z_3^2}{z_4} \right]} \operatorname{erfc}(\sqrt{\gamma}) dz_4 dz_3 dz_2 d\gamma \quad (\text{G.27})$$

which presents the performance of the Alamouti-coded OFDM system over a UWA channel that is only correlated in time. Analogously, if we consider the Alamouti-coded OFDM system over the UWA channel that is only correlated in space, i.e.,  $\rho_T = \rho_{x,T} = 0$  and  $\rho_x \neq 0$ , then the BEP in (G.26) reduces to

$$P_b = \frac{1}{32(\sigma_0^4 - \rho_x^2)} \int_0^\infty \int_{4\sigma_0^4\gamma/\gamma^2}^\infty \int_\zeta^\infty \int_0^\omega \frac{z_2 z_3 (z_3 - \zeta)}{(\omega^2 z_4 - \omega z_4^2) \cdot \zeta} I_0 \left( \frac{z_3 \rho_x}{\sigma_0^4 - \rho_x^2} \right) \cdot I_0 \left( \frac{(z_3 - \zeta) \rho_x}{\sigma_0^4 - \rho_x^2} \right) e^{-\frac{\sigma_0^2}{2(\sigma_0^4 - \rho_x^2)} \left[ \frac{(z_3 - \zeta)^2}{\omega - z_4} + \omega + \frac{z_3^2}{z_4} \right]} \operatorname{erfc}(\sqrt{\gamma}) dz_4 dz_3 dz_2 d\gamma. \quad (\text{G.28})$$

## VI. NUMERICAL RESULTS

In this section, we illustrate the theoretical BEP results presented in (G.26), (G.27), and (G.28) for different maximum Doppler frequencies  $f_{\max}^R$  and different normalized transmit hydrophone spacings  $\delta_T/\lambda$ . The correctness of the theoretical results has been confirmed by system simulations. In the simulation setup, an OFDM system with  $K = 64$  subcarriers and channel bandwidth  $B = 4000$  Hz is considered. The symbol duration  $T_s$  equals 16 ms, and the central carrier frequency  $f_c$  has been set to 10 kHz. The speed of sound  $c_s$  is assumed to be 1500 m/s which results in a wavelength  $\lambda$  of 15 cm. The remaining parameters have been set as follows:  $y_1^T = y_2^T = y_1^R = y_2^R = 50$  m,  $D = 1$  km and  $\alpha_v^R = 0$ . As mentioned in Section III-B, for the parametrization of the UWA channel simulator the MESS has been used.

The BEP performance of the Alamouti-coded OFDM system over the spatio-temporally correlated UWA channel is shown in Fig. G.2 for different maximum Doppler frequencies  $f_{\max}^R$  and different hydrophone spacings  $\delta_T$ . It can be concluded that both the maximum Doppler frequencies and hydrophone spacing influence the system performance. With reference to Fig. G.2, the BEP described in (G.26) fits closely to the one obtained by simulations.

Fig. G.3 illustrates the BEP performance of an Alamouti-coded OFDM system for the special case where the UWA channel is only correlated in time for  $f_{\max}^R = 5$  Hz and  $f_{\max}^R = 50$  Hz (see (G.27)). As can be seen in this figure, the BEP performance experiences a degradation if the maximum Doppler frequency  $f_{\max}^R$  increases.

For the special case that the UWA channel is only correlated in space, the BEP performance of Alamouti-coded OFDM systems is depicted in Fig. G.4 for differ-

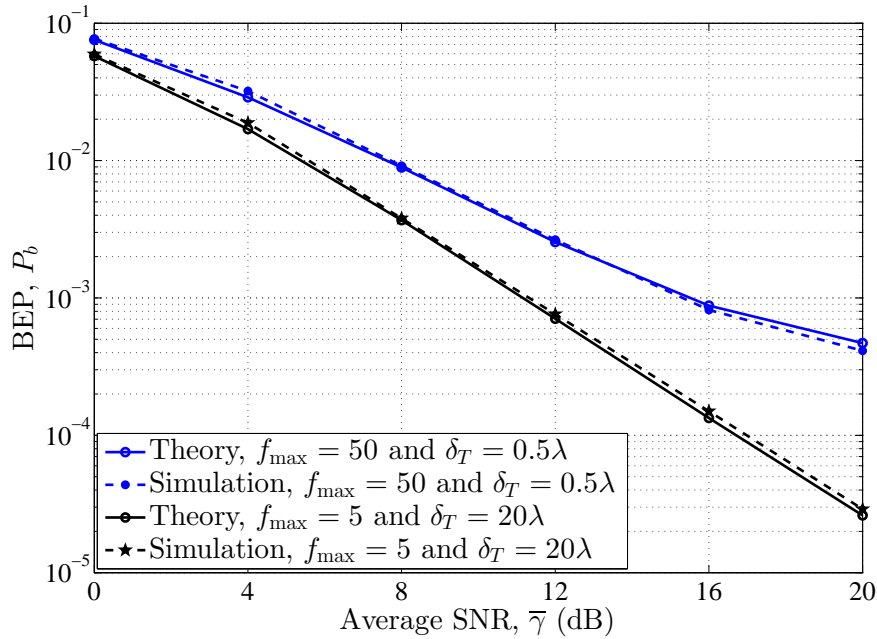


Figure G.2: The BEP performance of an Alamouti-coded OFDM system over an UWA channel correlated in space and time for different values of the maximum Doppler frequencies  $f_{\max}^R = 5$  Hz and  $f_{\max}^R = 50$  Hz and hydrophone spacing  $\delta_T = 0.5\lambda$  and  $\delta_T = 20\lambda$ .

ent hydrophone spacings  $\delta_T = 0.5\lambda$  and  $\delta_T = 20\lambda$  (see (G.28)). From this figure, we can conclude that the performance improves if the hydrophone spacing  $\delta_T$  increases. As can be observed the figures, the theoretical results have been validated by simulation results.

## VII. CONCLUSION

In this paper, the performance of Alamouti-coded OFDM systems over a proposed UWA channel correlated in time and/or space has been analyzed. The channel envelope can change during two consecutive transmission time slots which accounts for realistic UWA propagation scenarios. An exact analytical expression for the BEP of the system has been derived for a spatio-temporally correlated UWA channel. The derived expression for the BEP has been reduced to the special cases that the UWA channel is either correlated in time or correlated in space. The simulation results show that the performance of Alamouti-coded OFDM systems over the UWA channel depends strongly on the value of the STVCTF evaluated at the symbol duration and the antenna separation.

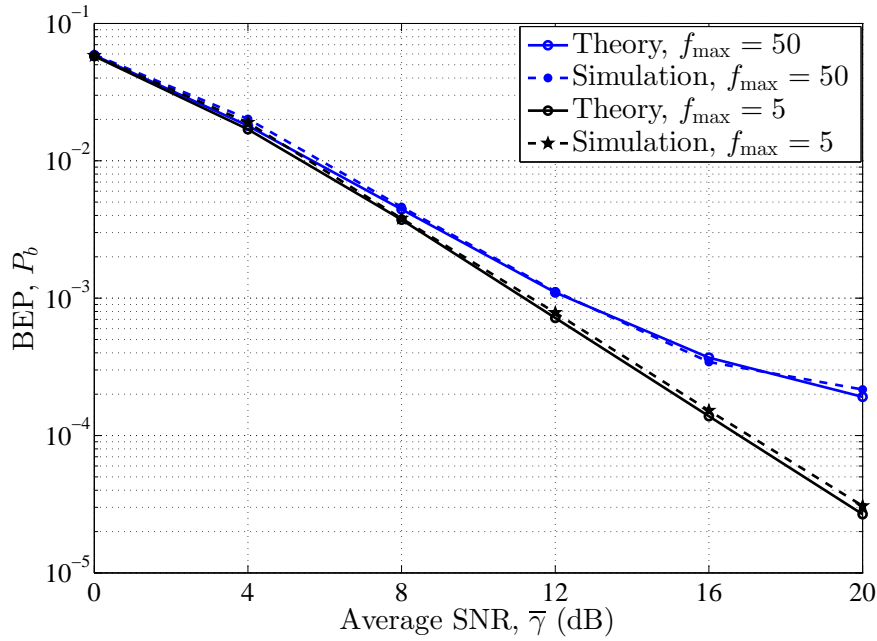


Figure G.3: The BEP performance of an Alamouti-coded OFDM system over UWA channels, which are only correlated in time for different values of the maximum Doppler frequencies  $f_{\max}^R = 5$  Hz and  $f_{\max}^R = 50$  Hz.

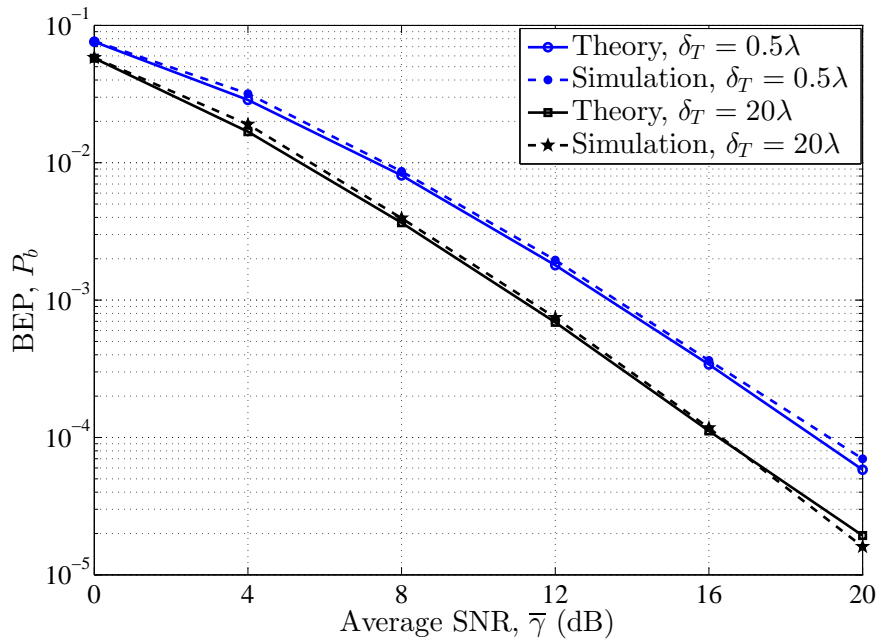


Figure G.4: The BEP performance of an Alamouti-coded OFDM system over UWA channels, which are only correlated in space for different values of the hydrophone spacing  $\delta_T = 0.5\lambda$  and  $\delta_T = 20\lambda$ .

## PAPER G: REFERENCES

- [1] G. Abreu and R. Kohno. Non-differential space-time transmission diversity in fast fading. In *Proc. 13th IEEE Int. Symp. Pers., Indoor and Mobile Radio Commun. (PIMRC)*, pages 74–78, Lisbon, Portugal, Sep. 2002.
- [2] S. M. Alamouti. A simple transmit diversity technique for wireless communications. *IEEE J. Sel. Areas Commun.*, 16(8):1451–1458, October 1998.
- [3] T. M. Duman and A. Ghrayeb. *Coding for MIMO Communication Systems*. Chichester: John Wiley & Sons, 2007.
- [4] H. Eghbali, M. Stojanovic, and S. Muhaidat. Differential decoding for SFBC OFDM systems in underwater MIMO channels. In *Proc. IEEE Int. Conf. Acoustics, Speech and Signal Processing (ICASSP)*, pages 8102–8105, May 2014.
- [5] A. Goldsmith. *Wireless Communications*. Cambridge University Press, 2005.
- [6] B. Li et al. MIMO-OFDM for high-rate underwater acoustic communications. *IEEE J. Ocean. Eng.*, 34(4):634–644, Oct. 2009.
- [7] B. Li and M. Stojanovic. A simple design for joint channel estimation and data detection in an Alamouti OFDM system. In *IEEE OCEANS*, pages 1–5, Sep. 2010.
- [8] Y. Ma and M. Pätzold. Performance comparison of space-time coded MIMO-OFDM systems using different wideband MIMO channel models. In *Proc. 4th IEEE Int. Symp. Wireless Commun. Syst. (ISWCS)*, pages 762–766, Trondheim, Norway, Oct. 2007.
- [9] Y. Ma and M. Pätzold. Performance analysis of Alamouti coded OFDM systems over Rayleigh fading channels correlated in space and time. In *Proc. IEEE 71st Vehicular Technol. Conf. (VTC), Spring*, pages 1–6, Taipei, Taiwan, May 2010.
- [10] Y. Ma and M. Pätzold. Performance analysis of STBC-OFDM systems in temporally and spatially correlated fading channels. In *Proc. Wireless Commun. and Netw. Conf. (WCNC)*, pages 1–5, Sydney, Australia, Apr. 2010.

## PAPER G: REFERENCES

- [11] M. Naderi, M. Pätzold, and A. G. Zajić. A geometry-based channel model for shallow underwater acoustic channels under rough surface and bottom scattering conditions. In *Proc. 5th Int. Conf. Commun. and Electron. (ICCE)*, pages 112–117, DaNang, Vietnam, Jul./Aug. 2014.
- [12] A. Papoulis. *Probability, Random Variables, and Stochastic Processes*. New York, NY, USA: McGraw-Hill, 4rd edition, 2002.
- [13] M. Pätzold. *Mobile Fading Channels*. Chichester, U.K.: John Wiley & Sons, 2nd edition, 2011.
- [14] M. Stojanovic. MIMO OFDM over underwater acoustic channels. In *Proc. IEEE Conf. Signals, Syst. and Computers (ASILOMAR), Conf. Record of the Forty-Third Asilomar*, pages 605–609, Nov. 2009.
- [15] V. Tarokh, H. Jafarkhani, and A. R. Calderbank. Space-time block coding for wireless communications: performance results. *IEEE J. Sel. Areas Commun.*, 17(3):451–460, March 1999.
- [16] E. V. Zorita and M. Stojanovic. Space-frequency block coding for underwater acoustic communications. *IEEE J. Ocean. Eng.*, 40(2):303–314, Apr. 2015.

## **PAPER G: REFERENCES**